The Ross Ice Shelf Geophysical and Glaciological Survey (RIGGS): Introduction and Summary of Measurements Performed

Charles R. Bentley

Glaciological Studies on the Ross Ice Shelf, Antarctica, 1973–1978

Robert H. Thomas, Douglas R. MacAyeal, David H. Eilers, and David R. Gaylord

Papers 1 and 2 in

The Ross Ice Shelf: Glaciology and Geophysics
Antarctic Research Series Volume 42

Charles R. Bentley and Dennis E. Hayes, Editors

American Geophysical Union

THE ROSS ICE SHELF: GLACIOLOGY AND GEOPHYSICS
Antarctic Research Series Volume 42

CHARLES R. BENTLEY AND DENNIS E. HAYES, EDITORS

Published under the aegis of the
Board of Associate Editors, Antarctic Research Series
Charles R. Bentley, Chairman
Samuel C. Colbeck, Robert H. Eather, David H. Elliot, Dennis E. Hayes, Louis S. Kornicker, Heinz H. Lettau, and Bruce C. Parker

Library of Congress Cataloging in Publication Data
Forthcoming
ISBN 0-87590-195-6
ISSN 0066-4634

Published by the
AMERICAN GEOPHYSICAL UNION
With the aid of grant DPP-80-19997 from the National Science Foundation

Printed in the United States of America

Seismic Studies on the Grid Western Half of the Ross Ice Shelf: RIGGS I and RIGGS II

James D. Robertson and Charles R. Bentley

Seismic Studies on the Grid Eastern Half of the Ross Ice Shelf: RIGGS III and RIGGS IV

Donald G. Albert and Charles R. Bentley

RIGGS III: Seismic Short-Refraction Studies Using an Analytical Curve-Fitting Technique

Joseph F. Kirchner and Charles R. Bentley

Papers 3, 4, and 5 in

The Ross Ice Shelf: Glaciology and Geophysics
Antarctic Research Series Volume 42

Charles R. Bentley and Dennis E. Hayes, Editors

American Geophysical Union

THE ROSS ICE SHELF: GLACIOLOGY AND GEOPHYSICS
Antarctic Research Series Volume 42

CHARLES R. BENTLEY AND DENNIS E. HAYES, EDITORS

Published under the aegis of the
Board of Associate Editors, Antarctic Research Series
Charles R. Bentley, Chairman
Samuel C. Colbeck, David H. Elliot, E. Imre Freidmann, Dennis E. Hayes, Louis S. Kornicker, John Meriwether, and Charles R. Stearns

Library of Congress Cataloging in Publication Data
Forthcoming
ISBN 0-87590-195-6
ISSN 0066-4634

Published by the
AMERICAN GEOPHYSICAL UNION
With the aid of grant DPP-89-15494 from the National Science Foundation

Printed in the United States of America

The Ross Ice Shelf: Glaciology and Geophysics
Antarctic Research Series, Volume 42, Paper 1, Pages 1-20

THE ROSS ICE SHELF GEOPHYSICAL AND GLACIOLOGICAL SURVEY (RIGGS): INTRODUCTION AND SUMMARY OF MEASUREMENTS PERFORMED

Charles R. Bentley

Geophysical and Polar Research Center, University of Wisconsin
Madison, Wisconsin 53706

Abstract. By the end of the 1960's the Ross Ice Shelf was already one of the better explored regions in Antarctica, yet glaciological and geophysical measurements had been limited largely to studies at Little America, the International Geophysical Year traverse loop around the shelf, and an L-shaped movement survey. Consequently, when plans were being made for drilling an access hole to the ocean beneath the interior of the shelf, it was decided to conduct an airlifted survey covering the entire ice shelf: the Ross Ice Shelf Geophysical and Glaciological Survey (RIGGS). Measurements of many kinds were carried out at the 200 RIGGS stations over the 5-year period 1973-1978. Quantities determined included accumulation rate, strain rate, ice thickness, subglacial water depth, and gravity at 75-95% of the sites; temperatures and movement rate at 40-50% of the sites; seismic and radio wave velocities and electrical resistivities at 10-20 sites; and radar polarization at six sites. More extensive programs, including core drilling to 50-100 m, tidal-gravity recording, and long seismic refraction profiles to investigate submarine geologic structure, were carried out at 10 primary and supplementary base camps. In addition, 13,500 km of airborne radar sounding were completed. Detailed seasonal tabulations of the types and locations of measurements are presented in this paper, along with a brief season-by-season narrative.

Introduction

The Ross Ice Shelf is a tabular mass of thick, permanent (on a human time scale) floating ice attached to the grounded Antarctic ice sheet. Lying between 160°E and 150°W longitude and 78°S and 85°S latitude and bounded on the south and west by the Transantarctic Mountains, on the north by the Ross Sea, and on the east by Marie Byrd Land (Figure 1), the shelf covers about 520,000 km^2 (slightly larger than Spain; slightly smaller than France). It has been a familiar feature of the southern continent since it was discovered by James Clark Ross, aboard Erebus and Terror in 1841. Roald Amundsen (from "Framheim" next to the Bay of Whales) and Robert F. Scott (from Ross Island) both used the Ross Ice Shelf as an access to the deeper interior of the continent, and Wright and Priestley [1922], with Scott's expedition of 1910-1913, carried out extensive studies of the ice shelf in the vicinity of Ross Island.

Pre-RIGGS Measurements

Measurements of surface heights across the ice shelf were made on both Scott's and Amundsen's 1911-1912 journeys to the south pole (Figure 2). Along Scott's route the height increased to 50 m at 79°S and then remained essentially constant to 83°S, a fact taken as a clear demonstration that the ice shelf is afloat [Wright and Priestley, 1922; Simpson, 1923; Wright, 1925]. The same flat character was found on Amundsen's route across the eastern ice shelf, along which the corresponding figure was 60 m [Mohn, 1915; Simpson, 1919]. Amundsen's eastern party under K. Prestrud also discovered the grounded ice of Roosevelt Island, measuring a maximum surface elevation of about 260 m some 65 km south of "Framheim."

Further confirmation that the ice shelf is afloat came with the first inland measurement of its movement rate. "The fortunate rediscovery of one of Scott's Discovery depots by members of Shackleton's Nimrod Expedition gives a good average value for the movement of this point in an interval of 6 1/2 years. Roughly, the annual movement off Minna Bluff was found to be about 500 yards in a north-northeasterly direction. The rate of movement is large . . . and may possibly be taken as confirmation of the fact that the Ross Barrier is generally afloat" [Wright, 1925]. That same rediscovery also led to the first measurement of accumulation rate in the interior, an average of 7 1/2 in./yr (190 mm/yr) of water over 6 1/2 years. (The nearest RIGGS measurements of velocity and accumulation rate, at a point 50 km to the south, are 660 m/yr along azimuth 030° and 160 mm/yr of water.)

The second Antarctic expedition based at the Bay of Whales was Rear Admiral Richard E. Byrd's First Antarctic Expedition, 1928-

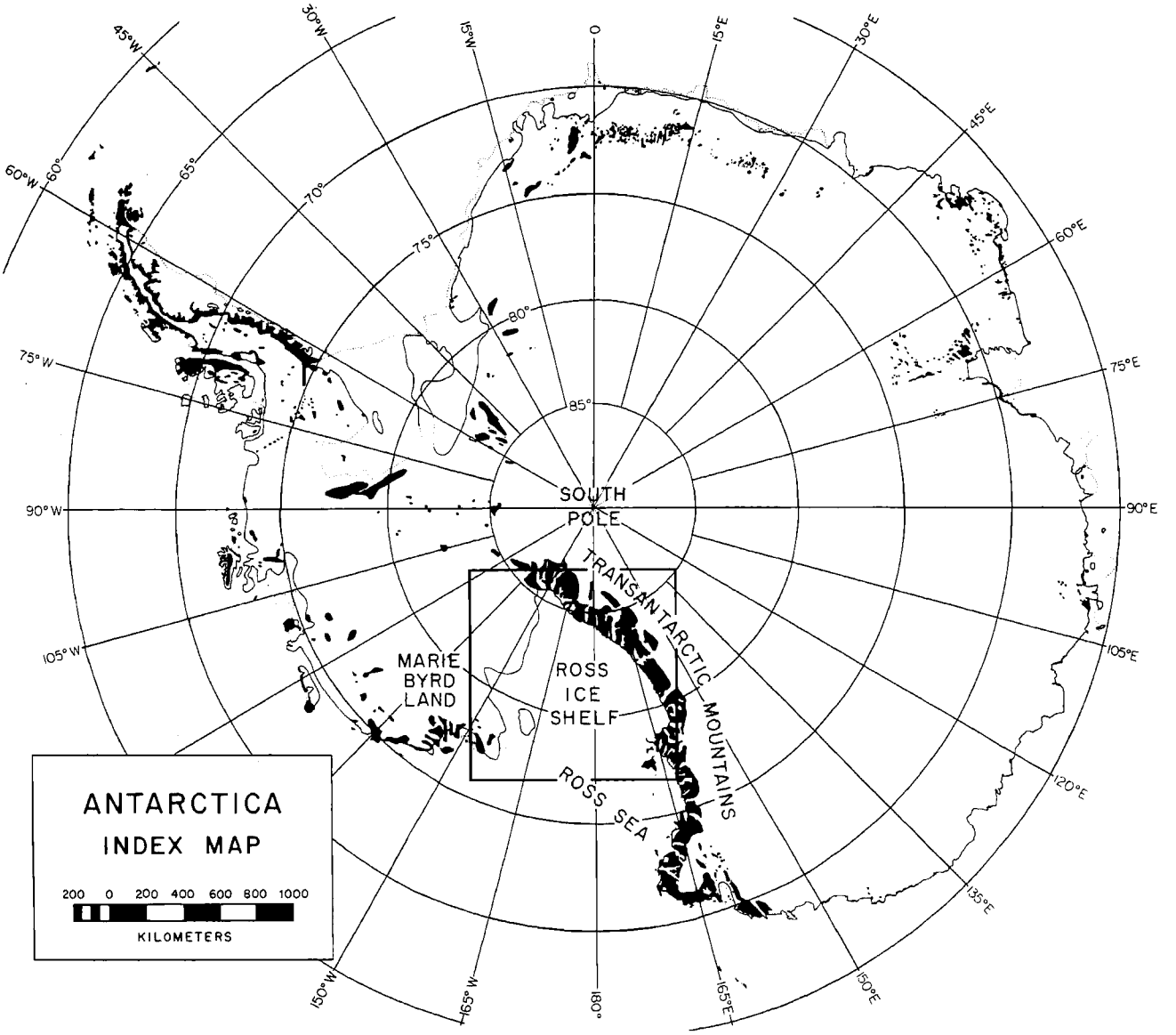

Fig. 1. Index map of Antarctica. Maps of the Ross Ice Shelf in Figures 2-4 cover the area outlined.

1930, which established "Little America" on the eastern side of the bay in January 1929. One important scientific accomplishment of that expedition was the sledging journey across the Ross Ice Shelf to the Queen Maud Mountains by a party under the direction of Byrd's chief scientist, L. M. Gould. Gould's principal contribution was in his geological studies, but he did also observe that the ice shelf itself probably moved at a rate of more than 5 ft/d (550 m/yr) and was mostly floating except where heavily crevassed [Gould, 1935].

Geophysical investigation of the shelf was inaugurated by T. C. Poulter during the Second Byrd Antarctic Expedition, 1933-1935. Using a Seismograph Service Corporation seismic system, Poulter recorded seismic shots at 122 locations around the Bay of Whales. He also successfully employed a modified McComb-Romberg seismograph containing a horizontal pendulum as a tilt meter to measure tilting of the ice at Little America in response to ocean tidal displacement. Among the scientific results of Poulter's seismic survey were direct confirmations that the ice shelf was floating to at least 10 miles (16 km) south of the barrier and that the ice rise southeast of Little America, named Roosevelt Island by

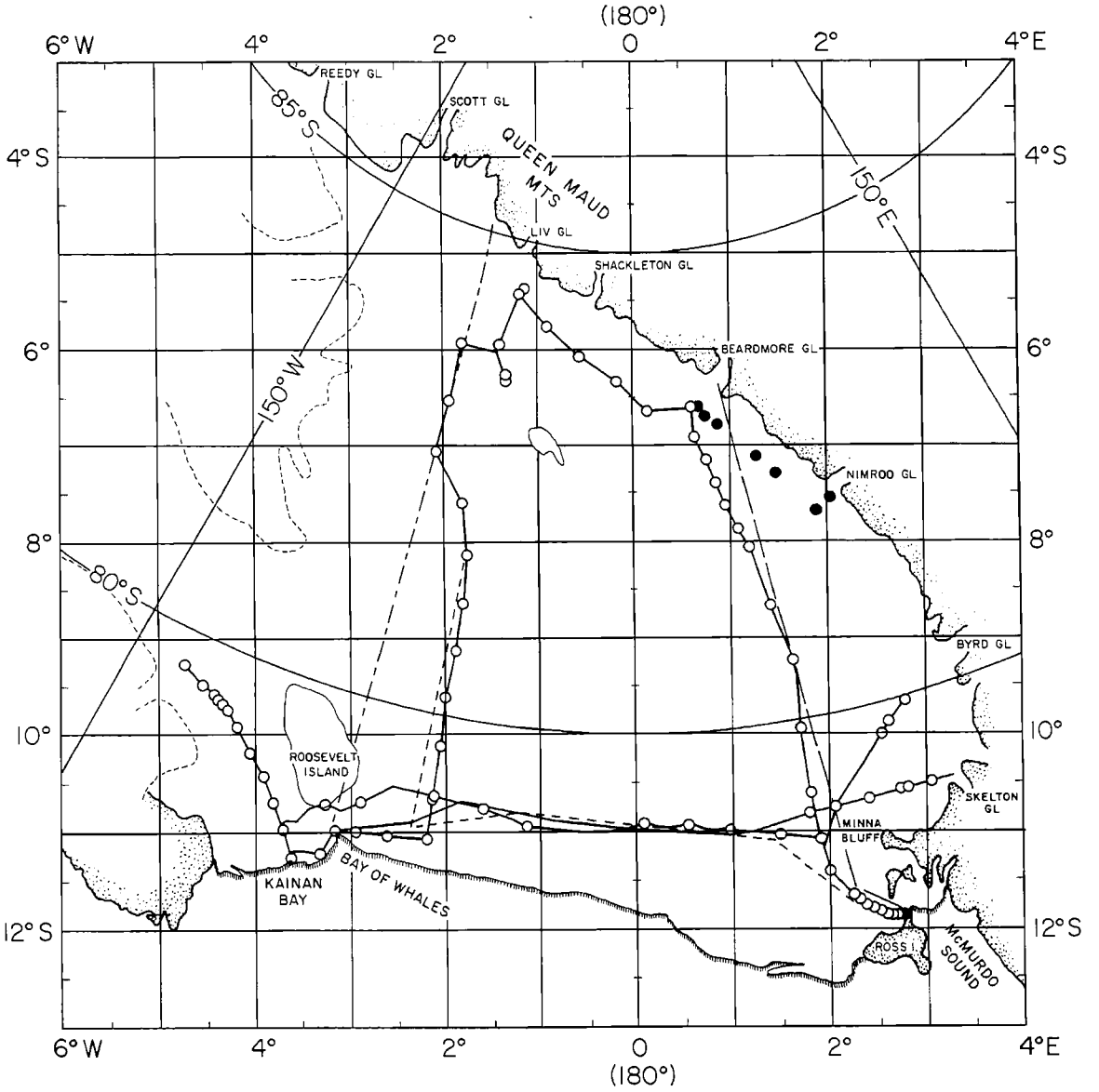

Fig. 2. Map of Ross Ice Shelf, showing stations and travel routes from which quantitative data were collected prior to RIGGS. Open circles and connecting track denote seismic traverses 1957-1960 (the circles denote seismic reflection stations). Solid circles denote movement measurements by Swithinbank [1963]. The long dashed line represents Scott's route 1911-1912; the long-and-short-dashed line, Amundsen's route 1911-1912; and the short-dashed line, Ross Ice Shelf Survey 1959-1966. The IGY "Little America V" station was at Kainan Bay.

Byrd, was grounded [Poulter, 1947a]. Poulter's actual values of ice thickness and depth to the ocean floor are in error, because in assigning a seismic wave velocity to the ice shelf he made the assumption, subsequently proven incorrect, that unfrozen seawater saturated the shelf below sea level.

Early measurements on the physical properties of the Ross Ice Shelf were made between February 1940 and January 1941 by Wade [1945]. Unfortunately, owing to the failure of Byrd's giant, wheeled, oversnow vehicle (the "Snow Cruiser"), the early termination of the Antarctic Service Expedition because of World War II, and his own commitment to the geological program, Wade's measurements were restricted to the immediate vicinity of Little America III (also located on the Bay of Whales).

Nevertheless, Wade (with L. A. Warner) was able to study densities, crystal sizes and orientation, and compaction rates in a 7-m snow pit, to measure the surface accumulation (840 mm of snow in 348 days), to determine the temperature at 15 different depths down to 41 m, and to demonstrate that the compaction rates depended upon the temperature in the firn. Wade's deep pit was studied in early 1957 by a party from the International Geophysical Year (IGY) station at Little America V on Kainan Bay (Figure 2), and data were obtained for the snow accumulation for the 17.6 elapsed years [Hoinkes, 1962].

Glaciological and geophysical investigations on the Ross Ice Shelf during the IGY years involved winter studies at the stations in 1957, 1958, and 1959 and summer and fall traverses in 1957-1958, 1958-1959, and 1959-1960.

The principal 1957 and 1958 winter studies at Little America V (LAS) involved (1) seismic measurements of ice thickness and water depth, (2) snow studies in a 20-m pit and on cores augered to a total depth of 40 m, (3) temperature observations to 11 m over a period of 20 months, (4) snow accumulation determinations from a network of over 100 stakes, from strain gauge compaction studies in the deep pit, and from oxygen isotope studies on 165 samples taken from depths between 15 and 19 m in the deep pit, (5) horizontal strain measurements from a network survey of 20 stakes through a period of 600 days, (6) oceanographic observations in Kainan Bay, including tidal current measurements coordinated with gravity meter observations at the station over a period of 31 days, and (7) a seismic refraction profile to determine sediment thickness seafloor seismic velocities [Crary, 1961a, b; Thiel et al., 1960].

In the winter of 1959 a reduced traverse crew at Scott Base carried out a glaciological program on the Ross Ice Shelf near McMurdo Sound [Stuart and Bull, 1963].

The summer and fall traverses were designed to obtain elevations by altimetry, to determine ice thickness and water depth from seismic observations, to measure gravity and magnetism, and to ascertain the annual accumulation rate of snow from pit stratigraphy over as large an area as possible. The traverses that worked all or partially on the Ross Ice Shelf (see Figure 2) included (1) the Ross Ice Shelf Traverse (RIST) from LAS counterclockwise around the ice shelf, (2) a 1958 fall traverse that extended RIST 250 km southeastward from LAS, (3) the 1958-1959 Victoria Land Traverse I, which crossed the Ross Ice Shelf from LAS to Skelton Glacier, adding traverse stations from Minna Bluff to Skelton Glacier, where a measurement was made of the volume of ice discharged into the Ross Ice Shelf using seismic sounding of ice thickness across Skelton Inlet (the embayment in front of Skelton Glacier) and the movement of stakes set out along the seismic line and resurveyed on return of the traverse 68 days later (an extension of RIST was also made on the return of this traverse from Minna Bluff to McMurdo Station), (4) the 1959-1960 Victoria Land Traverse II, which added more stations between McMurdo Station and the Skelton Inlet, and (5) a fall traverse in 1960 from McMurdo Station toward Byrd Glacier [Crary et al., 1962; Wilson and Crary, 1961; Stuart and Heine, 1961; Bennett, 1964].

In 1958-1959 an airlifted traverse studied ice thickness, subglacial rock topography, and ice movement across the 15-km-wide contact zone between the Ross Ice Shelf and the continental ice sheet near 80°S, 150°W [Thiel and Ostenso, 1961].

Deep drilling in the ice at LAS was started in October 1958 by the Snow, Ice and Permafrost Research Establishment (now the Cold Regions Research and Engineering Laboratory) of the U.S. Army. The hole at LAS was drilled to a depth of 255 m, where a crack permitted seawater to enter [Ragle et al., 1960]. Core recovery was nearly 100%, and the cores have been extensively investigated.

A special research project of IGY was undertaken to study the deformation of the Ross Ice Shelf north of Roosevelt Island in the summers of 1957-1958 and 1958-1959. The area between Roosevelt Island and the Bay of Whales contains a system of parallel crevasses and intersecting ridges and troughs; because the structural features are analogous to those of deformed sedimentary rocks, the project was designed as a model study of conventional geological structures. The observations included triangulation, topographic mapping of deformed ice layers, temperature measurements in the ice, snow accumulation, and measurements of strain [Zumberge et al., 1960; Kehle, 1964].

In 1960-1962, Swithinbank [1963] carried out ice movement rates related to the Ross Ice Shelf when he measured the velocities of seven outlet glaciers flowing through the Transantarctic Mountains. Ice thicknesses were calculated from gravity observations on the grounded glaciers and from elevation measurements on those that are floating. This work led to an estimate of the mass flux into the ice shelf [Giovinetto et al., 1966]. C. W. M. Swithinbank (personal communication, 1979) also measured ice shelf velocities at seven sites on the ice shelf between Beardmore and Nimrod Glaciers (Figure 2, solid circles).

The next important program was the Ross Ice Shelf Survey (RISS), which comprised measurements of the velocity vectors and snow accumulation rates along a trail from Ross Island nearly to Roosevelt Island, thence southward for about 300 km (Figure 2). Markers were set out for the movement measurements in the summer of 1962-1963 [Hofmann et al., 1964], and

the remeasurement was carried out in 1965-1966 [Dorrer et al., 1969]. As part of the 1962-1963 survey, snow accumulation was measured at 1800 bamboo poles along the "Dawson Trail" between Little America V and McMurdo stations; the heights of the poles had previously been measured during 1959-1960 [Heap and Rundle, 1964].

Also during the 1960's, a glaciological and geophysical program was carried out on Roosevelt Island. The field program was inaugurated in 1961-1962 to determine the mass balance, strain rates, velocities, and thickness of the ice dome and to measure the physical characteristics of the ice-bedrock interface and the underlying rock. The first survey was completed in the 1962-1963 season [Clapp, 1965], and the resurvey was carried out in 1967-1968 (unpublished reports by J. L. Clapp [1970], M. P. Hochstein [1965], and C. R. Bentley [1966]; see also Thomas et al. [1980]).

During the 1960's early studies of electromagnetic wave propagation in the ice were begun. A. H. Waite continued his pioneering radar work of the IGY in 1961-1962 and the next two seasons, when he made the first airborne ice thickness sounding surveys over, among other places, the marginal parts of the Ross Ice Shelf. Detailed studies on the McMurdo Ice Shelf, Skelton Glacier, and Roosevelt Island were undertaken in 1964-1965 using Waite's equipment [Jiracek and Bentley, 1971].

In 1967-1968 there began a long and fruitful series of radar sounding flights carried out in a joint United States-United Kingdom program. Many of these sounding flights crossed the Ross Ice Shelf, leading to a much improved map of the ice shelf thickness [Robin, 1975]. Data were collected by personnel at the Scott Polar Research Institute (SPRI) using SPRI equipment mounted on a U.S. C-130 Hercules aircraft.

RISP/RIGGS

Soon after the successful completion of the borehole at Little America V there was speculation on the possibility of drilling a hole several hundred kilometers inland from the ice front. In 1969, J. W. Brodie suggested a multidisciplinary study centered around a drill hole through the Ross Ice Shelf so it would be possible to study not only the ice but also the ocean and ocean floor beneath the ice shelf. Such a hole would thus be of great interest not only to glaciologists but also to oceanographers, biologists, and geologists.

This suggestion was enthusiastically received, and planning for the Ross Ice Shelf Project (RISP) began, both nationally in the United States and internationally through the Scientific Committee for Antarctic Research in 1970 [Zumberge, 1971]. It was apparent from the outset that a survey of ice thicknesses and water depths below the ice would be necessary in order to find an optimum site for the drill hole, and it was soon recognized that the value of the survey would be greatly enhanced if it were viewed as part of a comprehensive geophysical and glaciological program for study of the whole Ross Ice Shelf and the solid earth beneath. Consequently, in 1973-1974 the Ross Ice Shelf Geophysical and Glaciological Survey (RIGGS) commenced under the direction of the Geophysical and Polar Research Center, University of Wisconsin-Madison; it continued, with a hiatus in 1975-1976, through the austral summer of 1977-1978. (The early objective of the survey, to select a site for the RISP drill hole, was attained in the first season. For reports on RISP, see Clough and Hanson [1979] and the series of papers that follow in the same issue of Science.)

The RIGGS program was a cooperative effort involving the Geophysical and Polar Research Center at the University of Wisconsin-Madison (radar sounding, seismic reflection and refraction measurements, resistivity soundings, and gravity surveys), the University of Maine-Orono (measurements of strain rate, 10-m temperature, and surface accumulation), the U.S. Geological Survey (absolute movement of the ice), and the University of Copenhagen (accumulation and oxygen isotope studies). Associated studies were carried out by the University of Nevada Desert Research Institute (near-surface snow studies in 1974-1975), State University of New York at Buffalo (SUNY-Buffalo; shallow core drilling in 1976-1977 and 1977-1978), and Virginia Polytechnic Institute and State University (V.P.I.; ocean tide observations beneath the shelf during all four seasons).

In the planning for RIGGS it was agreed to use a rectangular "grid" system of coordinates. Grid directions and positions refer to a transverse Mercator system that has its origin at the south pole, its equator along longitudes 90°W to 90°E, and its prime meridian along longitudes 0°-180°. Grid north is toward Greenwich. The grid system has the advantages of rectangular coordinates and uniform azimuthal directions; it maintains the familiar sense of the points of the compass, and regional maps fit without rotation into a map of Antarctica as a whole. It is used henceforth throughout this volume.

Methods and Techniques

Each season's work involved setting up one or two base camps around which detailed local surveys were conducted and from which remote stations, positioned roughly on a 55-km grid (Figure 3), were occupied by means of De Havi-

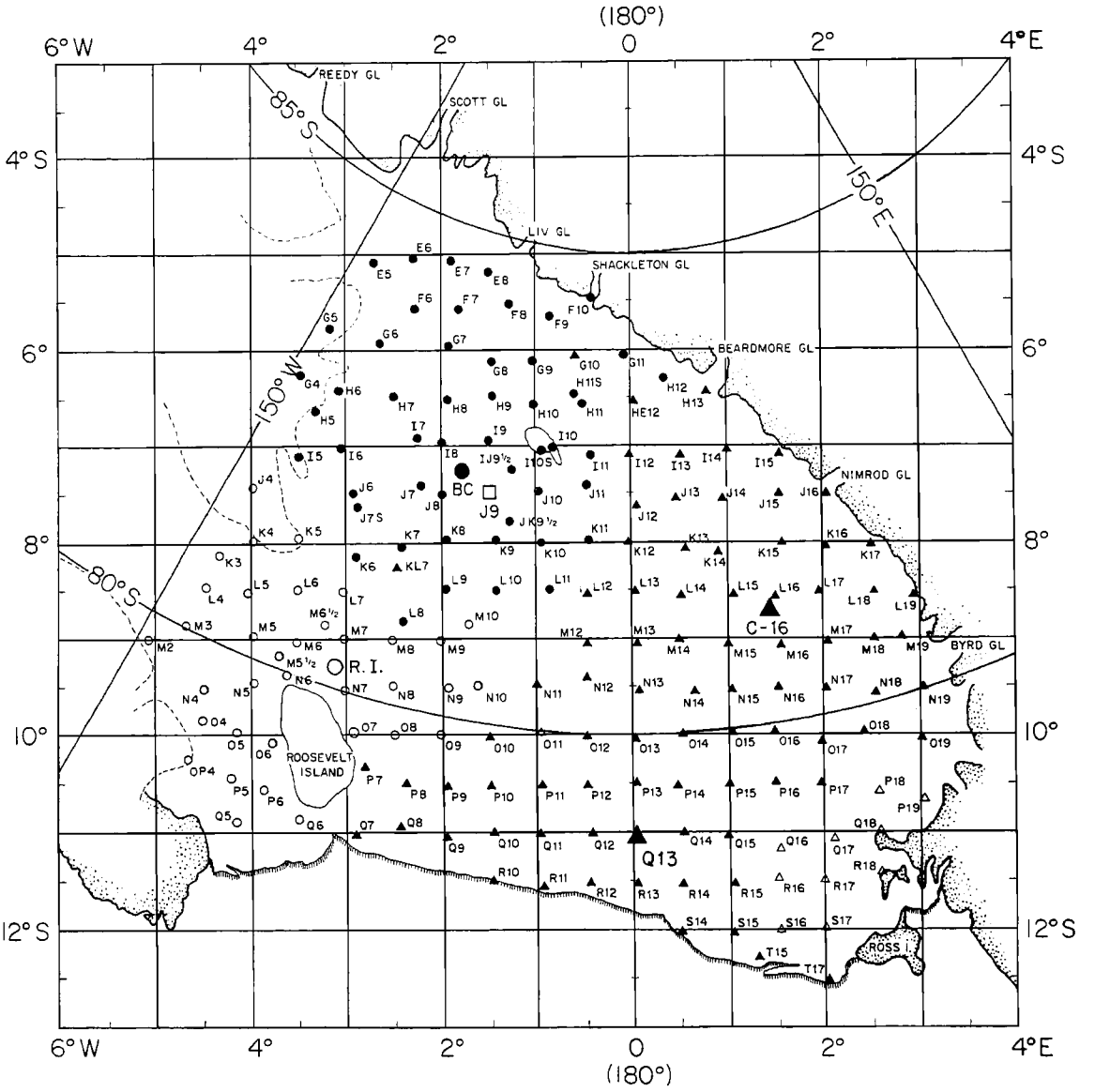

Fig. 3. Map of Ross Ice Shelf, showing RIGGS surface stations. RIGGS I (1973-1974) stations are represented by solid circles, RIGGS II (1974-1975) by open circles, RIGGS III (1976-1977) by solid triangles, and RIGGS IV (1977-1978) by open triangles. The large symbols denote base camps. The open square labeled J9 is the RISP drill site, which was the location of extensive RIGGS surface measurements.

land Twin Otter aircraft. The basic program for each site comprised the establishment (and subsequent remeasurement) of strain networks, gravity observations, and both radar and seismic sounding. Since high-frequency radio waves do not penetrate seawater, whereas seismic waves are reflected poorly from the ice-water boundary but strongly from the seafloor, the primary design of the sounding program was to combine radar measurements of ice thickness with seismic measurements of water depth. Nevertheless, seismic reflections from the ice-water interface were also recorded wherever they could be observed.

At most of the stations during RIGGS I (1973-1974) and at a dozen in the second season, the horizontal gravity gradient was determined by taking readings at the corners of the triangular strain networks. These measurements ended after RIGGS II (1974-1975) and were replaced by an emphasis during RIGGS III (1976-1977) and IV (1977-1978) on radar reflection profiling around parts of the strain networks. Radar profiling was carried

out at only a quarter of the remote sites during the first two seasons.

Positioning by satellite observations was carried out at 123 sites; 80 of them were reoccupied after 1 or 2 years to determine the velocity of the ice shelf. The positions of most of the other sites were determined by sun shots; the remaining few were located either by the inertial navigation system of the aircraft or by optical resection.

Two procedures for determining surface mass balance were routinely used: (1) the heights from the snow surface to the tops of all stakes in each strain network were measured and then remeasured upon subsequent reoccupation of the site; (2) at 60% of the sites, 10-m-long cores were collected for determination of the depth to dated radioactive fallout horizons. A second purpose of the core collection was to study oxygen isotope ratios. Temperatures were usually measured in the 10-m holes.

At 14 scattered stations a more extensive geophysical program was carried out. It comprised any or all of (1) seismic short-refraction shooting to measure seismic wave velocities in the upper 100 m of the ice shelf, (2) radar variable-angle reflection determinations of average electromagnetic wave speed, hence electrical permittivity, in the solid ice, and (3) soundings yielding electrical resistivity as a function of depth within the ice shelf. Densities were calculated from the seismic velocities; the electrical resistivity measurements led to estimates of englacial temperatures. Finally, at the four RIGGS base stations and at the RISP drill camp (J9DC), seismic long-refraction shooting, to examine the thickness of submarine sediments and the upper crustal structure beneath the ice shelf, and a variety of special studies, were conducted. Upon return to J9DC in 1978-1979, sonic logging in a 155-m RISP core hole was undertaken.

All the techniques are discussed in greater detail in the succeeding papers in this volume. A complete listing of the 193 RIGGS surface stations, indicating what kinds of measurement were made at each and by which participating organization, is given in Table 1, and a season-by-season summary is presented in Table 2. Station positions in Table 1 are given in grid coordinates with precision (0.01°) sufficient for plotting or locating on a map. The accompanying paper by Thomas et al. [1984] includes a tabulation giving the most precisely known geographical and grid coordinates of most of the sites (for the exceptions, see the footnotes to Table 1).

The RIGGS program was not limited to the observations on the surface of the ice shelf. Although the initial plan was to make ice thickness measurements only at the surface stations, it became clear during the first season that ice thickness variations were too complex to be detailed with measurements only at the basic network. Consequently, antennas were fitted to the Twin Otter, and a program of radar ice thickness profiling from the air that continued through the succeeding field seasons was begun. The airborne radar measurements were carried out late in each season to permit close ties to the network of already occupied surface stations (when they could be found). This reduced navigational and closure errors and permitted many detailed variations of ice shelf thickness to be drawn with confidence. In all, 13,500 km of airborne radar sounding were completed (Figure 4).

Season-by-Season Summary

RIGGS I (1973-1974)

In mid-December, Station BC was established in the grid northwestern part of the ice shelf, and the initial occupation of the first set of remote sites was carried out. By the end of January, when the work terminated, 52 remote stations had been occupied (Figure 3). In addition to the standard program, stratigraphic studies were made in pits 3 or 4 m deep at BC, I10 (Crary Ice Rise), and G11. Strain lines that were longer than normal were emplaced at two remote stations: H5, where distances were measured and an optical leveling traverse run along a 10-km line of stakes placed across the grounding line between the inland ice sheet and the ice shelf, and G11, where stakes were emplanted along a 5-km line roughly perpendicular to the direction of ice flow in an attempt to measure shear in the ice shelf as it passes the Transantarctic Mountains.

A program around the base camp yielded 50 km of radar and gravity profiling and two electrical resistivity profiles oriented at right angles to one another. A long seismic refraction profile was attempted, but despite extension of the profile to a distance of 20 km, no energy was received along paths penetrating the ocean floor. A long seismic refraction profile that did record energy through the bedrock was completed on Crary Ice Rise (I10S). Two 40-km-long strain networks comprising double lines of stakes were established, one between BC and J9 and one on Crary Ice Rise. The latter network was intended to link the ice rise to the ice shelf; unfortunately, the ice rise was larger than expected, and the shelf was not reached. However, two ice shelf stations 15 and 25 km to the grid northeast were eventually tied into the strain network on the ice rise by tellurometer and theodolite observations. One large strain rosette with 5-km legs was established at BC.

The V.P.I. ocean tide program was begun

TABLE 1. Complete Listing of RIGGS Stations and the Measurements Made at Each

		Position			Surface Measurements			Drilling			Seismic[g]				Radar[g]					Gravity		
	Season of First Measurement	Grid Latitude, °S	Grid Longitude, °E or °W	Type of Measurement[a]	Velocity[b]	Strain and Accumulation[c]	Shallow Sample Collection[d]	10-m Core Collection[e]	Temperature in 10-m Holes[c]	50-100 m Core Drilling[f]	Short Refraction (P Wave)	Short Refraction (S Wave)	Reflection from Base of Ice	Reflection from Seafloor	Ice Thickness	Profiling	Wide-Angle Reflection	Polarization	Electrical Resistivity	Value[g]	Gradient[g]	Tidal[h]
Main base camps																						
BC	I	7.24	1.80W	1	X	X[i]	X	X	X		X	X		X	X	X	X		X	X	X	X
RI	II	9.30	3.10W	1	X	X	X	X	X		X	X	X	X	X	X	X		X	X	X	X
Q13	III	11.04	0.01E	1	X	X	X	X	X	X	X	X	X	X	X	X	X		X	X	X	
C-16	III	8.69	1.45E	1	X	X[i]		X	X	X	X	X		X	X	X	X	X	X	X	X	X
Remote stations																						
E5	I	5.08	2.71W	1				X	X					X	X					X	X	
E6	I	5.03	2.30W	3		X								X	X					X	X	
E7	I	5.07	1.90W	2		X		X	X					X	X					X	X	
E8	I	5.19	1.51W	2		X	X	X	X				X	X	X	X				X	X	
F6	I	5.58	2.27W	2		X	X								X					X	X	
F7	I	5.59	1.81W	1	X	X	X	X	X				X	X	X	X				X	X	
F8	I	5.52	1.27W	2		X	X								X					X	X	
F9	I	5.65	0.86W	1	X	X	X	X	X				X	X	X					X	X	X
F10	I	5.50	0.40W	4		X									X					X	X	
G4	I	6.24	3.48W	1				X	X				X	X	X					X	X	
G5	I	5.78	3.17W	1	X[j]	X[j]	X	X	X						X					X	X	
G6	I	5.92	2.63W	1	X			X	X				X	X	X					X		
G7	I	5.95	1.93W	2,4											X					X	X	
G8	I	6.11	1.46W	1	X	X	X	X	X				X	X	X					X	X	
G9	I	6.10	1.02W	2		X									X					X	X	

G10	III	6.06	0.60W	1	X	X	X	X											X	X
G11	I	6.04	0.07W	2		X								X					X	X
H5	I	6.62	3.34W	1	X[k]	X[k]	X	X	X				X	X	X	X			X	X
H6	I	6.41	3.09W	1		X	X	X	X					X	X				X	X
H7	I	6.55	2.49W	1		X		X	X		X	X	X	X	X				X	X
H8	I	6.51	1.93W	1	X	X	X	X	X					X	X				X	
H9	I	6.49	1.45W	1	X	X	X	X	X				X	X	X				X	X
H10	I	6.56	1.01W	1	X	X	X	X	X				X	X	X				X	X
H11	I	6.55	0.51W	2		X									X		X		X	X
H11S[ℓ]	I	6.46	0.61W	1				X			X	X	X	X	X				X	
HE12	III	6.54	0.03E	1	X	X	X													
H12	I	6.28	0.35E	1	X	X	X	X	X				X	X	X	X			X	X
H13	III	6.43	0.79E	1	X	X		X	X		X			X	X	X	X	X	X	
I5	I	7.10	3.51W	1	X[k]	X[k]	X	X	X				X	X	X	X			X	X
I6	I	7.01	3.04W	2		X		X					X	X	X				X	X
I7	I	6.91	2.26W	1		X		X	X				X	X	X				X	
I8	I	6.98	2.00W	1	X	X	X	X	X					X	X				X	X
I9	I	6.95	1.50W	2		X		X	X					X	X	X			X	X
I10	I	7.01	0.82W	2		X	X								X	X			X	X
I10S[ℓ]	I	7.05	0.95W	1	X[j]		X	X			X	X	X	X	X				X	
I11	I	7.09	0.43W	1		X		X						X	X				X	X
I12	III	7.09	0.02W	1		X		X	X				X	X					X	
I13	III	7.10	0.52E	1	X	X		X	X				X	X					X	
I14	III	7.04	0.99E	1	X	X		X	X				X	X	X	X			X	
I15	III	7.08	1.53E	1	X	X		X	X					X	X	X			X	
IJ9½[m]	I	7.24	1.24W	3										X	X				X	
J4	II	7.42	3.99W	1	X	X	X	X	X				X	X	X				X	
J6	I	7.50	2.94W	1	X[k]	X[k]	X	X	X				X	X	X				X	X
J7	I	7.41	2.23W	2		X	X	X							X				X	X
J7S[ℓ]	I	7.63	2.89W	1							X		X	X	X					
J8	I	7.50	2.00W	1		X	X	X	X					X	X				X	
J9[h]	I	7.48	1.50W	1		X		X	X					X	X				X	X
J9DS[h]	II	7.48	1.50W	1			X				X			X	X	X			X	
J9DC[h]	III	7.49	1.50W	1			X			X	X	X	X	X	X	X	X	X		X
J10	I	7.47	0.98W	1	X	X	X	X	X					X	X				X	X
J11	I	7.41	0.48W	2		X									X				X	X
J12	III	7.63	0.04E	2		X							X	X					X	
J13	III	7.53	0.46E	1	X	X		X	X					X	X	X			X	
J14	III	7.55	0.94E	2		X	X						X	X	X	X			X	
J15	III	7.48	1.53E	1	X	X	X	X	X				X	X	X	X			X	

TABLE 1. (continued)

		Position			Surface Measurements			Drilling			Seismic[g]				Radar[g]					Gravity		
	Season of First Measurement	Grid Latitude, °S	Grid Longitude, °E or °W	Type of Measurement[a]	Velocity[b]	Strain and Accumulation[c]	Shallow Sample Collection[d]	10-m Core Collection[e]	Temperature in 10-m Holes[c]	50-100 m Core Drilling[f]	Short Refraction (P Wave)	Short Refraction (S Wave)	Reflection from Base of Ice	Reflection from Seafloor	Ice Thickness	Profiling	Wide-Angle Reflection	Polarization	Electrical Resistivity	Value[g]	Gradient[g]	Tidal[h]
Remote stations																						
J16	III	7.50	2.04E	1				X	X				X	X	X	X	X			X		
JK9½[m]	I	7.77	1.26W	3									X	X	X							
K3	II	8.13	4.34W	1	X	X	X	X	X				X	X	X					X		
K4	II	7.98	3.99W	2		X								X	X					X		
K5	II	7.95	3.50W	2		X								X	X					X		
K6	I	8.15	2.90W	2		X									X					X	X	
K7	I	8.04	2.42W	1		X		X	X					X	X					X	X	
K8	I	7.97	1.96W	2		X									X					X	X	
K9	I	7.97	1.43W	1		X		X	X					X	X					X	X	
K10	I	8.00	0.95W	1	X	X		X	X				X	X	X	X				X	X	
K11	I	7.96	0.45W	1	X	X	X	X	X		X	X	X	X	X					X	X	
K12	III	8.00	0.03W	1		X		X	X					X	X	X				X		
K13	III	8.05	0.56E	1	X	X		X	X				X	X						X		
K14	III	8.09	0.90E	1	X	X		X	X					X	X	X				X		
K15	III	8.00	1.56E	2		X							X	X	X	X				X		
K16	III	8.04	2.02E	1	X	X		X	X				X	X	X	X				X		
K17	III	8.02	2.50E	1	X	X		X	X					X	X	X				X		
KL7	III	8.25	2.47W	1			X							X	X	X	X			X		
L4	II	8.45	4.48W	2		X							X	X	X	X			X	X	X	
L5	II	8.50	4.02W	2		X		X	X				X	X	X					X		

L6	II	8.48	3.51W	2		X			X				X	X					X		
L7	II	8.50	3.02W	2		X	X	X	X				X	X					X		
L8	I	8.81	2.41W	2		X								X					X	X	
L9	I	8.49	1.96W	1		X		X					X	X					X	X	
L10	I	8.49	1.43W	2		X								X					X	X	
L11	I	8.48	0.88W	1		X		X					X	X					X	X	
L12	III	8.53	0.48W	1	X	X		X	X			X	X						X		
L13	III	8.51	0.02E	1	X	X		X	X			X	X						X		
L14	III	8.54	0.51E	1				X	X			X	X						X		
L15	III	8.54	1.05E	2				X					X	X	X				X		
L16	III	8.56	1.49E	1		X		X	X			X	X	X	X				X		
L17	III	8.49	1.96E	1	X	X		X	X				X	X	X				X		
L18	III	8.50	2.53E	1	X	X		X	X			X	X	X	X				X		
L19	III	8.56	2.91E	1	X	X		X	X			X	X	X	X				X		
M2	II	9.00	5.07W	2		X		X	X			X	X	X	X				X	X	
M3	II	8.85	4.68W	1	X	X	X	X	X			X	X	X					X		
M5	II	8.97	3.99W	2		X							X	X					X		
M5½m	II	9.18	3.71W	3										X					X		
M6	II	9.02	3.52W	2		X	X	X	X			X	X	X					X		
M6½ (ML6)	II	8.85	3.22W	2		X						X	X	X					X		
M7	II	9.00	3.01W	2		X	X	X					X	X					X		
M8	II	9.01	2.52W	2		X							X	X	X				X		
M9	II	9.02	2.01W	2		X						X	X	X	X				X	X	
M10	II	8.84	1.72W	1	X	X	X	X	X				X	X	X	X			X	X	
M12	III	9.05	0.47W	2		X						X	X						X		
M13	III	9.05	0.03E	1	X	X		X	X			X	X						X		
M14	III	8.99	0.49E	1						X			X	X	X	X	X	X	X		
M15	III	9.05	0.99E	1	X	X		X					X	X	X				X		
M16	III	9.06	1.53E	1				X	X			X	X						X		
M17	III	9.03	2.02E	1	X	X		X	X			X	X						X		
M18	III	9.00	2.52E	2								X	X						X		
M19	III	9.02	2.82E	1				X	X			X	X						X		
N4	II	9.51	4.50W	1	X	X	X	X				X	X	X					X	X	
N5	II	9.45	3.96W	2		X						X	X	X	X				X	X	
N6	II	9.38	3.64W	2		X						X	X	X	X				X		
N7	II	9.53	3.01W	2		X						X	X	X	X				X	X	
N8	II	9.49	2.51W	1	X	X	X	X	X				X	X	X				X		
N9	II	9.49	1.97W	1			X	X	X				X	X					X		
N10	II	9.49	1.63W	2		X							X	X	X				X		
N11	III	9.46	1.01W	1		X		X	X				X	X					X		

TABLE 1. (continued)

		Position			Surface Measurements			Drilling			Seismic[g]				Radar[g]					Gravity		
	Season of First Measurement	Grid Latitude, °S	Grid Longitude, °E or °W	Type of Measurement[a]	Velocity[b]	Strain and Accumulation[c]	Shallow Sample Collection[d]	10-m Core Collection[e]	Temperature in 10-m Holes[c]	50-100 m Core Drilling[f]	Short Refraction (P Wave)	Short Refraction (S Wave)	Reflection from Base of Ice	Reflection from Seafloor	Ice Thickness	Profiling	Wide-Angle Reflection	Polarization	Electrical Resistivity	Value[g]	Gradient[g]	Tidal[h]
Remote stations																						
N12	III	9.40	0.51W	1	X	X		X	X				X	X	X	X				X		
N13	III	9.54	0.06E	1	X	X		X	X				X	X						X		
N14	III	9.54	0.62E	2		X							X	X						X		
N15	III	9.52	1.01E	1				X	X				X	X						X		
N16	III	9.50	1.51E	1		X		X	X				X	X						X		
N17	III	9.51	2.01E	3									X	X						X		
N18	III	9.56	2.52E	1	X	X		X	X				X	X						X		
N19	III	9.51	3.02E	1				X	X		X			X	X	X	X	X	X	X		
04	II	9.85	4.50W	2		X	X						X	X	X	X				X	X	
05	II	9.98	4.15W	1	X	X	X	X					X	X	X					X		
06	II	10.09	3.79W	2		X		X	X				X	X	X					X	X	
07	II	9.98	2.92W	2		X			X					X	X	X				X		
08	II	10.00	2.50W	2		X		X	X				X	X	X					X		
09	II	10.00	2.02W	2		X		X	X				X	X	X					X		
010	III	10.03	1.52W	3																		
011	IV	9.98	0.96W	2							X			X	X	X	X		X	X		
012	III	10.01	0.49W	1	X	X		X	X					X	X					X		
013	III	10.05	0.01E	1	X	X								X	X	X				X		
014	III	10.00	0.51E	1	X	X	X	X	X					X	X	X				X		
015	III	9.98	1.02E	1	X	X	X							X	X	X				X		

O16	III	9.96	1.46E	1	X	X		X	X				X	X						X		
O17	III	10.07	1.99E	2		X							X	X						X		
O18	III	9.95	2.41E	1				X	X				X	X						X		
O19	III	10.03	3.00E	1				X	X		X		X	X	X	X	X		X	X		
OP4	II	10.26	4.68W	2		X							X	X	X	X				X	X	
P5	II	10.44	4.21W	2		X					X	X	X	X	X	X				X	X	
P6	II	10.56	3.86W	1	X	X	X	X	X				X	X	X					X		
P7	III	10.31	2.82W	1	X	X	X	X	X						X					X		
P8	III	10.50	2.38W	3		X	X								X	X				X		
P9	III	10.52	1.98W	1	X	X	X	X	X				X	X	X	X				X		
P10	III	10.52	1.51W	1	X	X	X								X	X				X		
P11	III	10.52	0.96W	1	X	X	X	X						X	X					X		
P12	III	10.52	0.49W	1	X	X	X							X	X	X				X		
P13	III	10.49	0.01E	1	X	X	X							X	X					X		
P14	III	10.51	0.46E	1		X	X							X	X					X		
P15	III	10.50	0.99E	1	X	X								X	X	X				X		
P16	III	10.47	1.47E	1	X	X		X	X					X	X	X				X		
P17	III	10.50	1.96E	1	X	X		X	X					X	X	X				X		
P18[m]	IV	10.59	2.58E	4										X	X	X				X		
P19[m]	IV	10.66	3.03E	4									X	X	X	X				X		
Q5	II	10.90	4.15W	2		X							X	X	X					X	X	
Q6	II	10.85	3.49W	1	X	X	X	X	X				X	X	X					X		
Q7	III	11.01	2.91W	1		X	X							X	X	X				X		
Q8	III	10.92	2.44W	1	X	X	X	X	X					X	X					X		
Q9	III	11.04	1.97W	1	X	X	X							X	X	X				X		
Q10	III	11.00	1.46W	1	X	X	X	X	X					X	X	X				X		
Q11	III	11.00	0.99W	1	X	X	X							X	X	X				X		
Q12	III	11.00	0.43W	1	X	X	X	X						X	X	X				X		
Q14	III	11.00	0.52E	1	X	X	X							X	X					X		
Q15	III	11.01	0.99E	1	X	X		X	X					X	X	X				X		
Q16[m]	IV	11.16	1.51E	4									X	X	X	X				X		
Q17[m]	IV	11.06	2.10E	4										X	X	X				X		
Q18[m]	IV	11.02	2.58E	4											X	X				X		
R10	III	11.49	1.49W	1		X	X						X	X	X					X		
R11	III	11.54	0.95W	1	X	X	X	X	X				X	X	X	X				X		
R12	III	11.51	0.46W	1		X	X						X	X	X	X				X		
R13	III	11.52	0.03E	1	X	X	X	X	X					X	X	X				X		
R14	III	11.51	0.50E	1		X	X	X	X					X	X	X				X		
R15	III	11.51	1.02E	1	X	X	X							X	X	X				X		
R16	IV	11.48	1.50E	1				X	X		X		X	X	X	X	X	X		X		

TABLE 1. (continued)

	Season of First Measurement	Position			Surface Measurements			Drilling			Seismic[g]				Radar[g]					Gravity		
		Grid Latitude, °S	Grid Longitude, °E or °W	Type of Measurement[a]	Velocity[b]	Strain and Accumulation[c]	Shallow Sample Collection[d]	10-m Core Collection[e]	Temperature in 10-m Holes[c]	50-100 m Core Drilling[f]	Short Refraction (P Wave)	Short Refraction (S Wave)	Reflection from Base of Ice	Reflection from Seafloor	Ice Thickness	Profiling	Wide-Angle Reflection	Polarization	Electrical Resistivity	Value[g]	Gradient[g]	Tidal[h]
Remote stations																						
R17	IV	11.49	2.00E	1									X	X	X	X				X		
R18	IV	11.41	2.58E	1				X	X					X	X	X				X		
S14	III	12.01	0.49E	1	X	X								X	X					X		
S15	III	12.03	1.01E	1	X	X								X	X					X		
S16	IV	12.00	1.51E	1									X	X	X	X				X		
S17	IV	11.99	2.00E	1									X	X	X	X				X		
T15	III	12.28	1.28E	1	X	X	X	X	X					X	X	X				X		
T17	III	12.51	2.01E	1				X	X						X	X				X		
T17S[m]	III	12.53	2.01E	3										X								
Supplementary base camps																						
C-7	II	11.0	0.6W	3			X															
C-7-3	III	11.67	0.03E	3						X												
C-13	II	10.5	1.9E	3																		X
C-36	II	10.0	1.9W	3			X															X
RI dome	III	10.09	3.30W	1			X			X												

[a]Types of position measurement are (1) satellite observations (U.S. Geological Survey); (2) solar observations (University of Maine); (3) inertial navigation system on aircraft; (4) resection (University of Wisconsin).

[b]Measurements made by U.S. Geological Survey.

[c]Measurements made by University of Maine.

[d]Measurements made by University of Nevada.

[e]Measurements made by University of Copenhagen.
[f]Measurements made by University of New York at Buffalo (SUNY-Buffalo).
[g]Measurements made by University of Wisconsin.
[h]Measurements made by Virginia Polytechnic Institute.
[i]Strain measurement only.
[j]Remeasured during RIGGS III.
[k]Remeasured during RIGGS II and again during RIGGS III.
[ℓ]Precise positions for these stations were measured but are not given in the accompanying paper by Thomas et al. [1984]. Those positions are H11S: 83°30'25"S, 174°34'00"W; I10S: 82°53'26"W; J7S: 81°53'27"S, 159°41'32"W. The position at I10S was remeasured by Doppler-satellite after 3 years; there was no measurable change.
[m]These stations are not listed in the accompanying paper by Thomas et al. [1984]; no positions more precise than those given here were measured.
[n]J9, J9DS, and J9DC are RIGGS I, II, and III designations. Camps were within 1 km of each other. Different position for J9DC reflects 3 years of ice shelf movement.

this season at BC. The experimental arrangement at BC, and at other recording sites in succeeding seasons, consisted of a LaCoste and Romberg recording gravimeter placed on a platform mounted on timbers set well into firn and housed in a 5-m-by-5-m Jamesway. The gravimeter was maintained by a technician who made frequent calibration tests and beam and level adjustments to the instrument.

Late in the season a ground party collected ice samples containing rock fragments and a few microfossils from a highly disturbed region 1/2 km to the grid south of Crary Ice Rise [Gaylord and Robertson, 1975].

Airborne radar sounding began on January 29; in the 3 days before the Twin Otter departed from the base camp, 3000 km of airborne radar profiling were completed (Figure 4).

RIGGS II (1974-1975)

The first part of the 1974-1975 season was devoted to the remeasurement of strain networks already planted in the grid northwestern part of the ice shelf. Starting in late November from base station BC, and using a Twin Otter generously provided by the British Antarctic Survey (BAS), all but six of the strain rosettes were located and successfully remeasured. The strain networks covering larger areas near stations BC, J9, H5, and G11 were also remeasured, and a leveling survey was completed along the 40-km strain line between BC and J9. The new positions of 15 stations were determined by satellite observations.

Geophysical work during the 1974-1975 season also began in late November 1974 with radar measurements, concentrating on the mapping of crevasses in the underside of the ice shelf ("bottom crevasses"), at the proposed RISP drill site (J9DS).

The "Roosevelt Island" (RI) base camp (so called because of its proximity to Roosevelt Island, even though it was on the ice shelf) was established on December 5; remote work from that camp began on December 16, continuing until January 27, 1975, when all personnel returned to McMurdo. Surveying during this period was hampered by fog and whiteouts; as a result, airborne operations were conducted only during 55% of the field season. Nevertheless, 37 remote stations were occupied during the second season's survey.

Local investigations around the Roosevelt Island camp included 50 km of radar and gravity profiling, a 40-km-long strain network along the local flow line, a 28-km seismic refraction profile that successfully recorded energy along paths through bedrock, studies of seismic velocity and of electromagnetic wave velocity in the ice, and one electrical resistivity profile. A total of 4200 km of airborne radar sounding was completed using the Twin Otter.

TABLE 2. Summary of Stations and Types of Measurement at Each

	Measuring Agency*	RIGGS Season of First Measurement I	II	III	IV	Total
Stations						
Base camps		1	4	4	0	9
Remote stations		52	37	84	11	184
Positioning						
Satellite observations	a	32	12	74	5	123
Solar observations	b	17	25	8	1	51
Aircraft navigation system		3	4	6	0	13
Resection	f	2	0	0	5	7
Surface measurements						
Ice shelf velocity	a	18	10	52	0	80
Strain	b	44	35	69	0	148
Accumulation	b	43	35	68	0	146
Shallow sample collection	c	0	22	51	0	73
Drilling						
10-m core collection	d	36	19	55	2	112
Temperature in 10-m hole	b	29	17	50	2	98
50-100 m core drilling	e	0	0	5	0	5
Seismic measurements						
Short refraction P wave	f	6	3	7	2	18
Short refraction S wave	f	5	2	3	0	10
Reflection from base of ice	f	21	24	39	6	90
Reflection from seafloor	f	38	37	79	10	164
Radar						
Ice thickness	f	53	38	60	11	162
Profiling	f	9	16	49	11	85
Wide-angle reflection	f	2	2	9	2	15
Polarization	f	0	0	5	1	6
Electrical Resistivity	f	1	2	6	1	10
Gravity						
Value	f	51	38	81	11	181
Gradient	f	44	12	2	0	58
Tidal	g	2	3	2	0	7

*Measurements were made by (a) U.S. Geological Survey; (b) University of Maine; (c) University of Nevada; (d) University of Copenhagen; (e) State University of New York at Buffalo; (f) University of Wisconsin; and (g) Virginia Polytechnic Institute.

The University of Nevada snow-sampling program, comprising season-long measurements at site C-7 (65 km from the front of the Ross Ice Shelf) and J9DS, collection of samples from shallow pits at nine RIGGS sites ranging from RI to E8, and near-surface snow sampling at 45 other RIGGS stations, was undertaken during this season.

Tidal measurements were carried out by V.P.I. at C-13, C-36, and RI.

RIGGS III (1976-1977)

The third season of RIGGS was characterized by the occupation of new remote stations using two Twin Otters operating concurrently from two new base camps, C-16 and Q13, and by early season operations at two other camps, RI and the RISP drilling camp, J9DC. During the early season all the University of Wisconsin geophysicists were at J9DC, while the resurveying

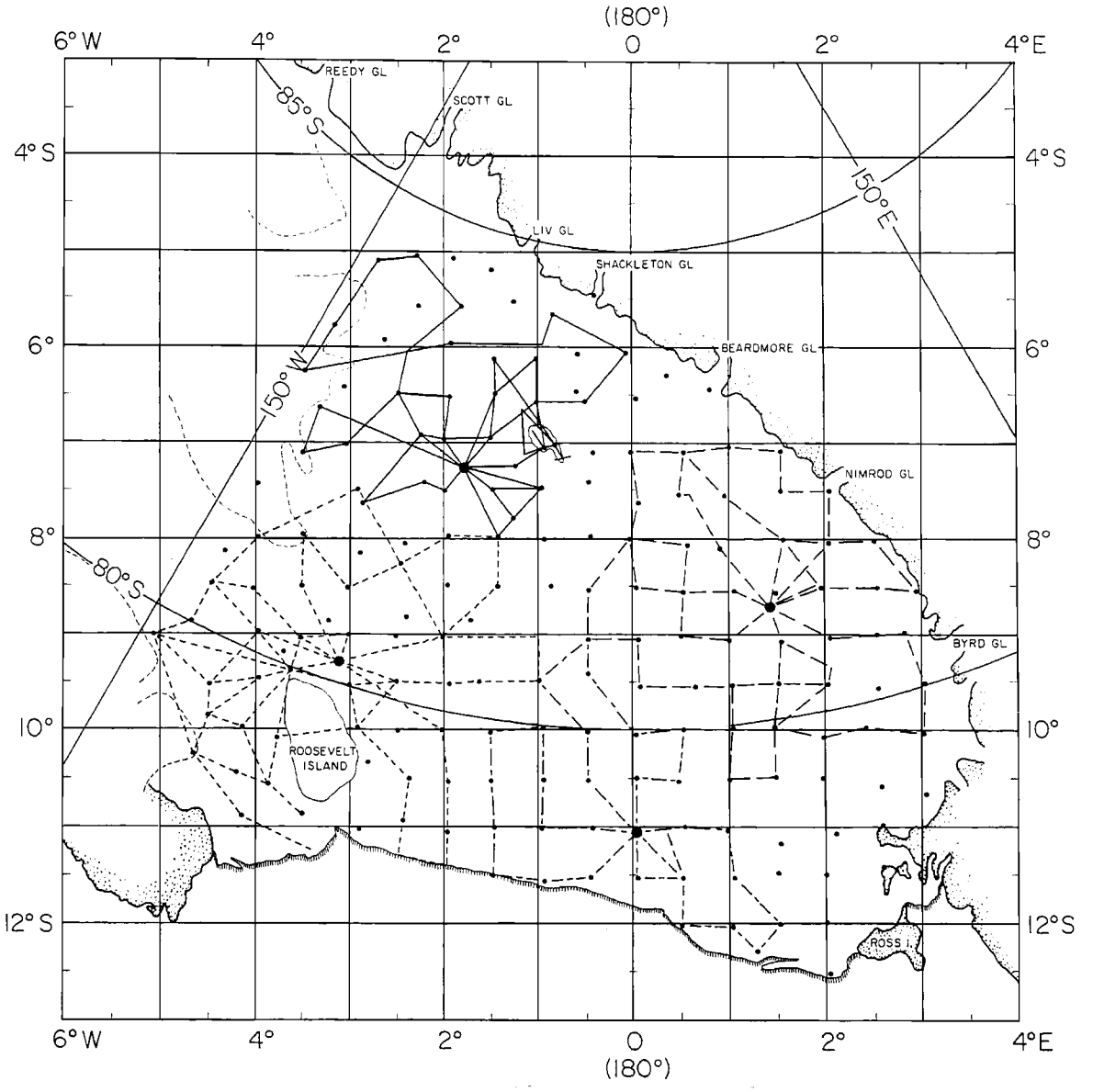

Fig. 4. Map of Ross Ice Shelf, showing RIGGS radar flight lines. RIGGS I (1973-1974) flight lines are represented by solid lines, RIGGS II (1974-1975) by short-dashed lines, RIGGS III (1976-1977) by long-dashed lines, and RIGGS IV (1977-1978) by long-and-short-dashed lines. Large circles denote base camps; small circles denote surface stations (see Figure 3).

at previously established remote sites was being conducted by University of Maine and U.S. Geological Survey parties from RI; in the later part of the season the disciplinary groups were split so that all the normal measurements could be made at each new remote site.

Part of the geophysical program at J9DC extended the mapping of the complex pattern of bottom crevasses in the area and confirmed that the location selected for the RISP access hole was satisfactorily undisturbed. Other geophysical work carried out in November included (1) ice thickness profiling of an area 3 x 5 km with a 0.5-km spacing, (2) wide-angle radar reflection profiling along two 1-km tracks perpendicular to each other, (3) experiments with collinear radar antennas, which provide a better near-surface resolution than is obtained from parallel antennas, (4) seismic P wave refraction shooting to a distance

of 2 km along three azimuths differing by 60°, with closely spaced receivers at short shot-receiver distances, (5) seismic S wave refraction shooting along two mutually perpendicular lines extending to a range of 400 m with both SV and SH waves recorded, (6) determinations of ice thickness and water depth beneath the ice from shots fired in the bottom of an abandoned 150-m core hole, (7) a gravity survey along the radar-profiling network, (8) electrical resistivity profiling on two mutually perpendicular lines extending to 600 and 700 m, (9) measurement of ultrasonic wave velocities in three directions on ice core samples [Kohnen and Bentley, 1977], and (10) a complete radar polarization experiment, with each antenna being rotated stepwise in 15° increments. Early in December the geophysical party split into two groups, one going to base camp RI and the other to the new base station at C-16.

Field work at RI began in early November with the resurvey of the 40-km network of stakes near the camp. All of the remote-station strain networks that were emplanted during 1974-1975, and several from the 1973-1974 season, were located and remeasured by mid-December, again using a BAS Twin Otter. After the geophysicists arrived, occupation of new remote stations in the grid southwestern quadrant of the ice shelf began. Also, two electrical resistivity profiles at the base camp, a third 170 km upstream along the flow line, and a wide-angle radar reflection profile on grounded ice just upstream from the Steershead Crevasses (100 km grid northeast of RI) were completed. At the end of December the entire group moved to Q13 base camp (Figure 3), where the occupation of new remote stations continued until late January.

At C-16 most of the first month was spent doing geophysical and glaciological surveying near the camp, owing to late arrival of the supporting Twin Otter airplane and operational difficulties after it arrived. The following measurements were made. (1) Surface topography and ice thickness were surveyed on a network 5 x 2 km with 1/2-km spacing, revealing ice thickness waves about 25 m in amplitude and a little more than 1 km in length. An additional 11-km line with accurate leveling, emplacement of strain stakes, and radar ice thickness measurements was established normal to the "waves." (2) Strain networks were established along two 40-km lines. (3) Short seismic P wave, SV wave, and SH wave refraction profiles were completed along three azimuths at 60° angles to each other. (4) A seismic wide-angle reflection profile was completed out to a distance of 2.5 km. (5) A 400-kg seismic refraction shot was recorded at distances of 23 and 26 km. (6) Two electrical resistivity profiles at right angles to each other were completed. (7) Radar wide-angle reflection profiles were carried out along the same two lines as the electrical resistivity profiles. (8) A radar polarization study similar to that at J9DC was made. (9) Seismic reflection soundings of water depth and gravity profiling were extended 10 km from the station along each of the four cardinal points of the compass. A fifth gravity line was completed along a diagonal direction to improve the coverage over a remarkable, nearly circular, negative gravity anomaly that was revealed by the first four lines of measurements.

The station program at Q13 was similar to the one at C-16, except that more extensive radar profiling, for defining bottom-crevasse patterns and for delineation of internal layering within the ice, took the place of extensive surface topography and gravity mapping. Work completed included (1) three wide-angle radar reflection profiles, (2) one electrical resistivity profile, (3) 50 km of radar profiling (on the surface), (4) 30 km of gravity profiling, (5) 2 km of seismic profiling along the radar wide-angle lines, (6) two short seismic refraction profiles along which all three components of wave motion were recorded, (7) radar polarization experiments, (8) a seismic wide-angle profile, and (9) a 375-kg seismic refraction shot recorded at 23 and 25 km.

Despite the slow start for the airlifted program, by the completion of the season at the end of January, 84 stations had been occupied (Figure 3). In addition to the usual measurements, radar polarization studies were carried out at three remote stations (H13, M14, and N19), as well at at J9DC and C-16. Airborne radar sounding was completed along 4500 km of flight lines (Figure 4).

The 1976-1977 austral summer marked the initial field season for the SUNY-Buffalo program of core drilling on the ice shelf. A 100-m core was collected at J9DC, and 50-m cores were collected at C-7-3, approximately 20 km from the ice front, and on the ice dome of Roosevelt Island. The V.P.I. ocean tide measurements were made at three more sites: F9, J9DC, and C-16.

RIGGS IV (1977-1978)

Field work for the last season of RIGGS began at base station Q13 on December 23, 1977. During the last week of December, five new remote field sites were occupied, and early in January, airborne radar sounding was made along 1800 km of flight lines.

When not flying, the geophysical group continued detailed experiments around Q13. The new measurements included (1) a seismic sur-

face wave experiment, carried out with shot sizes of 0.5-22 kg, shot depths of 1-5 m, and shot-detector distances of 1.5 and 10 km, (2) continuous radar-sounding profiles along the axis of, and perpendicular to, a topographical depression approximately 5 m deep and 2 km across located 10 km grid west of Q13, (3) a gravity line 45 km long, running grid east-west through Q13, and two supplementary 10-km lines along grid NW and grid SW, (4) an 800-m-long electrical resistivity profile along a line perpendicular to the 1976-1977 profile and the extension of the latter to 700 m, (5) two radar wide-angle reflection profiles, (6) a 350-kg seismic refraction-reflection shot recorded at distances of 10 and 31 km grid west of camp, (7) seismic uphole velocity experiments in a 100-m hole and in several holes of 5 m or less, and (8) radar surface wave measurements made for testing the effect of various antenna orientations.

On January 16, operations were moved to C-16, where near-camp work continued as the opportunity arose. Measurements made near C-16 included remeasurement of the strain networks along the two 40-km lines, a radar wide-angle experiment, and 30-kg and 300-kg seismic reflection shots fired in a 100-m hole. Late in the season the inertial navigation system on the Twin Otter failed, making station relocation impossible. Thereafter, the Twin Otter was flown out of McMurdo Station to establish six new stations in the McMurdo area (Figure 3). Positions were found by resection on geographical landmarks.

During this last season of RIGGS, SUNY-Buffalo obtained 100-m ice cores from sites Q13, C-16, and J9DC; downhole temperatures were measured in each hole. For surface chemical sampling and surface-to-core tie-in studies, two pits adjacent to each other were excavated 5 or 6 km from each of the drill sites. Ultraclean, detailed collections were made in one pit for further laboratory investigations of seasonal and positional variations in chemical constituents and for further characterization of the glacio-chemical regimes represented on the Ross Ice Shelf. Detailed density and stratigraphic measurements were conducted in the other pit to obtain recent rates of surface accumulation.

The V.P.I. ocean tide program on the Ross Ice Shelf finished with measurements for 39 days at site 019 and 30 days at site C-16; the latter measurements were a repetition of those obtained the previous year.

Acknowledgments. Work on this report was supported by National Science Foundation grant DPP-8119989. The field work summarized here was supported by many research grants which are acknowledged in the individual papers. This is contribution 409 of the Geophysical and Polar Research Center, University of Wisconsin-Madison.

References

Bennett, H. F., A gravity and magnetic survey of the Ross Ice Shelf area, Antarctica, Res. Rep. 64-3, 97 pp., Geophys. and Polar Res. Center, Univ. of Wis., Madison, 1964.

Clapp, J. L., Summary and discussion of survey control for ice flow studies on Roosevelt Island, Antarctica, Res. Rep. 65-1, 103 pp., Geophys. and Polar Res. Center, Univ. of Wis., Madison, 1965.

Clough, J. W., and B. L. Hansen, The Ross Ice Shelf Project, Science, 203, 433-434, 1979.

Crary, A. P., Glaciological studies at Little America Station, 1957 and 1958, IGY Glaciol. Rep. 5, Am. Geogr. Soc., New York, 1961a.

Crary, A. P., Marine sediment thickness in the eastern Ross Sea area, Antarctica, Geol. Soc. Am. Bull., 72, 787-790, 1961b.

Crary, A. P., E. S. Robinson, H. F. Bennett, and W. W. Boyd, Jr., Glaciological studies of the Ross Ice Shelf, Antarctica, 1957-60, IGY Glaciol. Rep. 6, Am. Geogr. Soc., New York, 1962.

Dorrer, E., W. Hofmann, and W. Seufert, Geodetic results of the Ross Ice Shelf Survey expeditions, 1962-63 and 1965-66, J. Glaciol., 8, 69-90, 1969.

Gaylord, D. R., and J. D. Robertson, Sediments exposed on the surface of the Ross Ice Shelf, Antarctica, J. Glaciol., 14, 332-333, 1975.

Giovinetto, M. B., E. S. Robinson, and C. W. M. Swithinbank, The regime of the western part of the Ross Ice Shelf drainage system, J. Glaciol., 6, 55-68, 1966.

Gould, L. M., Structure of the Queen Maud Mountains, Antarctica, Geol. Soc. Am. Bull., 46, 1367, 1935.

Heap, J. A., and A. S. Rundle, Snow accumulation on the Ross Ice Shelf, Antarctica, in Antarctic Snow and Ice Studies, Antarc. Res. Ser., vol. 2, edited by M. Mellor, pp. 119-125, AGU, Washington, D. C., 1964.

Hofmann, W., E. Dorrer, and K. Nottarp, The Ross Ice Shelf Survey (RISS) 1962-1963, in Antarctic Snow and Ice Studies, Antarc. Res. Ser., vol. 2, edited by M. Mellor, pp. 83-118, AGU, Washington, D. C., 1964.

Hoinkes, H. C., The settling of firn at Little America III, 1940-58, J. Glaciol., 4, 111-120, 1962.

Jiracek, G. R., and C. R. Bentley, Velocity of electromagnetic waves in Antarctic ice, in Antarctic Snow and Ice Studies II, Antarc. Res. Ser., vol. 16, edited by A. P. Crary, pp. 199-208, AGU, Washington, D. C., 1971.

Kehle, R., Deformation in the Ross Ice Shelf

Antarctica, Geol. Soc. Am. Bull., 75, 259-286, 1964.

Kohnen, H., and C. R. Bentley, Ultrasonic measurements on ice cores from Ross Ice Shelf, Antarctica, drill hole, Antarct. J. U.S., 12, 148-150, 1977.

Mohn, H., Roald Amundsen's Antarctic Expedition, Scientific Results Meteorology, 78 pp., Jacob Dybwad, Kristiania, 1915.

Poulter, T. C., Seismic measurements on the Ross Ice Shelf, I, EOS Trans. AGU, 28, 162-170, 1947a.

Poulter, T. C., Seismic measurements on the Ross Ice Shelf, II, EOS Trans. AGU, 28, 367-384, 1947b.

Ragle, R. H., B. L. Hansen, A. J. Gow, and R. W. Patenaude, Deep core drilling in the Ross Ice Shelf, Little America V, Antarctica, Tech. Rep. 70, U.S. Snow, Ice and Permafrost Res. Estab., Wilmette, Ill., 1960.

Robin, G. de Q., Ice shelves and ice flow, Nature, 253, 168-172, 1975.

Simpson, G. C., British Antarctic Expedition 1910-13, Meteorology 1, 326 pp., Thacker, Spink, Calcutta, 1919.

Simpson, G. C., British Antarctic Expedition 1910-13, Meteorology 3, 835 pp., Harrison and Sons, London, 1923.

Stuart, A. W., and C. Bull, Glaciological observations on the Ross Ice Shelf near Scott Base, Antarctica, J. Glaciol., 4, 399-414, 1963.

Stuart, A. W., and A. J. Heine, Glaciological work of the 1959-1960 U.S. Victoria Land Traverse, J. Glaciol., 3, 997-1002, 1961.

Swithinbank, C. W. M., Ice movement of valley glaciers flowing into the Ross Ice Shelf, Antarctica, Science, 141, 523-524, 1963.

Thiel, E., and N. A. Ostenso, The contact with the Ross Ice Shelf and the continental ice sheet, Antarctica, J. Glaciol., 3, 823-832, 1961.

Thiel, E., A. P. Crary, R. A. Haubrich, and J. C. Behrendt, Gravimetric determination of ocean tide, Weddell and Ross seas, Antarctica, J. Geophys. Res., 65, 629-636, 1960.

Thomas, R. H., D. R. MacAyeal, D. H. Eilers, and D. R. Gaylord, Glaciological studies on the Ross Ice Shelf, Antarctica, 1973-1978, in The Ross Ice Shelf: Glaciology and Geophysics, Antarc. Res. Ser., vol. 42, edited by C. R. Bentley and D. E. Hayes, pp. 21-53, AGU, Washington, D. C., 1984.

Thomas, R. H., D. R. MacAyeal, C. R. Bentley, and J. L. Clapp, The creep of ice, geothermal heat flow and Roosevelt Island, J. Glaciol., 25, 47-60, 1980.

Wade, F. A., The physical aspects of the Ross Ice Shelf, in Proc. Am. Philos. Soc., 89, 160-173, 1945.

Wilson, C. R., and A. P. Crary, Ice movement studies on the Skelton Glacier, J. Glaciol., 3, 873-878, 1961.

Wright, C. S., The Ross Barrier and the mechanism of ice movement, Geogr. J., 65, 198-213, 1925.

Wright, C. S., and R. E. Priestley, Glaciology, British (Terra Nova) Antarctic Expedition 1910-13, xx + 581 pp., Harrison & Sons, London, 1922.

Zumberge, J. H., Ross Ice Shelf Project, Antarct. J. U.S., 6, 258-263, 1971.

Zumberge, J. H., M. Giovinetto, R. Kehle, and J. Reid, Deformation of the Ross Ice Shelf near the Bay of Whales, Antarctica, IGY Glaciol. Rep. 3, 148 pp., Am. Geogr. Soc., New York, 1960.

(Received August 9, 1983;
revised March 26, 1984;
accepted March 27, 1984.)

The Ross Ice Shelf: Glaciology and Geophysics
Antarctic Research Series, Volume 42, Paper 2, Pages 21-53

GLACIOLOGICAL STUDIES ON THE ROSS ICE SHELF, ANTARCTICA, 1973-1978

Robert H. Thomas[1], Douglas R. MacAyeal[2], David H. Eilers[3], and David R. Gaylord[4]

Abstract. The Ross Ice Shelf Geophysical and Glaciological Survey (RIGGS) yielded measurements of ice velocities, strain rates, accumulation rates, and 10-m temperatures, which are presented in this paper. Near the grounding line between the ice shelf and the West Antarctic ice sheet, ice velocity ranges from a few meters per year to several hundred meters per year in ice streams. Ice velocity increases as the ice moves seaward, reaching more than 1 km yr^{-1} in the central portions of the ice front. Ice velocity at Little America V is double earlier estimates. An apparent increase in velocity along parts of the ice front between 1965 and 1975 may simply represent errors in the different estimates. Most of the drainage from West Antarctica into the Ross Ice Shelf flows down two major ice streams, each of which discharges more than 20 km^3 of ice each year. Another of the West Antarctic ice streams, previously thought to be very active, is almost stagnant, with drainage rates that are less than half the total snow accumulation within its catchment area, which presumably is growing thicker. Measurement of strain rates is described in detail, and the significance of the various components of the strain rate and rotation rate tensors is discussed. The rate at which the ice shelf thins by creep increases towards the ice front, where the magnitude of vertical strain rates is determined by ice thickness. Intense convergence makes the vertical strain rate positive where major glaciers from the Transantarctic Mountains enter the ice shelf. In contrast, areas of sluggish ice dragged forward by neighboring fast ice streams, undergo rapid longitudinal extension and creep thinning. Accumulation rates from stake measurements support results from analysis of ice cores: values are lower than expected over much of the ice shelf. In a large part of the ice shelf near the West Antarctic ice sheet, 10-m temperatures are about 1°C higher than values that were obtained during the International Geophysical Year (1957-1958). Although this paper does not contain a detailed analysis of the results, there is a brief review of how they can be used to investigate various aspects of ice shelf dynamics.

Contents

Introduction

Ice shelves form where ice flows off a grounded ice sheet onto the sea and spreads out to produce a nearly flat slab of floating ice. Most present-day ice shelves are in Antarctica, where they partially fill the major embayments and serve to smooth the outlines of the continent (Figure 1). Because ice shelves rest on sea water, they possess an almost frictionless bed of known temperature, so that ice velocities and strain rates are nearly independent of depth [Sanderson and Doake, 1979], and the boundary conditions are well defined. Moreover, because ice shelves are so flat, conditions change slowly over distances comparable to the ice thickness.

Historically, ice shelves have been used as highways to the ice sheet, and ease of access has encouraged numerous studies of ice shelf behavior, particularly near the seaward edge, or ice front, where the expedition stations were established. During the International Geophysical Year (1957-1958), a group working out of Little America V (Figure 2) circumnavigated the Ross Ice Shelf and measured gravity, ice thickness, depth to seabed, 10-m temperatures, and snow-accumulation rates at 90 stations [Crary et

[1]California Institute of Technology, Jet Propulsion Laboratory, Pasadena, California 91109. Currently at Code EE-8, NASA Headquarters, Washington, D.C. 20546.
[2]Geophysical Fluid Dynamics Laboratory, Princeton University, Princeton, New Jersey 08540.
[3]1018 Castilian Court, #314, Glenview, Illinois 60025.
[4]Department of Geology, University of Wyoming, Laramie, Wyoming 82070.

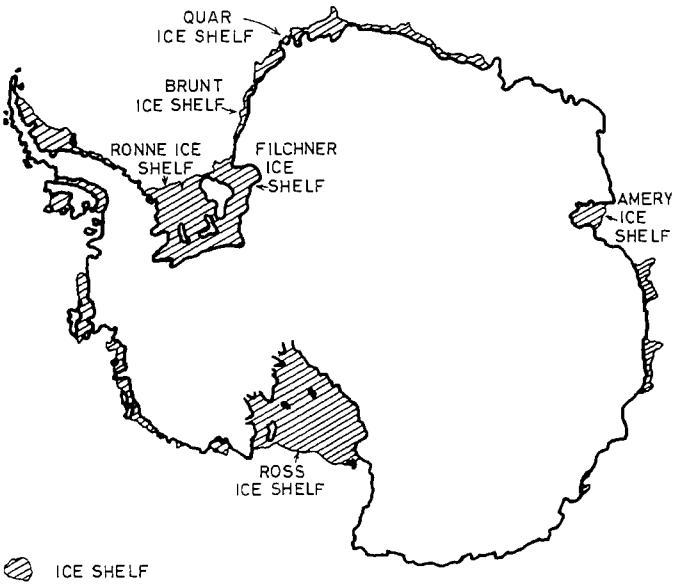

Fig. 1. Antarctica, showing the ice shelves. The Quar Ice Shelf is often referred to as the 'Maudheim Ice Shelf.'

al., 1962]. More detailed glaciological work near Little America V gave estimates of strain rates and bottom-melting rates [Crary, 1961]. In addition, a hole was drilled through the 257-m thick ice shelf [Bender and Gow, 1961] to give ice temperatures consistent with the estimates of bottom melting rates derived from the surface measurements [Crary, 1961; Shumskiy and Zotikov, 1969]. Examination of the physical characteristics of ice from the hole [Gow, 1963] has shown how the ice fabric (crystal size and c axis orientation) varies with depth as a consequence, perhaps, of the strain history of the ice shelf. Almost 20 years after this hole was drilled, chemical and isotopic analyses of the ice continue to pose glaciological problems that remain unsolved [Langway et al., 1974; Dansgaard et al., 1977].

Other work during the IGY included a detailed study of ice deformation in the area of fractured ice shelf near the Bay of Whales, immediately to the (grid) south of Roosevelt Island [Zumberge et al., 1960]. Repeated measurements of the exposed length of almost 2000 bamboo poles along a tractor trail between the Bay of Whales and Ross Island gave snow-accumulation rates along most of the Ross Ice Front [Heap and Rundle, 1964]. The same route was used for two survey traverses which yielded ice velocities at 103 markers [Dorrer et al., 1969]. Velocities were also measured, near Ross Island by Stuart and Heine [1961] and Swithinbank [1970] and on and near the major valley glaciers that flow through the Transantarctic Mountains into the ice shelf [Swithinbank, 1964; personal communication, 1979]. An extensive program of airborne radio-echo sounding by the Scott Polar Research Institute in cooperation with the National Science Foundation yielded ice thicknesses over most of the ice shelf [Robin, 1975].

The positions of RIGGS stations are shown in Figure 2. (In order to maintain consistency with other RIGGS reports, this and other map figures are presented in the 'grid' system. This rectangular system has its origin at the South Pole and a north-south direction parallel to the Greenwich meridian with north towards Greenwich. One grid degree equals 1° of geographic latitude.) Glaciological observations included the measurement of strain rates, accumulation rates, and ice velocities. At some of the stations, 10-m holes were cored for oxygen isotope analysis, and for beta particle scanning to give long-term accumulation rates; temperatures were measured at the bottom of these holes. Acquisition and analysis of the 10-m firn cores were by a group from the University of Copenhagen, and the results have already been published [Clausen and Dansgaard, 1977; Dansgaard et al., 1977; Clausen et al., 1979]. Precise position fixes at approximately half of the stations provided the data necessary for the estimates of ice velocity. These data were obtained by using light-weight satellite-tracking equipment by members of the United States Geological Survey under the direction of W. MacDonald and W. Kosco. Here we shall present the following results: ice veloci-

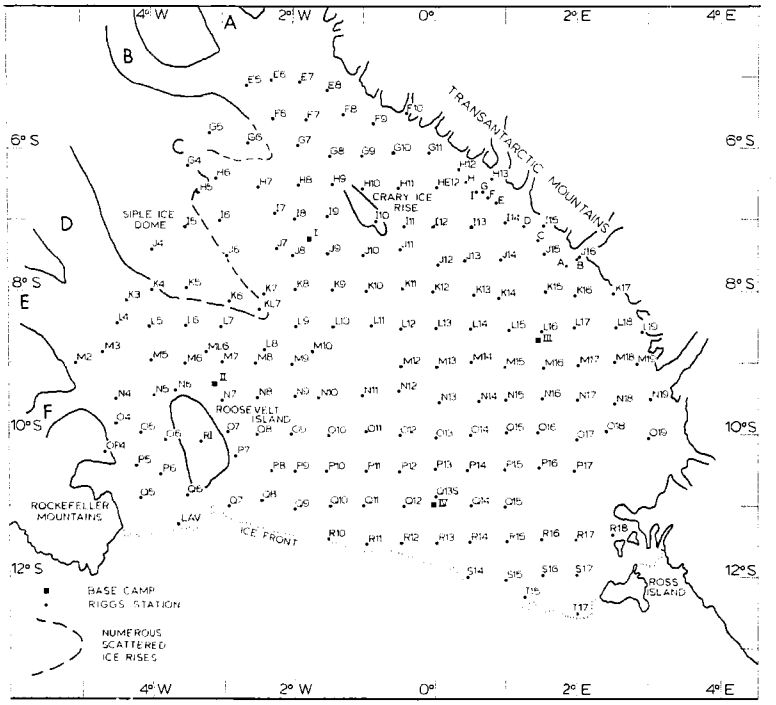

Fig. 2. The Ross Ice Shelf, showing the positions of RIGGS stations and base camps. The base camps are (I) 'Base Camp' (BC), (II) 'Roosevelt Island' (R.I.), (III) Crary station #16 (C-16), and (IV) RIGGS station Q13. Stations A to I close to the Transantarctic Mountains were established by C. Swithinbank in 1961 (personal communication, 1979). Station LAV is Crary's base camp, Little America V [Crary, 1961]. The bold capitals A to F mark the positions of ice streams that flow from the West Antarctic ice sheet into the Ross Ice Shelf. Note that the coordinates on this, and other diagrams, are grid coordinates. This rectangular system has its origin at the South Pole and a north-south direction parallel to the Greenwich meridian with north toward Greenwich. One grid degree equals one degree of geographic latitude.

ties, strain rates, snow-accumulation rates from stake measurements, and 10-m temperatures. Ice shelf parameters derived from these data (steady state particle paths; ice shelf flow parameters; stress distribution; etc.), and comparison of the measured ice velocities with those generated by a finite element model of the ice shelf have been published elsewhere [Thomas and MacAyeal, 1982; MacAyeal and Thomas, 1982].

Strain Rates

Before introducing RIGGS results, we shall describe how field measurements are used to give the deformation rate tensor. For a more thorough introduction to tensor analysis the reader is referred to Nye [1957].

The rate of deformation of an ice sheet at any point can be fully expressed with respect to mutually-perpendicular axes (x, y, and z) by the sum of two second-rank tensors:

$$\begin{bmatrix} \dot{\varepsilon}_{xx} & \dot{\varepsilon}_{xy} & \dot{\varepsilon}_{xz} \\ \dot{\varepsilon}_{yx} & \dot{\varepsilon}_{yy} & \dot{\varepsilon}_{yz} \\ \dot{\varepsilon}_{zx} & \dot{\varepsilon}_{zy} & \dot{\varepsilon}_{zz} \end{bmatrix} + \begin{bmatrix} 0 & \dot{\omega}_{xy} & \dot{\omega}_{xz} \\ \dot{\omega}_{yx} & 0 & \dot{\omega}_{yz} \\ \dot{\omega}_{zx} & \dot{\omega}_{zy} & 0 \end{bmatrix}$$

where

$$\dot{\varepsilon}_{ij} = \frac{1}{2}\left\{\frac{\partial U_i}{\partial j} + \frac{\partial U_j}{\partial i}\right\} \qquad (1)$$

$$\dot{\omega}_{ij} = \frac{1}{2}\left\{\frac{\partial U_i}{\partial j} + \frac{\partial U_j}{\partial i}\right\} \qquad (2)$$

and U_i is the velocity in the i direction. The tensor involving $\dot{\varepsilon}_{ij}$ describes the strain rate and, because $\dot{\varepsilon}_{ij} = \dot{\varepsilon}_{ji}$, it is symmetric. The tensor involving $\dot{\omega}_{ij}$ describes the rate of rotation of the deformed material, and this is an antisymmetric tensor because $\dot{\omega}_{ij} = -\dot{\omega}_{ji}$.

For any set of axes, there are 9 unknowns that must be measured to give the two tensors. When measurements are made at the surface of an ice sheet or glacier, this surface is defined as the xy plane. Then, because the surface cannot support a shear stress, we assume that there is no shear strain at the surface in the xz and yz planes. This means that

$$\frac{\partial U_x}{\partial z} = \frac{\partial U_z}{\partial x} = \frac{\partial U_y}{\partial z} = \frac{\partial U_z}{\partial y} = 0$$

We make the additional assumption that ice is incompressible so that $\Sigma\, \partial U_i/\partial i = 0$. This assumption does not apply to the upper layers of firn, where the vertical velocity gradient is dominated by the densification process. Consequently, we define $\partial U_z/\partial z$ as the vertical velocity gradient due to creep of the ice, and the upper layers of firn are regarded as an equivalent thickness of solid ice. (Note that we shall use the term 'vertical' to signify the z direction.) We can then write $\dot{\varepsilon}_{zz} = -(\dot{\varepsilon}_{xx} + \dot{\varepsilon}_{yy})$. Finally, we assume zero rotation in the vertical planes, so that $\dot{\omega}_{xz} = \dot{\omega}_{zx} = \dot{\omega}_{yz} = \dot{\omega}_{zy} = 0$.

The deformation rate is now completely specified by the two tensors:

$$\begin{bmatrix} \dot{\varepsilon}_{xx} & \dot{\varepsilon}_{xy} \\ \dot{\varepsilon}_{xy} & \dot{\varepsilon}_{yy} \end{bmatrix} + \begin{bmatrix} 0 & \dot{\omega}_{xy} \\ -\dot{\omega}_{xy} & 0 \end{bmatrix}$$

This representation of the deformation rate and the physical significance of the tensor components are illustrated in Figure 3. The rotation-rate tensor (the one involving $\dot{\omega}_{xy}$) expresses the part of the deformation that corresponds to rigid body rotation. By isolating this part of the deformation, the strain rate tensor is not affected by rotation of the material. Thus, on an ice shelf for instance, evaluation of the strain rate tensor requires measurements on the surface of the ice shelf without reference to any external coordinate system. By contrast, the rotation-rate tensor is measured by observing the change in azimuth, with respect say to true north, of a direction on the surface of the ice shelf. This change in azimuth is generally caused by both shear deformation and absolute rotation (Figure 3).

The simplest way to measure the tensor components is to observe the relative displacement and absolute rotation over some appropriate time interval, Δt, of three stakes that initially form a right-angled triangle on the x and y axes (Figure 4). In the example shown,

$$\frac{\partial U_x}{\partial y} = \frac{\beta}{\Delta t};\quad \frac{\partial U_y}{\partial x} = \frac{-\alpha}{\Delta t}$$

$$\dot{\varepsilon}_{xx} = \frac{\partial U_x}{\partial x} = \frac{1}{\Delta t} \ln \frac{OA'}{OA} \sim \frac{1}{\Delta t} \left\{ \frac{OA' - OA}{OA} \right\}$$

$$\dot{\varepsilon}_{yy} = \frac{\partial U_y}{\partial y} = \frac{1}{\Delta t} \ln \frac{OB'}{OB} \sim \frac{1}{\Delta t} \left\{ \frac{OB' - OB}{OB} \right\}$$

$$\dot{\varepsilon}_{xy} = \frac{1}{2\Delta t} (\beta - \alpha);\quad \dot{\omega}_{xy} = \frac{1}{2\Delta t} (\beta + \alpha) = \dot{\varepsilon}_{xy} + \frac{\alpha}{\Delta t}$$

Note that in this case $\partial U_x/\partial y$ is positive because U_x increases with increasing y to give a clockwise motion of B to B'. However, the clockwise motion of A to A' is associated with a decrease in U_y for increasing x, so $\partial U_y/\partial x = -\alpha$. For right-handed axes, like those in Figure 4, the rotation rate $\dot{\omega}_{xy}$ is positive for clockwise rotation, and the shear strain rate $\dot{\varepsilon}_{xy}$ is positive if the right angle AOB decreases during deformation.

So far, the choice of x and y axes has been arbitrary. A different set of axes would give different values for the components of the strain rate tensor, but not for the rotation rate. An important property of the strain rate tensor, and of any symmetric second-rank tensor, is the existence of principal axes. These are the axes (1,2) about which the shear component $\dot{\varepsilon}_{12}$ of the strain rate is zero, and the longitudinal strain rates $\dot{\varepsilon}_{11}$ and $\dot{\varepsilon}_{22}$ reach a maximum and a minimum, respectively. The rate at which the principal axes rotate is then $\dot{\omega}_{12}$, which we shall write as $\dot{\omega}$ because it has the same value as $\dot{\omega}_{xy}$. The relationship between the tensor components for arbitrary axes and those along the principal axes are derived in any standard text book [e.g., Nye, 1957; Jaeger, 1969]. If θ is the angle, measured counterclockwise, between the principal axis (1) and an arbitrary x axis, then

$$\dot{\varepsilon}_{xx} = \frac{1}{2} (\dot{\varepsilon}_{11} + \dot{\varepsilon}_{22}) + \frac{1}{2} (\dot{\varepsilon}_{11} - \dot{\varepsilon}_{22}) \cos 2\theta \quad (3)$$

$$\dot{\varepsilon}_{yy} = \frac{1}{2} (\dot{\varepsilon}_{11} + \dot{\varepsilon}_{22}) - \frac{1}{2} (\dot{\varepsilon}_{11} - \dot{\varepsilon}_{22}) \cos 2\theta \quad (4)$$

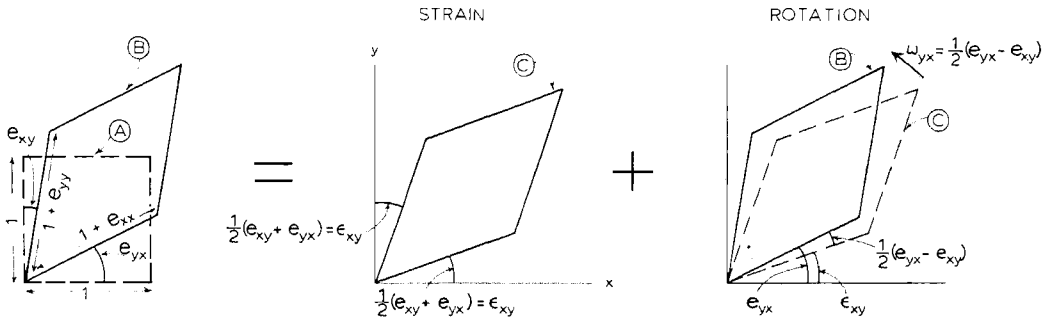

Fig. 3. Deformation of a unit square. The square (A) is infinitesimally deformed to become the parallelogram (B) after a time interval Δt, so that $\partial U_i/\partial_j \simeq e_{ij}/\Delta t$; e_{ij} components are defined in the figure. The deformation consists of strain to form a parallelogram (C) symmetrically placed with respect to the axes, and a rotation of the parallelogram from (C) to (B). The rotation does not affect the longitudinal strains, so $e_{xx} = \epsilon_{xx}$, etc.

and

$$\dot{\varepsilon}_{xy} = -\frac{1}{2}(\dot{\varepsilon}_{11} - \dot{\varepsilon}_{22}) \sin 2\theta \qquad (5)$$

Thus, values of $\dot{\varepsilon}_{xx}$, $\dot{\varepsilon}_{yy}$ and $\dot{\varepsilon}_{xy}$ that result from the measurement described can be used to solve these equations for $\dot{\varepsilon}_{11}$, $\dot{\varepsilon}_{22}$, and θ. However, this measuring technique requires rather precise placement of the markers. An easier method involves measurement of longitudinal strain rates in any three directions, x, x', and x" on the surface of the ice sheet. Equation (3) then becomes

$$\dot{\varepsilon}_{xx} = \frac{1}{2}(\dot{\varepsilon}_{11} + \dot{\varepsilon}_{22}) + \frac{1}{2}(\dot{\varepsilon}_{11} - \dot{\varepsilon}_{22}) \cos 2\theta$$

$$\dot{\varepsilon}_{x'x'} = \frac{1}{2}(\dot{\varepsilon}_{11} + \dot{\varepsilon}_{22}) + \frac{1}{2}(\dot{\varepsilon}_{11} - \dot{\varepsilon}_{22}) \cos 2(\theta + \phi)$$

$$\dot{\varepsilon}_{x''x''} = \frac{1}{2}(\dot{\varepsilon}_{11} + \dot{\varepsilon}_{22}) + \frac{1}{2}(\dot{\varepsilon}_{11} - \dot{\varepsilon}_{22}) \cos 2(\theta + \psi)$$

where ϕ is the (anticlockwise) angle between x and x', and ψ is the angle between x and x". Solution of these three equations gives $\dot{\varepsilon}_{11}$, $\dot{\varepsilon}_{22}$, and θ.

Although the strain rate tensor can be determined by measurements in only three directions, there is no data redundancy to provide a check on observation errors. Moreover, there is always the possibility of losing one of the stakes comprising a strain network. For these reasons, strain networks on glaciers generally consist of more than three stakes. For RIGGS, we used a pattern of stakes similar to that described by Kehle [Zumberge et al., 1960]. These 'strain rosettes' consisted of three aluminum poles (A, B, and C) planted to form an approximately equilateral triangle, with a fourth stake (O) at the center (Figure 5). The distances and angles from the central to the peripheral stakes were measured when the station was established, and again one or two years later. Distances OA, OB, and OC were in the range 1 → 1.5 km.

Errors in the principal components of the strain rate tensor resulting from these measurements are inversely proportional to the sine of the smallest angle between any two directions, so the equilateral rosette in Figure 5 represents the optimum condition.

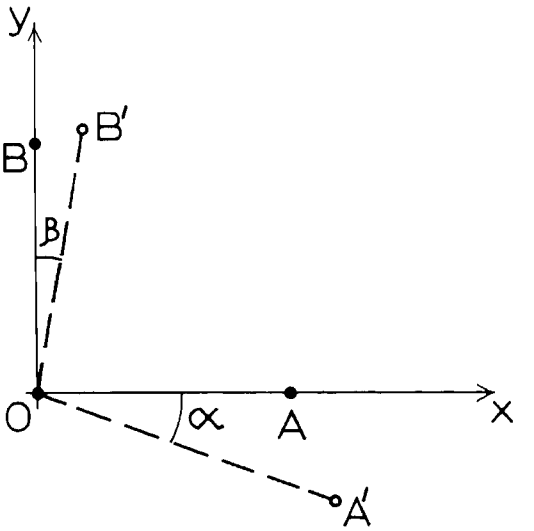

Fig. 4. Measurements of the strain rate and rotation rate tensors, using three stakes that, initially, form a right-angled triangle.

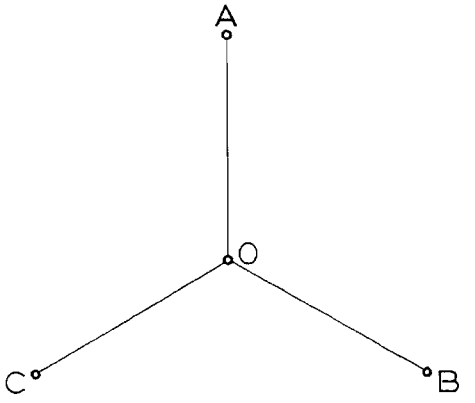

Fig. 5. A strain rosette. The distances and angles from the central stake O, to peripheral stakes A, B, and C, are measured on at least two separate occasions. On the Ross Ice Shelf, OA, OB, and OC were between 1 and 1.5 km in length.

The field measurements yield strain rate tensors for a total of five sets of directions: (OA,OB,OC), (AB,BC,CA), (OA,AB,BO), (OB,BC,CO), and (OC,CA,AO). The minimum angle of separation in the first two sets of directions is 60°, but for the last three sets the minimum is 30°, which reduces the expected accuracy by a factor of almost 2. In Figure 6, the five values of principal strain rates for Station H10 (Figure 2) are shown plotted in their various triangles. Although the calculated values apply to the entire relevant triangle, they are assigned to the triangle center. The values plotted at O were obtained from directions OA, OB, and OC; those plotted nearby were from AB, BC, and CA. There is good agreement between the different values, as was the case for most RIGGS stations. When there were significant differences they appeared to represent a real variation across the rosette in an area undergoing intense shear.

As a check on the uniformity of strain rates, measurements were made on several rosettes with legs of 1 → 1.5 km planted within strain networks up to 8 km wide. Although there were detectable strain rate gradients across the larger networks, results from the smaller rosettes showed excellent agreement with the regional strain rates, except again in regions of strong shear that develop near ice rises and between streams of ice that flow at different speeds. Strain rates measured in these shear bands must be regarded as spot values, but most of the RIGGS data yielded strain rates that represent the regional values.

In most cases the values of the principal strain rates ($\dot{\varepsilon}_{11}$ and $\dot{\varepsilon}_{22}$) derived from the two sets of directions at 60° to each other agreed to better than 10^{-4} yr^{-1} (usually less than 5% difference), and the principal axes were generally coincident to within 2° of arc. However, the precision to which principal axis orientation can be estimated depends not only on observation errors, but also on the magnitude of the difference between $\dot{\varepsilon}_{11}$ and $\dot{\varepsilon}_{22}$. When there is zero difference, the principal axes can take any orientation, so that the effect of observation errors on orientation increases as $\dot{\varepsilon}_{11} \to \dot{\varepsilon}_{22}$.

For the strain rate tensor calculated from observed strains in the OA, OB, and OC directions, the effect of errors in observing the angles is negligible [Zumberge et al., 1960, p. 75]. In this case the errors in strain rate are due solely to errors in measuring distance. For a typical rosette with OA $\sim$ OB $\sim$ OC $\sim$ 1300 m these are $\sim \pm$ 0.02 m when the rosette is planted and $\sim \pm$ 0.03 m when the rosette is remeasured (the increase is due to possible tilt of the stakes during the intervening period). Errors in the estimates of strain for each leg are then $\sim \pm \sqrt{0.0013}/1300$. These lead to errors in the principal components of the strain tensor of $\sim \pm 5 \times 10^{-5}$. Most of the rosette remeasurements were made after an interval of about one year, so anticipated errors in the principal strain rates are

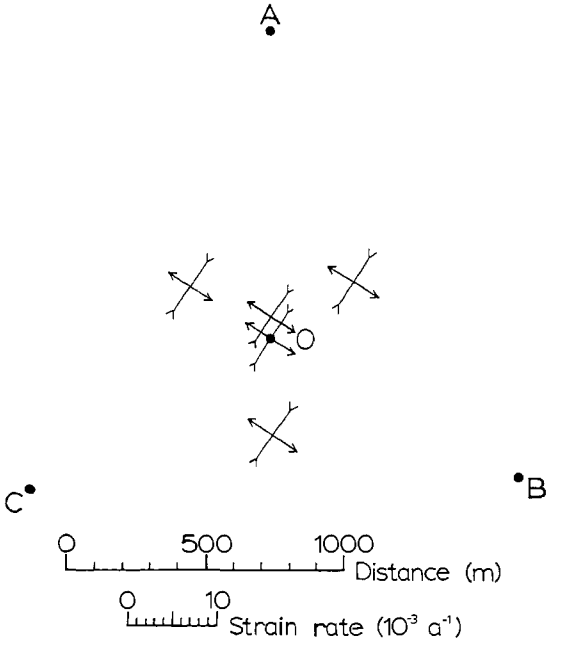

Fig. 6. Strain rate tensors resulting from the rosette at station H10. The value at O was obtained from the strains that were measured along OA, OB, and OC; the value near O was from triangle ABC, and the other values were from the triangles of which they form the centers.

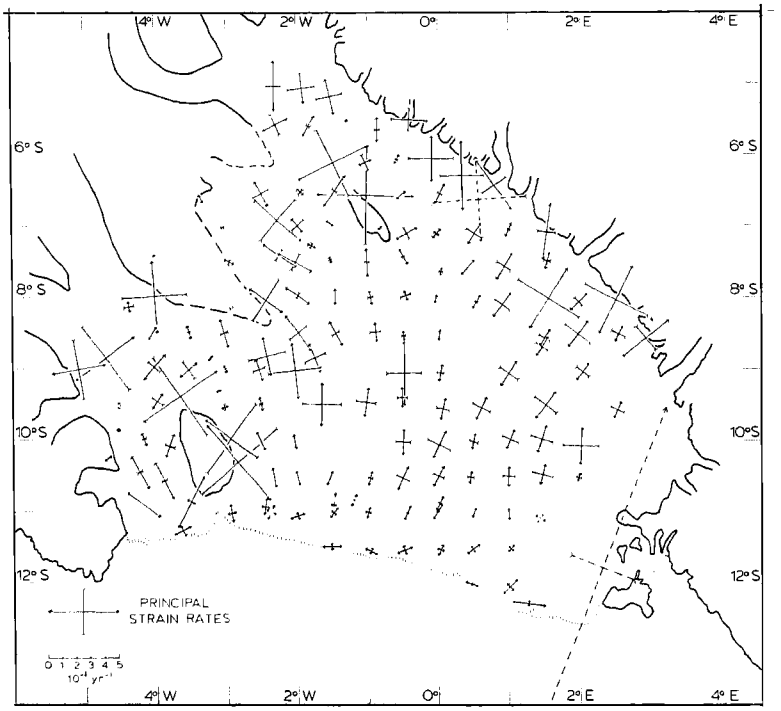

Fig. 7. The strain rate field on the Ross Ice Shelf resulting from the RIGGS measurements. The strain rates depicted by the broken lines are from earlier measurements (E. Dorrer, personal communication, 1979; C. Swithinbank, personal communication, 1979).

$\sim \pm 5 \times 10^{-5}$ yr^{-1}. For 35 stations near Roosevelt Island, measurements covered a two-year period, reducing expected errors to $\sim \pm 3 \times 10^{-5}$ yr^{-1}. These estimates are supported by the good agreement between the values of $\dot{\varepsilon}_{11}$ and $\dot{\varepsilon}_{22}$ derived from the five sets of directions within any one rosette.

Principal components of the strain rate tensors for the RIGGS stations are given in the appendix Table A1 and in Figure 7. In most cases the values are averages of all five estimates, and the quoted errors are the standard deviations of the averages. At a few stations no errors are quoted; these are stations where one of the stakes was lost before remeasurement, so that only one estimate of the strain rate tensor could be made. Most of the stations where the errors significantly exceed $\pm 10^{-4}$ yr^{-1} are either in shear bands or near grounded ice rises. For instance, all the stations nearest to the Transantarctic Mountains have large errors, and this is an area where we expect high strain rate gradients and a significant variation across a rosette, so that the standard deviation is an indication of the magnitude of strain rate gradients rather than of observing errors.

The rotation rate $\dot{\omega}$ is obtained by observing the rate of rotation of one of the rosette legs. Then, with the x axis along this direction, the observed rotation rate $\partial U_y/\partial x$ is due partly to shear ($\dot{\varepsilon}_{xy}$) and partly to rotation ($\dot{\omega}$) of the principal axes. From equations (1) and (2)

$$\dot{\omega} = \dot{\varepsilon}_{xy} - \frac{\partial U_y}{\partial x}$$

where $\dot{\varepsilon}_{xy}$ can be calculated from the principal strain rates by using (5). Values of $\dot{\omega}$ for most of the RIGGS stations are included in the appendix Table A1. Errors are difficult to estimate; they are compounded of errors in the strain rate measurements and errors in repeated measurements of true azimuth. They are probably approximately 10^{-4} yr^{-1} larger than the estimated strain rate errors.

With the ice shelf deformation expressed as the magnitude and direction of principal components of the strain rate and rotation rate tensors, the velocity gradients in any direction can be calculated readily, using equations (1)-(5). Of particular interest are the velocity gradients along, and perpendicular to, the direction of movement. Choosing the x axis to be in the direction of ice movement, the product of velocity U_x and longitudinal strain rate $\dot{\varepsilon}_{xx}$ is the acceleration of a particle of ice as it

moves seaward, the lateral strain rate $\dot{\varepsilon}_{yy}$ gives the flow line divergence, $\partial U_x/\partial y$ is the velocity gradient transverse to the flow direction and $\partial U_y/\partial x$ gives the flow line curvature. The values of $\dot{\varepsilon}_{xx}$, $\dot{\varepsilon}_{yy}$, and $\dot{\varepsilon}_{xy}$ can be found by using (3)-(5). Rearrangement of (1) and (2) gives

$$\frac{\partial U_x}{\partial y} = \dot{\varepsilon}_{xy} + \dot{\omega} \qquad (6)$$

$$\frac{\partial U_y}{\partial x} = \dot{\varepsilon}_{xy} - \dot{\omega} \qquad (7)$$

Then, the radius of flow line curvature is

$$R = \frac{U_x}{\dot{\varepsilon}_{xy} - \dot{\omega}} \qquad (8)$$

where R is positive for anticlockwise curvature.

The strain rates represented by broken lines in Figure 7 are the previously unpublished results of Charles Swithinbank (near the mouth of the Beardmore Glacier) and of Egon Dorrer (near the ice front). Swithinbank's measurements were made by using a Kehle strain rosette with 300-m legs, and the different results from the five sets of directions within the rosette showed excellent consistency. Where there were significant deviations from a straight line in the stake traverse used by Dorrer et al. [1969] to measure ice velocity, the strain rate tensor could be calculated from the survey data. We have included in Figure 7 the results from these stations of Dorrer et al.: R5, R17, R53, R57, and R69. The traverse made a sharp turn at R69 (close to Roosevelt Island), and the strain rates here should be the most reliable. At R53 and R57, the deviation from a straight line was small, and the calculated strain rates are less reliable. At R5 and R17, the deviation exceeded 30° of arc and, generally, this would be sufficient to give strain rates of acceptable accuracy. However, at R5 (close to Ross Island) there is both rapid shear perpendicular to the traverse, and a very large strain rate gradient along the traverse. Under these conditions, even when observing errors are small, the calculated strain rate tensor is misleading, particularly the component perpendicular to the traverse. In this case, the very large extending strain rate is almost certainly an artifact resulting from the situation of R5; it is unlikely to be real.

Vertical strain rates $\dot{\varepsilon}_{33}$ were calculated for each station, assuming the ice to be incompressible so that

$$\dot{\varepsilon}_{33} = -(\dot{\varepsilon}_{11} + \dot{\varepsilon}_{22}) \qquad (9)$$

and isolines of vertical strain rate are shown in Figure 8. These results will be discussed in the final section.

Ice Velocities

Before RIGGS, movement of the Ross Ice Shelf had been measured near Ross Island [Stuart and Heine, 1961; Swithinbank, 1970] near the Transantarctic Mountains [Swithinbank, 1964; personal communication, 1979] and near the ice front and south of Roosevelt Island [Dorrer et al., 1969]. Robin [1975] extrapolated these data across the ice shelf by adopting a pattern of mass balance for the upper and lower surfaces of the ice shelf and applying volume conservation principles to measured ice thickness profiles. This procedure involves the implicit assumption that the ice shelf is in steady state, with thickness profiles that are time invariant. A major aim of glaciological field work is to check whether this is so. Consequently, as part of RIGGS, the U.S. Geological Survey made accurate position fixes at approximately half of the stations by using satellite Doppler-tracking equipment (Geoceiver or JMR-1). For most of the RIGGS program a Geoceiver was used and, although this equipment is heavier than the JMR-1, it is reliable and robust. The JMR-1 was used during the 1976-1977 season, not long after its appearance on the market. It offers the major advantage of light weight (about 80 lbs, in comparison with 250 lbs for the Geoceiver) and the capability of providing real time computation of positions in the field. Most of the problems that were experienced with satellite tracking were due to failure of the small generators used to provide power. A weakness in the JMR-1 antenna that caused minor problems has since been rectified by the manufacturers.

Station positions were obtained by the 'point-positioning' method [Defense Mapping Agency, 1972]; data collected by one instrument were sufficient to give an absolute position by adopting the ephemeris appropriate to the observed satellite. Most stations were occupied for between 3 and 5 hours and, with precise ephemerides available for two satellites, this generally allowed sufficient time to track at least four satellite passes. Satellite tracking can be done either automatically or manually. Automatic tracking can lead to problems for two reasons: first, because the data have to be 'unscrambled' for analysis, and second,

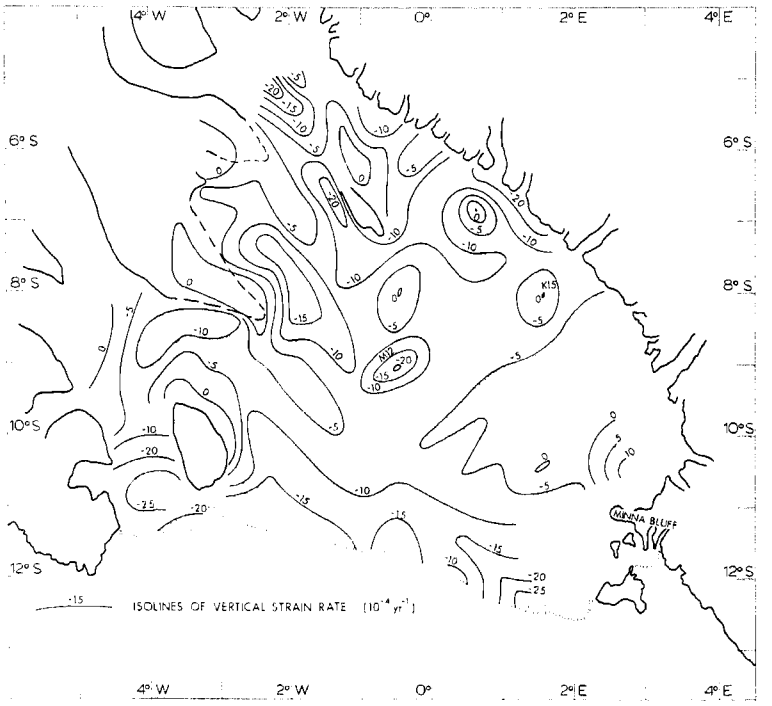

Fig. 8. Vertical strain rates on the Ross Ice Shelf. The data for the area near Minna Bluff are from Crary and Wilson [1961].

because two satellites often rise above the horizon at approximately the same time, with the strong possibility that the instrument will track the wrong one. Consequently, except during the first season of RIGGS, almost all tracking was done manually.

Position accuracy depends on the number and geometry of satellite passes recorded by the tracking equipment. In general, a vertical as well as horizontal position is obtained, and the limiting accuracy for the point-positioning method gives a root mean square radial error of 1.6 m. This applies to solutions with as few as 35 passes or as many as 200 [Schwarz et al., 1972]. An approximate estimate of root mean square radial error in meters for a solution with a small number of passes n is $(8.74/\sqrt{n})$. Thus, for a four-pass solution, the estimated error is approximately 4 m. However, although this estimate is supported by results from the Geoceiver test program [Defense Mapping Agency, 1972] we regard it as an optimistic estimate since it is based on data that were collected under ideal conditions in the United States. Instead, we have adopted error estimates that are approximately double those given by the above expression. This is consistent with the recommendation of W.R. MacDonald (personal communication, 1973) who, after a thorough examination of available data, suggested that a position accuracy of 6-8 m is the best that can be expected from a four-pass solution. In doing this, we probably err on the conservative side, because the systematic part of the estimated error does not contribute to errors in calculated velocities. Many more than four satellite passes were tracked at each of the base camps, and position errors at these stations are probably less than ± 3 m. Correction for movement during satellite tracking at these stations was made by assigning the calculated position to an epoch time at the middle of the observation period. At some field stations, fewer than four passes were monitored, and occasionally only one 'good' pass was observed. During data reduction and analysis it was possible to obtain an indication of position errors for these one-pass solutions from the consistency of the data and the geometry of the satellite orbit (W.R. MacDonald, personal communication, 1973).

Most of the stations were reoccupied after one year, but there was a two-year period before reoccupation of stations J4, K3, M3, N4, N8, O5, P6, Q6, and R.I., all near Roosevelt Island. In most cases, the position fixes included estimates of station elevation, which should not change significantly between observations. If the two values for station elevation differed by more than 15 m the position data were not used to calculate ice velocities. The average difference between the remaining pairs

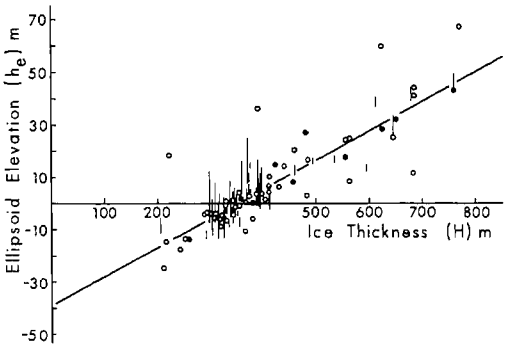

Fig. 9. A plot of surface elevation (h_e), with respect to the NWL-9D ellipsoid, against ice shelf thickness (H). The values of h_e are from the satellite-tracking program, and the values of H are from the RIGGS geophysics program [C.R. Bentley, personal communication, 1979]. The hollow circles refer to stations where h_e was measured on only one occasion; the vertical lines indicate the spread of values when h_e was measured more than once; the solid circles refer to stations where separately-measured values of h_e differ by less than 3 m.

of surface-elevation estimates was 4.3 m. This may be the best available estimate of actual position errors.

The calculated surface elevations obtained from the satellite-tracking program were with respect to the NWL-9D ellipsoid (semi-major axis 6,378,145 m; flattening: 1/298.25), and they could not be compared directly with estimates of surface elevation above sea level calculated from ice thicknesses. However, by making some simplifying assumptions, comparison of these two sets of data gives an indication of consistency. Assume that the difference between sea level and the ellipsoid is Δh and that this is constant over the Ross Ice Shelf (Δh is positive if the ellipsoid lies above sea level). Then the elevation of a station (h_s) with respect to sea level is related to the elevation with respect to the ellipsoid (h_e) by

$$h_s = h_e + \Delta h \qquad (10)$$

For a floating ice shelf of thickness H, the surface elevation is also given by

$$h_s = H\left(1 - \frac{\rho_i}{\rho_w} + \frac{C\,\rho_i}{\rho_w}\right) \qquad (11)$$

where ρ_i and ρ_w are the densities of bubble-free ice and sea water, respectively, and C is the length of the equivalent vertical column of air contained within the ice shelf. Then, if C is constant over the ice shelf, a plot of h_e against H should give a straight line of slope $(1 - \rho_i/\rho_w)$ and of intercept $\{C\,\rho_i/\rho_w - \Delta h\}$. Such a plot, using data from all the RIGGS stations where the necessary measurements were made, is shown in Figure 9. The slope of the regression line for all 103 data points is 0.111, which is close to the calculated value of 0.110 obtained by taking ρ_i = 917 kg m^{-3} and ρ_w = 1030 kg m^{-3}. Values of h_e for five of the stations differ from the regression line by more than 15 m. These are all stations with only one measurement of the elevation, so we have no check on consistency. If these data are rejected, the slope of the regression line remains virtually the same, but the coefficient of determination increases from 0.75 to 0.87 (a value of unity would imply that all the data points lie on the regression line). The intercept at H = 0 is reduced from -38.4 m to -39.2 m. Clearly, it makes little difference to the numerical results whether we accept or reject these five data points. Here, we choose to reject them, so that

$$\frac{C\,\rho_i}{\rho_w} - \Delta h \sim -39.2 \text{ m} \qquad (12)$$

Results from drill holes on the Ross Ice Shelf [Crary, 1961; C.C. Langway, personal communication, 1975] indicate that C = 16 ± 1 m. Substituting this value into (12) gives Δh = 53.4 m, with an error of perhaps ± 2 m. This is remarkably close to the value of Δh = 53.6 m measured independently at McMurdo by comparing sea level with long-term satellite-tracking observations (W. Kosco, personal communication, 1980). Most of the data in Figure 9 have values of h_e within 10 m of the regression line. This lends confidence to our assumptions concerning C and Δh and to the reliability of velocities derived from the position fixes.

Only about half of the station positions were fixed by satellite-Doppler tracking. Velocities at other stations were interpolated by using the measured strain rates, which give ice velocity gradients. In general, since the strain rates change slowly between neighboring stations, a good approximation to the strain rates at an arbitrary point can be obtained by linear interpolation between adjacent stations. In principle, the velocity field can be reconstructed from the strain rate field if the absolute velocity and ice shelf rotation rate are known at one point [Thomas, 1976a]. In reality, however, there are regions within the ice shelf where linear interpolation of strain rates is not appropriate, and where the rotation rate changes rapidly between

stations (e.g., station R5 of Dorrer et al. [1969] that was discussed at the end of the last section). In reconstructing the velocity field, errors are cumulative, and they increase rapidly with increasing distance from the 'known' station. Consequently, extrapolation from a station with known velocity should be done over limited distances only, and if possible the extrapolation should include other stations with known velocities, as a check on the accuracy of velocity estimates. On the Ross Ice Shelf, most of the 64 stations where ice velocity was obtained from repeated precise position fixes were used to control the velocity field reconstuction.

Interpolation of ice velocities between selected control stations (A and E in Figure 10) generally involved no more than three 'unknown' stations. The sequence of calculations was:

1. The average strain rate component along the line from station A (with known velocity) to a neighboring station B, calculated from the strain rate tensors at A and B, was multiplied by the distance AB to give the annual change in distance between the two stations. Assuming, for the moment, zero rotation of the line AB, the ice velocity at B was then calculated.

2. The velocity at C was calculated by using the strain rate components along both AC and BC, and the velocities at A and B. By using strain rates along both AC and BC this calculation incorporated the effects of rotation of BC with respect to AB. However, if there was rotation of the line AB, then the velocity calculated for C (and for any subsequent stations) must be corrected for this rotation.

3. Stage (2) was repeated for a fourth station D, using B and C as 'base' stations, and finally for E, using C and D as 'base' stations.

4. All of the calculated velocities require correction for rotation of the line AB. This had the same effect as rigid rotation of the entire ice shelf. In principle, the rotation rate could be estimated by averaging rotation rates for the appropriate direction that were calculated from observed strain rates and rotation rates at A and B. However, rotation rates were not observed at each station, and we had no check on the accuracy of those that were. Consequently, the rotation rate was obtained by comparing the known and the calculated velocities for the second control station E. In the example shown in Figure 10, the rotation correction to the calculated velocity at E is Δ, and it is applied at right angles to the direction AE. The angular rotation rate that must be applied to all calculated velocities is then + Δ/AE (positive in this case because it is applied in a clockwise direction). As an example of how the correction is applied, consider the velocity at C. There, the rotation correction is + AC(Δ/AE), and it is applied perpendicular to the direction AC (Figure 10).

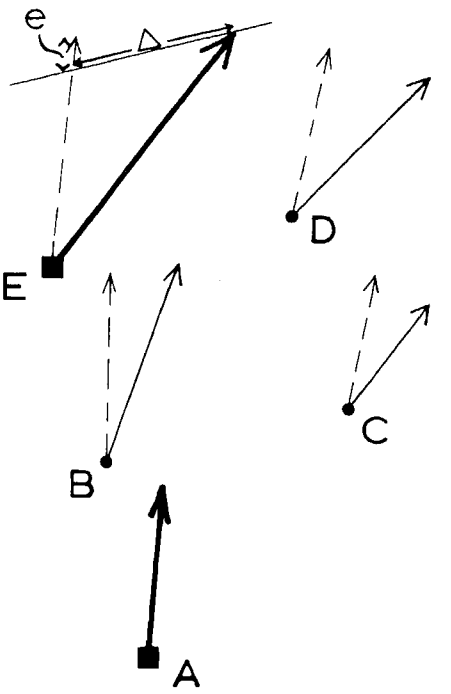

Fig. 10. Extrapolation of ice velocities from a control station A, to stations B, C, and D. Station E is another control station that is included in order to provide a check on accuracy. The broken line vectors are the velocities obtained without taking account of rotation. The bold vectors at A and E are velocities resulting from the satellite-tracking program. The extrapolated velocity at E can be adjusted to fit the observed value by clockwise rotation of the entire net, but there is still a residual error, e, and this gives an indication of actual velocity errors at the intermediate stations. After the rotation correction is applied, the velocities at B, C, and D become those depicted by the solid vectors.

In the example shown in Figure 10 there is a residual difference (e) between observed and calculated velocities at E that cannot be ascribed to rotation effects. This represents the cumulative effects of errors in the velocities observed at the control stations and in the measured strain rates and of deviations from the assumed linear variation of strain rates between stations. Generally, e was less than 20 m yr^{-1}, and no attempt was made to distribute this residual error among stations

B, C, and D. The assumption of linear variation of strain rates cannot be applied over the entire ice shelf, particularly in the discrete zones of intense shear. When the extrapolation route lay across these shear zones, the residual error became unacceptably large. Fortunately, the large number of stations with known velocity allowed considerable choice of extrapolation route, so that these 'error zones' could be avoided. Moreover, several values of the velocity at any given station could be calculated by using different extrapolation routes and different control stations. Comparison of the results gave a standard deviation that was usually less than 25 m yr^{-1}. This gives some indication of actual errors, since errors in the observed velocities at control stations, and in the observed strain rates, were probably random. The small differences between observed and calculated velocities at control stations that were included in the extrapolation net indicate that velocities derived from the satellite Doppler tracking data are, at any event, consistent.

Most of the stations with unacceptably large errors were near Roosevelt Island, or midway between Roosevelt Island and Crary Ice Rise, where there is strong convergence as two ice streams meet. Significant improvement in the velocity estimates for these stations was achieved by extrapolating from nearby control stations by using both the longitudinal strain rate between stations and the transverse velocity gradients calculated from the observed values of rotation rate and the strain rate tensor, as described in the last section.

All ice velocities resulting from the RIGGS program are listed in the appendix Table A1. Error estimates have not been included, since they are based on internal consistency rather than independent checks. Nevertheless, we can provide these broad guidelines. Velocity errors at the four base camps are probably less than ± 5 m yr^{-1}; at the other control stations, they are less than ± 15 m yr^{-1}; at most of the remaining stations, they are less than ± 30 m yr^{-1}. The few stations where errors may be significantly larger are indicated in the appendix Table A1.

The velocities are also shown in Figure 11, together with a selection of other available measurements. The observations by Dorrer et al. [1969] were made at 133 stations, but for the sake of clarity, they are not all included in Figure 11. Estimates of velocity based on comparison of astrofixes are of significantly lower accuracy, and they have not been included. The velocity at Little America V is from extrapolation of the RIGGS measurements, using the strain rates for LAV that were obtained by Crary [1961]. Our value is considerably larger than Crary's estimate, and there are small differences between our velocity estimates and those of Dorrer et al. [1969]. We shall discuss these differences in the final section of this paper.

Snow Accumulation

Measurements of accumulation rates by the analysis of β particle activity to detect bomb horizons in 10-m cores were made at almost half of the RIGGS stations by a group from the University of Copenhagen. These results have already been published [Clausen and Dansgaard, 1977; Clausen et al., 1979], and they indicate that accumulation rates in the (grid) northwestern part of the ice shelf are only about half the previous estimates from analysis of pit stratigraphy [Crary et al., 1962].

At each of the rosette stations, the exposed lengths of the four aluminum stakes and four bamboo poles were measured when planted and again when revisited. The eight measurements at each station were averaged to give the snow accumulation rate. The stake measurements provide an independent estimate of accumulation rates, albeit for only a one- or two-year period.

Snow pits were dug at several stations to give density profiles. There was no clear trend in these pits toward increasing density in the upper 3 m. Density values for individual 100-mm increments varied between 300 kg m^{-3} and 500 kg m^{-3}, but average values for each of the top 3 m were within less than 5% of 390 kg m^{-3}, and this was the value that was used to calculate accumulation rates from the stake measurements. In view of the lack of any clear trend in the near-surface density/depth curves, we did not apply a settling correction.

The results of the stake measurements are included in the appendix Table A1, and in Figure 12 they are shown as contours of equal snow accumulation rate. We stress that most of the data were collected over a period of only one year, so there is a high probability that the measurements do not represent long-term accumulation rates. Nevertheless, where our results overlap those of Clausen and Dansgaard [1977] and Clausen et al. [1979], they show excellent agreement. There are differences in detail, but the important conclusion of Clausen and Dansgaard [1977], that in the (grid) northwestern quadrant of the ice shelf accumulation rates are lower than expected, is supported by our measurements.

We should note that the density measurements of Crary et al. [1962] show a greater variability than ours, both with depth and with position. Their data suggest that the

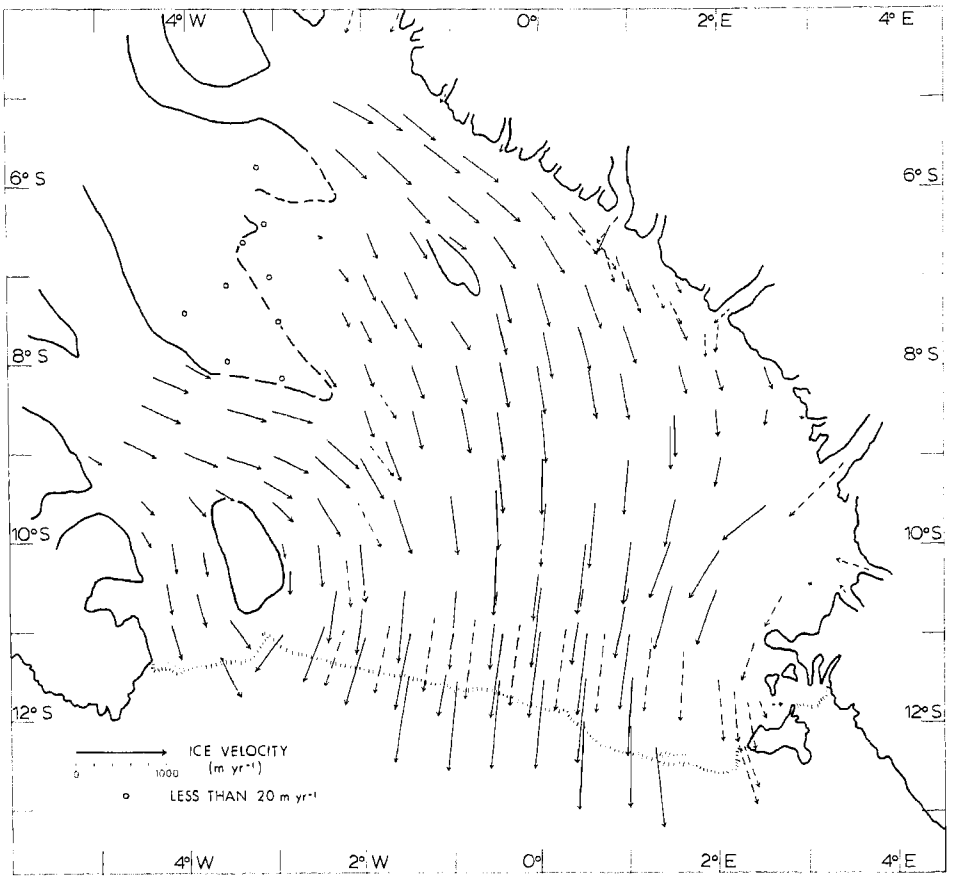

Fig. 11. Ice velocities on the Ross Ice Shelf. Values from RIGGS measurements are depicted by the solid vectors. The broken-line vectors are from earlier measurements [Stuart and Heine, 1961; Wilson and Crary, 1961; Swithinbank, 1964; 1970; personal communication, 1979; Dorrer et al., 1969].

settling correction would increase our estimates of snow accumulation by about 2% over most of the ice shelf, with up to 5% increase where measurements were made over a two-year period. At the same time, lower densities for the top meter would decrease most of our estimates by up to 13%, with maximum correction immediately to the (grid) north of Roosevelt Island. This correction decreases more or less linearly away from the maximum until, in the extreme (grid) north and southeast, there would be only a 5% increase. For most of the stations the net effect would be a correction of less than 10 mm of ice yr^{-1}.

Ten-Meter Temperatures

J. Nielsen and S. Hansen, from the University of Copenhagen, who drilled the 10-m holes for snow samples, also measured the temperatures at the bottom of the holes, using a glass-bead thermistor and a D.C. Wheatstone's Bridge on loan from the Cold Regions Research and Engineering Laboratories. The thermistors usually remained down hole for at least one hour, and often for several hours. Readings were taken frequently (usually every 5 min); after about 10 min, temperatures were found to follow closely Newton's law of cooling. This states that, for an object at temperature θ_t, the rate of warming or cooling ($\partial\theta/\partial t$) at time t is proportional to the temperature difference relative to the ambient temperature (θ_a):

$$\frac{\partial\theta}{\partial t} = b\ (\theta_a - \theta_t)$$

where b is a positive constant. Integrating gives

$$\ln\ |\theta_a - \theta_t| = a - b\ t$$

where a is another positive constant, and t

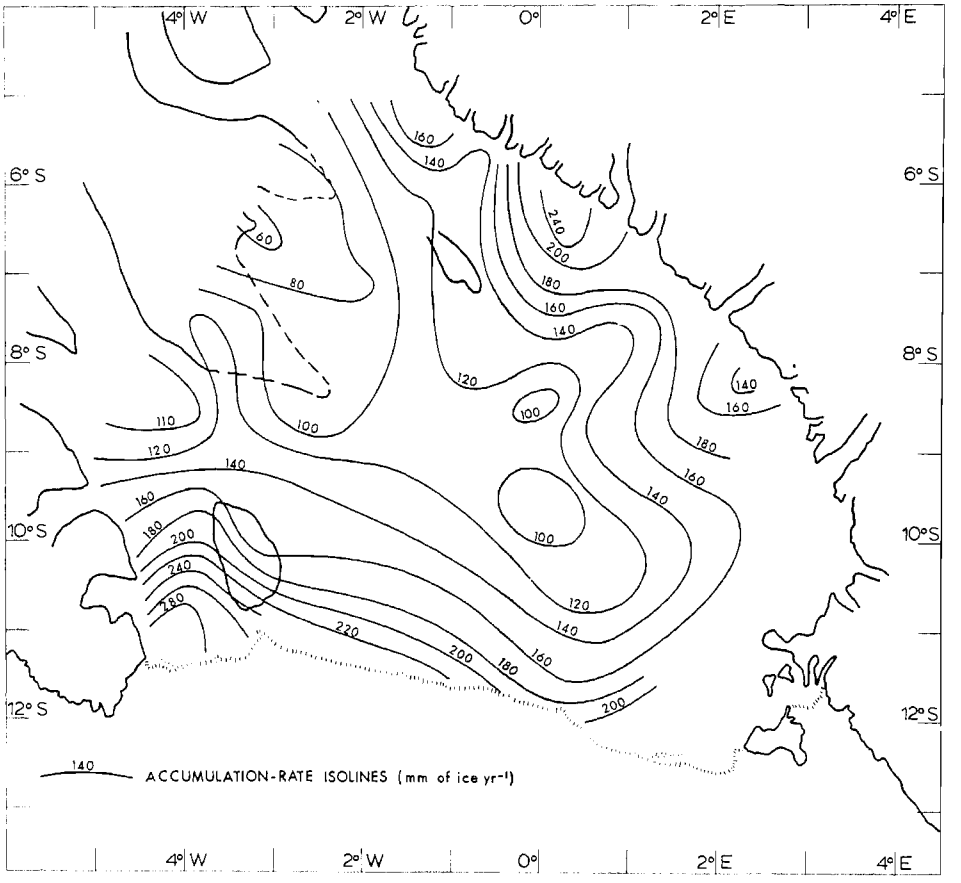

Fig. 12. Accumulation rates from stake measurements on the Ross Ice Shelf.

is the time since observations began. Measurements give θ and t, and θ_a is the value that gives the best straight line for a plot of $|\theta_a - \theta_t|$ against t. This can be obtained either graphically or by using a computer.

Errors may arise from instrument errors, distortion of the temperature field by the existence of the hole, convective air flow, or insufficient data to provide an adequate cooling curve. Instrument errors contribute an uncertainty of less than 10^{-2}°C to the measured temperature [Narod, 1976]. Drilling was done with a SIPRE hand drill, so heating effects were small, and they decayed with time after drilling was complete. Temperatures are also affected by firn that drops down the hole during final removal of the drill, and this error also decays with time. Because the air in the hole has thermal properties that are different from the surrounding snow, there is a distortion in the temperature field that increases after drilling to reach a maximum after an hour or two [Sanderson, 1977]. However, for the vertical temperature gradients expected at the bottom of the hole (~ 0.1°C m^{-1}), the error is approximately 10^{-2}°C. To minimize the effects of convective air flow, a styrofoam disk was mounted above the thermistor so that it loosely plugged the hole. Throughout the measurement, the top of the hole was covered to prevent snow falling into the hole and to reduce airflow.

Measurements at some stations over periods of 12 hours or more gave some indication of the time necessary to obtain sufficient data. In general, measurements that extended over an hour gave a cooling curve that determined the ambient temperature within a few hundredths of a degree. However, accuracy deteriorated rapidly for measurements lasting less than 40 min. Measurements with different thermistors down the same hole, and with the same thermistor down adjacent holes, showed agreement to better than 0.1°C.

In an area of little or no melt, such as the Ross Ice Shelf, 10-m temperatures are approximately representative of the average surface air temperature. However, even at 10-m depth, the firn temperatures do respond to seasonal changes in the air temperature. For instance, at Little America V, with a seasonal range in air temperature of approxi-

mately 35°C, the annual temperature cycle at 10-m has a total range of 0.8°C, with a phase lag of about 7 months [Crary et al., 1962]. The seasonal range in air temperature is probably approximately constant over the ice shelf, and core hole data indicate that the density/depth (and therefore thermal diffusivity/depth) curves show little variation. Consequently, we have used the Little America data to correct observed 10-m temperatures to average values.

Solution of the heat equation for an accumulating surface undergoing sinusoidal changes in temperature with time [Carslaw and Jaeger, 1959, p. 389] gives a theoretical estimate of the amplitude and phase lag of the temperature wave at any depth. Because thermal diffusivity changes with depth, we regarded the snow pack as a pile of 1-m thick layers, each with a different density and thermal diffusivity. Then, with Yen's [1965] relationship between thermal conductivity and firn density, we obtained excellent agreement with the observed temperature wave amplitude and phase lag at Little America V. This was considered to be sufficient justification to use the calculated amplitude and phase lag from the model to correct temperatures measured at depths other than 10 m.

The resulting estimates of 10-m temperatures corrected for seasonal variations are listed in the appendix Table A1. These values represent the average temperature at 10 m. Generally, this is warmer than the average surface temperature because there is a temperature gradient through the ice shelf, from the cold upper surface to the warm base. The temperature gradient is enhanced near the surface, because the thermal conductivity of firn is less than that of ice [Thomas, 1975; MacAyeal, 1979]. Consequently, average temperatures at a depth of 10 m on the Ross Ice Shelf are approximately 1° to 2°C warmer than average surface temperatures. However, since uncorrected 10-m temperatures are more often reported in polar regions than average surface temperatures, we have not corrected our measurements to the surface.

Our values are plotted as isolines of 10-m temperatures in Figure 13. Although these show close agreement with those of Crary et al. [1962], there has been an increase, by approximately 1°C, in the grid western part of the ice shelf. This is compatible with observed increases in air temperatures at Byrd and McMurdo stations during the same period (1958-1974) [Thomas, 1976b]. However, there does not appear to be a similar increase in 10-m temperatures in the grid eastern portion of the ice shelf. Indeed, there may have been a decrease in a small area grid west of Minna Bluff.

Field Measurements

The pattern of stakes (strain rosettes) used to measure strain rates was described in the section entitled 'Strain Rates' and is illustrated in Figure 5. For most of the rosettes, the direction from O to A was magnetic north. The central station was also the position that was occupied by the satellite-tracking equipment and the geophysics group from the University of Wisconsin. The stakes that formed the rosette were aluminum poles 3.7 m (12 feet) long and 25 mm in diameter, jointed in the middle to allow setting-up of a tripod over the stake site. They were planted vertically in the snow to a depth of about 1 m. Near each aluminum pole a flagged bamboo was also planted; these were more readily visible than the aluminum poles, and they made excellent markers to assist in relocation of the rosettes. The flags were color-coded to distinguish between central and peripheral stakes.

Sun observations were made at most of the rosettes. These provided approximate position fixes that could be used to assist in relocation of the rosettes. Clearly, they were of lower accuracy than the positions from satellite tracking, but the observations were made even at the satellite-tracking stations, since they provided a back-up position in the event of equipment malfunction. The sun observations also gave true azimuths of the rosette legs OA, OB, and OC. These oriented the strain rate tensors, and comparison with repeat observations yielded rotation rates for the ice.

Distances were measured with Tellurometer CA-1000 and CD-6 electronic distance measurers. These are both lightweight instruments with low power consumption, and they behaved well at temperatures above -20°C. Below this temperature, measurements could be made with the instruments enclosed within styrofoam-insulated boxes, but this technique was only partially successful. Fortunately, temperatures on the Ross Ice Shelf during most of the field season (mid-November to late-January) are well above -20°C. The manufacturers claim of a measurement accuracy of approximately ± 0.02 m for the CA-1000, and ± 0.01 m for the CD-6 at the ranges involved in rosette measurement, was supported by field measurements every season of the same distance using each of the instruments. Although consistency between instruments does not provide a test of absolute accuracy, it does provide a sufficient test of errors involved in the measurement of strain, which is a change in length divided by a length. Despite its greater accuracy and simplicity in operation, the CD-6 is less versatile than the CA-1000,

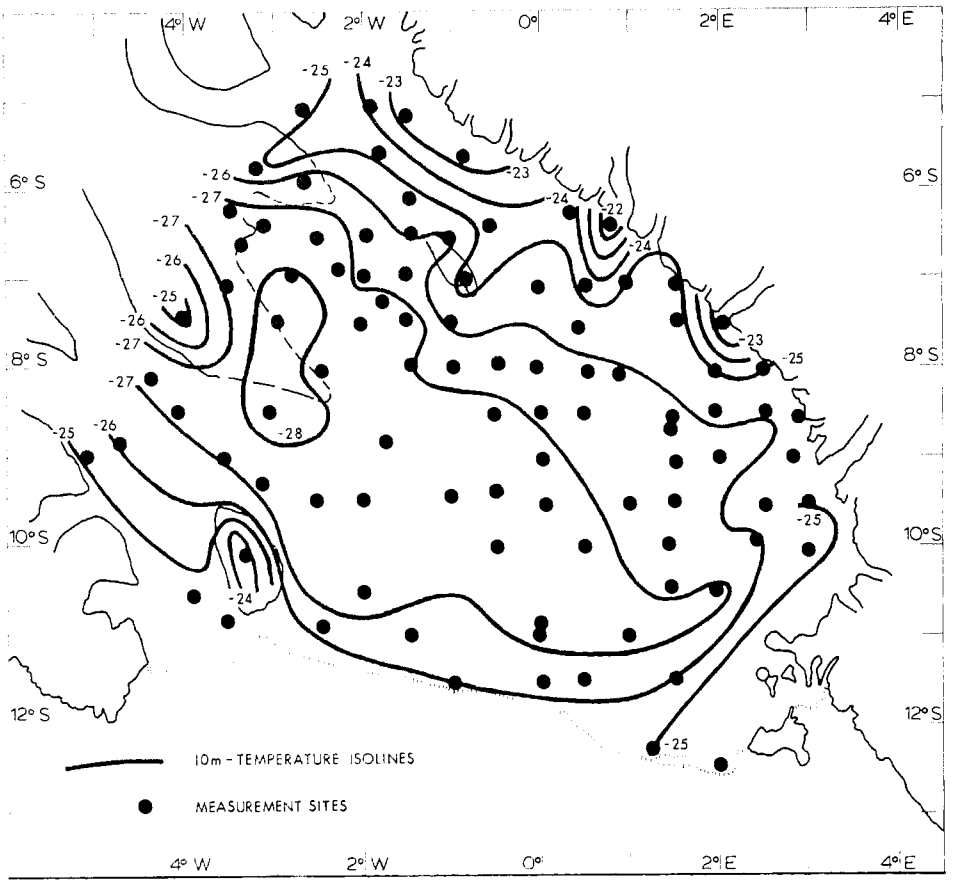

Fig. 13. Ten-meter temperatures on the Ross Ice Shelf. Measured temperatures have been corrected for seasonal variations to give equivalent average values.

primarily because of its short range and inability to make measurements through obstacles such as fog and drifting snow. Both types of instruments were moderately susceptible to physical damage or electronic failure -- successful completion of the field work was possible only by starting each season with three or four working units. A comparison of the two instruments is given in Table 1.

Because the instruments weighed so little they could be mounted directly above the theodolite. They could also be mounted directly on to the lower section of the aluminum pole that formed the station marker; this was how most of the measurements were made. A short aluminum rod that fit snugly into the aluminum pole was threaded to screw into the tripod mount of the instrument. In this way, errors due to centering the instrument over the station were minimized, and measurements could be completed very quickly. All three distance measurements for one rosette could be completed in less than an hour, including the travel time taken by the operator manning the remote unit. Transport was by small Skidoo 'Elan' motor toboggans. These were well suited to a field operation supported by light airplane since, with a weight of approximately 120 kg, they could easily be lifted into and out of a De Havilland 'Twin Otter' airplane. They were reliable -- and one vehicle survived all four field seasons, a remarkable achievement for a light vehicle in Antarctica.

Three types of theodolite were used for measuring angles: Wild T-2 (with a resolution of 1" of arc), Leitz TM-10C (3" of arc), and a Wild T-16 (6" of arc). The Wild T-16 gave a position accuracy that was slightly worse than that resulting from the distance measurements. Consequently, most of the measurements were made with the Leitz instruments, which were sufficiently precise, easy to use and low in cost. All the survey equipment was overhauled and tested at the end of each season by the relevant manufacturers.

A complete RIGGS field party generally consisted of two glaciologists, one 10-m core driller, one satellite tracker and two or three geophysicists. However, many of

TABLE 1. Comparison of the Two Tellurometer Electronic Distance Measurers That Were Used by the RIGGS

Distance Measurers	Maximum Range, km	Minimum Range, m	Accuracy	Carrier	Weight (With Battery), kg	Operating Temperature, °C
CA-1000	> 30	50	$<0.01\ m + \frac{Distance}{200,000}$	Radio waves, which provide two advantages: (1) Two-way speech communication. (2) Distances can be measured through obstacles that are either natural (thick fog or falling snow) or man-made (boxes, tents, etc.).	4	-20°C to +50°C
CD-6	2-3	20	$0.005\ m + \frac{Distance}{200,000}$	Infrared light	4	-20°C to +44°C

the stations were visited by only the glaciologists and geophysicists. When the stations were reoccupied one or two years later, the field party consisted of either the two glaciologists, or the glaciologists and the satellite tracker.

The observation sequence at a typical RIGGS station was

1. Immediately on arrival, the satellite-tracking equipment was started, and vertical angles into the sun were observed to obtain a 'position line' for the station.

2. One man planted the central 'O' aluminum stake close to the satellite-tracking antenna. At the same time the other glaciologist traveled magnetic north for approximately 1.5 km, to plant the 'A' stake. The 1.5 km was estimated by aligning, from the remote station, two sights that were 10 mm apart and held 300 mm from the eye, with two flags planted 50 m apart at the central station. This provided a remarkably good estimate and, unless the terrain dictated otherwise, most of the rosettes have legs of approximately equal length. As soon as the 'A' station was planted, the distance OA was measured by using one of the Tellurometer distance measurers.

3. The remote operator moved across the rosette to plant the 'B' and 'C' stakes, and to measure the distances OB and OC. Hand signals from the central stake indicated when the remote man had traversed the necessary 120° of arc between stakes. Within 2 m of each stake, a flagged bamboo was planted for identification. All aluminum poles were aligned vertically with the help of a rod level; all stakes were planted to a depth of about 1 m, and the lengths exposed above snow level were measured at both the aluminum and the bamboo poles.

4. After measurement of the distance OC the remote man returned to 'O', while the central operator set his theodolite over the 'O' stake. Horizontal angles subtended at 'O' by the peripheral stakes were then measured.

5. Finally, horizontal and vertical angles were observed into the sun to determine the true azimuth of one of the rosette legs and a second position line for the station.

This entire procedure could be completed in 2.5 hours when the station was planted and in 1.5 hours when it was revisited. Completion of the satellite tracking (for five passes) and of the 10-m coring and temperature measurements generally took at least 3 hours, depending on the geometry of the satellite orbits and the tiredness of the driller.

Discussion

Although this paper does not include a detailed analysis of the glaciological results of RIGGS, there are several features

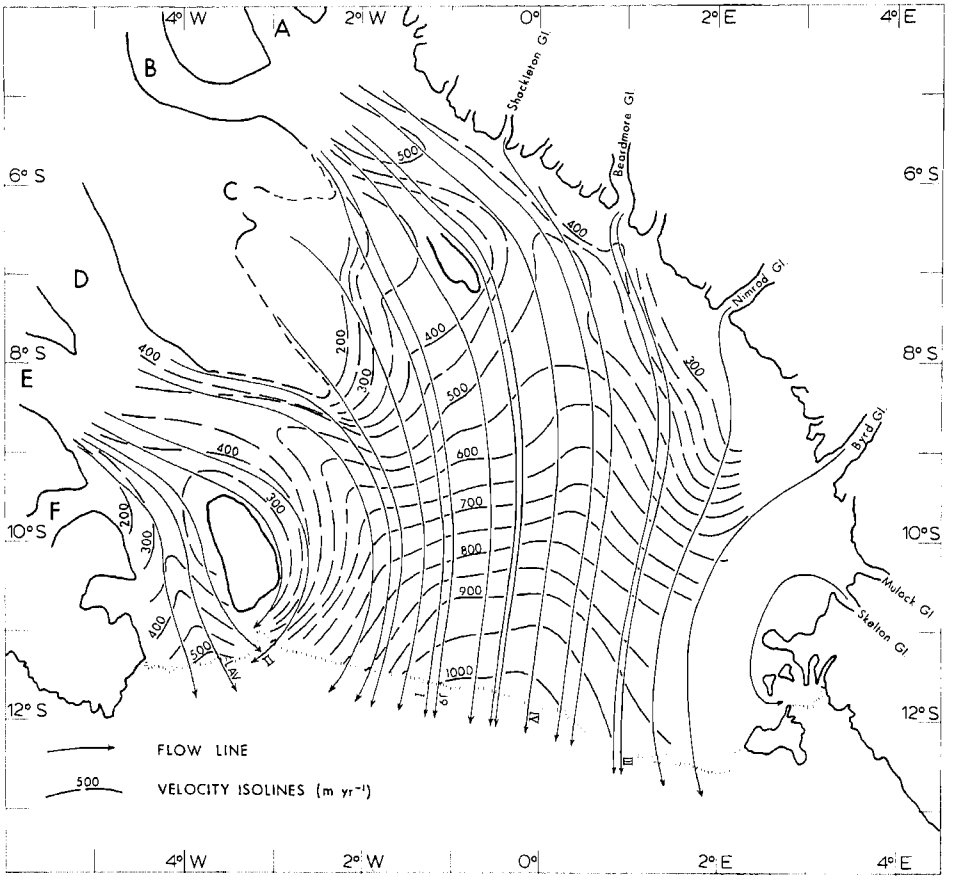

Fig. 14. Velocity field of ice flow on the Ross Ice Shelf. The labelled flow lines are those that pass through the four RIGGS camps ((I) BC, (II) R.I., (III) C-16, and (IV) Q13), the RISP borehole at J9, and Little America V. Apart from the Skelton Glacier flow line, and the seaward portion of the Byrd Glacier flow line, the information shown here is based solely on RIGGS data.

of our results that are discussed below. By using the velocity data to reconstruct flow line routes across the ice shelf we are able to provide possible explanations for the 'anomalous' strain rate data. Comparison of our velocity results with earlier estimates reveals what may be real changes over a 10-year period. Finally, we shall briefly discuss ways in which our data can be used, together with results from other RIGGS programs, to investigate various aspects of ice shelf dynamics.

Flow line routes across the ice shelf were reconstructed from the RIGGS velocity data, using observed strain rates to give flow-line curvature and divergence as described earlier. The calculated flow lines, together with velocity isolines, are shown in Figure 14. Unfortunately, our data do not extend into the mouths of the West Antarctic ice streams (B through F), and we cannot delineate precisely the bands of ice shelf formed from each of these ice streams. However, it appears that most of the ice draining into the ice shelf from West Antarctica flows down Ice Streams B and E. With a width where it becomes afloat of approximately 50 km, a velocity greater than 500 m yr^{-1}, and a thickness close to 800 m, Ice Stream B drains more than 20 km^3 of ice each year; this is approximately equal to the total outflow from 7 of the major glaciers (not including Byrd Glacier) that drain the East Antarctic ice sheet through the Transantarctic Mountains [Swithinbank, 1964]. Although Ice Stream E is somewhat slower and thinner than Ice Stream B, it is considerably wider, and its total ice drainage may exceed 24 km^3 yr^{-1}. This, and the estimate for Ice Stream B, show good agreement with the 'balance' drainage rates [Rose, 1979], indicating that the drainage basins for these ice streams are approximately in balance.

It is useful to compare ice drainage from these ice streams with that from some of the

more active East Antarctic glaciers. Hays Glacier has a drainage basin that lies within a zone of very high snow accumulation, and despite its rather small catchment area, it reaches a speed of 1400 m yr^{-1} where it becomes afloat, and discharges approximately 3 km^3 of ice yr^{-1} [Meier, 1977]. The Shirase Glacier has a larger drainage basin, and velocities at the ice front are approximately 2500 m yr^{-1}; the total discharge is about 8 km^3 yr^{-1} [Nakawo et al., 1978]. The Byrd Glacier also has a large catchment area, albeit in a zone of low accumulation rates; it has a speed, near the point where it becomes afloat, of more than 800 m yr^{-1} [Swithinbank, 1964] and a total discharge into the Ross Ice Shelf of about 18 km^3 yr^{-1} (C. Swithinbank, personal communication, 1980). The Lambert Glacier has probably an even larger catchment area, perhaps more than 10^6 km^2, and total drainage into the Amery Ice Shelf is approximately 12 km^3 yr^{-1} [Allison, 1979]. The extremely high discharge rates of the major West Antarctic ice streams are largely due to higher inland accumulation rates; to find comparable discharge rates in East Antarctica it will be necessary to examine areas where snow accumulation is higher than average. The Stancomb-Wills Glacier probably drains such an area. It flows into the Brunt Ice Shelf to form a floating tongue between 50 and 100 km wide. Ice velocities from comparison of astro-fixes at two points on opposite sides of this floating tongue give speeds of 1.3 km yr^{-1} and 1.5 km yr^{-1} [Thomas, 1973a]. The smaller value was obtained from observations over a two-year period, and errors are unlikely to exceed $\pm$ 200 m yr^{-1}. If the ice thickness is 300 m (a modest estimate), the moving ice tongue represents ice discharge from Stancomb-Wills Glacier exceeding 20 km^3 yr^{-1}. Slessor Glacier, which feeds the fast-moving Filchner Ice Shelf, may also possess large discharge rates.

The flow lines that pass through the four RIGGS base camps, the RISP drill hole (J9) and Little America V (LAV) are also shown in Figure 14. RIGGS camp B.C., originally planned as the drill hole site, is on ice that originated in the shear zone on the grid south side of Ice Stream B. Although the ice at J9 is from nearer the center of Ice Stream B, it may have been affected by the shear zone, and this could complicate interpretation of the ice core. The ice at station R.I. is from Ice Stream E, as is that at LAV. The ice at C-16 is from Beardmore Glacier, and that at Q13 is from either Ice Stream A or Ice Stream B. Our estimated ice velocity at LAV (511 m yr^{-1}) is double the value of 255 m yr^{-1} obtained by Crary [1961] from comparison of the position of a bay in the ice front with an observation that was made 46 years earlier. However, our value is acceptably close to the value of 458 m yr^{-1} based on a comparison of positions of the same bay over a period of 23 years [Wexler, 1960]. It seems likely that the bay suffered major calving during the first half of the 46-year period between the position fixes used by Crary.

Robin [1975] has also reconstructed flow lines and velocity isolines for the Ross Ice Shelf. He extrapolated ice velocity data across the ice shelf by applying volume conservation principles to measured ice thickness profiles. Despite the limited velocity data available to Robin, his reconstruction shows a remarkable similarity to ours. However, there are some important differences that merit discussion. Robin's Ice Stream E is considerably less active than our measurements suggest, but this results from his use of Crary's low estimate of ice velocity at LAV. Of greater significance is that Ice Streams C and D appear to be considerably less active than was implied by Robin's analysis. An independent estimate of the activity of these ice streams is provided by the work of Rose [1979], who calculated 'balance' discharge rates sufficient to drain exactly the snow accumulation within the catchment areas. Our estimate of ice discharge for Ice Stream D ($\sim$ 10 km^3 yr^{-1}) is in good agreement with Rose's estimate of 11 km^3 yr^{-1}. However, Rose obtained the same discharge rate for Ice Stream C, and this is more than double the value that we obtain. Indeed Ice Stream C is moving only slightly faster than the slow-moving ice that drains Siple Ice Dome, and that comprises more than half of the ice shelf flow band between the flow bands of Ice Streams B and D. Radio-echo measurements on Ice Stream C reveal bedrock topography and marginal crevasses typical of a very large and active ice stream [Rose, 1979], but the crevasses are probably buried, since we found no sign of them when flying over the ice stream. It appears that Ice Stream C has been active in the past, but currently it is out of balance, with drainage removing less than half of the total snow catchment. If this is correct, then the ice stream must be growing thicker and perhaps, as suggested by Rose [1979], it is in a quiescent stage following a surge that occurred some time during the last 1000 years. Alternatively, the lower reaches of Ice Stream C may have run aground comparatively recently to form a large apron of flat sluggish ice, which is thickening as ice from upstream continues to flow into it [Thomas, 1979].

One effect of the lower than expected discharge from Ice Stream C is to allow Ice Stream B to flow more to the (grid) west

than is shown in Robin's [1975] flow line map. Thus, our results indicate that at least half of Ice Stream B flows to the (grid) west of Crary Ice Rise, and, at the ice front, the boundary between Ice Stream B (West Antarctic ice) and Ice Stream A (predominantly East Antarctic ice) is slightly to the (grid) west of the 0° meridian (flow line IV in Figure 14).

An interesting feature of Ice Stream B is the velocity minimum to the (grid) north of Crary Ice Rise. Ice velocity near the grounding line exceeds 500 m yr^{-1}, but then there is a steady deceleration for almost 200 km. We expect ice flowing towards Crary Ice Rise to decelerate, but this steady deceleration continues within the 130-km wide channel between Crary Ice Rise and the Transantarctic Mountains. To a lesser extent there is a similar deceleration in the channel (grid) west of Roosevelt Island, and this is largely the result of shear at the channel sides slowing down the ice shelf. However, for Ice Stream B, there is also strong convergence, with ice flowing into the channel, both from Ice Stream A and from valley glaciers that flow through the Transantarctic Mountains. This increases the 'bottleneck' effect so much that there is positive vertical creep in a sizeable area (grid) north of Crary Ice Rise (Figure 8). Within this region the ice shelf grows thicker by creep, an effect that was not expected to occur in a floating ice shelf, except immediately upstream from grounded ice rises [Robin, 1975]. Even where the ice shelf is not confined by nearby ice rises, there appears to be a tendency toward positive vertical creep wherever there is strong converging flow. This is particularly apparent at Swithinbank's station I, downstream from Beardmore Glacier, where vertical creep within a small area reaches $+5 \times 10^{-4}$ yr^{-1}. The apparently anomalous strain rates at K15 may also represent the effects of convergence, this time between the main ice shelf flow and Nimrod Glacier. This possibility is supported by the similarity between the strain rate tensors at I and K15, relative to the local velocity directions (Figure 7). (The large standard deviation at K15 (appendix Table A1) in comparison with that at I, almost certainly is a consequence of the relative size of the rosettes at these stations. The rosette legs at I were only 300 m long in comparison with 1500 m at K15, and so were far less affected by the strain rate gradient.)

Unfortunately, we have no strain rate data near the mouth of the Byrd Glacier, where we might expect another zone of strong compression. However, the major convergence between the Byrd Glacier and the main stream of the ice shelf flow occurs $\sim$ 230 km into the ice shelf at (grid) coordinates 1.5 east and 10.5 south, where there is a small area with positive vertical strain rates. Farther to the (grid) east there is a zone of far more intense creep thickening, which probably results from a combination of two effects: strong convergence of ice from the Byrd, Mulock, and Skelton Glaciers, and compression as the ice approaches Minna Bluff. The zone of creep thickening immediately upstream of Roosevelt Island is expected, but its persistence along the (grid) east side of the island is not. Perhaps it is an 'extrusion effect' associated with lateral compression as the ice shelf is forced to pass between Ross Island and Roosevelt Island. Weak zones of convergence, such as those between Ice Streams B and C, and between Ice Streams C and D, cause near-zero, but not positive, vertical strain rates.

The zone of creep thickening downstream from Crary Ice Rise may be caused by convergence of the two halves of Ice Stream B after passing Crary Ice Rise, or it may be associated with the unexpected zone of rapid thinning further downstream at M12, where the strain rates are much larger than at neighboring stations (Figure 7). K. Jezek (personal communication, 1980) has found evidence, from a study of radio echo records, suggesting grounding in this area. If there is grounding slightly upstream of M12, then transition from creep thickening to thinning and rapid extension is what we would expect.

In general, there is a tendency for creep-thinning rates to increase as the ice moves seaward, presumably because of diminishing drag due to shear at the sides and obstructions to flow, such as grounded ice rises [Budd, 1966; Thomas, 1973b]. The vertical strain rates at, and near to, the ice front appear to be controlled by ice thickness, with creep thinning reaching a maximum where the ice is thickest, as predicted by theory [Weertman, 1957]. Away from the ice front, there are four areas where vertical strain rates fall below -15×10^{-4} yr^{-1}. We have already suggested that the minimum at M12 may be associated with possible upstream grounding. The minimum immediately to the (grid) west of Crary Ice Rise is in an area of massive crevassing, where the ice shelf is clearly in a state of lateral tension. The portion of Ice Stream B that flows on this side of Crary Ice Rise is able to spread sideways into the embayment occupied by slow-moving Ice Stream C. Almost certainly, there is another zone of rapid creep thinning immediately downstream of the ice rise but it is not shown in Figure 8, simply because we did not have a station in the area. The large minimum in vertical strain rates downstream of Ice Stream C probably is

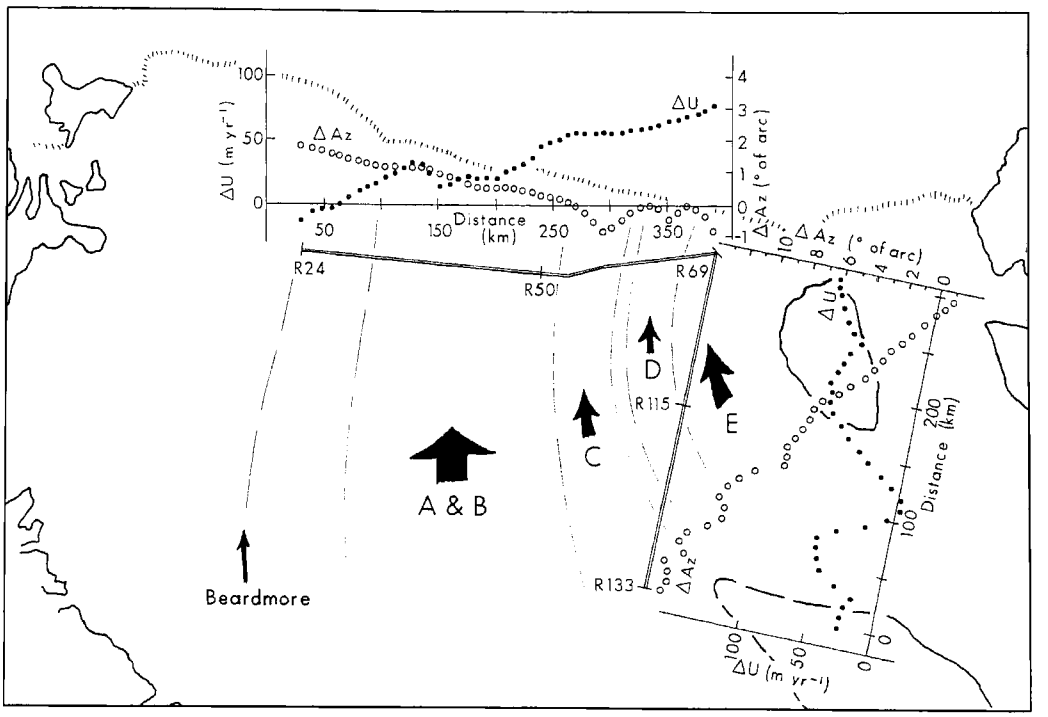

Fig. 15. Comparison of RIGGS ice velocities with those of Dorrer et al. [1969]. ΔU is the difference in speed ($U_R - U_D$), where subscript R refers to RIGGS data, and subscript D refers to those of Dorrer et al. [1969]. ΔAz is the difference in velocity direction ($Az_R - Az_D$). ΔU (solid circles) and ΔAz (open circles) are plotted against distance along a portion of the survey traverse of Dorrer et al. [1969], shown here as the double line. The broken lines indicate flow lines that define the boundaries between ice that originates in ice streams A to E, and the route of ice from Beardmore Glacier.

caused by stretching of the ice shelf in the direction of movement, as sluggish ice from Ice Stream C is dragged forward by the fast-moving Ice Stream B. Finally, the minimum near the mouth of Ice Stream B is associated with rapid lateral spreading of fast-moving ice toward the large embayment to the (grid) north. In contrast, there is creep thickening at the mouth of Ice Stream E where, apparently, lateral spreading is limited, perhaps because there is inflow from both Ice Streams D and F.

The velocities measured by Swithinbank in 1961 at stations A through H show good agreement with our observations in the same area, and there is general agreement between our results and those of Dorrer et al. [1969]. However, there are some differences that may be indicative of a real change during the decade that separated the two surveys. Dorrer et al. [1969] measured ice velocities along a traverse that started at Ross Island, extended most of the way to Roosevelt Island, and then ran true south for almost 300 km. The portion of the Dorrer traverse that passes through the area occupied by RIGGS stations is shown in Figure 15. In order to make a comparison between our velocity estimates and those of Dorrer et al., we reduced our values to equivalent velocities at the Dorrer stations, using our measured strain rates to interpolate between the RIGGS stations. We then had two independent estimates of velocity at Dorrer stations R24 through R133. The difference in speed and direction (positive clockwise) between our estimates (U_R) and those of Dorrer et al. [1969] are plotted in Figure 15. Errors in most of our interpolations are probably less than $\pm$ 30 m yr^{-1} in speed, and $\pm$ (30/U_R) radians in direction; they may increase by 50% or more in the region between R120 and R133. Errors in the estimates of Dorrer et al. increase progressively away from Ross Island. Estimated standard errors [Dorrer, 1970] reach maxima of $\pm$ 6 m yr^{-1} in speed at R69 and $\pm$ 1° of arc in direction at R133. Actual errors may be significantly larger than these estimates, since the traverse was anchored to fixed ground at only one end. Here we assume that the velocity differences along the section R24 to R69 are not significant unless they exceed 40 m yr^{-1} and 3° of arc; from R69 to R120 these 'significance

limits' increase to 50 m yr^{-1} and 5° of arc; they increase again to 60 m yr^{-1} and 10° of arc between R120 and R133. Where Dorrer's traverse passes close to the site of a RIGGS satellite-tracking station these estimates may be as much as double the actual significance limits. However, by retaining the most conservative estimates, we hope to minimize ambiguity in our interpretation.

Along the traverse from R24 to R50, the differences plotted in Figure 15 lie below the assumed significance limits. Then, from R50 to R69, the difference in speed increases from 46 m yr^{-1} to 78 m yr^{-1}, and this may represent a real increase in velocity, since the RIGGS data in this area are well controlled by satellite-tracking stations. Differences in the movement direction along the entire traverse from R24 to R69 are less than 2° of arc, well below the significance limit. The velocity difference continues to be above the significance level for approximately 100 km (grid) north of R69. Further to the (grid) north the velocity difference decreases, but the azimuth difference increases to more than 3° greater than the significance limit.

There appear to be two possible explanations for these differences. First, there has been a real increase in the velocity of Ice Stream E, with a clockwise rotation of velocity vectors in the ice from Ice Stream C caused, perhaps, by Ice Stream B having a progressively-increasing influence on this ice. There is no evidence in Figure 15 for an increase in the velocity of Ice Stream B, but possibly a decrease in activity of Ice Stream C would lead to a clockwise rotation of velocity vectors, as Ice Stream B shifted to the (grid) west. The other possibility is a systematic error in either Dorrer's results or in ours, resulting in a divergence between the two sets of data that steadily increases from zero at R24 to a maximum of approximately 80 m yr^{-1} at R69 and along the traverse from R69 to R133. Errors in the RIGGS velocities are probably random, and we would not expect them to produce a progressively increasing divergence. However, this is precisely what we would expect from an azimuth error in one of the legs near R24 of the Dorrer traverse. This error could have occurred in either the first or the second survey; it would have resulted in a rotation of the entire traverse beyond R24, and this would have introduced a progressive increase in velocity errors to a maximum at R69, which would have remained constant between R69 and R133, as suggested by Figure 15. A velocity divergence of about 80 m yr^{-1} at R69 and through to R133 would correspond to an error of approximately 130 s of arc in angle measurement at, or near, R24 during one of the traverse surveys. This is unlikely; five full sets of observations were made of each traverse angle, and the resulting mean square error of all observations was less than one second of arc [Dorrer et al., 1969]. Moreover, the observed true azimuth at R133 differed from the propagated traverse azimuth by only 23 s of arc [Dorrer, 1970]. However, since we have no independent checks on errors in either the Dorrer or RIGGS survey, we cannot be sure that the differences between the two sets of velocity estimates represent a real change. E. Dorrer (personal communication, 1980) suggests that small systematic theodolite turning errors may have been introduced to his traverse between R23 and R37, when appreciable friction was experienced in turning the alidade.

Some of the data that we present in this paper have already been used to investigate the dynamics of parts of the ice shelf. Mass balance calculations for the (grid) western half of the ice shelf indicate that, whereas much of the ice shelf appears to be approximately in steady state, the ice in the (grid) northwest corner may be growing thicker by approximately 0.3 m yr^{-1} [Thomas and Bentley, 1978; MacAyeal and Thomas, 1979]. At the time of these analyses ice velocities in the (grid) east were not available, so some of the velocities, particularly in the region between Crary Ice Rise and Roosevelt Island, were interpolated between the values of Dorrer et al. [1969]. Our present estimate of the velocity field in this area differs significantly from that used in our mass balance calculations, which must therefore be revised. The area in the (grid) northwest, which appears to be thickening, will not be affected by the modified velocity estimates.

Particle path calculations have been completed for several flow lines, in order to estimate the depths of prescribed age horizons within the ice shelf [Thomas and MacAyeal, 1982]. Comparison of these 'steady state' estimates with age/depth relationships obtained from drill hole observations will provide an indication of past departures from steady state. These results will also be useful in planning where to obtain new ice cores from the ice shelf.

All of the RIGGS results, taken together, will provide a unique test of theoretical ice shelf models, particularly of elaborate computer models. As a first step, we can investigate the effects on ice shelf dynamics of shearing at the sides and between ice streams moving at different speeds, and on compression upstream from ice rises. Ice shelf strain rates increase with increasing ice thickness, and decrease with increasing restraints to ice movement. Thus, in gener-

al, the effect of ice shelf margins, and of ice rises, is to reduce the creep rate. The geometry of the margins, and the distribution of tributary ice streams, also have an influence. For instance, even immediately upstream from an ice rise, where restraints to movement are very large, there may be rapid extending creep, in a direction perpendicular to the flow direction, if the geometry of the margins allows lateral expansion to occur. If lateral expansion cannot occur, then the longitudinal compression that is inevitable upstream from an ice rise must be balanced by vertical extension, and the ice shelf thickens. Thus, the strain rate tensor on an ice shelf is determined by local ice thickness, ice shelf geometry, the distribution of ice rises and tributary ice streams, and the creep properties of the ice [Thomas, 1973b]. With assumed ice creep properties, we can use the RIGGS measurements to calculate the force acting at any point to restrict ice movement. This provides important information that will help us to predict how ice shelves will respond to prescribed constraints, such as changes in sea level or an altered climate [Thomas et al., 1979].

TABLE A1, Part 1. Positions, Temperatures and Accumulation Rates at RIGGS Stations

	Positions					Ten-Meter	Accumulation
	Geographic		Grid			Temperature	Rate
Station	South Latitude	West Longitude	South Latitude	East or West Longitude	Year	°C	m yr^{-1} of ice
Base Camps							
I (BC)	82°32'19"	166°00'48"	7°14'25"	1°48'12"W	1973	-27.6	
II (RI)	80°11'30"	161°33'41"	9°18'17"	3°06'08"W	1974	-27.5	0.15
III (C-16)	81°11'38"	189°30'09"	8°41'07"	1°27'14"E	1976	-26.4	
IV (Q13)	78°57'27"	180°04'39"	11°02'33"	0°00'54"E	1976	-27.1	0.16
Remote Stations							
E5	84°14'45"	151°54'27"	5°04'35"	2°42'35"W	1973	-25.8	
E6	84°28'	155°28'	5°02'	2°18'W	1973		0.12
E7	84°35.1'	159°27'	5°04.2'	1°54.0'W	1973	-23.9	0.14
E8	84°36.0'	163°46'	5°11.1'	1°30.6'W	1973	-22.5	0.18
F6	83°58.7'	157°49'	5°34.6'	2°16.4'W	1973		0.06
F7	84°07'11"	162°03'52"	5°35'40"	1°48'39"W	1973	-24.9	0.12
F8	84°20.0'	167°02½'	5°31.3'	1°16.2'W	1973		0.20
F9	84°17'23"	171°22'29"	5°38'45"	0°51'23"W	1973	-22.4	0.12
F10	84°29.2'	175°50'	5°29.9'	0°24.0'W	1973		0.17
G4	82°51'22"	150°53'15"	6°14'29"	3°28'32"W	1973	-27.7	
G5	83°24'38"	151°12'55"	5°46'31"	3°10'23"W	1973	-25.1	0.08
G6	83°31'02"	156°01'32"	5°55'25"	2°38'03"W	1973	-26.4	
G7	83°44.8'	162°02'	5°56.9'	1°55.7'W	1973		
G8	83°43'15"	166°31'15"	6°06'22"	1°27'49"W	1973	-25.4	0.11
G9	83°49.1'	170°31'	6°05.8'	1°01.1'W	1973		0.11
G10	83°54'34"	174°21'36"	6°03'40"	0°35'55"W	1976		0.14
G11	83°57.6'	179°17½'	6°02.4'	0°04.6'W	1973		0.26
H5	82°35'26"	153°14'50"	6°36'59"	3°20'07"W	1973	-27.3	0.05
H6	82°52'53"	154°16'02"	6°24'46"	3°05'27"W	1973	-27.4+	0.06
H7	82°59'50"	159°12'03"	6°36'47"	2°29'12"W	1973	-27.8	0.06
H8	83°12'34"	163°28'37"	6°30'37"	1°55'52"W	1973	-26.5	0.12
H9	83°20'51"	167°25'27"	6°29'34"	1°26'54"W	1973	-25.9	0.14
H10	83°21'33"	171°14'07"	6°33'48"	1°00'43"W	1973	-26.2	0.13
H11	83°25.7'	175°33'	6°33.1'	0°30.6'W	1973		0.16
H12	83°42'25"	183°08'46"	6°17'01"	0°20'43"E	1973	-24.6	0.30

Table A1, Part 1. (continued)

Station	Positions: Geographic South Latitude	Geographic West Longitude	Grid South Latitude	Grid East or West Longitude	Year	Ten-Meter Temperature °C	Accumulation Rate m yr^{-1} of ice
HE12	83°27'54"	180°13'55"	6°32'06"	0°01'35"E	1976		0.19
H13	83°31'30"	186°59'33"	6°25'37"	0°47'18"E	1976	-21.1	0.19
I5	82°04'39"	153°40'04"	7°06'02"	3°30'51"W	1973	-27.0	0.10
I6	82°21.4'	156°32'	7°00.6'	3°02.6'W	1973		0.07
I7	82°44.1'	161°53½'	6°54.3"	2°15.5'W	1973	-27.4	0.07
I8	82°44'18"	164°03'11"	6°58'56"	1°59'42"W	1973	-26.7	0.03
I9	82°53.4'	167°48'	6°56.9'	1°30.1'W	1973	-26.1	0.14
I10	82°56.3'	173°19'	7°00.7'	0°49.3'W	1973		0.10
I11	82°54'05"	176°31'30"	7°05'08"	0°25'49"W	1973		0.16
I12	82°54'48"	179°49'09"	7°05'12"	0°01'21"W	1976	-25.7	0.22
I13	82°52'51"	184°10'44"	7°06'01"	0°31'08"E	1976	-24.8	0.16
I14	82°53'21"	188°00'17"	7°02'30"	0°59'25"E	1976	-24.9	0.22
I15	82°45'34"	192°11'35"	7°04'38"	1°31'45"E	1976	-25.5	0.16
J4	81°34'38"	151°43'48"	7°25'05"	3°59'21"W	1974	-24.5	0.12
J6	81°56'41"	158°34'39"	7°29'56"	2°56'32"W	1973	-28.5	0.09
J7	82°15.6'	163°17'	7°24.8'	2°13.6'W	1973		0.09
J8	82°14'01"	165°02'50"	7°30'12"	2°00'14"W	1973	-27.7	0.08
J9	82°22'28"	168°38'44"	7°28'35"	1°30'05"W	1973	-27.6	0.09
J10	82°27'40"	172°31'23"	7°28'29"	0°58'52"W	1973	-25.9	0.13
J11	82°34.2'	176°17½'	7°24.9'	0°28.8'W	1973		0.11
J12	82°22.4'	180°18'	7°37.6'	0°02.4'E	1976		0.14
J13	82°27'07"	183°29'39"	7°32'02"	0°27'36"E	1976	-25.4	0.15
J14	82°23.6'	187°04'	7°33.0'	0°56.2'E	1976		0.12
J15	82°21'48"	191°33'08"	7°28'55"	1°31'46"E	1976	-25.5	0.19
J16	82°13'30"	195°12'27"	7°30'10"	2°02'22"E	1976	-22.2	
K3	80°46'53"	151°52'54"	8°07'50"	4°20'41"W	1974	-27.2+	0.10
K4	81°04.4'	153°27'	7°59.1'	3°59.4'W	1974		0.12
K5	81°18.8'	156°16½'	7°57.2'	3°29.8'W	1974		0.13
K6	81°21.1'	160°23'	8°08.8'	2°54.2'W	1973		0.09
K7	81°36'30"	163°16'00"	8°02'11"	2°24'58"W	1973	-27.7	0.11
K8	81°47.3'	166°09½'	7°58.4'	1°57.8'W	1973		0.09
K9	81°53'59"	169°49'39"	7°58'23"	1°25'50"W	1973	-27.0	0.12
K10	81°56'40"	173°13'53"	7°59'58"	0°56'58"W	1973	-26.6	0.15
K11	82°01'32"	176°45'55"	7°57'42"	0°26'60"W	1973	-26.4+	0.15
K12	81°59'47"	179°47'50"	8°00'13"	0°01'42"W	1976	-26.4	0.11
K13	81°56'00"	183°57'27"	8°02'51"	0°33'24"E	1976	-26.3	0.13
K14	81°51'48"	186°21'03"	8°05'12"	0°54'00"E	1976	-26.1	0.14
K15	81°51.0'	191°01'	7°59.9'	1°33.5'E	1976		0.18
K16	81°42'52"	194°05'51"	8°02'10"	2°01'05"E	1976	-25.0	0.15
K17	81°35'55"	197°18'50"	8°01'15"	2°30'01"E	1976	-25.0	0.09
KL7	81°23'04"	163°19'37"	8°15'12"	2°28'19"W	1976		
L4	80°26.2'	152°02½'	8°27.6'	4°27.5'W	1974		0.12
L5	80°36.0'	154°41½'	8°29.9'	4°01.1'W	1974	-27.2+	0.10
L6	80°49.0'	157°31½'	8°29.1'	3°30.6'W	1974		0.11
L7	80°58.9'	160°27½'	8°30.0'	3°01.0'W	1974	-28.4	0.11
L8	80°52.0'	164°42'	8°48.6'	2°24.6'W	1973		0.08
L9	81°17'03"	166°59'53"	8°29'33"	1°57'39"W	1973		0.10

Table A1, Part 1. (continued)

Station	Positions: Geographic South Latitude	Positions: Geographic West Longitude	Positions: Grid South Latitude	Positions: Grid East or West Longitude	Year	Ten-Meter Temperature °C	Accumulation Rate m yr^{-1} of ice
L10	81°23.2'	170°27½'	8°29.7'	1°25.7'W	1973		0.10
L11	81°28'26"	174°03'16"	8°28'49"	0°52'59"W	1973		0.12
L12	81°27'37"	176°46'55"	8°31'35"	0°28'46"W	1976	-27.4	0.10
L13	81°29'12"	180°06'27"	8°30'48"	0°00'57"E	1976	-26.7	0.08
L14	81°26'58"	183°24'11"	8°32'08"	0°30'27"E	1976	-26.6	
L15	81°24.0'	187°00'	8°32.1'	1°02.9'E	1976		
L16	81°18'52"	189°54'39"	8°33'21"	1°29'42"E	1976	-26.2	0.16
L17	81°16'52"	193°00'53"	8°29'42"	1°57'49"E	1976	-25.8	0.16
L18	81°07'49"	196°33'32"	8°30'07"	2°31'40"E	1976	-25.9	0.17
L19	80°57'28"	198°47'23"	8°33'37"	2°54'45"E	1976	-25.8	0.21
ML6 (M6½)	80°34.9'	160°00'	8°51.0'	3°13.3'W	1974		0.12
M2	79°40.2'	150°37'	9°00.1'	5°04.2'W	1974	-25.2	0.10
M3	79°59'27"	152°06'16"	8°50'46"	4°40'58"W	1974	-26.1+	0.11
M5	80°10.6'	156°00'	8°58.4'	3°59.7'W	1974		0.13
M6	80°19.3'	158°40'	9°00.9'	3°31.2'W	1974	-27.1	0.12
M7	80°30.9'	161°31½'	8°59.7'	3°00.3'W	1974		0.13
M8	80°38.8'	164°21'	9°00.4'	2°31.4'W	1974		0.12
M9	80°45.5'	167°26'	9°01.2'	2°00.7'W	1974		0.12
M10	80°59'48"	168°59'38"	8°50'16"	1°43'08"W	1974	-27.7	0.12
M12	80°56.1'	177°01'	9°03.1'	0°28.3'W	1976		0.14
M13	80°57'04"	180°10'01"	9°02'56"	0°01'35"E	1976	-27.2	0.12
M14	80°59'51"	183°07'04"	8°59'21"	0°29'23"E	1976		
M15	80°53'58"	186°16'01"	9°02'46"	0°59'36"E	1976		0.20
M16	80°48'39"	189°34'44"	9°03'40"	1°31'45"E	1976	-26.3	
M17	80°45'01"	192°36'25"	9°01'36"	2°01'08"E	1976	-26.2	0.19
M18	80°39.5'	195°37½'	8°59.8'	2°31.0'E	1976		
M19	80°33'02"	197°22'45"	9°01'05"	2°49'21"E	1976	-25.7	
N4	79°28'50"	154°40'28"	9°30'30"	4°29'59"W	1974		0.16
N5	79°45.1'	157°17'	9°27.2'	3°57.4'W	1974		0.15
N6	79°56.3'	158°48'	9°22.8'	3°38.4'W	1974		0.16
N7	80°00.3'	162°29'	9°31.9'	3°00.5'W	1974		0.13
N8	80°11'18"	165°12'28"	9°29'11"	2°30'18"W	1974	-27.1+	0.15
N9	80°18'38"	168°16'27"	9°29'14"	1°58'09"W	1976	-27.4	
N10	80°22.1'	170°15½'	9°29.6'	1°37.6'W	1974		0.12
N11	80°29.2'	173°54'	9°27.5'	1°00.6'W	1976	-27.6	0.11
N12	80°35'06"	176°54'23"	9°24'05"	0°30'29"W	1976	-27.6	0.10
N13	80°27'40"	180°21'01"	9°32'19"	0°03'30"E	1976	-27.1	0.06
N14	80°26.4'	183°42'	9°32.4'	0°37.0'E	1976		0.08
N15	80°25'28"	186°01'54"	9°31'21"	1°00'22"E	1976	-26.9	
N16	80°23'02"	189°02'59"	9°29'47"	1°30'45"E	1976	-26.4	0.13
N17	80°16'	191°54'	9°31'	2°00'E	1976		
N18	80°06'37"	194°45'19"	9°33'49"	2°31'08"E	1976	-25.7	0.17
N19	80°01'18"	197°36'39"	9°30'38"	3°01'08"E	1976	-24.9	
04	79°10.4'	155°26½'	9°50.8'	4°30.0'W	1974		0.16
05	79°11'25"	157°24'34"	9°58'49"	4°09'09"W	1974		0.20
06	79°13.6'	159°25'	10°05.1'	3°47.2'W	1974		0.23
07	79°36.1'	163°42'	9°58.8'	2°55.1'W	1974		0.13
08	79°41.2'	165°56½'	10°00.3'	2°30.3'W	1974		0.16

Table A1, Part 1. (continued)

Station	Positions: Geographic South Latitude	Positions: Geographic West Longitude	Positions: Grid South Latitude	Positions: Grid East or West Longitude	Year	Ten-Meter Temperature °C	Accumulation Rate m yr^{-1} of ice
09	79°47.6'	168°34½'	10°00.3'	2°01.4'W	1974		0.15
010	79°52'	171°22'	10°02'	1°31'W	1977		
011	79°58.6'	174°29'	9°58.6'	0°57.8'W	1977		
012	79°58'34"	177°12'51"	10°00'43"	0°29'14"W	1976	-27.5	0.11
013	79°57'05"	180°02'59"	10°02'55"	0°00'31"E	1976		0.10
014	79°59'00"	182°53'57"	10°00'14"	0°30'24"E	1976	-27.1	0.13
015	79°58'11"	185°50'07"	9°58'42"	1°01'11"E	1976		0.11
016	79°56'09"	188°21'47"	9°57'26"	1°27'50"E	1976	-26.6	0.16
017	79°44.1'	191°12'	10°04.2'	1°59.6'E	1976		0.12
018	79°45'55"	193°36'52"	9°56'50"	2°24'33"E	1976	-26.1	
019	79°31'48"	196°38'15"	10°01'54"	2°59'52"E	1976	-25.3	
OP4	78°44.4'	155°33½'	10°15.0'	4°39.5'W	1974		0.16
P5	78°44.3'	158°01½'	10°26.6'	4°12.8'W	1974		0.23
P6	78°45'34"	159°53'18"	10°33'19"	3°51'54"W	1974	-24.6	0.27
P7	79°18'37"	164°42'30"	10°18'41"	2°49'09"W	1976	-27.0	0.13
P8	79°14'	167°13'	10°30'	2°23'W	1976		0.18
P9	79°17'40"	169°21'45"	10°31'18"	1°58'34"W	1976	-27.4	0.19
P10	79°22'18"	171°49'12"	10°31'13"	1°30'44"W	1976		0.15
P11	79°26'04"	174°48'34"	10°31'20"	0°57'21"W	1976		0.18
P12	79°28'16"	177°18'19"	10°31'02"	0°29'42"W	1976		0.15
P13	79°30'49"	180°03'52"	10°29'11"	0°00'42"E	1976		0.11
P14	79°28'30"	182°31'49"	10°30'53"	0°27'53"E	1976		0.10
P15	79°27'19"	185°23'39"	10°29'53"	0°59'29"E	1976		0.10
P16	79°25'46"	188°00'29"	10°28'03"	1°28'21"E	1976	-26.3	0.14
P17	79°19'02"	190°34'15"	10°30'05"	1°57'35"E	1976	-27.3	0.16
Q5	78°20.1'	159°09'	10°54.8'	4°07.2'W	1974		0.31
Q6	78°36'01"	162°09'28"	10°51'05"	3°29'34"W	1974	-24.5	0.25
Q7	78°36'40"	165°12'59"	11°00'43"	2°54'22"W	1976		0.27
Q8	78°48'32"	167°23'27"	10°55'16"	2°26'35"W	1976	-26.3	0.21
Q9	78°47'03"	169°53'08"	11°02'29"	1°58'11"W	1976		0.16
Q10	78°54'25"	172°24'52"	10°59'46"	1°27'52"W	1976	-26.5	0.18
Q11	78°57'33"	174°51'14"	10°59'47"	0°59'25"W	1976		0.17
Q12	78°59'22"	177°44'50"	11°00'07"	0°25'58"W	1976		0.15
Q13S	79°08'13"	180°04'39"	10°51'47"	0°00'53"E	1976	-27.2	0.13
Q14	78°59'30"	182°42'49"	10°59'46"	0°31'16"E	1976		0.12
Q15	78°56'36"	185°09'33"	11°00'43"	0°59'39"E	1976	-27.0	0.14
R10	78°25'04"	172°36'11"	11°29'09"	1°29'28"W	1976		0.27
R11	78°25'07"	175°17'47"	11°32'33"	0°56'59"W	1976	-26.0	0.21
R12	78°28'45"	177°41'18"	11°30'41"	0°27'53"W	1976		0.18
R13	78°28'49"	180°09'55"	11°31'11"	0°02'00"E	1976	-26.3	0.16
R14	78°28'57"	182°30'35"	11°30'23"	0°30'16"E	1976	-26.4	0.16
R15	78°26'49"	185°05'15"	11°30'27"	1°01'28"E	1976		0.17
R16	78°25'13"	187°27'49"	11°28'54"	1°30'15"E	1977	-26.0	
R17	78°20'05"	189°51'20"	11°29'35"	1°59'48"E	1977		
R18	78°18'00"	192°45'06"	11°24'41"	2°34'57"E	1977	-22.2	

Table A1, Part 1. (continued)

Station	Positions: Geographic South Latitude	Positions: Geographic West Longitude	Positions: Grid South Latitude	Positions: Grid East or West Longitude	Year	Ten-Meter Temperature °C	Accumulation Rate m yr^{-1} of ice
S14	77°58'57"	182°20'16"	12°00'27"	0°29'25"E	1976		0.19
S15	77°55'56"	184°48'10"	12°01'31"	1°00'37"E	1976		0.26
S16	77°54'19"	187°09'23"	12°00'02"	1°30'24"E	1977		
S17	77°50'37"	189°27'46"	11°59'27"	1°59'55"E	1977		
T15	77°39'24"	185°55'45"	12°16'38"	1°16'30"E	1976	-25.1	0.26
T17	77°19'31"	189°06'33"	12°30'54"	2°00'24"E	1977	-24.5	
Other Sites							
LAV	78°10'29"	162°13'14"	11°15'38"	3°36'39"W	1956		0.27
A	82°09'	193°37'	7°38'	1°51'E	1960		0
B	82°12'	195°01'	7°32'	2°01'E	1960		0.05
C	82°34'	191°13'	7°17'	1°27'E	1960		0.28
D	82°48'	190°00'	7°05'	1°15'E	1960		0.31
E	83°11'	187°16'	6°46'	0°52'E	1960		0.19
F	83°17'	186°14'	6°41'	0°44'E	1960		0.25
G	83°22'	185°45'	6°36'	0°40'E	1960		0.21
H	83°31'	183°55'	6°28'	0°27'E	1960		0.31
I	83°22'03"	185°04'00"	6°36'24"	0°35'09"E	1960		
RI Dome	79°23'18"	161°53'11"	10°05'09"	3°17'57"W	1974	-23.6	

Station positions are appropriate to the date of installation, listed in the third column as the commencement of the field season; thus, "1973" refers to the 1973-1974 field season. Ten-meter temperatures are corrected for seasonal variation to their equivalent average values. A superscript $^{+}$ next to a temperature value means that the measurement was actually made at a depth less than 10 m, as follows: H6, 8 m, -29.2°; K3, 7 m, -28.5°; K11, 8 m, -27.5°; L5, 8 m, -28.2°; M3, 6 m, -27.3°; N8, 8 m, -28.1°. The listed "ten-meter temperatures" are extrapolated at these stations. Accumulation rates are from repeated stake measurements. At most of the stations the results that are presented here were obtained by remeasurement after one year. However, at all the stations that were planted in 1974 the interval was two years, and at G5 and F10 it was three years. Some of the stations were not revisited, and there are no accumulation data at these stations. The data for Little America V (LAV) are from Crary [1961], and those from stations A - I are previously unpublished material; they are included here by kind permission of Charles Swithinbank, who made the measurements.

TABLE A1, Part 2. Velocities, Principal Strain Rates, and Rotation Rates at RIGGS Stations

Station	Ice Shelf Velocity: Speed m yr^{-1}	Ice Shelf Velocity: Azimuth Geographic °	Ice Shelf Velocity: Azimuth Grid °	Principal Strain Rates: $10^5\ \dot{\varepsilon}_{11}$ yr^{-1}	Principal Strain Rates: $10^5\ \dot{\varepsilon}_{22}$ yr^{-1}	Principal Strain Rates: Azimuth of $\dot{\varepsilon}_{11}$ Geographic °	Principal Strain Rates: Azimuth of $\dot{\varepsilon}_{11}$ Grid °	Rotation Rate $10^5\ \dot{\omega}$ rad. yr^{-1}
Base Camps								
I (BC)	352	318.2	152.2	70 ± 1	-30 ± 2	100	294	
II (RI)	362	281.7	120.1	27 ± 3	-6 ± 4	45	243	276
III (C-16)	480	9.1	179.6	142 ± 4	-87 ± 1	39	210	63
IV (Q13)	965	8.0	187.9	116 ± 2	-12 ± 4	29	209	

Table A1, Part 2. (continued)

Station	Ice Shelf Velocity: Speed m yr^{-1}	Azimuth: Geographic °	Azimuth: Grid °	Principal Strain Rates: $10^5 \dot{\varepsilon}_{11}$ yr^{-1}	$10^5 \dot{\varepsilon}_{22}$ yr^{-1}	Azimuth of $\dot{\varepsilon}_{11}$: Geographic °	Azimuth of $\dot{\varepsilon}_{11}$: Grid °	Rotation Rate $10^5 \dot{\omega}$ rad. yr^{-1}
Remote Stations								
E6	(509)	(273.5)	(118.0)	359 ± 30	-103 ± 6	155	0	
E7	(484)	(287.0)	(127.6)	218 ± 45	-192 ± 16	152	353	
E8	(449)	(293.5)	(129.7)	256 ± 19	-177 ± 13	152	348	
F6	(473)	(290.7)	(132.9)	204 ± 19	-149 ± 4	41	243	
F7	530	295.9	133.8	165 ± 7	-22 ± 16	12	210	
F8	(497)	(296.3)	(129.3)	18 ± 3	-13 ± 1	40	233	
F9	493	297.0	125.6	171 ± 4	-31 ± 3	172	1	
F10	[81 ± 2]	[11.0]	[195.2]	258 ± 28	-152 ± 68	89	273	-555
G5	0			0 ± 0.9	-7 ± 0.3	38	247	
G8	384	306.0	139.5	543 ± 46	-496 ± 8	50	243	
G9	(450)	(300.8)	(130.3)	90 ± 3	-111 ± 3	58	247	
G10	487	305.4	131.0	75 ± 8	-14 ± 7	21	207	-153
G11	(420)	(318.1)	(138.8)	322 ± 91	-311 ± 102	179	0	-253
H5	9	296.0	142.8	56 ± 3	-8 ± 1	127	334	
H6	(0)			4 ± 3	-6 ± 5	100	306	
H7*	(54)	(270.0)	(110.8)	197 ± 13	-129 ± 3	130	331	
H8	(302)	(322.4)	(158.9)	67 ± 2	-43 ± 6	115	312	
H9	348	316.0	148.6	270 ± 19	-28 ± 27	22	215	
H10	223	298.3	127.1	672 ± 36	-668 ± 14	82	271	
H11	(432)	(321.0)	(145.4)	78 ± 5	-3 ± 5	44	228	
H12	272	326.1	143.0	488 ± 82	-311 ± 63	181	358	-419
HE12	500	328.4	148.2	153 ± 11	-23 ± 10	25	205	207
H13	345	32.4	205.4	416 ± 30	-190 ± 23	152	325	-1529
I5	6	306.0	152.3	0 ± 1	-3 ± 1	175	21	
I6	(0)			30 ± 4	0 ± 1	57	260	
I7	(178)	(303.7)	(141.8)	440	-373	113	311	
I8	(320)	(318.6)	(154.6)	121	-113	123	319	
I9	(340)	(322.7)	(154.9)	59	-3	116	308	
I10	(0)	(0.0)	(186.8)	32 ± 0.8	-3 ± 0.3	41	228	
I11	(447)	(341.5)	(165.0)	171 ± 7	-78 ± 8	57	240	
I12	(501)	(342.4)	(162.6)	84 ± 7	38 ± 3	42	222	60
I13	511	344.3	160.1	172 ± 35	-120 ± 34	37	213	-78
I14	(395)	(347.4)	(159.4)	97 ± 3	-16 ± 5	32	204	-108
I15	135	344.4	152.2	396 ± 49	-124 ± 49	20	188	-298
J4	0			13 ± 0.2	1 ± 0.4	48	256	15
J6	6	300.0	141.4	79 ± 19	-29 ± 11	92	293	
J7	(188)	(314.7)	(151.4)	278 ± 14	-78 ± 14	107	304	
J8	(265)	(319.1)	(154.0)	269 ± 2	-116 ± 2	102	297	
J9	(370)	(320.5)	(151.9)	44 ± 1	23 ± 3	152	343	
J10	388	319.0	146.5	201 ± 1	-24 ± 3	170	357	
J11	(468)	(343.6)	(167.3)	124 ± 1	-15 ± 1	147	331	
J12	(532)	(348.4)	(168.1)	53 ± 0.1	24 ± 0.7	11	191	60
J13	507	347.9	164.4	131 ± 1	-7 ± 1	46	223	130
J14	(452)	(348.5)	(161.4)	212 ± 4	-106 ± 4	37	210	-22
J15	271	346.2	154.6	120 ± 3	-45 ± 2	25	193	28

Table A1, Part 2. (continued)

Station	Ice Shelf Velocity			Principal Strain Rates				Rotation Rate
		Azimuth				Azimuth of $\dot{\varepsilon}_{11}$		
	Speed m yr^{-1}	Geographic °	Grid °	$10^5\ \dot{\varepsilon}_{11}$ yr^{-1}	$10^5\ \dot{\varepsilon}_{22}$ yr^{-1}	Geographic °	Grid °	$10^5\ \dot{\omega}$ rad. yr^{-1}
K3	436	266.0	114.1	77 ± 6	-62 ± 7	137	345	-63
K4*	(325)	(271.0)	(117.6)	502 ± 43	-445 ± 71	150	357	-831
K5*	(0)			4 ± 1	0 ± 1	187	31	-7
K6*	(0)			6 ± 1	-11 ± 3	133	333	
K7	(118)	(309.5)	(146.2)	291 ± 41	-339 ± 44	108	305	
K8	(270)	(324.3)	(158.1)	204 ± 1	-31 ± 3	110	304	
K9	(406)	(330.3)	(160.5)	110 ± 6	-9 ± 4	170	0	
K10	447	337.8	164.6	108	-29	163	350	
K11	516	345.2	168.4	71 ± 5	-73 ± 1	157	340	
K12	(547)	(350.3)	(170.5)	63 ± 1	8 ± 4	11	191	-10
K13	550	354.3	170.3	98 ± 0.2	-11 ± 1	32	208	41
K14	525	356.0	169.6	203 ± 2	-125 ± 3	42	216	-63
K15*	(332)	(355.3)	(164.3)	488 ± 118	-489 ± 122	43	212	
K16	241	357.8	163.7	163 ± 10	-73 ± 31	59	225	-89
K17	263	358.0	160.7	521	-489	44	207	-354
L4	(465)	(266.7)	(114.7)	4 ± 1	-9 ± 4	17	225	-23
L5	(460)	(265.1)	(110.4)	105 ± 2	-4 ± 1	5	210	-42
L6	(462)	(260.5)	(103.0)	98 ± 1	23 ± 1	141	343	-28
L7	(477)	(266.0)	(105.6)	206 ± 11	-51 ± 9	143	343	29
L8	(504)	(296.3)	(131.6)	275 ± 9	-262 ± 6	152	347	
L9	(318)	(327.7)	(160.7)	298 ± 4	-150 ± 6	130	323	
L10	(445)	(336.0)	(165.5)	194 ± 4	-51 ± 12	141	331	
L11	(506)	(343.3)	(169.2)	138 ± 7	-65 ± 2	169	355	
L12	537	349.0	172.2	68 ± 3	-23 ± 0	170	353	93
L13	582	355.4	175.3	76 ± 1	-2 ± 1	8	188	72
L16	(462)	(8.7)	(178.8)	141 ± 1	-84 ± 5	40	210	42
L17	302	8.6	175.6	223	-218	50	217	-99
L18	181	26.3	189.7	115 ± 3	-108 ± 7	42	205	93
L19	33	35.4	196.6	412 ± 43	-206 ± 76	69	230	-44
ML6 (M6½)	(457)	(268.0)	(108.0)	43 ± 1	15 ± 1	23	223	148
M2*	(165)	(276.4)	(125.8)	381 ± 24	-411 ± 7	49	258	511
M3	414	269.3	117.2	513 ± 52	-544 ± 71	25	233	375
M5	(400)	(268.0)	(112.0)	233 ± 5	-106 ± 7	17	221	148
M6	(404)	(267.7)	(109.0)	160 ± 15	-141 ± 20	31	232	123
M7	(451)	(277.4)	(115.9)	55 ± 1	18 ± 3	140	338	261
M8	(528)	(296.1)	(131.8)	156 ± 1	-80 ± 4	146	342	287
M9	(526)	(317.6)	(150.1)	392 ± 5	-370 ± 11	162	355	-11
M10*	(470)	(328.3)	(159.3)	212 ± 5	-148 ± 7	147	338	49
M12	(599)	(351.8)	(174.8)	451 ± 105	-242 ± 73	177	0	-193
M13	616	1.1	180.9	116 ± 13	-40 ± 9	11	191	86
M15	610	11.9	185.6	203 ± 13	-154 ± 6	39	213	37
M17	333	24.4	191.8	145	-109	49	216	48
N4	229	290.8	136.1	42 ± 1	-18 ± 3	154	359	99
N5*	(300)	(297.0)	(139.7)	131 ± 4	-85 ± 7	11	214	172
N6*	(231)	(279.0)	(120.2)	626 ± 45	-649 ± 57	34	235	542
N7	(309)	(295.3)	(132.8)	51 ± 5	-39 ± 8	56	254	375

Table A1, Part 2. (continued)

Station	Ice Shelf Velocity			Principal Strain Rates				Rotation Rate
		Azimuth				Azimuth of $\dot{\varepsilon}_{11}$		
	Speed m yr^{-1}	Geographic °	Grid °	$10^5\ \dot{\varepsilon}_{11}$ yr^{-1}	$10^5\ \dot{\varepsilon}_{22}$ yr^{-1}	Geographic °	Grid °	$10^5\ \dot{\omega}$ rad. yr^{-1}
N8	484	313.8	148.6	102 ± 1	-15 ± 1	153	348	366
N10	(635)	(332.2)	(161.9)	300 ± 20	-272 ± 15	172	2	126
N11	(648)	(347.8)	(173.9)	204	-122	2	188	
N12	660	354.8	177.9	140 ± 12	-67 ± 8	176	359	49
N13	(705)	(3.4)	(183.0)	154 ± 2	-79 ± 1	13	193	12
N14	(734)	(9.7)	(186.0)	171 ± 6	-134 ± 7	29	205	-41
N16	(546)	(217.0)	(28.0)	228	-182	45	216	-22
N18	628	66.2	231.4	126 ± 6	-101 ± 9	38	203	-52
04	(207)	(305.3)	(149.9)	25 ± 6	-16 ± 5	151	356	197
05	343	329.7	172.3	95 ± 1	-19 ± 1	138	341	161
06*	(275)	(329.9)	(170.5)	174 ± 14	-65 ± 12	179	20	-50
07*	(173)	(332.0)	(168.3)	448 ± 22	-579 ± 18	109	305	487
08	(472)	(340.2)	(174.2)	140 ± 0	-2 ± 0.4	140	334	344
09	(643)	(343.4)	(174.8)	105 ± 3	-6 ± 2	161	352	305
012	784	0.2	183.0	181 ± 6	-98 ± 2	180	3	
013	815	7.2	187.2	202 ± 6	-163 ± 4	25	205	
014	(786)	(10.2)	(187.3)	116 ± 3	-54 ± 2	16	193	239
015	701	13.7	187.9	150 ± 9	-119 ± 6	28	202	-105
016	681	29.2	200.8	198 ± 24	-155 ± 15	26	198	-37
017	(638)	(43.4)	(212.2)	257 ± 20	-250 ± 19	14	183	-84
OP4				48 ± 1	2 ± 0.4	29	233	14
P5	(340)	(327.9)	(169.9)	252 ± 2	-30 ± 2	130	332	-40
P6	378	325.4	165.5	285 ± 2	-27 ± 2	134	334	-97
P7	258	346.8	182.1	683 ± 24	-712 ± 26	124	319	936
P8	(589)	(356.6)	(189.4)	138 ± 1	-0.2 ± 1	157	350	
P9	724	357.2	187.8	104 ± 1	7 ± 3	156	347	423
P10	809	357.4	185.6	106 ± 1	-7 ± 1	15	203	
P11	890	0.1	185.3	98 ± 2	-21 ± 1	8	193	132
P12	(885)	(3.3)	(186.0)	181 ± 3	-93 ± 2	21	204	-9
P13	(893)	(7.8)	(187.7)	154 ± 4	-70 ± 2	25	205	
P14	(849)	(11.7)	(189.2)	91 ± 1	-44 ± 1	11	188	-91
P15	798	17.2	191.8	140 ± 1	-86 ± 3	7	182	-60
P16	(746)	(24.4)	(196.4)	140 ± 44	-144 ± 21	21	193	-190
P17	661	30.8	200.2	56 ± 3	-22 ± 2	28	197	-335
Q5	(395)	(324.1)	(165.0)	288 ± 24	-7 ± 12	105	306	128
Q6	384	308.2	146.0	399 ± 7	65 ± 8	9	207	-475
Q7	(523)	(21.7)	(216.5)	134 ± 2	61 ± 4	155	350	
Q8	662	8.4	201.0	119 ± 3	68 ± 1	176	9	308
Q9	(794)	(6.7)	(196.8)	111 ± 2	51 ± 7	60	250	462
Q10	(875)	(4.0)	(191.6)	88 ± 6	41 ± 11	30	218	
Q11	942	4.8	189.9	77 ± 2	31 ± 1	~ 10	~ 195	
Q12	950	6.1	188.4	110 ± 1	20 ± 2	22	204	
Q13S				111 ± 2	-21 ± 1	26	206	
Q14	921	10.5	187.8	73 ± 1	6 ± 2	24	201	
Q15	842	13.1	187.9	85 ± 3	5 ± 2	2	177	
R10	(984)	(2.3)	(189.7)	134 ± 0	54 ± 1	81	268	114

Table A1, Part 2. (continued)

Station	Ice Shelf Velocity			Principal Strain Rates				Rotation Rate
		Azimuth				Azimuth of $\dot{\varepsilon}_{11}$		
	Speed m yr^{-1}	Geographic °	Grid °	$10^5\ \dot{\varepsilon}_{11}$ yr^{-1}	$10^5\ \dot{\varepsilon}_{22}$ yr^{-1}	Geographic °	Grid °	$10^5\ \dot{\omega}$ rad. yr^{-1}
R11	1007	1.0	185.7	94 ± 7	48 ± 3	112	297	105
R12	(1002)	(3.5)	(185.8)	117 ± 9	68 ± 8	67	249	112
R13	998	6.1	185.9	77 ± 1	54 ± 4	24	204	
R14	(954)	(9.0)	(186.5)	110 ± 1	49 ± 1	54	231	426
R15	876	9.5	184.4	61 ± 4	51 ± 1	48	223	
S14	(978)	(6.1)	(183.8)	92 ± 2	15 ± 1	111	289	689
S15	(920)	(5.6)	(180.8)	135 ± 7	71 ± 3	50	225	-1111
T15	916	0.2	174.3	233 ± 12	41 ± 8	103	277	-1836
Other Sites								
LAV	(511)	(315.5)	(153.3)	129	81	45	243	
A	[270 ± 30]	[13 ± 10]	[179.0]					
B	[292 ± 8]	[22 ± 4]	[187.0]					
C	[280 ± 8]	[345 ± 1]	[154.0]					
D	[291 ± 18]	[344 ± 2]	[154.0]					
E	[420 ± 34]	[347 ± 2]	[160.0]					
F	[380 ± 16]	[350 ± 30]	[164.0]					
G	[370 ± 8]	[333 ± 10]	[147.0]					
H	[350 ± 33]	[325 ± 15]	[141.0]					
I				587 ± 6	-640 ± 19	1	176	-132

Estimated speed errors are ±5 m yr^{-1} at the four base camps, ±15 m yr^{-1} at the rest of the satellite-tracking stations (the values that are not in parentheses), and less than ±30 m yr^{-1} at interpolated stations (values in parentheses). At the stations marked with an asterisk errors may be significantly greater than ±30 m yr^{-1}. The values in square parentheses were obtained by resection into the Transantarctic Mountains. Azimuths for the velocities and the strain rates are taken clockwise from true or grid north. In most cases, strain rates are averages of the five values resulting from a strain rosette. At some of the rosettes, only three of the stakes could be found for remeasurement; errors were not estimated at those sites. The rate at which the principal axes rotate ($\dot{\omega}$) is positive if clockwise. At most of the stations the results that are presented here were obtained by remeasurement after one year. However, at all the stations that were planted in 1974 the interval was two years, and at G5 and F10 it was three years. Velocity measurements at H5, I5, and J6 were made over an interval of two years. Some of the stations were not revisited, so there are no velocity or strain rate data at these stations; they are, therefore, omitted from this part of Table A1. Except for the ice velocity (our work), the data for Little America V (LAV) are from Crary [1961]. Data from stations A - I are previously unpublished material; they are included here by kind permission of Charles Swithinbank, who made the measurements.

Acknowledgments. The results presented here represent the fruits of the labor of many individuals; we sincerely thank them all. They include our field assistants, Paul Gurling, Paul Burton (both 'on loan' from the British Antarctic Survey), Eldon Penn, Jeff Lingham, David Schilling, Mark Jordan, and Mark Hyland; the U.S. Geological Survey personnel who operated the satellite-tracking equipment, W. Schoonmacher, M. Crutcher, R. Worcester, J. Sorensen, D. Hall, D. Chun, and R. Wilson; and the two Danes who measured the 10-m temperatures, J. Nielsen and S. Hansen. The RISP Management Office, under the direction of John Clough, did a splendid job of looking after the myriad details that can make Antarctic work so tedious, and Karl Kuivinen and Bill Rierden displayed extraordinary patience in handling our day-to-day problems in the field. We thank the Twin Otter pilots and engineers, without whom none of this work could have been accomplished. British Antarctic Survey pilots Bert Conchie and Giles Kershaw relocated 78 of the 82 stations planted from camps B.C. and R.I., despite continual problems from the Litton Inertial Navigation Unit (INU) used for airplane navigation.

Station relocation from camps C-16 and Q13 was also delayed by INU problems. Nevertheless, the two Canadian pilots, Gene Kopek and Hugh Danforth, willingly worked long hours, often in poor weather, to relocate strain rosettes during the brief periods when the INU was functioning. We are all indebted to the National Science Foundation for funding this work, and to members of the Division of Polar Programs who help to smooth the way for investigators to work in Antarctica. We thank Charles Swithinbank and Egon Dorrer for providing their unpublished data, and for allowing us to include them here. We have greatly benefitted from numerous discussions with other RIGGS investigators, particularly the group from the University of Wisconsin-Madison, headed by Charles R. Bentley. For the first two seasons of RIGGS we were able to borrow a Wild T-16 theodolite from the South Dakota Geological Survey, and throughout the entire period of RIGGS the Tellurometer Company loaned us back-up distance-measuring equipment. We also thank James Zumberge for his part in conceiving the Ross Ice Shelf Project, and for his determination in ensuring its healthy birth. Finally, the senior author gives sincere thanks to Robert Rutford, who, as first Director of the RISP Management Office, made it possible for him to become part of RIGGS.

References

Allison, I., The mass budget of the Lambert Glacier drainage basin, Antarctica, J. Glaciol., 22, 223-246, 1979.

Bender, J. A., and A. J. Gow, Deep drilling in Antarctica, in General Assembly of the International Union of Geodesy and Geophysics, Publ. 55, pp. 132-141, International Association of Hydrological Sciences, Paris, 1961.

Budd, W. F., The dynamics of the Amery Ice Shelf, J. Glaciol., 5, 335-358, 1966.

Carslaw, H. S., and J. C. Jaeger, Conduction of Heat in Solids, 2nd ed., 510 pp., Clarendon, Oxford, 1959.

Clausen, H. B., and W. Dansgaard, Less surface accumulation on the Ross Ice Shelf than hitherto assumed, in Symposium on Isotopes in Snow and Ice, Publ. 118, pp. 172-176, International Association of Hydrological Sciences, Paris, 1977.

Clausen, H. B., W. Dansgaard, J. Nielsen, and J. W. Clough, Surface accumulation on the Ross Ice Shelf, Antarct. J. U.S., 14(5), 68-72, 1979.

Crary, A. P., Glaciological studies at Little America station, Antarctica, 1957 and 1958, IGY Glaciol. Rep. 5, Am. Geogr. Soc., New York, 1961.

Crary, A. P., and C. R. Wilson, Formation of 'blue' glacier ice by horizontal compressive forces, J. Glaciol. 3, 1045-1050, 1961.

Crary, A. P., E. S. Robinson, H. F. Bennett, and W. W. Boyd, Jr., Glaciological studies of the Ross Ice Shelf, Antarctica, 1957-1960, IGY Glaciol. Rep., 6, Am. Geogr. Soc., New York, 1962.

Dansgaard, W., S. J. Johnsen, H. B. Clausen, C. U. Hammer, and C. C. Langway, Jr., Stable isotope profile through the Ross Ice Shelf at Little America V, Antarctica, in Symposium on Isotopes in Snow and Ice, Publ. 118, pp. 322-325, International Association of Hydrological Sciences, Paris, 1977.

Defense Mapping Agency, Report of the DoD geoceiver test program, Rep. 0001, 184 pp., Washington, D. C., 1972.

Dorrer, E., Movement determination of the Ross Ice Shelf, Antarctica, in International Symposium on Antarctic Glaciological Exploration, Publ. 86, pp. 467-471, International Association of Scientific Hydrology, Paris, 1970.

Dorrer, E., W. Hofmann, and W. Seufert, Geodetic results of the Ross Ice Shelf survey expeditions, 1962-63 and 1965-66, J. Glaciol., 8, 67-90, 1969.

Gow, A. J., The inner structure of the Ross Ice Shelf at Little America V, Antarctica, as revealed by deep core drilling, in General Assembly of the International Union of Geodesy and Geophysics, Publ. 61, pp. 272-284, International Association of Scientific Hydrology, Paris, 1963.

Heap, J. A., and A. S. Rundle, Snow accumulation on the Ross Ice Shelf, Antarctica, in Antarctic Snow and Ice Studies, Antarctic Res. Ser., vol. 2, pp. 127-155, AGU, Washington, D.C., 1964.

Jaeger, J. C., Elasticity, Fracture and Flow, 3rd ed., 268 pp., Methuen, London, 1969.

Langway, C. C., Jr., M. Herron, and J. H. Cragin, Chemical profile of the Ross Ice Shelf at Little America V, Antarctica, J. Glaciol., 13, 431-435, 1974.

MacAyeal, D. R., Transient temperature-depth profiles of the Ross Ice Shelf, M.S. thesis, Univ. of Maine, Orono, 1979.

MacAyeal, D. R., and R. H. Thomas, Numerical modeling of ice shelf motion, Ann. Glaciol., 3, 189-194, 1982.

MacAyeal, D. R., and R. H. Thomas, Ross Ice Shelf temperatures support a history of ice-shelf thickening, Nature, 282, 703-705, 1979.

Meier, S., Die kustennahe Eisdecke des westlichen Enderby-Landes, Antarktis, 104 pp., Geographisch-Kartographische Anstalt Gotha, Leipzig, 1977.

Nakawo, M., Y. Ageta, and A. Yoshimura, Discharge of ice across the Soya Coast, in

Glaciological Studies in Mizuho Plateau, East Antarctica, 1969-1975, edited by T. Ishida, pp. 235-244, National Institute of Polar Research, Tokyo, 1978.

Narod, B. B., Bridge optimization for thermistor measurements, J. Glaciol., 16, 169-275, 1976.

Nye, J. F., Physical Properties of Crystals, 322 pp., Oxford University Press, New York, 1957.

Robin, G. de Q., Ice shelves and ice flow, Nature, 253, 168-172, 1975.

Rose, K. E., Characteristics of ice flow in Marie Byrd Land, Antarctica, J. Glaciol., 24, 63-75, 1979.

Sanderson, T. J. O., An error in ice-temperature measurement, J. Glaciol., 18, 329-333, 1977.

Sanderson, T. J. O., and C. S. M. Doake, Is vertical shear in an ice shelf negligible?, J. Glaciol., 22, 285-292, 1979.

Schwarz, C. R., C. B. Sharp, and R. W. Smith, Field operations with miniature satellite doppler positioning equipment, paper presented at the Convention of the American Society of Photogrammetry, American Congress on Surveying and Mapping, Washington, D.C., 1972.

Shumskiy, P. A., and I. A. Zotikov, Bottom melting of ice shelves in Antarctica, in Antarctica, Commission Reports, 1962, pp. 90-112, Program for Scientific Translations, Jerusalem, 1969.

Stuart, A. W., and A. J. Heine, Glaciological work of the 1959-60 U.S. Victoria Land traverse, J. Glaciol., 3, 997-1002, 1961.

Swithinbank, C., To the valley glaciers that feed the Ross Ice Shelf, Geogr. J., 130, 1-47, 1964.

Swithinbank, C. W. M., Ice movement in the McMurdo Sound area of Antarctica, in International Symposium on Antarctic Glaciological Exploration, Publ. 86, pp. 472-487, International Association of Scientific Hydrology, Paris, 1970.

Thomas, R. H., The dynamics of the Brunt Ice Shelf, Coats Land, Antarctica, Sci. Rep., 79, Br. Antarct. Surv., Cambridge, England, 1973a.

Thomas, R. H., The creep of ice shelves: theory, J. Glaciol., 12, 45-53, 1973b.

Thomas, R. H., Liquid brine in ice shelves, J. Glaciol., 14, 125-136, 1975.

Thomas, R. H., Ice velocities on the Ross Ice Shelf, Antarct. J. U.S., 11(4), 279-281, 1976a.

Thomas, R. H., The distribution of 10-m temperatures on the Ross Ice Shelf, J. Glaciol., 16, 111-117, 1976b.

Thomas, R. H., The dynamics of marine ice sheets, J. Glaciol., 24, 167-177, 1979.

Thomas, R. H., and C. R. Bentley, The equilibrium state of the eastern half of the Ross Ice Shelf, J. Glaciol., 20, 509-518, 1978.

Thomas, R. H., and D. R. MacAyeal, Derived characteristics of the Ross Ice Shelf, Antarctica, J. Glaciol., 28, 397-412, 1982.

Thomas, R. H., T. J. O. Sanderson, and K. E. Rose, Effect of climatic warming on the West Antarctic ice sheet, Nature, 277, 355-358, 1979.

Weertman, J., Deformation of floating ice shelves, J. Glaciol., 3, 38-42, 1957.

Wexler, H., Heating and melting of floating ice shelves, J. Glaciol., 3, 626-646, 1960.

Wilson, C. R., and A. P. Crary, Ice movement studies on the Skelton Glacier, J. Glaciol., 3, 873-878, 1961.

Yen, Y. C., Effective thermal conductivity and water vapor diffusivity of naturally compacted snow, J. Geophys. Res., 70, 1821-1825, 1965.

Zumberge, J. H., M. Giovinetto, R. Kehle, and J. Reid, Deformation of the Ross Ice Shelf near the Bay of Whales, Antarctica, IGY Glaciol. Rep., 3, 148 pp., Am. Geogr. Soc., New York, 1960.

(Received April 15, 1980;
revised August 10, 1981;
accepted February 2, 1982.)

The Ross Ice Shelf: Glaciology and Geophysics
Antarctic Research Series, Volume 42, Paper 3, Pages 55-86

SEISMIC STUDIES ON THE GRID WESTERN HALF OF THE ROSS ICE SHELF: RIGGS I AND RIGGS II

James D. Robertson

ARCO Oil and Gas Company, Dallas, Texas 75221

Charles R. Bentley

Geophysical and Polar Research Center, University of Wisconsin, Madison, Wisconsin 53706

Abstract. Airlifted geophysical surveys were carried out on the grid western half of the Ross Ice Shelf, Antarctica, during the austral summers of 1973-1974 and 1974-1975, as part of the Ross Ice Shelf Geophysical and Glaciological Survey (RIGGS). Seismic reflection records were obtained at 76 stations, seismic short-refraction records at nine stations, seismic long-refraction records at four stations, radar-sounding reflection records at 93 stations, and gravity measurements at 89 stations. The seismic results, supplemented by radar-sounding measurements of ice thickness, are discussed here. The P wave velocity increases from about 500 m s^{-1} at the surface to 3811 ± 7 m s^{-1} at depths of 70-80 m in the ice, and the S wave velocity increases from about 300 m s^{-1} at the surface to about 1970 m s^{-1} at 60 m. The maximum P wave velocity is significantly lower than the maximum velocity (3850 m s^{-1}) in grounded ice sheets at the same mean annual surface temperature. The average P wave velocity through the ice shelf is 3688 ± 15 m s^{-1}. Densities and elastic moduli computed from seismic velocities are consistent with densities measured on ice cores and elastic moduli determined in laboratory experiments on ice. Significant depths in the densification process of the firn have been located by analysis of the seismic velocity gradients at 11 ± 2 m (the "critical depth"), 25 ± 10 m (significance uncertain), and 46 ± 8 m (the firn-ice boundary). There is S wave velocity anisotropy in the firn that probably is caused by layered structure, but comparison between seismic and radar echo times shows no evidence of an average preferred orientation of crystallographic c axes in the body of the ice shelf. A complete listing of ice and water layer thicknesses and ocean bottom elevations is given. These results have already been discussed elsewhere. Sea bottom slopes are locally similar to regional slopes, which suggests that the seabed is relatively smooth at wavelengths of a few kilometers. Interval velocities and acoustic impedances in the layer of sediment at the seafloor match those expected for unconsolidated glacial marine till. A seismic reflector at a depth of 50-150 m within the till probably correlates with a glacial erosional surface previously discovered in sediments in the Ross Sea. The best estimate of the P wave velocity in seismic basement at long-refraction seismic stations is 5.5-5.7 km s^{-1}. One or two kilometers of lower-velocity rocks and sediments overlie basement beneath three floating stations; on Crary Ice Rise basement lies about three quarters of a kilometer beneath the ice.

Contents

TABLE 1. Summary of Seismic and Surface Radar Measurements, RIGGS I and II

	RIGGS I (1973-1974)	RIGGS II (1974-1975)	Total
Seismic reflection stations	39	37	76
P wave short-refraction profiles	7	3	10
S wave short-refraction profiles	6	2	8
Long-refraction profiles	2	2	4
Seismic wide-angle ice bottom reflection stations	4	5	9
Sediment interval velocity determinations	3	1	4
Sea bottom slope determinations	3	6	9
Sea bottom reflection coefficient determinations	4	5	9
Surface radar-sounding stations	55	38	93

Introduction

The experiments discussed in this paper were carried out during the Ross Ice Shelf Geophysical and Glaciological Survey (RIGGS) field seasons from December 15, 1973, to February 3, 1974 (RIGGS I), and from November 22, 1974, to January 27, 1975 (RIGGS II). For a summary of RIGGS see Bentley, [1984]. Herein we analyze the seismic data (Table 1) in full; radar results are introduced as needed to aid interpretation. The major topics covered are (1) the physical properties of the ice shelf, (2) ice thickness and subglacial ocean depth, and (3) the character of the ocean floor.

In general, airlifted stations were occupied during good weather, and geophysical work was conducted around the base camps during poor weather. Remote survey stations were occupied by two teams of three or four geophysicists each, the teams occupying alternate stations. The basic series of measurements taken at a remote site consisted of seismic reflection shots, radar soundings, and gravity readings. Whenever possible, radar and gravity profiling were conducted locally around the site. At selected stations, more extensive experiments, such as wide-angle radar and seismic soundings and short refraction shooting, were performed.

Seismic shots were recorded on two Texas Instruments model 7000B 24-trace seismic systems during RIGGS I and on one model 7000B and one SIE model RS-49R 24-trace seismic system during RIGGS II. Two Randall Electronics (SPRI Mark II) 35-MHz radar-sounding systems were used to make radar measurements, supplemented during RIGGS II by a 150-MHz radar system built by the University of Wisconsin Department of Electrical Engineering.

In addition to the main text, this paper includes several appendices, containing extensive site-by-site data and other supplementary information, on microfiche (back pocket of this book).

Physical Properties of the Ross Ice Shelf

Near-Surface Compressional and Shear Wave Velocities

Velocities of both compressional (P) and shear (S) waves, designated v_p and v_s, respectively, increase rapidly as functions of depth in the upper 50 m of the ice shelf owing to the compaction and recrystallization of annual snow layers into ice. Below the firn-ice boundary at about 50 m the increase is steady but slower until, at 80 m or so, the velocities attain their maximum values. Velocities decrease downward through the lower shelf, despite a slow increase in density, owing to the increase of temperature with depth [Gow, 1963; Clough and Hansen, 1979]. The bottom surface of the floating shelf is necessarily at the freezing point of seawater, whereas the mean annual surface temperatures in the survey area of RIGGS I and II average about -26°C [Thomas, 1976; Crary et al., 1962a; b]. The best estimates of the temperature coefficients of v_p and v_s in ice are -2.3 m s^{-1} K^{-1} and -1.2 m s^{-1} K^{-1}, respectively [Kohnen, 1974], indicating a probable decrease in v_p of more than 50 m s^{-1} and in v_s of more than 25 m s^{-1} in the lower part of the Ross Ice Shelf.

An important consequence of the existence of an internal seismic velocity maximum is that the complete velocity-depth function in the ice shelf cannot be determined directly. Short-refraction profiles can be used to determine only the velocity structure down to the velocity maximum: below that, only the average velocity between the velocity maximum and the bottom of the ice can be determined (from oblique reflection soundings).

Ten P wave short-refraction profiles were recorded at the following nine sites during RIGGS I and II: H7, H11S, I10S, J7S, J9DS, K11, P5, the RIGGS I base camp (BC), and the RIGGS II base camp (RI). Station locations are shown in Figure 1. Station J9DS, about half a kilometer grid southwest of station

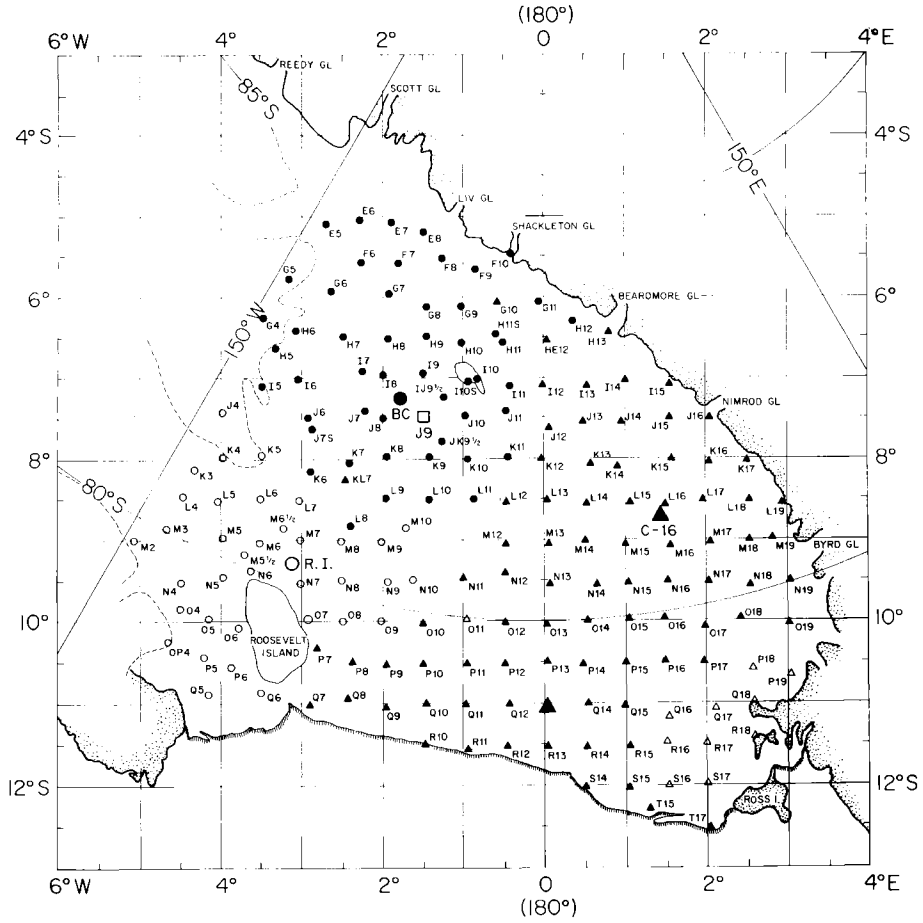

Fig. 1. Map of RIGGS stations [from Bentley, 1984]. Stations occupied during RIGGS I and II are indicated by solid circles and open circles, respectively. Stations J9DS and J9DC are at essentially the same location as station J9. In the rectangular grid coordinate system shown, meridians are parallel to the Greenwich meridian, with grid north toward Greenwich. The origin of the system is at the South Pole, and 1° of grid latitude or longitude equals 1° of geographic latitude.

J9, designates the site selected for the Ross Ice Shelf Project (RISP) drilling through the ice shelf. Two profiles were recorded at BC, one (BC-A) parallel to a glaciological strain line between BC and J9 and the other (BC-B) perpendicular to BC-A. S wave short-refraction profiles, including two at BC, were recorded at all P wave short-refraction sites except J7S and J9DS.

The normal field procedure was to lay out a 24-geophone, 2-m-interval in-line spread and to shoot blasting caps (for P) or hit a 4" x 4" stake transversely (for S) at both ends of the spread and at distances to 50, 100, 150, 200, and 250 m from one end. Two shots usually were fired (or hit) at each distance, and shots were recorded at the fastest available paper speed, about 0.8 m s^{-1} for the 7000B systems and 0.6 m s^{-1} for the RS-49R system, to provide maximum resolution of first breaks. Shot instants were provided by a geophone placed next to the stake or on a metal plate over the cap.

Travel times were picked to a precision of 0.1 ms with the aid of a seven-power measuring magnifier; the accuracy of the travel times is estimated to be 0.3 ms. Graphs of travel time versus distance were plotted and observed to possess the smoothly varying curved shape, concave toward the distance axis, that is characteristic of refraction profiling in the dry snow zone of an ice sheet. At nearly all stations, P wave travel time data were extended beyond the limit of the short-refraction records by picking first P arrivals from long-refraction or reflection seismograms. Instrumental calibration corrections have been applied as discussed in Appendix A (on microfiche).

Short-refraction travel times were con-

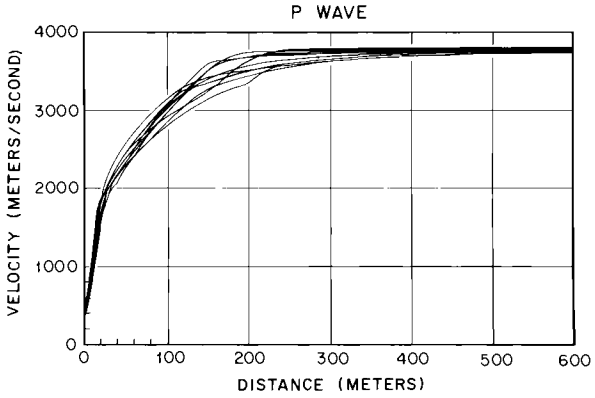

Fig. 2. Apparent v_p versus distance at 10 short-refraction stations. (Two curves are indistinguishable in this plot.)

verted to velocities versus depth through the intermediate step of computing apparent seismic velocity (the velocity with which a wave appears to travel along a line of geophones), as a function of distance. The apparent velocity at any point is equal to the inverse of the slope of the travel time curve at that point. Slopes may be obtained graphically or numerically. Particular numerical differentiation techniques that we tested were (1) the three-point central difference approximation, (2) fitting of least squares straight lines to sets of data points, and (3) least squares fitting of a second-degree polynomial to a set of data points followed by analytical differentiation of the polynomial.

After some experimentation, we chose the graphical method for determining slopes at distances of less than 200-300 m, where the curvature of the travel time is noticeable, and numerical method 2 for larger distances. (Method 1 was too unstable for accurate results, whereas method 3 did not yield a sufficiently good fit to the observed data.) Slopes were plotted against distance and smoothed graphically.

Curves of apparent velocity versus distance for the short-refraction sites are shown in Figures 2 and 3. Discrete values of velocity versus distance at each site are listed in Appendix B1 (on microfiche).

Since seismic velocities increase with density [Robin, 1958] and densities, averaged over a seismic wavelength (about a meter), increase uniformly with depth in the ice shelf [Gow, 1963], we can safely assume that the seismic velocities are continuous, monotonically increasing functions of depth. Thus the velocity-distance data could be converted to velocity-depth data by means of the Wiechert-Herglotz-Bateman (WHB) integral (see, e.g., Grant and West, [1965, p. 138]):

$$z_i = \frac{1}{\pi} \int_0^{x_i} \cosh^{-1} (pv_i)\, dx \qquad (1)$$

where v_i is v_p or v_s at depth z_i as observed at distance x_i and p is the slope of the travel time curve at distance $x < x_i$.

A computer program called WHB was written to evaluate equation (1) by fitting a second-degree Lagrange polynomial to sets of three values of the inverse hyperbolic cosine. The mathematics of the numerical integration and a listing, explanation, and test of the program were presented by Robertson [1975]. The velocity-depth output is presented graphically in Figures 4 (v_p) and 5 (v_s) and tabulated in Appendix B1 (microfiche). The estimated standard error in individual values of velocity for both v_p and v_s is ± 30 m s^{-1} at the surface diminishing to ± 20 m s^{-1} at 20 m and to ± 10 m s^{-1} at 50 m.

There is an increase in v_p from about 500 m s^{-1} at the surface to about 3800 m s^{-1} at depths of 70 or 80 m; v_s ranges from about 300 m s^{-1} at the surface to about 1970 m s^{-1} at 60 m. (Because of the very gradual velocity gradients near the velocity maxima, it is not certain that the indicated difference in depth to maximum v_p and to maximum v_s is real.) Values averaged over all the profiles on the grid western part of the Ross Ice Shelf are listed in Table 2.

Maximum Compressional and Shear Wave Velocities

As was previously mentioned, density and temperature changes in the ice shelf combine to produce a maximum in seismic velocities. We designate the maximum velocity in general by v_{max}, or specifically for P and S waves, by $(v_p)_{max}$ and $(v_s)_{max}$, respectively. There are several ways to calculate v_{max}: (1) one

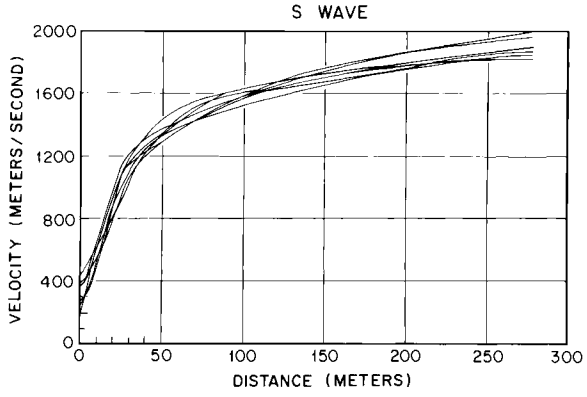

Fig. 3. Apparent v_s versus distance at eight short-refraction stations. (Two curves are indistinguishable in this plot.)

TABLE 2. Average Wave Velocities and Densities Calculated From v_p as a Function of Depth

Depth, m	v_p, m s^{-1}	v_s, m s^{-1}	ρ, kg m^{-3}
0	440 ± 30	304 ± 32	344 ± 3
2.5	999 ± 33	547 ± 20	392 ± 3
5	1472 ± 41	755 ± 16	442 ± 5
10	2112 ± 25	1116 ± 16	529 ± 4
15	2456 ± 27	1343 ± 14	587 ± 5
20	2709 ± 29	1489 ± 13	637 ± 6
25	2928 ± 29	1592 ± 11	684 ± 7
30	3119 ± 31	1666 ± 11	730 ± 8
35	3284 ± 31	1729 ± 11	772 ± 8
40	3420 ± 30	1782 ± 11	808 ± 8
45	3533 ± 31	1828 ± 12	838 ± 9
50	3618 ± 28	1869 ± 14	861 ± 8
55	3679 ± 24		877 ± 6
60	3719 ± 20		887 ± 5
65	3744 ± 15		894 ± 4
70	3763 ± 11		898 ± 3

The error estimates for the velocities are standard errors in the means; for the densities they correspond to the standard error in v_p propagated through equation (2).

may construct a travel time plot using several shots at distances greater than that at which v_{max} is expected first to be observed; the slope of the plot, which should be a straight line, is $(v_{max})^{-1}$; (2) a cross-spread velocity may be calculated for a single shot at a sufficient distance from the spread; (3) multiple surface reflections from shots at great distances may be picked; the interval between successive surface multiples is equal to the time intercept of the maximum velocity line extrapolated linearly back to zero distance.

To implement method 1, a minimum distance for sampling v_{max} must be chosen. We will call that distance x_{min}. Crary et al. [1962a; b] proposed 100 m as the depth of maximum seismic velocity in the Ross Ice Shelf. To sample this depth, the shot-geophone distance on the surface should be at least 5 or 6 times the depth, or 500 or 600 m. A more conservative choice of x_{min} is 1000 m. Several seismic shots at distances greater than 600 m were recorded at stations BC, H12, I10S, and RI. Values of $(v_p)_{max}$ at those stations calculated by the least squares technique assuming x_{min} = 600 m and x_{min} = 1000 m are presented in Table 3. There is no significant difference between the two sets of results. There do, however, appear to be significant differences between stations: in particular, $(v_p)_{max}$ at station RI is significantly higher than that at station BC (by 44 ± 8 m s^{-1}), even though

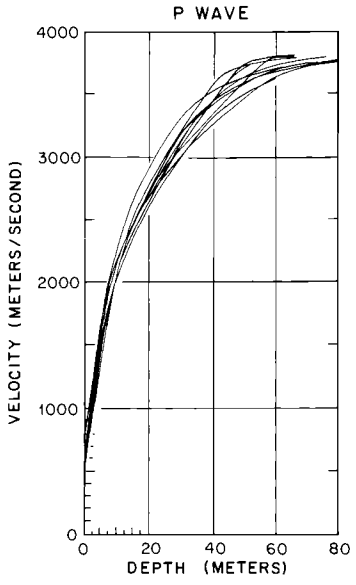

Fig. 4. P wave velocity versus depth at short-refraction stations.

both profiles were reversed. Since it is $(v_p)_{max}$ at station RI that is out of line with the others and with previous measurements [Crary et al., 1962a], we suggest that there may be some effect of crystalline anisotropy there. The average value of $(v_p)_{max}$ at the other three stations is 3796 ± 4 m s^{-1} for x_{min} = 600 m; if we include station RI, the mean is 3811 ± 11 m s^{-1}.

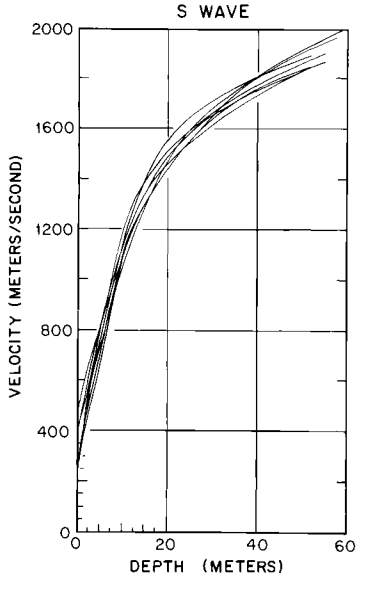

Fig. 5. S wave velocity versus depth at short-refraction stations. (Two curves are indistinguishable in this plot.)

TABLE 3. Values of $(v_p)_{max}$ From Travel Time Plots

Station	Shot Locations	Maximum Distance, m	Minimum Distance, m	n	Intercept, ms	$(v_p)_{max}$, m s^{-1}	Minimum Distance, m	n	Intercept, ms	$(v_p)_{max}$, m s^{-1}
BC	W	2340	624	58	23	3771 ± 5	1000	38	20	3750 ± 8
	E	1342	629	41	31	3816 ± 8				3896 ± 27
Mean (BC)						3794 ± 7				3796 ± 20
H12		2770	600	134	24	3800 ± 4	1008	107	24	3803 ± 3
I10S		4396	613	66	26	3789 ± 6	1005	49	26	3789 ± 8
RI	W	4869	611	74	33	3869 ± 3	1022	57	35	3877 ± 2
	E	4865	621	47	27	3807 ± 4				3795 ± 2
Mean (RI)						3838 ± 4				3836 ± 2
Overall Mean						3811 ± 11				3824 ± 9

Calculated from first arrival travel times on shots at distances greater than 600 m and distances greater than 1000 m. E and W denote shot points to the grid east and grid west of the recording spread, respectively; n is the number of travel time points used in each velocity determination.

The substantial differences in velocities in the two directions at stations BC and RI probably result from sloping iso-velocity surfaces. How large a dip would be required depends strongly on the details of the geometry. For example, if one takes as an approximation a two-layered system comprising a layer of constant velocity equal to 3000 m s^{-1} (the mean velocity above 100 m) overlying a sloping refractor with velocity equal to v_{max}, a dip of about half a degree is indicated. If, on the other hand, one imagines an uppermost layer of surficial snow with a dipping base, a dip only one tenth as large, i.e., 1 m per kilometer, would be needed.

Turning to method 2, numerous individual seismograms were recorded at distances greater than 600 m; a least squares cross-spread velocity was calculated for each. The results are presented in Table 4. The average $(v_p)_{max}$ from 30 stations is 3804 ± 6 m s^{-1}. To test for a dependence of $(v_p)_{max}$ on x_{min}, we have taken means separately for $x_{min} < 1$ km and $x_{min} > 1$ km at the four stations (BC, H12, I105, and RI) where there were shots in both ranges of x_{min}. The average $(v_p)_{max}$ for those four stations for $x_{min} < 1$ km is 3814 ± 5 m s^{-1} whereas for $x_{min} > 1$ km it is 3819 ± 21 m s^{-1}. Clearly the difference is not significant. The possibility of a dependence of $(v_p)_{max}$ on ice thickness also was examined. The average value of $(v_p)_{max}$ at the 16 stations where the ice thickness is greater than 500 m is 3812 ± 9 m s^{-1}, whereas at the 14 stations where the ice thickness is less than 500 m it is 3796 ± 7 m s^{-1}, again not a significant difference. There is no prominent pattern in the regional distribution of maximum P wave velocities.

Method 3, measuring v_{max} by means of multiple surface reflections, is possible only when several clear surface-reflected waves are recorded at a large shot-spread distance. A seismogram from station H12 containing good surface multiples is reproduced in Figure 6, and an illustrative drawing of surface multiples is shown in Figure 7. Let P_n be the arrival time of the multiple that has been reflected n-1 times at the surface, and let δ_{n-1} be the time difference between P_n and P_{n-1}. For any n such that x/n is greater than the minimum distance for the ray path to reach the velocity maximum, $\delta_{n-1} = \delta_{n-2} = . . . = \delta_1$ is the time intercept of the maximum velocity travel time line, and all the P_n are points on that line [Bentley et al., 1957; Bentley, 1964]. This analytical scheme follows directly from the basic seismic refraction principle that intercept time is equal to the difference between the actual travel time of a wave and the time that would be needed for the wave to

TABLE 4. Values of $(v_p)_{max}$ from Cross-Spread Velocities

Station	n	Minimum Distance, m	Maximum Distance, m	$(v_p)_{max}$, m s^{-1}
BC	11	892	1233	3789 N
	12	658	1000	3806 W
	12	1158	1500	3762 W
	16	751	1370	3815 W
	13	1658	2340	3765 W
	10	689	1309	3763 W
	14	621	1056	3832 E
	23	629	1342	3822 E
Mean (BC)				3794 ± 10
G5	14	608	1087	3861
	14	613	1087	3892
Mean (G5)				3876 ± 16
G6	16	692	1375	3760
H7	8	783	1096	3816
H8	21	724	1399	3767
H11S	11	853	1197	3816
H12	14	608	1070	3812
	24	600	1370	3822
	24	900	1670	3840
	24	1200	1970	3838
	24	1500	2270	3847
	24	2000	2770	3850
Mean (H12)				3835 ± 6
I8	22	738	1442	3824
I10S	20	613	1313	3809
	12	1023	1786	3834
	10	1583	2284	3807
	10	2679	3380	3820
	7	3818	4396	3755
Mean (I10S)				3809 ± 10
J7S	11	748	1029	3840
J9DS	13	625	1339	3780
J10	22	656	1412	3808
K3	14	609	1077	3768
K4	21	624	1305	3825
K5	13	610	1135	3771
L5	21	706	1450	3782
M2	23	774	1518	3863
M3	16	611	1105	3791
M5	17	616	1141	3811
M8	16	606	1134	3804
M9	22	630	1310	3785
M10	24	623	1366	3751
N7	23	665	1408	3852
N8	22	738	1480	3822

TABLE 4. (continued)

Station	n	Minimum Distance, m	Maximum Distance, m	$(v_p)_{max}$, m s^{-1}
05	18	601	1189	3830
06	22	601	1282	3771
07	17	775	1518	3773
08	12	684	1023	3758
09	12	952	1296	3813
RI	21	627	1269	3799 W
	24	1135	1869	3857 W
	24	4135	4869	3885 W
	24	1131	1865	3816 E
	14	4162	4865	3870 E
	24	640	1364	3841 S
Mean (RI)				3845 ± 13
Overall mean				3804 ± 6

Values of $(v_p)_{max}$ calculated from cross-spread velocities on individual shots at distances greater than 600 m; n is the number of travel time points on each shot. The standard errors of the individual cross-spread values of $(v_p)_{max}$ were all < ±5 m s^{-1}. Symbols N, E, S, and W after velocities at stations BC and RI indicate shots grid north, east, south, and west, respectively, of the recording spread.

move in a straight line from shot to detector at the highest velocity encountered along the refraction path [Dobrin, 1960]. The results of the analyses of surface multiples are listed in Table 5. The average $(v_p)_{max}$ for four stations is 3828 ± 9 m s^{-1}. Note that the difference between velocities shot in opposite directions at BC and RI, previously attributed to sloping iso-velocity planes, again appears. That implies that the slope, if it is real, must extend to the full length of the profile: 2 km at BC and 5 km at RI.

The average $(v_p)_{max}$ as calculated by methods 1, 2, and 3, 3811 ± 7, may be compared with other values from refraction shooting on ice shelves: 3810 m s^{-1} at Ellsworth Station on the Filchner Ice Shelf [Thiel and Behrendt, 1959], 3810 m s^{-1} at Maudheim [Robin, 1958], and 3789 ± 7 m s^{-1} on the Ross Ice Shelf (Crary et al. [1962a]; average of 18 measurements in their Table 7). All these values of $(v_p)_{max}$ are substantially lower than those commonly found on grounded ice sheets. (Thiel and Ostenso [1961] obtained a larger value (3839 m s^{-1} between 85 m and 110 m in depth) using a downhole geophone in a borehole at Little America V, but the difference is statistically not significant. They make no determination of error limits, but an uncertainty in travel time of 0.5 ms, such as we estimate for our work, would have produced a 300 m s^{-1} uncertainty in velocity over the 25-m interval.) Kohnen [1974] presents a compilation from various investigators of 31 values of wave speeds in grounded ice: they ranged from 3836 to 3950 m s^{-1}, depending on temperature, with a velocity of 3850 m s^{-1} corresponding to -24°C, the measured temperature at 80-m depth in the drill hole at station J9DC [Clough and Hansen, 1979]. (Station J9DC is the station where the RISP drilling actually took place in 1976-1978; it is about 2 km from the preselected site, J9DS.) This discrepancy between ice shelves and the grounded ice sheet has been noted previously by Thiel and Ostenso [1961] and Bentley [1964] and has been attributed variously to differences in density structure, temperature structure, and crystal orientation between ice shelves and grounded ice sheets [Thiel and Ostenso, 1961], but no quantitatively satisfactory explanation yet exists.

Ultrasonic velocity measurements on core samples from the Ross Ice Shelf and sonic velocity logging in the RISP drill hole at station J9DC might be expected to shed light on the matter, but they fail to do so. The logging yielded minimum velocities slightly less than 3800 m s^{-1} [Bentley and Jezek, 1981], consistent with the refraction results, whereas the ultrasonic measurements gave velocities comparable to, or higher than, those on grounded ice [Bennett, 1972; Kohnen and Bentley, 1977], except after the ice had relaxed, leading to the formation of microcracks [Kohnen and Gow, 1979]. The

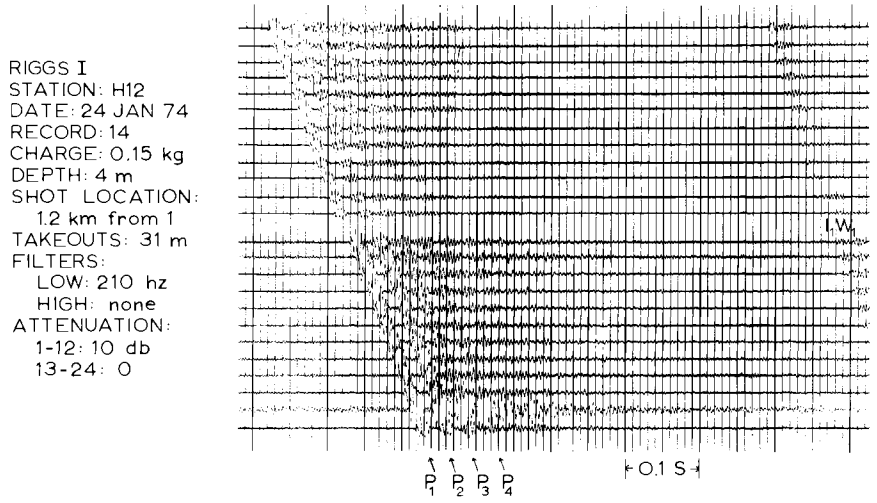

Fig. 6. Seismogram from station H12 illustrating P waves multiply reflected from the surface (P_n).

observed fabrics (roughly a 25°-30° surface cone [see Kohnen and Gow, 1979]) should not lead to an appreciable lowering of the wave velocity according to the curves given by Bennett [1972].

Primarily because of the difficulty in generating S waves, $(v_s)_{max}$ was poorly determined during RIGGS I and II. The only determination was at station BC, where the least squares inverse slope of six arrivals between 813 and 2090 m is 1970 ± 44 m s^{-1}. This can be compared with 1978 m s^{-1} obtained at Little America V through borehole logging (Thiel and Ostenso, [1961]; no error cited) and to 12 values for grounded ice sheets ranging from 1934 to 1960 m s^{-1}, averaging 1945 ± 8 m s^{-1}, tabulated by Kohnen [1974] from his work and that of Bentley et al. [1957] in Greenland and Bentley [1971] in Antarctica.

Average Compressional Wave Velocity

The average P wave velocity, $\bar{v}_p$, through the whole ice shelf may be calculated by the oblique reflection technique if reflections from the ice-water interface (called I_1 reflections after the notation of Crary et al. [1962a]) are received over a reasonable interval of distance on one or more seismograms at a station. Enough good I_1 reflections (or doubly reflected I_2 arrivals in the case of station Q5) to determine $\bar{v}_p$ were recorded on ten profiles at nine stations during RIGGS I and II. A determination on each of two perpendicular profiles was possible at station Q5. A typical seismogram is reproduced in Figure 8. Recordings were made at paper speeds of about 300 mm s^{-1}, and travel times have been picked to the nearest millisecond with an estimated uncertainty of ±2 ms. Low-cut filtering in the 100- to 300-Hz range and high amplifier gain were found to produce the clearest reflected signals and were used generally in recording. Charge sizes ranged from 1/3 to 5 lb (0.15 to 2.3 kg) of Dupont HDP primers or Seismogel; shot holes were 4 or 5 m deep. Reflection times have been corrected for uphole travel, and average velocities have been obtained by least squares fitting of regression lines to graphs of travel time squared, t^2, versus x^2 (Table 6).

Ice thickness was measured by radar along the seismic lines at three of the stations. At those stations, $\bar{v}_p$ has been corrected for the slope of the ice-water interface according to the formula

$$\bar{v}_p^2 t_2 = x^2 + 4h_i^2 + 4h_i x \sin \beta$$

where h_i is the ice thickness and β is the slope of the ice-water interface relative to the surface, positive when the ice thickens with increasing x.

One should find that $\bar{v}_p$ increases as ice thickness increases, since the thicker the ice, the less the proportion of the wave path

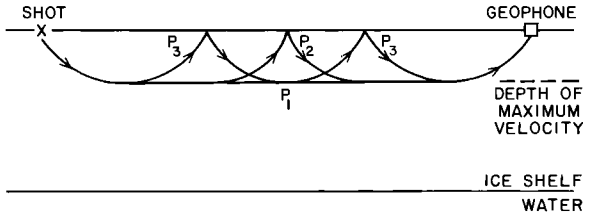

Fig. 7. Schematic diagram of P_n waves.

TABLE 5. Values of $(v_p)_{max}$ Calculated From Multiple Surface Reflections

Station	Shot Location	Shot No.	Trace	Shot Distance, m	Multiples Used	$(v_p)_{max}$, m s^{-1}	Average
BC	W	31	4	1751	P_1, P_2	3774 ± 1	
			5	1782		3799 ± 1	
			8	1875		3774 ± 1	3782 ± 14
	E	74	22	1292		3828 ± 1	
			23	1322		3830 ± 1	
			24	1352		3842 ± 1	3833 ± 8
Mean (BC)							3808 ± 11
H12		14	15	1689	P_1, P_2, P_3	3824 ± 2	
			16	1721		3838 ± 7	
			17	1752		3819 ± 5	
			20	1846		3821 ± 1	3824 ± 5
Mean (H12)							3824 ± 5
I10S		10	20	1662	P_1, P_2, P_3	3806 ± 2	
			22	1724		3796 ± 4	3801 ± 7
Mean (I10S)							3801 ± 7
RI	W	B20	1	4135	P_1, P_2, P_3, P_4	3894 ± 4	
			2	4166		3891 ± 1	
			4	4227		3879 ± 1	
			5	4257		3877 ± 1	
			6	4288		3882 ± 1	3885 ± 7
	E	B50	19	4712	P_1, P_2, P_3, P_4	3818 ± 1	
			20	4743		3819 ± 1	
			21	4773		3823 ± 1	
			22	4804		3824 ± 1	
			24	4865		3821 ± 1	3821 ± 3
Mean (RI)							3853 ± 6
Overall mean							3828 ± 9

Symbols E and W denote shots grid east and grid west, respectively, of the recording spread.

in low-velocity firn. However, when $\bar{v}_p$ is plotted against ice thickness (Figure 9) together with a theoretical curve calculated using the data in Table 2 and the assumption that $\bar{v}_p$ decreases linearly from 3811 m s^{-1} at 100 m to 3770 m s^{-1} at the ice-water interface owing to increasing ice temperature, it becomes clear that the expected effect is too small to be seen. The mean value from the RIGGS stations, 3688 ± 15 m s^{-1}, agrees well with the theoretical curve. This indicates that there is no broadly consistent effect of anisotropy in the ice.

Density and Elastic Moduli

Calculation of the variation of the elastic moduli between the surface of the ice shelf and the depth of maximum seismic velocity is possible when v_p, v_s, and density ρ all are known as functions of depth.

Lacking direct measurements of ρ, one may calculate it from the semiempirical equation of Kohnen [1972]:

$$\rho(z) = \frac{0.915 \text{ Mg m}^{-3}}{1 + \left[\frac{(v_p)_{max} - v_p(z)}{2250}\right]1.22} \qquad (2)$$

0.915 Mg m^{-3} is the approximate density of bubbly glacier ice at the depth of $(v_p)_{max}$. We have set $(v_p)_{max}$ = 3850 m s^{-1}, the expected value at a temperature of -24°C. During RIGGS II a hole was drilled to a depth of 100 m at station J9DS. Densities measured on segments of the recovered core [Langway, 1975] are compared in Figure 10 with seismically computed densities. The good agreement supports the use of Kohnen's equation for other locations where no drill holes are available.

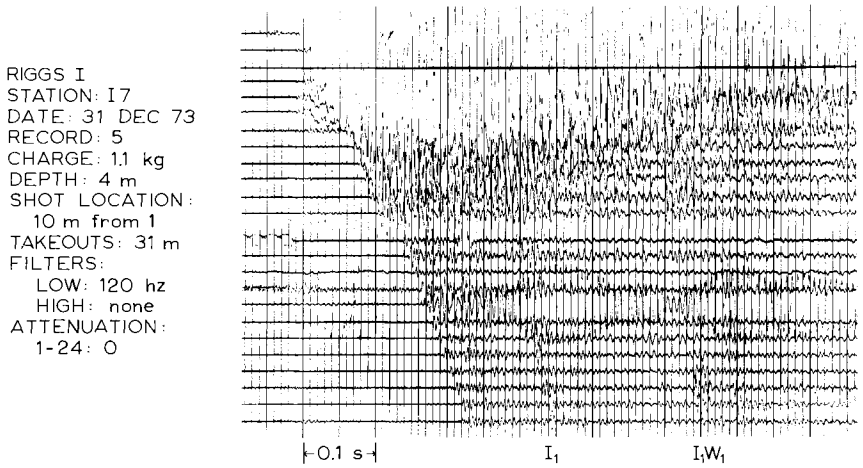

Fig. 8. Seismogram from station I7 illustrating the ice bottom (I_1) and ocean bottom (I_1W_1) reflections.

The use of $(v_p)_{max} = 3850$ m s^{-1} implies that a glacier ice density of 0.915 Mg m^{-3} (Kohnen [1972], discusses this choice of density) corresponds to that velocity, whereas $(v_p)_{max}$ in the ice shelf was only 3811 m s^{-1} and the measured maximum density in the ice shelf, at Little America V, is only 0.915 Mg m^{-3}. The density difference that would result from using 3811 m s^{-1} and 0.912 Mg m^{-3} in equation (2) rather than 3850 m s^{-1} and 0.912 Mg m^{-3} is within 10% of 0.007 Mg m^{-3} for depths of 25 m and greater (less at lesser depths). That is not enough to affect significantly the agreement between measured and calculated densities shown in Figure 10.

Densities and elastic moduli computed at the RIGGS short-refraction sites are tabulated in Appendix B2 (microfiche). Average densities computed from the averaged v_p versus z data are included in Table 2. The elastic moduli are plotted in Figures 11 to 15 as functions of density, since density is a more fundamental property than depth.

Poisson's ratio (Figure 11) displays a large amount of scatter at the lower densities, which probably reflects both the complex texture of partially compacted, granular, near-surface firn and the

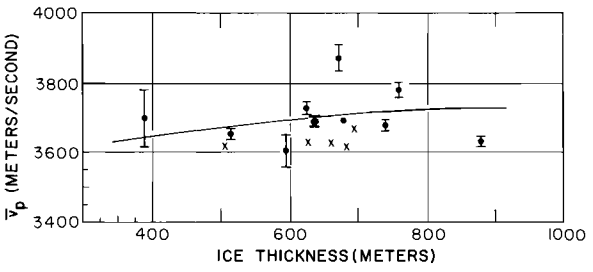

Fig. 9. Mean P wave velocity through the ice shelf, $\bar{v}_p$, versus ice thickness. Solid dots with error bars are RIGGS data; crosses denote values from Crary et al. [1962a]. The continuous line is a theoretical relationship based on measured and inferred v_p in the shelf. The large solid circle with error bars is the average from the RIGGS stations.

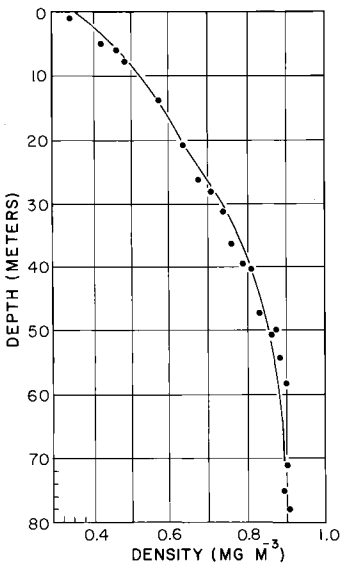

Fig. 10. Density versus depth at station J9DS, as measured on ice cores (points) and computed from v_p by equation (2) (solid line).

TABLE 6. $\bar{v}_p$ Determined From Oblique Reflections

Station	Shot No.	Ice Thickness, m	n	Minimum Distance, m	Maximum Distance, m	Slope of Ice-Water Interface, deg	Slope Correction, m s^{-1}	Corrected $\bar{v}_p$, m s^{-1}
E8	1	830	22	41	804	+1.4	+35	3638 ± 12
F9	2	640	24	10	803			3693 ± 7
H11S	3, 4, 5	600	24	10	947	+0.4	+11	3733 ± 18
I7	3	510	10	459	798			3653 ± 15
K3	4	760	8	363	1015			3781 ± 22
L5	4	730	13	706	1451			3680 ± 16
M2	2	670	9	774	1113			3869 ± 39
N6	3	580	7	334	1048			3599 ± 51
Q5-1	2	400	11	31	339	+1.1	+18	3746 ±130
Q5-2	2	400	6	62	374	+1.3	+18	3669 ±101
Mean								3688 ± 15

There are n t^2-x^2 points on each profile. The slope of the ice-water interface was determined by radar at stations E8, H11S, and Q5. The listed value of $\bar{v}_p$ for those stations includes the slope correction. The other values of $\bar{v}_p$ are uncorrected. Profiles 1 and 2 at station Q5 were laid out nearly normal to each other.

difficulty of measuring seismic velocity accurately within a few meters of the surface. A summary of Poisson's ratio for dry snow by Mellor [1964] shows similar scatter. The remaining elastic moduli are reasonably regular functions of density. On the graph of Young's modulus (Figure 12) and, to a lesser extent, on the others, there is a clear suggestion of an increase at $\rho \approx 0.55$ Mg m^{-3} in the rate of change of modulus with density that probably reflects a change in densification mechanism (see next section). According to a review paper by Roethlisberger [1972], the most accurate values of the elastic moduli of idealized, nonporous, isotropic, polycrystalline ice are those computed by Brockamp and Querfurth [1964] and by Bennett [1968] from experimental data on elastic wave velocities in single ice crystals. Values so computed (plotted in Figures 11 to 15) are consistent with the trends of the data obtained from our short-refraction profiles.

Densification Horizons Derived from Seismic Velocity Gradients

Exponential functions of the form

$$dv_p/dz = (dv_p/dz)_o e^{-\gamma z} \qquad (3)$$

where $(dv_p/dz)_o$ and γ are constants, have been used successfully to approximate seg-

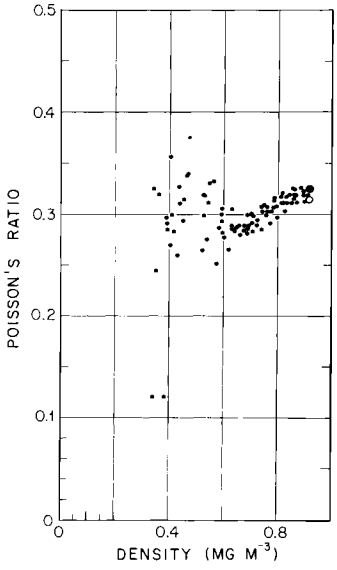

Fig. 11. Poisson's ratio versus density. RIGGS measurements are denoted by dots. Values of Poisson's ratio for solid ice from Brockamp and Querfurth [1964] and Bennett [1968] are denoted by an open circle and a solid circle, respectively.

ments of curves of the vertical gradient of v_p on the ice sheets of Greenland [Brockamp and Pistor, 1967] and Antarctica [Kohnen and Bentley, 1973; Robertson and Bentley, 1975]. Kohnen and Bentley [1973] correlated the depths at which the constants change at old and new Byrd stations with significant changes in the densification process of the firn. Robertson and Bentley [1975] analyzed 50 Antarctic profiles and found that 43 could be fit satisfactorily in sections by equation (3). Results from RIGGS short-refraction data are tabulated and plotted for individual stations in Appendix B3 (microfiche). Mean values and standard deviations of the velocity gradients are plotted in Figure 16.

Kohnen and Bentley [1973] and Robertson and Bentley [1975] identified one change in slope (called "B" by Robertson and Bentley [1975]) that appears to correlate with the "critical depth" of Anderson and Benson [1963]. Anderson and Benson [1963] explained the "critical depth" as the limit of "close random packing" below which grain packing is no longer an effective densification mechanism. However, Gow [1968] found that intergrain bonding is too well developed even at shallow depths to permit simple mechanical rearrangement of grains. Alley [1987a] has presented a theory that quantitatively explains densification at low densities by viscous grain boundary sliding; boundary "B" then corresponds to the depth below which power law creep dominates over grain boundary sliding.

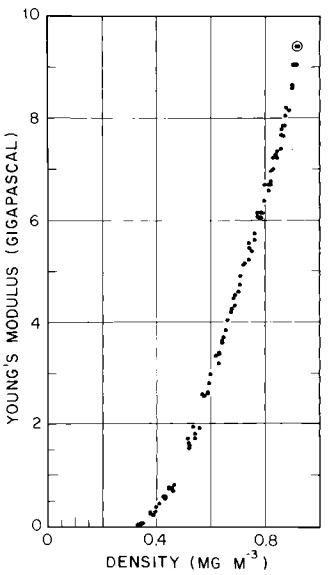

Fig. 12. Young's modulus versus density. RIGGS measurements are denoted by dots. The value for solid ice from both Brockamp and Querfurth [1964] and Bennett [1968] is denoted by concentric open and solid circles.

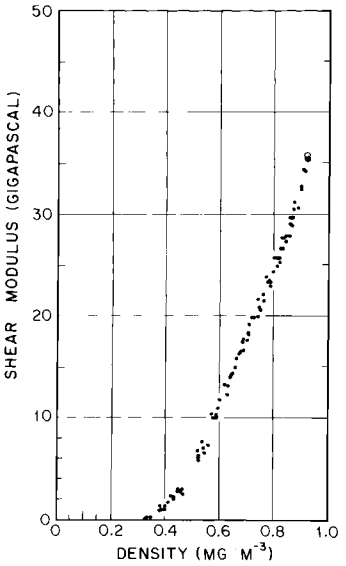

Fig. 13. Shear modulus versus density. RIGGS measurements are denoted by dots. Values for solid ice from Brockamp and Querfurth [1964] and Bennett [1968] are denoted by an open circle and a solid circle, respectively.

Another slope change ("D") correlates with the depth at which the firn becomes impermeable, by definition the firn-ice boundary. Robertson and Bentley [1975] identified a third break ("C") between B and D at stations where the mean annual accumulation is relatively high and suggested several possible explanations.

Depths to B, C, and D at RIGGS short-refraction stations are listed in Table 7. Mean depths to the horizons are 11 ± 2 m, 25 ± 10 m, and 46 ± 8 m, respectively. The first two values agree reasonably well with values of 9 ± 2 m and 28 ± 4 m for B and C calculated for the West Antarctic stations by Robertson and Bentley [1975].

Though it appears on three individual profiles (two at station BC and one at station H11S), C does not show up in the trend of the mean values of the RIGGS velocity gradients (Figure 16). This is expected from the previous finding that C tends to appear only where mean annual snow accumulation is relatively high. The annual accumulation generally is less than 100 mm of water in the grid western portion of the Ross Ice Shelf except near the ice front or the Transantarctic Mountains [Clausen et al., 1979]. The parameters of the least squares lines through the RIGGS mean values are $(dv_p/dz)_o$ = 283 ± 17 s^{-1}, γ = 110 ± 9 km^{-1} for the segment A-B; $(dv_p/dz)_o$ = 97 ± 4 s^{-1},

TABLE 7. Depths to Breaks in Plots of ln dv_p/dx Versus z From Short-Refraction Profiles

Station	B, m	C, m	D, m	$\dot{b}_o$, mm yr^{-1}	T, °C
BC-A	9	20	39	81	-27.6
BC-B	10	18	47	81	-27.6
H7	13		35	74	-27.8
H11S	11	36	55	118 (from H11)	-24.5*
I10S	12			62 (from I10)	-24.9*
J7S			44	75 (from J6)	-28.5 (from J6)
J9DS	14			90	-27.6 (from J9)
K11	8			100	-26.4†
P5	11			230	-24.5*
RI	13		54	121	-27.5
Mean	11 ± 2	25 ± 10	46 ± 8		

*Interpolated.

†Measured at 8-m depth instead of 10 m.

Blank spaces indicate that no distinct break was discernible (cf. Appendix B3). Accumulation rates ($\dot{b}_o$) are from Clausen et al. [1979] except at P15; ($\dot{b}_o$) there and all 10-m temperature values (T) are from Thomas et al. [1984]. Data from neighboring stations are indicated.

$\gamma = 34 \pm 1$ km^{-1} for the segment B-D; and $(dv_p/dx)_o = 1300 \pm 900$ s^{-1}, $\gamma = 90 \pm 9$ km^{-1} for the segment D-end. There is good agreement between the mean velocity gradient curve from this work and that for low accumulation rates from Robertson and Bentley [1975] (Figure 16).

Anisotropy

Naturally occurring single crystals of ice belong to the hexagonal crystallographic system; so their elastic properties are transversely isotropic with respect to the c axis (optic axis). When crystals are combined to form a polycrystalline mass such as an ice sheet, any nonrandom arrangement of the c axes produces directionally dependent seismic properties. Seismic velocity measurements on single ice crystals (see Roethlisberger, [1972], for a review) show that v_p can vary by as much as 5% as a function of the direction of wave propagation; the highest speed is parallel to the c axis. Variations are even greater for S waves: up to 18% for waves polarized in a plane containing the c axis. Evidence for seismic anisotropy in the Antarctic ice sheet has been presented by Bentley [1964, 1971] from refraction shooting; by Clough and Bentley [1970] from comparison between seismic and radar echo times; by Thiel and

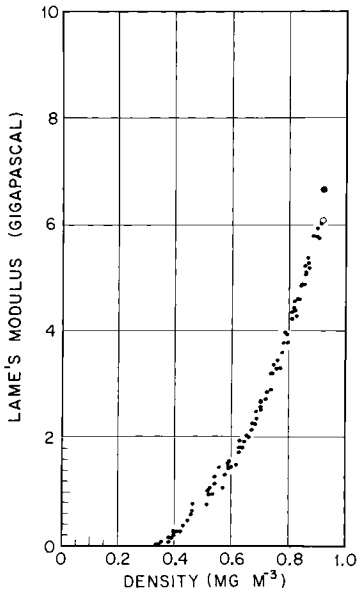

Fig. 14. Lamé's modulus versus density. RIGGS measurements are denoted by dots. Values for solid ice from Brockamp and Querfurth [1964] and Bennett [1968] are denoted by an open circle and a solid circle, respectively.

Ostenso [1961], Bentley [1972], and Bentley and Jezek [1981] from sonic logging in drill holes at Little America V, Byrd Station, and RIGGS station J9DS; and by Kohnen and Bentley [1977] and Kohnen and Gow [1979] from ultrasonic velocity measurements on ice cores from J9DS and Byrd Station, respectively. Core samples from the drill holes revealed a pronounced vertical (single-pole) orientation of c axes between the depths of 900 and 1800 m at Byrd Station [Gow, 1970a; Gow and Williamson, 1976] and various multipolar patterns of concentration at angles of 20° to 40° from the vertical, at depths between 65 m and the bottom of the ice shelf at Little America V [Gow, 1963, 1970b].

A different type of anisotropy was reported by Bennett [1968, 1972], who found from ultrasonic measurements on near-surface snow at Byrd Station that v_p is up to 1.5 times greater vertically than horizontally within a few meters of the surface. Some difference persists to a depth of about 30 m. Bennett [1968, 1972] attributed this effect to an unexplained "structural anisotropy." We believe it probably results from the textural anisotropy found by Alley [1987b] at another West Antarctic site: elongate grains preferentially bonded near their ends into vertical columns.

For seismic shooting on an anisotropic medium it is necessary to distinguish between

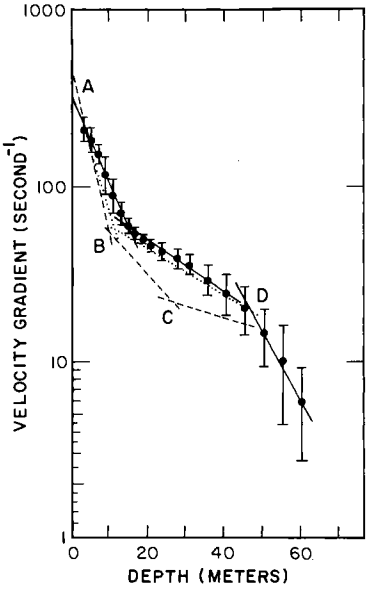

Fig. 16. Mean dv_p/dz versus depth for 10 short-refraction profiles from RIGGS I and II. Solid dots denote the RIGGS values; error bars denote the standard errors in the means. The dotted and dashed lines are mean curves from Robertson and Bentley [1975] for low (~100 ± 50 mm water per year) and high (~270 ± 100 mm water per year) surface accumulation rates, respectively.

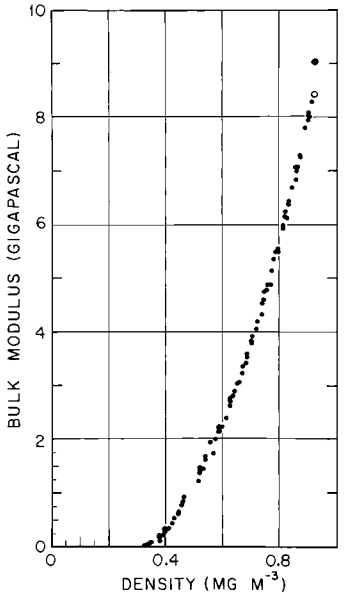

Fig. 15. Bulk modulus versus density. RIGGS measurements are denoted by dots. Values for solid ice from Brockamp and Querfurth [1964] and Bennett [1968] are denoted by an open circle and a solid circle, respectively.

v_{sh}, the speed of shear (SH) waves polarized horizontally, and v_{sv}, the speed of shear (SV) waves polarized in the plane of propagation. Evidence bearing on anisotropy in ice shelves from RIGGS I and II consists of (1) a comparison between v_{sv} and v_{sh} from short-refraction profiles at station RI and (2) a comparison between seismic and radar echo times.

Comparison between v_{sv} and v_{sh}. Two S wave short-refraction profiles were recorded along the same line at station RI. On the first, geophones were oriented transversely to the line, and the 4" x 4" stake was hit transversely to record the horizontally polarized SH waves. On the second, geophones were placed longitudinally, and the stake was hit along the line to record the SV waves, which are polarized in the plane of incidence. A schematic diagram is shown in Figure 17, a seismogram illustrating SV arrivals is reproduced in Figure 18, and the resulting velocity-depth curves are plotted in Figure 19.

The estimated error due to uncertainties in travel times is ±30 m s^{-1} at the surface for both v_{sv} and v_{sh}, diminishing to ±20 m s^{-1} at 20 m and to ±10 m s^{-1} at 50 m. This

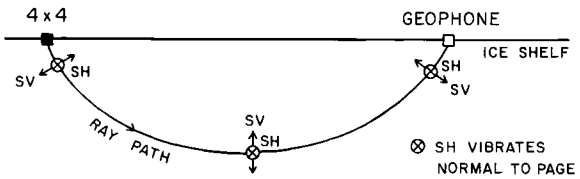

Fig. 17. Polarizations of SV and SH waves along a ray path in polar firn. SV waves are polarized as shown by arrows; SH waves are polarized normal to the page.

does not take into account errors in depth that arise from applying equation (1) to an anisotropic medium [Bennett, 1968, 1972]. Significant differences between v_{sv} and v_{sh} occur in the top few meters of snow, where v_{sv} is higher by up to 40%, and between 10 and 25 m, where it is less by as much as 8%. There is also a suggestion that v_{sv} is significantly less than v_{sh} below 55 m, but the data do not extend deep enough to be sure. The anisotropy very near the surface is consistent with Bennett's [1968, 1972] observations and Alley's [1987b] description of the firn as being bonded more strongly vertically than horizontally (see the discussion by Kirchner and Bentley [this volume]). The indicated higher v_{sh} at intermediate depths is unexpected and could result from errors associated with equation (1). If the difference is real, possible explanations include (1) some kind of anisotropy in the structure of the firn owing to high longitudinal strain rates in the ice shelf and (2) an abundance of horizontal ice lenses between 10 and 25 m.

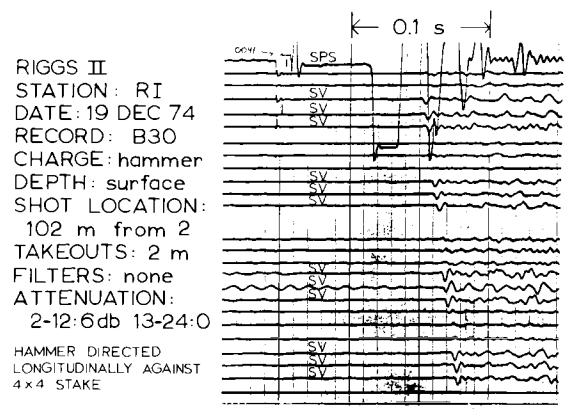

Fig. 18. Seismogram from station RI illustrating SV waves. "SPS" stands for shot-point seismometer, i.e., a geophone placed against the 4" x 4" stake.

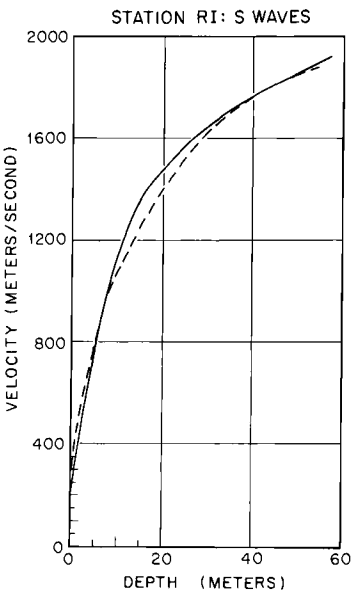

Fig. 19. S wave velocities versus depth at station RI. Solid line is v_{sh}; dashed line is v_{sv}.

Seismic versus radar echo times. Although seismic anisotropy can reach 5%, anisotropy in the electromagnetic wave speed at radar sounding frequencies is less than 0.5% [Johari and Jones, 1978]. Comparison of seismic and radar echo times from the same interface should, therefore, be a measure of anisotropy through variations in v_p. The wavelengths of electromagnetic and seismic waves in ice are not greatly different: about 5 m at 35 MHz and 20 m at 200 Hz, respectively. To make the comparison, we have plotted $\Delta h_i \equiv h_i(\text{radar}) - h_i(\text{seismic})$ versus ice thickness h_i computed from spot radar soundings at the various stations (Figure 20; see Table 8 for actual values). The estimated error in measuring either the seismic or the radar travel time is ±10 m; so the estimated error in a single measurement of Δh_i is ±14 m.

It is clear from Figure 20 that there is no significant correlation between Δh_i and h_i (the correlation coefficient is only 0.2). The mean value of Δh_i is -2.3 m with standard errors of 15.0 m for an individual value and 2.2 m for the mean. The individual standard error is essentially the same as estimated a priori on the basis of errors in time measurement, and the mean is not significantly different from zero. We conclude, therefore, that there is no indication of an overall systematic difference, such as could arise from anisotropy or different effective

reflection surfaces for seismic and electromagnetic waves.

At one station, I10S, Δh_i is particularly large and negative. This might be a statistical fluctuation, but it may be significant that I10S is on Crary Ice Rise. Where ice rests directly on soft, wet sediments, the acoustic impedance contrast at the boundary may be very low (as discussed further below). Thus it is possible that the seismic reflection recorded at I10S comes not from the base of the ice, but from a deeper horizon in the sedimentary column. Assuming $v_p = 1700$ m s^{-1} in the uppermost sediments leads to a seismic reflector depth of 20 m below the base of the ice. It is interesting to note that on the largest ice rise in the Ross Ice Shelf, Roosevelt Island, Δh is also large (60 m) but positive rather than negative, a circumstance that is much more difficult to explain. Only a special kind of sediment just below the ice would yield a dielectric contrast low enough to allow an explanation by penetration of the electromagnetic wave combined with reflection of seismic wave [Jiracek, 1967; Jiracek and Bentley, 1971].

If we neglect station I10S, there is, surprisingly, a difference between the mean values of Δh_i from the two seasons that is statistically significant at the 99% confidence level: 10.2 ± 4.0 m, or about 2% of the mean ice thickness. The individual season means are 4.2 ± 3.2 for RIGGS I and -6.0 ± 2.4 for RIGGS II; the latter also is significantly different from zero at the same level. Seismic and radar instrumentation was the same in both seasons, and timing was carefully checked; so there is no possibility of a 2% clock error in either kind of equipment. A possible physical explanation is that at many of the RIGGS II sites there has been a freezing on of a layer of sea ice of the order of 10 m thick. However, this does not accord well with the distribution of melting and freezing zones delineated by Neal [1979] from the analysis of radar echo amplitudes. Furthermore, no clear regional pattern is evident in the geographical distribution of Δh_i. Thus we have no firm explanation for the difference.

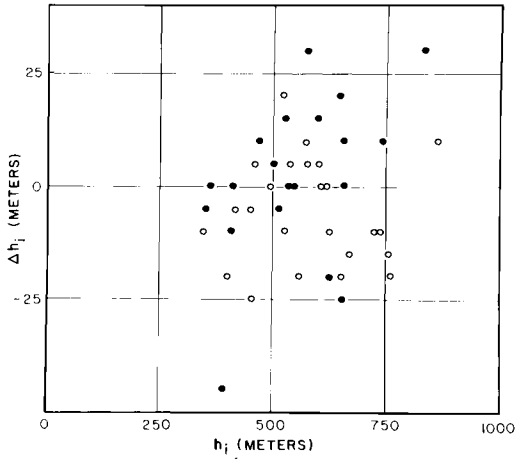

Fig. 20. Plot of $\Delta h_i = h_i$(radar) - h_i (seismic) versus h_i (radar). Solid circles are data from RIGGS I; open circles are from RIGGS II.

Ice Thickness and Sea Bottom Topography

Survey Results

The thickness of the ice shelf and the depth to the sea bottom beneath the shelf may be calculated from travel times of radar and seismic reflections when the electromagnetic and seismic wave speeds are known. Seismic wave speeds in the ice are derived from short-refraction profiling, maximum velocity calculations, and t^2 versus x^2 analyses as discussed in the preceding section. Radar reflection times in microseconds (t_r) were converted to ice thicknesses in meters (h_i) using the relation $h_i = 84.3t_r + 7.6$. The wave speed was taken from the accurate measurement by Robin [1975], and the additive constant was calculated from the excess thickness of the ice that is represented by the air in the firn [Shabtaie and Bentley, 1982] and the relationship between density and wave speed of Robin et al. [1969]. A constant value of 1.44 km s^{-1} is appropriate for the acoustic wave speed in seawater beneath the shelf [Crary et al., 1962a]. Radar sounding normally produces a clear, high-amplitude echo from the ice-water interface, but none deeper. The seismic technique, on the other hand, usually produces a recognizable ocean bottom echo, whereas the ice bottom echo often is lost in the noise of surface multiple and direct shear wave arrivals. The combination of the two methods thus is highly effective in determining both the ice thickness and the water depth.

Multiple seismic echoes were recorded at about 20% of the survey sites. A multiple is an arrival that has been reflected more than once off an interface (Figure 21); a particularly good example is shown in Figure 22. Multiples are useful in that various combinations of their arrival times often yield the arrival time of a fundamental reflection (for example, $I_2W_1 - I_1W_1 = I_1$) when the fundamental reflection itself is hidden in surface noise. I_1W_1 is virtually always present (if the ice is afloat) as the

TABLE 8. Ice Thicknesses (h_i), Water Layer Thicknesses (h_w), Depths to the Seafloor, and $\Delta h_i = h_i(\text{Radar}) - h_i(\text{Seismic})$

Station	h_i(Radar), m	h_i(Seismic), m	Δh_i, m	h_w, m	Depth to the Seafloor, m Below Sea Level
BC	480	NR		143	557
E5	783	NR		0	639
E6	733	NR		0	588
E7	834	NR		0	712
E8	859	828	31	189	940
F7	749	738	11	0	633
F9	665	643	22	159	737
G4	657	657	0	0	481
G5	556	NR		(0)	401
G6	606	577	33	0	477
G8	665	655	10	89	667
H5	631	653	-22	41	590
H6	657	NR		0	529
H7	505	499	6	21	456
H8	539	NR		30	496
H9	606	627	-21	72	597
H10	547	529	18	50	523
H11S	615	602	13	125	658
H12	412	411	1	461	803
I5	530	530	0	0	417
I6	547	545	2	85	558
I7	505	509	-4	152	587
I8	471	NR		105	510
I9	463	NR		150	548
I10S	345	389	-44	0	242
I11	488	NR		144	564
IJ9½	395	NR		211	548
J4	876	863	13	0	285
J6	539	533	6	21	487
J7S	480	470	10	41	454
J8	471	NR		159	564
J9	421	NR		236	596
J9DS	412	NR		244	596
J10	320	NR		296	566
JK9½	395	403	-8	326	664
K3	741	755	-14	66	712
K4	741	NR		158	804
K5	480	NR		64	477
K7	588	NR		53	473
K9	421	NR		199	559
K10	362	359	3	414	722
K11	345	348	-3	309	601
L4	716	725	-9	73	697
L5	724	734	-10	42	673
L6	682	NR		51	644
L7	539	NR		13	479
L9	370	NR		170	485
L11	370	NR		282	597
M2	657	672	-15	58	629
M3	741	762	-21	98	744

TABLE 8. (continued)

Station	h_i(Radar), m	h_i(Seismic), m	Δh_i, m	h_w, m	Depth to the Seafloor, m Below Sea Level
M5	623	NR		96	637
M6	606	606	0	109	634
M6½	615	625	-10	71	604
M7	581	NR		135	638
M8	480	NR		202	615
M9	446	449	-3	78	461
M10	370	NR		64	379
N4	631	651	-20	209	757
N5	539	558	-19	222	688
N6	581	576	5	218	721
N7	606	601	5	176	701
N8	522	NR		215	665
N9	370	NR		197	512
N10	387	NR		54	384
O4	513	525	-12	216	658
O5	581	571	10	211	714
O6	539	522	17	317	783
O7	320	NR		133	403
O8	463	462	1	186	584
O9	412	413	-1	190	542
OP4	497	495	2	0	113
P5	429	453	-24	198	565
P6	446	449	-3	304	687
Q5	379	398	-19	258	580
Q6	336	344	-8	396	680
RI	615	616	-1	152	685

NR, no I_1 reflection or multiples yielding I_1. Parentheses mean value is assumed.

strongest echo on the record. I_2W_1 can be distinguished from I_1W_2 by reasonableness of indicated ice and water layer thicknesses. I_1 arrives too early to be anything else. Usually the ice thickness is known independently anyway from radar echoes. Only at one or two stations in the entire RIGGS program was there any ambiguity in the interpretation of the multiple echoes.

Values of ice thickness, water thickness, and ocean bottom elevation are listed in Table 8. A more complete tabulation of survey data is in Appendix C (microfiche), including actual radar and seismic travel times, seismogram numbers, shot-geophone distances, methods of computation, use of multiples in calculation, etc. Ice thicknesses are estimated to be accurate to ±15 m, the standard error in the comparison of radar and seismic echo times. The accuracy of water layer thicknesses is estimated at ±5 m for the seismic multiple method of computation and ±10 m where ice thickness is determined only by radar (these errors are smaller than errors in ice thickness because of the low sound velocity in water). Elevation of the seafloor at floating stations was determined from the ice and water thicknesses by assuming hydrostatic equilibrium of the floating ice to calculate its surface elevation. At grounded stations, bed elevations were computed from ice thicknesses and barometric ties to the base camps. The data on water layer thickness and ocean bottom elevation have been included in the maps presented in the accompanying paper by Albert and Bentley [this volume], and previously in the work of Greischar and Bentley [1980] and Robertson et al. [1982]. The ice thickness values contributed to the ice thickness map published by Bentley et al. [1979], although that map was based primarily on airborne radar sounding.

Reflections recorded at stations E5, E6,

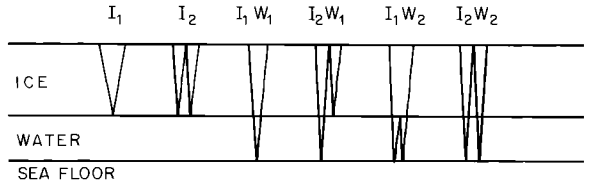

Fig. 21. Ray paths for multiple seismic reflections.

E7, G6, and H6 have been reinterpreted recently in light of the demonstration that the ice cannot be afloat there [Bentley et al., 1987; Shabtaie and Bentley, 1987]. The values in Table 8 and Appendix C (microfiche) reflect that reinterpretation and thus differ from the values given by Robertson [1975].

Sea Bottom Slopes

The local slope of the seafloor at a station can be computed if I_1W_1 reflections are recorded along perpendicular profiles ("L spreads"). Determinations of the local dip and strike of the seafloor have been made at nine sites (Table 9). Dips are all 1° or less.

L spread determinations are important first because bottom slope could be a significant source of error in the calculation of sea bottom elevation by the reflection technique. But for a bottom slope of only 1° (assuming also a flat ice-water interface and a 200-m-thick water layer) and an incident angle of 20° at the water-sediment boundary

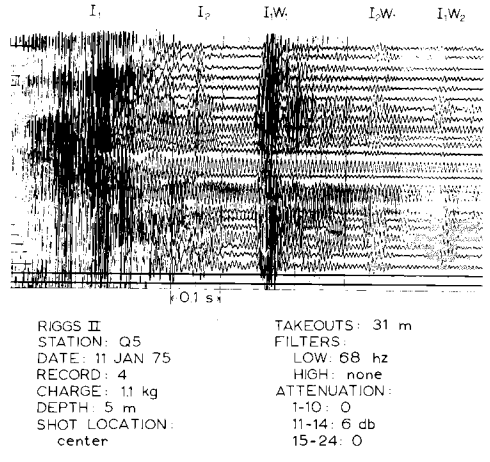

Fig. 22. Seismogram from station Q5 illustrating multiple seismic reflections. I_1 is obscured by direct arrivals through the ice.

(an extreme value), reflection times are changed by no more than 2 ms, even for a spread along the line of maximum dip. This difference corresponds to only a few meters in water depth, which is a negligible uncertainty.

Local slopes also provide some information on bottom irregularity through comparison with regional values. The directions of regional slope for the nine L spread stations have been picked from the map of submarine topography [Albert and Bentley, this volume] and are listed in Table 9. (Slope magnitudes are of the order of a few tenths of a degree; more precise estimates on the basis of the map are not justified.) Six of the nine local strikes are within 30° of the regional strikes. Regional and local dips are on the same side of strike at eight stations. It appears that short-wavelength topography (of the order of a few kilometers) superimposed on long-wavelength topography (tens of kilometers) is uncommon.

Finally, L spreads are useful in estimating the magnitudes of the topographic corrections that should be applied to values of gravity measured on the ice shelf. Owing to the small slopes, the topographic corrections to RIGGS gravity data are minimal.

Subbottom Characteristics

Information on the character of the sediments and bedrock beneath the Ross Ice Shelf was obtained by three seismic methods during RIGGS I and II: (1) determination of interval velocities in the sediments, (2) calculation of sea bottom reflection coefficients and acoustic impedances, and (3) seismic refraction shooting.

Interval Velocity

If seismic reflections are recorded from a sequence of flat, parallel layers, the "interval velocity" in the nth layer, v_n, is given by the equation [e.g., Dix, 1955]

$$v_n^2 = (\bar{v}_n^2 t_n - \bar{v}_{n-1}^2 t_{n-1})/(t_n - t_{n-1}) \qquad (4)$$

where $\bar{v}_j$ and t_j are the average velocity and the travel time, respectively, between the surface and the bottom of the jth layer. Equation (4) applies only for horizontal layering and only when t_n and t_{n-1} are measured along a ray for which the shot-geophone separation is small enough that sines and tangents of angles of incidence are approximately equal. Since these conditions were satisfied at seismic stations on the Ross Ice Shelf where good I_1W_1 reflections are recorded, equation (4) could be used to calculate the velocity in a sediment layer

TABLE 9. Local Slope of the Seafloor Determined by L Spread Reflection Shooting, Compared With Regional Values

Station	Local Values		Regional Values	
	Strike, deg	Dip	Strike, deg	Dip
H12	225	0.7°N	300	N
IJ9½	325	1.0°S	300	S
JK9½	310	0.3°N	315	none
N4	340	0.7°W	005	W
N5	300	0.4°SW	330	SW
O4	300	0.1°SW	300	N
P5	275	0.8°N	325	N
Q5	200	0.2°E	335	E
RI	270	0.7°S	285	S

Strikes and dips are given as grid azimuths.

below the seafloor if a good reflection from the base of the layer was received.

Good subbottom reflections were recorded at four stations: F9, I11, K11, and M9. (An example is shown in Figure 23.) Travel times, average velocities (determined by the t^2-x^2 method), and interval velocities (v_{sed}, calculated from equation (4)) at the four sites are presented in Table 10. The errors in v_{sed} were calculated from the errors in picking travel times and determining average velocities and do not include the possibility of violation of the assumptions in equation (4).

At stations I11 and M9, v_{sed} (2.5 and 2.6 km s^{-1}, respectively) is consistent with the sediment velocity (2.4 km s^{-1}) computed by Crary [1961] from seismic refraction shooting on sea ice near Little America V Station. Using reflection data, Crary [1961] determined in addition that v_{sed} increased from about 2.1 km s^{-1} at the seafloor to 2.9 km s^{-1} at a depth of 900 m below the seafloor. Similar results have been found from extensive sonobuoy measurements in the Ross Sea [Houtz and Davey 1973; Davey et al., 1983; Cooper et al., 1987]. Since the velocities at stations I11 and M9 are averages over only the upper 50 m of sediment, it appears that either v_{sed} is slightly higher at these sites than at the sites in the sea north of the ice shelf or there is a slight dip to the layers. The 3.2 km s^{-1} velocity at station K11 is substantially higher than that determined at I11 and M9; in fact, it seems unrealistically high for seafloor sediment, so it probably indicates a dipping subbottom reflector. The velocity calculated at station F9 (1.2 km s^{-1}), on the other hand, is too low to be real, so it is probably also distorted by dip.

Many sampling studies have shown that the sediments on the floor of the Ross Sea consist of poorly sorted clastic deposits of glacial origin [Phillippi, 1912; Stetson and Upson, 1937; Hough, 1950; Thomas, 1959, 1960; Hayes and Frakes, 1975; Barrett and McKelvey, 1981]. Based on the earlier of these analyses and, in particular, on a sediment core near Little America V [Thomas, 1960], Crary correlates his 2.4 km s^{-1} layer with a mixture of coarse and fine glacial till. It is likely that the 2.5 and 2.6 km s^{-1} layers at stations I11 and M9 also are glacial till.

The sediment layer sensed by the subbottom reflections undoubtedly is only a small part

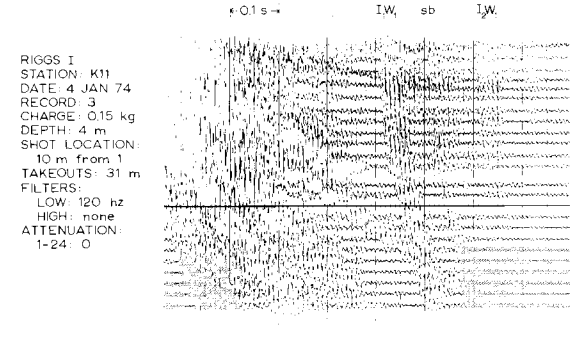

Fig. 23. Seismogram from station K11 illustrating a subbottom reflection ("sb").

TABLE 10. Interval Velocities and Layer Thicknesses, Uppermost Sea Bottom Sediment Layer

Station	Velocity, km s^{-1}	Thickness, m
G9	1.2 ± 0.2	110
I11	2.5 ± 0.2	45
K11	3.2 ± 0.1	156
M9	2.6 ± 0.4	54

of the total sedimentary column at the four RIGGS stations. Long-refraction profiling (see below) in the RIGGS area produces estimates in the range of 500-2000 m for the total thickness of the sedimentary section. Seismic profiler sections of the Ross Sea shelf likewise show that the sedimentary column generally is at least a kilometer thick (summarized by Davey, [1987]). The reflector at 50- to 150-m depth within the sedimentary section beneath the Ross Ice Shelf (Table 10) may correlate with a change in lithology or with an erosional interface. In the Ross Sea a widespread reflector within a few tens of meters of the seafloor (the "Ross Sea unconformity") has been found on profiler records [Houtz and Meijer, 1970; Houtz and Davey, 1973; Karl et al., 1987]. The unconformity was sampled at depths of 20, 20, and 30 m in three of the four holes drilled during Leg 28 of the Deep Sea Drilling Project and determined to be a glacial erosion surface [Hayes and Davey, 1975]. The seismic reflector at the RIGGS stations may be a continuation of the Ross Sea unconformity beneath the ice shelf. Depths to the interface are of the right order, and the ice shelf certainly would have been grounded in the RIGGS area if it were grounded farther to the north.

Sea Bottom Reflection Coefficients and Acoustic Impedances

Robin [1958] has shown that at vertical incidence, the energies per unit area of the I_1 and I_1W_1 reflections at the ice shelf surface are equal to

$$E(I_1) = \frac{E_o r_w^2}{4h_i^2} e^{-2\alpha h_i} \quad (5)$$

and

$$E(I_1W_1) = \frac{E_o (1 - r_w^2)^2 r_b^2}{4[h_i + h_w(v_w/v_p)]^2} e^{-2\alpha h_i} \quad (6)$$

where $E(I_1)$ is the energy of the I_1 reflection, $E(I_1W_1)$ is the energy of the I_1W_1 reflection, E_o is the outgoing energy per unit solid angle, r_w is the (amplitude) reflection coefficient at the ice-water boundary, r_b is the reflection coefficient at the water-sediment boundary, v_w is the sound velocity in seawater, and α is the energy attenuation coefficient in ice (the attenuation in the water is assumed to be negligible). A convenient way to determine r_b from the observed amplitudes of I_1 and I_1W_1 reflections is to take the ratio of equation (5) to equation (6); E_o and α are thus eliminated. The coefficient r_w may be calculated directly from the known velocities and densities of ice and seawater. Once r_b is determined, the acoustic impedance, z_b, of the sediment layer is easily calculated, since

$$z_b = \rho_w v_w \left(\frac{1 + r_b}{1 - r_b} \right) \quad (7)$$

where ρ_w is the density of seawater and $z_b = \rho_{sed} v_{sed}$, ρ_{sed} being the density of the uppermost sediments. Average values of r_b and z_b for nine stations at which both I_1 and I_1W_1 reflections at near-vertical incidence were recorded are listed in Table 11. The data that were used to determine the averages are listed in Table C4 of Appendix C (microfiche).

The differences between the acoustic impedances at the nine sites (Table 11) may result from variations in the lithologies of the upper few meters of bottom sediment. The impedance differences are small, however, and very likely are caused by minor individualities in a single general type of bottom sediment. The average acoustic impedance at the nine sites is (2.8 ± 0.2) Gg m^{-2} s^{-1}, where ±0.2 is the standard error of the mean.

The acoustic impedance gives an inverse relationship between v_{sed} and ρ_{sed}, whereas empirical relations between density and velocity in marine sediments, such as those given by Nafe and Drake [1963] and Hamilton [1971, 1982], are direct. Because of that, the two types of relations can be used effectively together to determine ρ_{sed} and v_{sed} separately (Figure 24). The values obtained in this way are ρ_{sed} = (1.72 ± 0.11) Mg m^{-3} and v_{sed} = (1630 ± 60) m s^{-1}. This velocity is lower than velocities from the refraction measurements in the Ross Sea cited above, but it refers only to the uppermost few meters of the sedimentary column.

Long-Refraction Studies

Unreversed seismic refraction profiles designed to record acoustic wave arrivals from the bedrock beneath the ice shelf were shot at stations BC, I10S, J9DS, and RI. In this section we present the travel time curves and a discussion of the data analysis. The geological interpretation of the results has already been discussed by Robertson et al. [1982] and is not repeated here. (The seismic interpretations shown here are slightly different from those of Robertson et al. [1982], but they are not different enough

TABLE 11. Sea Bottom Reflection Coefficients (r_b) and Acoustic Impedances (z_b)

Station	n	r_b	z_b, Gg m^{-2} s^{-1}
F9	4	0.260 ± 0.013	2.53 ± 0.07
E8	5	0.219 ± 0.014	2.33 ± 0.07
H9S	2	0.442 ± 0.003	3.84 ± 0.03
H11S	2	0.321 ± 0.018	2.89 ± 0.11
L5	2	0.236 ± 0.016	2.41 ± 0.09
N4	6	0.268 ± 0.022	2.59 ± 0.13
N5	3	0.215 ± 0.036	2.32 ± 0.17
P5	2	0.369 ± 0.019	3.23 ± 0.14
Q5	2	0.326 ± 0.004	2.92 ± 0.02
Overall mean		0.295 ± 0.031	2.78 ± 0.20

The numbers listed are the station means, taken from the data in Table D4. Here n is the number of individual measurements of r_b and z_b at each station. The overall means are unweighted, since the values of n are too small to give variances at the individual stations that are meaningful for weighting.

to invalidate their geological interpretation.)

General information about the profiles is presented in Table 12. Distances were either chained (station BC) or measured by Telluro-meter (stations I10S, J9DS, and RI). Use of the refraction technique on the ice shelf is complicated by the appreciable thickness of low-velocity seawater and sediments underneath high-velocity ice. Refracted energy from below the ice is not returned to the surface as a series of first arrivals unless large shot-spread separations are employed, and large distances in turn require large charge sizes.

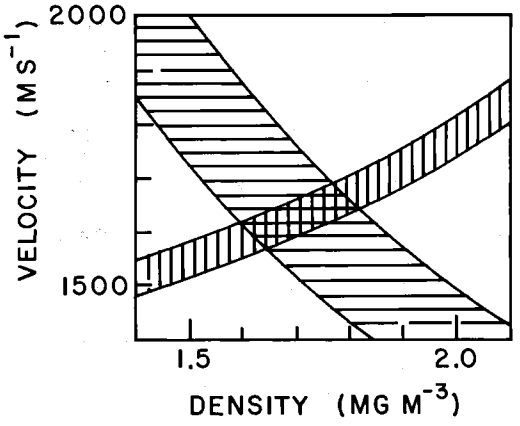

Fig. 24. Velocity versus density in sediments beneath the ice shelf. The zone with horizontal ruling corresponds to z_b = 2.78 ± 0.20 Gg m^{-2} s^{-1}. The zone with vertical ruling is from Nafe and Drake [1963] and Hamilton [1971, 1982].

On all long-refraction profiles there is evidence that a substantial layer of sediments overlies basement on the ocean floor. However, since the wave velocity in the sediment is almost surely less than that in ice, there is no way of measuring it by seismic refraction shooting on the ice shelf. We must assume a velocity; we choose the nearest actual velocity measurement, that by Crary [1961] on the sea ice near Little America V: 2.4 km s^{-1}. (As was pointed out above, our measurements of interval velocity refer only to the uppermost part of the sedimentary column.) To provide an indication of the effect of varying that velocity, we have routinely made calculations for v_{sed} = 2.4 ± 0.4 km s^{-1} and cited corresponding error bounds on affected thicknesses and depths.

Station BC. The long-refraction shot at BC did not yield a recorded arrival from bedrock (P_g). There are two possible explanations. The first is that the charge size was too small to generate sufficient energy even if the distance was great enough to have recorded P_g as a first arrival. The second is that although the charge was large enough, the distance was too short for P_g to be the first arrival.

One can make a rough calculation to try to determine which of the two explanations is

TABLE 12. Charge Sizes, Shot Hole Depths, and Distances for Long-Refraction Shooting

Station	Record Number	Shot Hole Depth, m	Charge Size, kg	Distance, km
BC	38	7	91	20.0
I10S	32	9	132	14.5
	33	8	113	12.6
	34	8	91	10.8
J9DS	A15	100	181	21.0
	B9			24.1
RI	A18	15	458	28.0
	B59			26.0
	B60			24.0

more likely. The major factors governing the amount of energy reaching a receiver from a seismic shot are (1) charge size and hole depth, (2) energy loss due to geometrical spreading, (3) energy loss due to attenuation, and (4) energy loss due to reflection at boundaries. The effect of the first factor on the amount of energy generated by a seismic shot in polar firn is poorly known. However, shot 34 at station I10S (Table 12) was the same size charge at nearly the same depth as the BC shot, and a good P_g was recorded from it (Figure 25); so it is convenient to use it as a standard of comparison. Amplitude diminishment from geometrical spreading is approximately inversely proportional to the distance; so the relative value of that factor for BC (compared with I10S) is 0.54. Approximate values of the specific dissipation constant Q^{-1} for ice, seawater, marine sediment, and basement-type rocks are 1.4×10^{-3} [Bentley and Kohnen, 1976], 5×10^{-6} [Bradley and Fort, 1966], 6×10^{-3} [Clay and Medwin, 1977, p. 259], and $(5\text{-}20) \times 10^{-4}$ [Bradley and Fort, 1966], respectively; we will use the larger of the figures for basement-type rocks in our calculations. The amplitude attenuation coefficient a for P waves is given by $a = \pi f Q^{-1}/v_p$, where f is the frequency of the signal. From Figure 25 we see that $f \simeq 15$ Hz; for bedrock we take $v_p = 5.7$ km s^{-1} (from station I10S). Then $a = 0.017$, 1.6×10^{-4}, 0.12 and 0.017 km^{-1} for ice, water, sediments, and bedrock, respectively. Using these coefficients and known layer thicknesses and distances and assuming the maximum sediment thickness for BC that would allow P_g to be a first arrival at 20 km, we obtain a relative attenuation factor, compared with I10S, of 0.64. Transmission losses have been calculated from the standard equation (calculable from equation (7)) using $\rho_{sed} = 2$ Mg m^{-3} and $v_s = 1.2$ km s^{-1} in the sediments; that relative factor amounts to 0.32.

Combining losses, we calculate that the amplitude of a P_g arrival at BC would be about one tenth as large as that at station I10S. Both shots were recorded on the same system at the same gain and filter settings. At station I10S the signal-to-noise ratio (Figure 29, record 34, traces 1-13) is about 10; so at BC the expected signal-to-noise ratio is about 1. Because of the frequency difference between signal and noise, it seems likely that some indication of P_g would have been discernible had it been present. Thus we believe an insufficient shot distance is the more likely explanation for the absence of P_g at BC.

If the shot distance was indeed too small, a minimum thickness of low-velocity sediments, for $v_g = 5.7$ km s^{-1} and $v_{sed} = 2.4 \pm 0.4$ km s^{-1}, is 1.9 ± 0.4 km.

Station I10S. Station I10S is a grounded station on Crary Ice Rise particularly suited to long-refraction profiling owing to the absence of the water layer. For this profile the geophone spread was fixed and the shots were fired at different locations. For planar interfaces with constant dips across the profile, the apparent velocities across the spread from one shot, and from different shots at the same detector, provide a seismic reversal. In reality, however, the dip under the shots and that under the spread are likely to be different, so neither is well constrained.

The mean apparent velocity for P_g across the records (Figures 25 and 26) from the three shots approximately 2 km apart is 5.72 ± 0.03 km s^{-1}. The mean is corrected

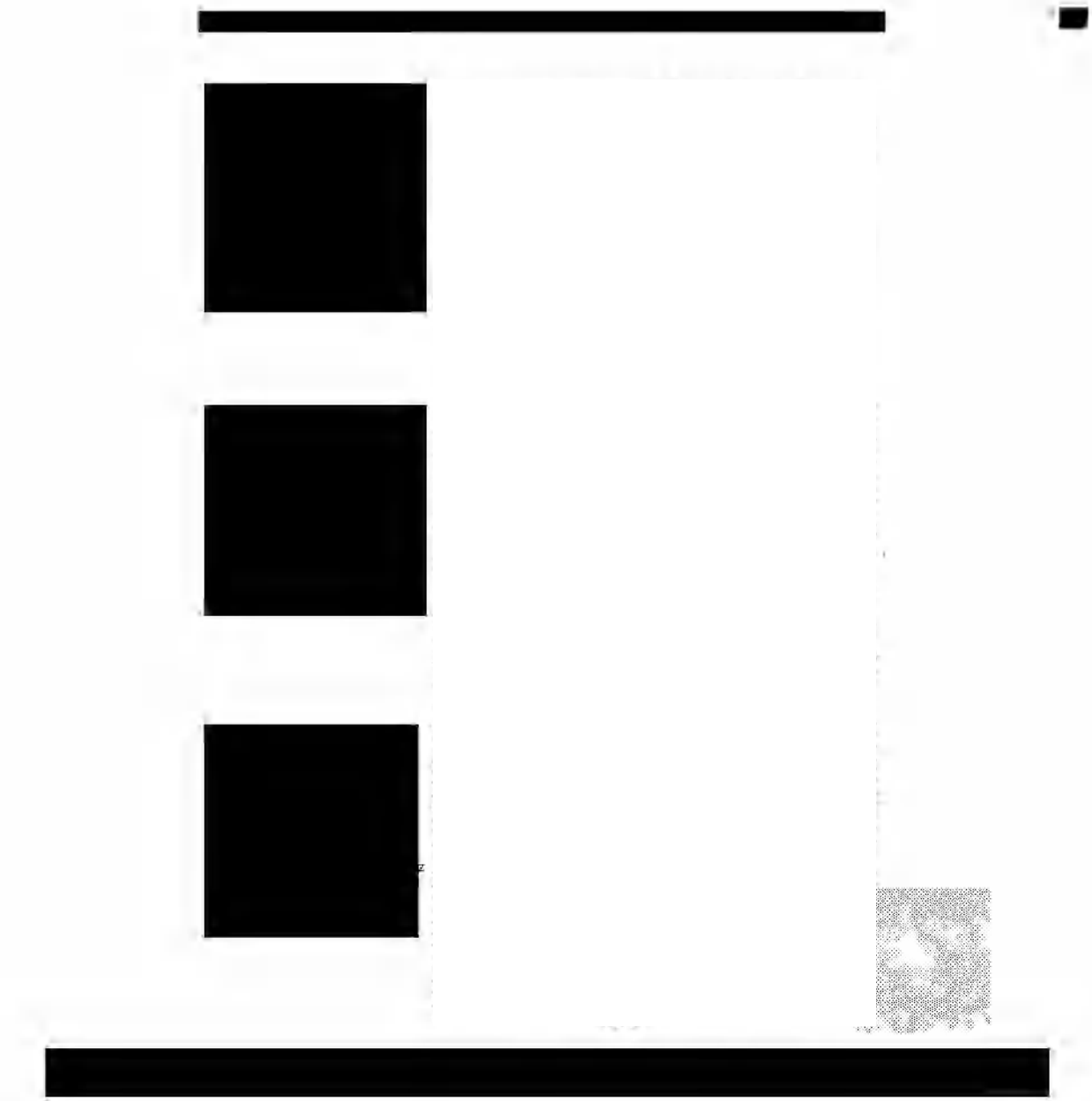

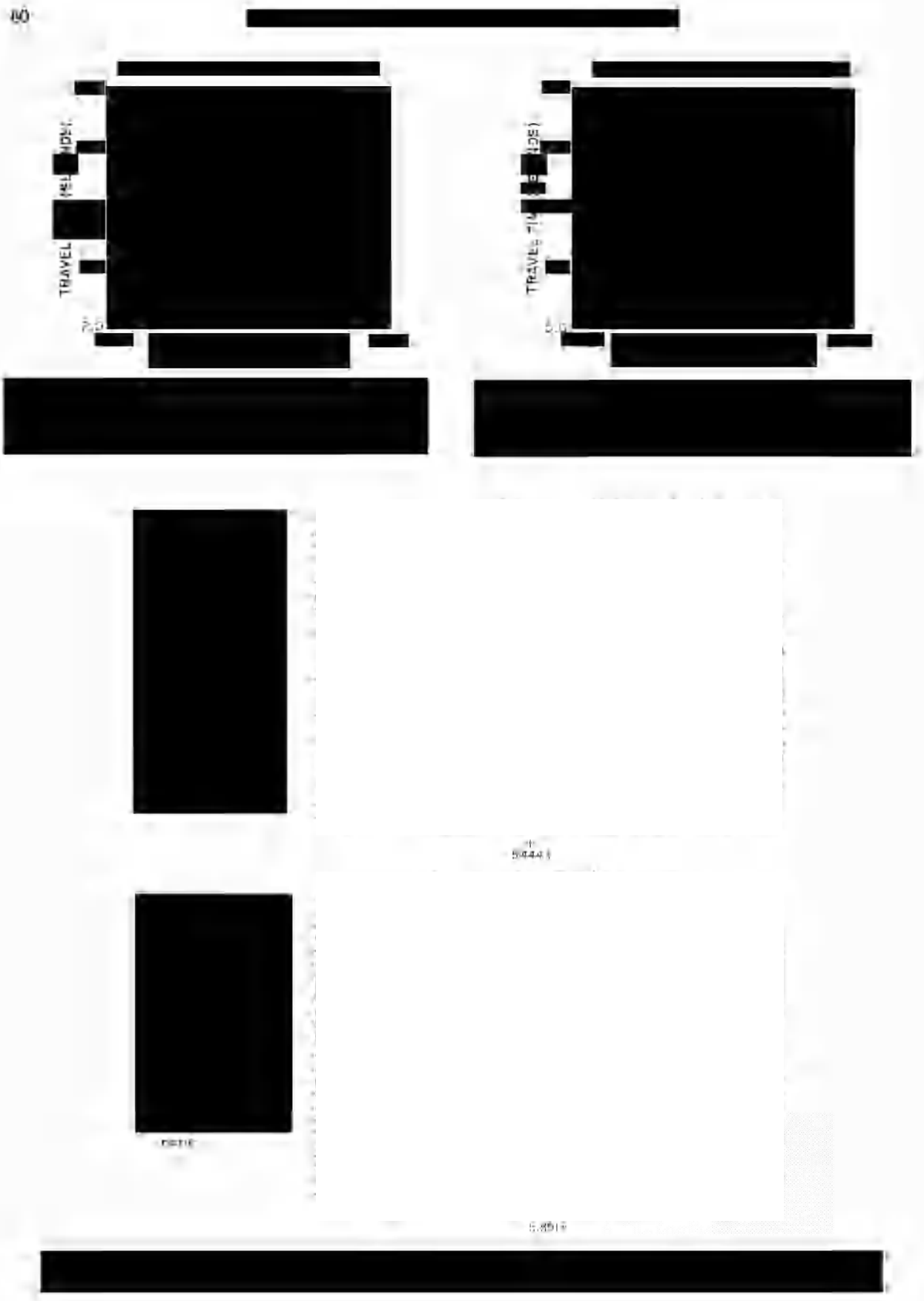

station I10S 75 km to the grid northeast, then the apparent velocities can be fit by the topography on the refractor shown in Figure 29. (A different wave velocity in the bedrock could be accommodated by a corresponding tilt to the bedrock surface in Figure 29 as a whole.) The full travel time at 24 km (5.98 s) then corresponds to an average sediment thickness of 1.7 ± 0.3 km.

Station RI. Although the first breaks are difficult to pick because the arrival amplitudes are small (Figure 30), there is a recognizable P_g wave group that can be correlated between records. The two peaks of that group are plotted in Figure 31, along with an estimated time for the first breaks. The apparent velocity v_g across the three records is 4.45 ± 0.02 km s^{-1}. However, from the minimum intercept time compatible with the known ice and water thicknesses it follows that v_g must actually be at least 4.8 km s^{-1}, corresponding to a minimum dip of 2°. But for v_g = 4.8 km s^{-1}, the overlying sediment layer would have to pinch out at one end of the profile (the sea bottom slope is 0.3°), which is unlikely. It is probable that the sedimentary layer is continuous, so v_g is greater than 4.8 km s^{-1}. How much greater it is not possible to determine. For lack of better evidence, we adopt the mean value found by M. P. Hochstein [Robertson et al., 1982] on Roosevelt Island: 5.5 km s^{-1}. That yields a mean dip of about 6° under the spreads. The total travel time to 28 km (6.25 s) constrains the sum of the sediment thicknesses beneath the shot and the 28-km spread to be 2.0 ± 0.4 km. If we assume that 1 km of sediment underlies the shot, then the topographic configuration beneath the spreads is as shown in Figure 32.

For ease of comparison, all four seismic sections (including the minimum-depth interpretation at station BC) are shown together in Figure 33.

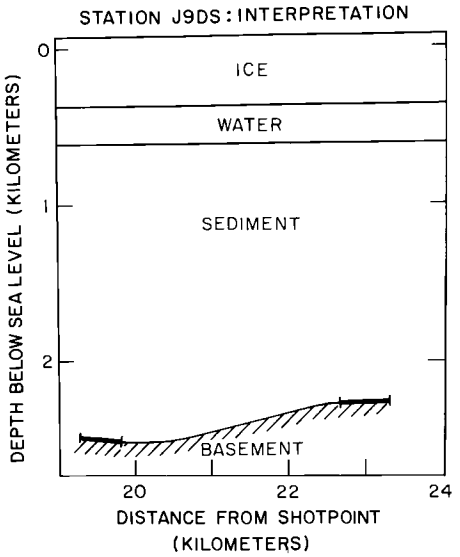

Fig. 29. Seismic interpretation at station J9DS.

Summary

Curves of seismic velocity versus depth in the firn, which have been computed from short-refraction travel time data at nine sites, possess the same smoothly varying curved shape, concave toward the depth axis, that has been found previously to be characteristic of the seismic velocity-depth function in ice sheets; v_p increases from about 500 m s^{-1} at the surface to 3800 m s^{-1} at depths of 70 or 80 m, and v_s ranges from about 300 m s^{-1} at the surface to about 1970 m s^{-1} at 60 m.

Recrystallization and densification of firn, which increase v_p and v_s, and increasing temperature with depth, which decrease both velocities, interact in the ice shelf to produce maximum velocities at a depth of about 100 m. Maximum v_p, as determined by three different methods, is 3811 ± 7 m s^{-1}, which is significantly lower than the average in grounded ice sheets (3850 m s^{-1}) at the same mean annual surface temperature. The reason for the difference has not yet been ascertained. At stations BC and RI, where the profiles were reversed, it appears that planes of constant velocity dip a few tenths of a degree.

The mean of 15 t^2-x^2 determinations of $\bar{v}_p$ in the ice shelf is 3688 ± 15 m s^{-1}. The scatter of the data is too large to verify the expected dependence of $\bar{v}_p$ on ice thickness.

Densities measured on a 100-m ice core obtained at station J9DS show good agreement with densities computed from the v_p versus depth curve at the same site from the equation of Kohnen [1972]. Kohnen's equation was therefore used to calculate densities at other geophysical stations lacking direct measurements; then ρ, v_p, and v_s were used to calculate Poisson's ratio, Young's modulus, the shear modulus, Lamé's modulus, and the bulk modulus as functions of density. The calculated values of the elastic moduli in solid ice are all consistent with values computed for idealized, nonporous, isotropic, polycrystalline ice from experimental data on acoustic velocities in single ice crystals.

Significant depths in the densification process of the firn may be located by approximating segments of dv_p/dx versus z

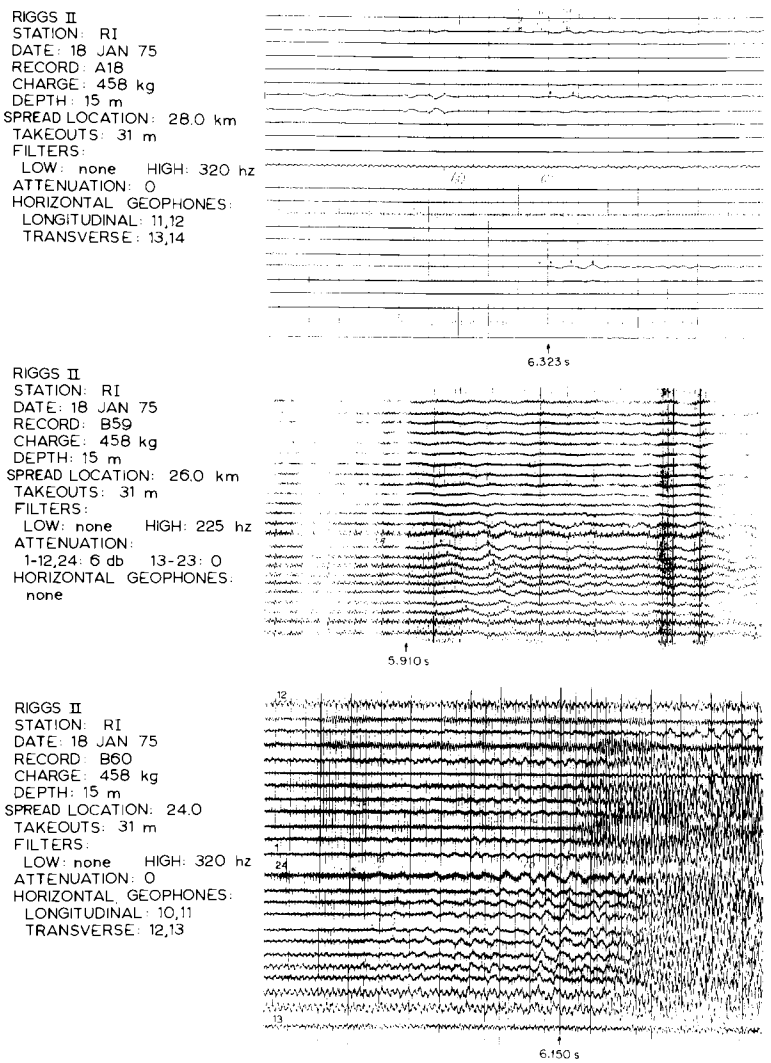

Fig. 30. Long-refraction seismograms from station RI. Note the unexpected numbering of traces corresponding to geophones 1-12 and 13-24 on record B60. Total travel times are marked at the bottom of each seismogram. The shot was grid southeast from the recording points.

with exponential functions. Mean depths to seismic horizons B (the limit of grain boundary sliding), C (glaciological significance unknown), and D (the firn-ice boundary) are 11 ± 2 m, 25 ± 10 m, and 46 ± 8 m, respectively. A curve of dv_z/dz versus z averaged over all stations does not show horizon C, a fact that is consistent with the low measured rates of snow accumulation on the ice shelf.

There is no overall mean difference between ice thicknesses calculated from radar echo times and those calculated from seismic reflections, although there is an unexplained suggestion that the mean difference for RIGGS I is 10 m or so greater than that for RIGGS II. Discrepancies between short-refraction SH and SV profiles at station RI are consistent with anisotropic snow structure in the top few meters of snow and with a zone of anisotropy, due perhaps to high longitudinal strain rates or an abundance of horizontal ice lenses, between 10 and 25 m.

The slopes of the seafloor at the nine stations where they were determined are all no greater than 1°. It appears that bottom slope is a negligible source of error in the measurement of sea bottom elevation by

reflections shooting and in the determination of gravity anomalies.

Interval velocities in the layer of sediment at the seafloor match those expected for unconsolidated glacial marine till. The subbottom reflecting interface lies within the total sedimentary section at a depth of 50-150 m below the seafloor and may correlate with the glacial erosional surface identified on profiler records as widespread in the Ross Sea and sampled during Leg 28 of the Deep Sea Drilling Project. The mean acoustic impedance of the bottom sediment at nine stations is 2.8 ± 0.2 Gg m^{-2} s^{-1}. Together with a standard curve of velocity versus density in marine sediments, this yields ρ = 1.7 ± 0.1 Mg m^{-3} and v_{sed} = 1630 ± 120 m s^{-1}; these also are consistent with a layer of unconsolidated glacial marine material at the seafloor.

Long-refraction shooting was carried out at four sites, with results summarized in Figure 33. At station BC, wave arrivals from bedrock were not recorded. The velocity in seismic basement on Crary Ice Rise (station I10S) is 5.7 km s^{-1}. A layer of lower velocity lies between the bottom of the ice and the basement; if a velocity in the layer of 2.4 ± 0.4 km s^{-1} is assumed, its calculated thickness on Crary Ice Rise is 750 ± 100 m.

Apparent velocities in basement at station J9DS range from 5.0 to 6.8 km s^{-1}. The scatter probably is caused by topography along the refractor. Since J9DS is close to I10S, the true velocity in basement may be about 5.7 km s^{-1}; if so, the seismic interpretation is characterized by a layer of sediments 1.7 ± 0.3 km thick and a mean 4° slope on the basement surface.

At station RI, if we assume that the true velocity in seismic basement is about 5.5 km s^{-1}, as appears likely from work on nearby Roosevelt Island, the dip along the refractor is about 6°, and an average of 1.0 ± 0.4 km of sediment lies between the sea bottom and the refractor.

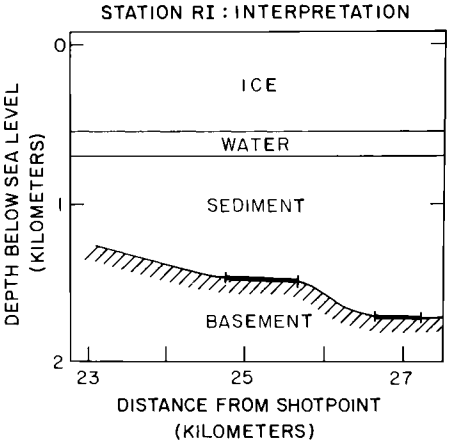

Fig. 32. Seismic interpretation at station RI.

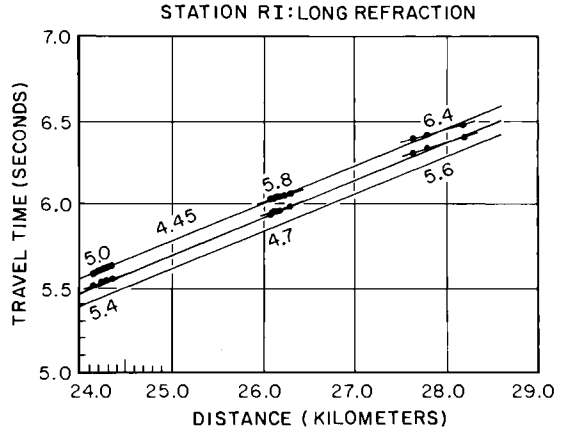

Fig. 31. Long-refraction travel time curve for station RI. The upper and lower sets of points correspond to the first two wave peaks in the refracted arrival. Numbers above and below the six sets of points and above the line connecting the upper three are apparent velocities. The lowest of the three parallel travel time lines approximately connects first arrival times.

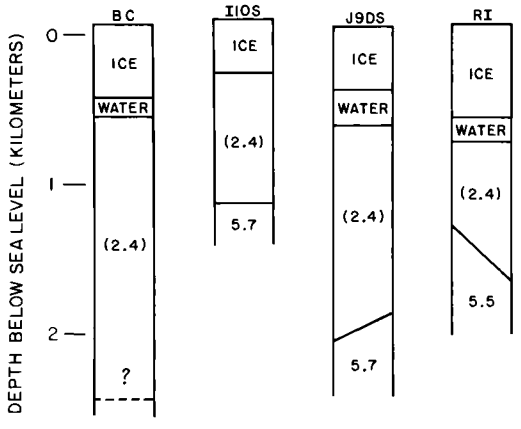

Fig. 33. Comparison of seismic interpretations at stations BC, I10S, J9DS, and RI. Values in parentheses denote assumed velocities.

Acknowledgments. During RIGGS I, the field party comprised C. R. Bentley (leader), S. Brandwein, J. W. Clough, T. Kolich, J. D. Robertson, B. K. Sternberg, and L. R. Whiting. For RIGGS II, Clough was the leader; Kolich, Robertson, and Whiting returned, and the other members were D. Borowski, K. C. Jezek, and J. F. Kirchner. The data on which this paper is based could never have been gathered without the tireless efforts of those field party members. We are especially grateful to J. W. Clough both for his valuable assistance in the field and his many helpful suggestions in the analysis of the data. R. H. Thomas and coworkers from the University of Nebraska assisted us by making electronic distance measurements for our seismic profiles. Logistic support was provided by the Ross Ice Shelf Project Management Office, Holmes and Narver, Inc., United States Naval Support Force, Antarctica, and Antarctic Development Squadron Six. We thank P. Dombrowski and S. H. Werther for drafting illustrations and A. N. Mares and J. V. Campbell for manuscript preparation. This work was supported by the National Science Foundation under grants DPP72-05802, DPP79-20736, and DPP-8119989. This is contribution 490 of the Geophysical and Polar Research Center, University of Wisconsin-Madison.

References

Albert, D. G., and C. R. Bentley, Seismic studies on the grid eastern half of the Ross Ice Shelf: RIGGS III and RIGGS IV, in The Ross Ice Shelf: Glaciology and Geophysics, Antarct. Res. Ser., vol. 42, edited by C. R. Bentley and D. E. Hayes, AGU, Washington, D. C., this volume.

Alley, R. B., Firn densification by grain-boundary sliding: A first model, J. Phys. Colloq. C1, Suppl. 3, 48, C1-249-C1-256, 1987a.

Alley, R. B., Texture of polar firn for remote sensing, Ann. Glaciol., 9, 1-4, 1987b.

Anderson, D. L., and C. S. Benson, The densification and diagenesis of snow, in Ice and Snow, edited by W. D. Kingery, pp. 391-411, MIT Press, Cambridge, Mass., 1963.

Barrett, P. J., and B. C. McKelvey, Cenozoic and tectonic history of the Transantarctic Mountains in the McMurdo Sound area, recent progress from drilling and related studies, Polar Rec., 20, 543-548, 1981.

Bennett, H. F., An investigation into velocity anisotropy through measurements of ultrasonic wave velocities in snow and ice cores from Greenland and Antarctica, Ph.D. dissertation, Univ. of Wis., Madison, Wis., 1968.

Bennett, H. F., Measurements of ultrasonic wave velocities in ice cores from Greenland and Antarctica, Res. Rep. 237, U.S. Army Cold Regions Research and Eng. Lab., Hanover, N. H., 1972.

Bentley, C. R., Structure of Antarctica and its ice cover, in Research in Geophysics, vol. 2: Solid Earth and Interface Phenomena, edited by H. Odishaw, pp. 335-389, MIT Press, Cambridge, Mass., 1964.

Bentley, C. R., Seismic anisotropy in the West Antarctic ice sheet, in Antarctic Snow and Ice Studies II, Antarct. Res. Ser., vol. 16, edited by A. P. Crary, pp. 131-177, AGU, Washington, D. C., 1971.

Bentley, C. R., Seismic wave velocities in anisotropic ice: A comparison of measured and calculated values in and around the deep drill hole at Byrd Station, Antarctica, J. Geophys. Res., 77, 4406-4420, 1972.

Bentley, C. R., The Ross Ice Shelf Geophysical and Glaciological Survey (RIGGS): Introduction and summary of measurements performed, in The Ross Ice Shelf: Glaciology and Geophysics, Antarct. Res. Ser., vol. 42, edited by C.R. Bentley and D.E. Hayes, pp. 1-20, AGU, Washington, D. C., 1984.

Bentley, C. R., and K. C. Jezek, RISS, RISP, and RIGGS: Post-IGY glaciological investigations of the Ross Ice Shelf in the U.S. program, J. R. Soc. N. Z., 11, 355-372, 1981.

Bentley, C. R., and H. Kohnen, Seismic refraction measurements of internal friction in Antarctic ice, J. Geophys. Res., 81, 1519-1526, 1976.

Bentley, C. R., P. W. Pomeroy, and H. J. Dorman, Seismic measurements on the Greenland ice cap, Ann. Geophys., 13, 253-285, 1957.

Bentley, C. R., J. W. Clough, K. C. Jezek, and S. Shabtaie, Ice thickness patterns and the dynamics of the Ross Ice Shelf, J. Glaciol., 24, 287-294, 1979.

Bentley, C. R., S. Shabtaie, D. D. Blankenship, S. T. Rooney, D. G. Schultz, S. Anandakrishnan, and R. B. Alley, Remote sensing of the Ross ice streams and adjacent Ross Ice Shelf, Antarctica, Ann. Glaciol., 9, 20-29, 1987.

Bradley, J. J., and A. N. Fort, Jr., Internal friction in rocks, in Handbook of Physical Constants, Mem. 97, edited by S. P. Clark, pp. 175-195, Geolological Society of America, Boulder, Colo., 1966.

Brockamp, B., and P. Pistor, Ein beitrag zur seismischen erforschung der struktur des Gronlandischen inlandeises, Polarforschung, 6, 133-146, 1967.

Brockamp, B., and H. Querfurth, Untersuchungen uber die elastizitats-konstanten von see und kunsteis, Polarforschung, 5, 253-262, 1964.

Clausen, H. B., W. Dansgaard, J. Nielson, and J. W. Clough, The surface accumulation on the Ross Ice Shelf, Antarct. J. U. S., 14, 68-72, 1979.

Clay, C. S., and H. Medwin, Acoustical Oceanography, 544 pp., John Wiley, New York, 1977.

Clough, J. W., and C. R. Bentley, Measurements of electromagnetic wave velocity in the East Antarctic ice sheet, IASH Publ., 86, 115-128, 1970.

Clough, J. W., and B. L. Hansen, The Ross Ice Shelf Project, Science, 203, 433-434, 1979.

Cooper, A. K., F. J. Davey, and J. C. Behrendt, Seismic stratigraphy and structure of the Victoria Land basin, western Ross Sea, Antarctica, in The Antarctic Continental Margin: Geology and Geophysics of the Western Ross Sea, CPCEMR Earth Sci. Ser., vol. 5B, pp. 27-76, Circum-Pacific Council for Energy and Mineral Resources, Houston, Texas, 1987.

Crary, A. P., Marine sediment thickness in the eastern Ross Sea area, Antarctica, Geol. Soc. Am. Bull., 72, 787-790, 1961.

Crary, A. P., E. S. Robinson, H. F. Bennett, and W. W. Boyd, Jr., Glaciological studies of the Ross Ice Shelf, Antarctica, 1957-1960, IGY Glaciol. Rep. 6, Am. Geogr. Soc., New York, 1962a.

Crary, A. P., E. S. Robinson, H. F. Bennett, and W. W. Boyd, Jr., Glaciological regime of the Ross Ice Shelf, J. Geophys. Res., 67, 2791-2807, 1962b.

Davey, F. J., Geology and structure of the Ross Sea Region, in The Antarctic Continental Margin: Geology and Geophysics of the Western Ross Sea, CPCEMR Earth Sci. Ser., vol. 5B, 1-15, Circum-Pacific Council for Energy and Mineral Resources, Houston, Texas, 1987.

Davey, F. J., K. Hinz, and H. Schroeder, Sedimentary basins of the Ross Sea, Antarctica, Antarctic Earth Science, edited by R. L. Oliver, P. R. James, and J. B. Jago, pp. 533-538, Australian Academy of Science, Canberra, 1983.

Dix, C. H., Seismic velocities from surface measurements, Geophysics, 20, 68-86, 1955.

Dobrin, M. B., Introduction to Geophysical Prospecting, 446 pp., McGraw-Hill, New York, 1960.

Gow, A. J., The inner structure of the Ross Ice Shelf at Little America V, Antarctica, as revealed by deep core drilling, IASH Publ., 61, 272-284, 1963.

Gow, A. J., Deep core studies of the accumulation and densification of snow at Byrd Station and Little America V, Antarctica, Res. Rep. 197, U.S. Army Cold Regions Res. and Eng. Lab., Hanover, N. H., 1968.

Gow, A. J., Deep core studies of the crystal structure and fabrics of Antarctic glacier ice, Res. Rep. 282, U.S. Army Cold Regions Res. and Eng. Lab., Hanover, N. H., 1970a.

Gow, A. J., Preliminary results of studies of ice cores from the 2164 m deep drill hole, Byrd Station, Antarctica, IASH Publ., 86, 78-90, 1970b.

Gow, A. J., and T. Williamson, Rheological implications of the internal structure and crystal fabrics of the West Antarctic ice sheet as revealed by deep core drilling at Byrd Station, Res. Rep. 76-35, U.S. Army Cold Regions Res. and Eng. Lab., Hanover, N. H., 1976.

Grant, F. S., and G. F. West, Interpretation Theory in Applied Geophysics, 583 pp., McGraw-Hill, New York, 1965.

Greischar, L. L., and C. R. Bentley, Isostatic equilibrium grounding line between the West Antarctic ice sheet and the Ross Ice Shelf, Nature, 283, 651-654, 1980.

Hamilton, E. L., Prediction of in-situ acoustic and elastic properties of marine sediments, Geophysics, 36, 266-284, 1971.

Hamilton, E. L., Sound velocity and related properties of marine sediments, J. Acoust. Soc. Am., 72, 1891-1904, 1982.

Hayes, D. E., and F. J. Davey, A geophysical study of the Ross Sea Antarctica, Initial Rep. Deep Sea Drill. Proj., 28, 887-907, 1975.

Hayes, D. E. and L. A. Frakes, General synthesis, Initial Rep. Deep Sea Drill. Proj., 28, 919-942, 1975.

Hough, J. L., Pleistocene lithology of Antarctic ocean bottom sediments, J. Geol., 58, 254-260, 1950.

Houtz, R., and F. J. Davey, Seismic profiler and sonobuoy measurements in Ross Sea, Antarctica, J. Geophys. Res., 78, 3448-3468, 1973.

Houtz, R., and R. Meijer, Structure of the Ross Sea shelf from profiler data, J. Geophys. Res., 75, 6592-6597, 1970.

Jiracek, G. R., Radio sounding of Antarctic ice, Res. Rep. 67-1, Univ. of Wis., Madison, Wis., 1967.

Jiracek, G. R., and C. R. Bentley, Velocity of electromagnetic waves in Antarctic ice, in Antarctic Snow and Ice Studies II, Antarct. Res. Ser., vol. 16, edited by A. P. Crary, pp. 199-208, AGU, Washington, D. C., 1971.

Johari, G. P., and S. J. Jones, The orientation polarization in hexagonal ice parallel and perpendicular to the c-axis, J. Glaciol., 21, 259-276, 1978.

Karl, H. A., E. Reimnitz, and B. D. Edwards, Extent and nature of the Ross Sea unconformity in the western Ross Sea, Antarctica, in The Antarctic Continental Margin: Geology and Geophysics of the Westen Ross Sea, CPCEMR Earth Sci. Ser., vol. 5B, pp. 77-92, Circum-Pacific Council for Energy and Mineral Resources, Houston, Texas, 1987.

Kirchner, J. F., and C. R. Bentley, RIGGS III: Seismic short-refraction studies using an analytical curve-fitting technique, in The Ross Ice Shelf: Glaciology and Geophysics, Antarct. Res. Ser., vol. 42, edited by C. R. Bentley and D. E. Hayes, AGU, Washington, D. C., this volume.

Kohnen, H., Uber die bezeihung zwischen seismischen geschwindigkeiten und der dichte in firn und eis, Z. Geophys., 38, 925-935, 1972.

Kohnen, H., The temperature dependence of seismic waves in ice, J. Glaciol., 13, 144-147, 1974.

Kohnen, H., and C. R. Bentley, Seismic refraction and reflection measurements at Byrd Station, Antarctica, J. Glaciol., 12, 101-111, 1973.

Kohnen, H., and C. R. Bentley, Ultrasonic measurements on ice cores from the RISP drill hole, Ross Ice Shelf, Antarctica, Antarct. J. U. S., 12, 148-150, 1977.

Kohnen, H., and A. J. Gow, Ultrasonic velocity investigations of crystal anisotropy in deep ice cores from Antarctica, J. Geophys. Res., 84, 4865-4874, 1979.

Langway, C. C., Jr., Antarctic ice core studies, Antarct. J. U. S., 10, 152-153, 1975.

Mellor, M., Snow and ice on the Earth's surface, Monogr. II-C, 163 pp., U.S. Army Cold Regions Res. and Eng. Lab., Hanover, N. H., 1964.

Nafe, J. E., and C. L. Drake, Physical properties of marine sediments, in The Sea, vol. 1, edited by M. N. Hill, pp. 794-815, John Wiley, New York, 1963.

Neal, C. S., Dynamics of the Ross Ice Shelf as revealed by radio echo sounding, J. Glaciol., 24, 295-307, 1979.

Phillippi, E., Die grundproben der Deutschen Sudpolar-Expedition 1901-03, Dtsch. Subpolar Exped., 2, 411-616, 1912.

Robertson, J. D., Geophysical studies on the Ross Ice Shelf, Antarctica, Ph.D. thesis, 214 pp., Univ. of Wis., Madison, Wis., 1975.

Robertson, J. D., and C. R. Bentley, Investigation of polar snow using seismic velocity gradients, J. Glaciol., 14, 39-48, 1975.

Robertson, J. D., C. R. Bentley, J. W. Clough, and L. L. Greischar, Sea-bottom topography and crustal structure below the Ross Ice Shelf, Antarctica, in Antarctic Geoscience, edited by C. Craddock, pp. 1083-1090, University of Wisconsin Press, Madison, Wis., 1982.

Robin, G. de Q., Seismic shooting and related investigations, in Norwegian-British-Swedish Antarctic Expedition, 1949-51, Scientific Results V, Glaciology III, 134 pp., Norsk Polarinstitutt, Oslo, 1958.

Robin, G. de Q., Velocity of radio waves in ice by means of a borehole interferometric technique, J. Glaciol., 15, 151-160, 1975.

Robin, G. de Q., S. Evans, and J. T. Bailey, Interpretation of radio echo sounding in polar ice sheets, Philos. Trans. R. Soc. London, Ser. A, 265, 437-505, 1969.

Roethlisberger, H., Seismic exploration in cold regions, Monogr. II-A2a, U.S. Army Cold Regions Res. and Eng. Lab., Hanover, N. H., 1972.

Shabtaie, S., and C. R. Bentley, Tabular icebergs: Implication from geophysical studies of ice shelves, J. Glaciol., 28, 413-430, 1982.

Stetson, H. C., and J. E. Upson, Bottom deposits of the Ross Sea, J. Sediment. Petrol., 7, 55-66, 1937.

Thiel, E., and J. C. Behrendt, Seismic studies on the Filchner Ice Shelf, Antarctica, 1957-58, IGY Glaciol. Rep. 2, Am. Geogr. Soc., New York, 1959.

Thiel, E., and N. A. Ostenso, Seismic studies on Antarctic ice shelves, Geophysics, 26, 706-715, 1961.

Thomas, C. W., Lithology and zoology of an Antarctic Ocean bottom core, Deep Sea Res., 6, 5-15, 1959.

Thomas, C. W., Late Pleistocene and Recent limits of the Ross Ice Shelf, J. Geophys. Res., 65, 1789-1792, 1960.

Thomas, R. H., The distribution of 10-m temperatures on the Ross Ice Shelf, J. Glaciol., 16, 111-117, 1976.

Thomas, R. H., D. R. MacAyeal, D. H. Eilers, and D. R. Gaylord, Glaciological studies on the Ross Ice Shelf, Antarctica, 1973-1978, in The Ross Ice Shelf: Glaciology and Geophysics, Antarct. Res. Ser., vol. 42, edited by C. R. Bentley and D. E. Hayes, pp. 21-53, AGU, Washington, D. C., 1984.

(Received December 23, 1987;
revised August 18, 1989;
accepted November 22, 1989.)

The Ross Ice Shelf: Glaciology and Geophysics
Antarctic Research Series, Volume 42, Paper 4, Pages 87-108

SEISMIC STUDIES ON THE GRID EASTERN HALF OF THE ROSS ICE SHELF: RIGGS III AND RIGGS IV

Donald G. Albert

U.S. Army Cold Regions Research and Engineering Laboratory
Hanover, New Hampshire 03755

Charles R. Bentley

Geophysical and Polar Research Center, University of Wisconsin
Madison, Wisconsin 53706

Abstract. Seismic P wave refraction experiments at three locations on the Ross Ice Shelf during 1976-1977 (RIGGS III) and 1977-1978 (RIGGS IV) reveal that the velocity increases monotonically in the firn from about 500 m s^{-1} at the surface to about 3800 m s^{-1} at a depth of 60 m. Maximum P wave velocities measured at four locations on the ice shelf show a large range of values primarily indicative of lateral inhomogeneities, but perhaps also resulting from anisotropy. The ice and water column thicknesses at station J9DC determined from reflection shooting are 414 ± 2 m and 244 ± 6 m, respectively. These values agree well with values of 417 ± 2 m and 240 ± 2 m measured in a borehole at that location. Water depths for 89 additional stations were determined using seismic reflections from the ocean floor together with ice thicknesses measured by radar and seismic techniques. Systematic differences that appear between ice thicknesses measured by the two techniques on RIGGS IV but not on RIGGS III most likely reflect an unrecognized systematic error in measurement. The amplitudes of ocean bottom and ice shelf bottom reflections at one station have been used, together with standard velocity-density curves, to calculate a density of 1.90 ± 0.12 Mg m^{-3} and a velocity of 1.72 ± 0.06 km s^{-1} in the uppermost sediment. Rayleigh, Love, and leaky-mode surface waves were recorded in experiments at station Q13. Theoretical surface wave dispersion curves calculated from measured body wave velocities give values higher than those observed. Dispersion curves calculated from several other velocity models indicate that agreement for the higher-mode surface waves can be obtained by modifying the S wave velocities in the upper few meters of the ice wherein they have not been determined accurately by the refraction shooting. Anisotropy may account for the differences between the observed and calculated values in the fundamental modes.

Contents

Introduction

The experiments discussed in this paper were carried out during the Ross Ice Shelf Geophysical and Glaciological Survey (RIGGS) field seasons from October 1976 to February 1977 (RIGGS III) and from December 1977 through January 1978 (RIGGS IV). Geophysical measurements were made at 94 stations, covering the grid eastern half of the Ross Ice Shelf. For a summary of RIGGS, see paper 1 of this volume [Bentley, 1984].

Seismic velocities in the ice shelf increase with depth to about 100 m because of compaction and recrystallization of the snow layers. Below this depth, the velocity decreases gradually downward because of increasing temperature [Crary et al., 1962a]. Consequently, refracted waves may be used to investigate the snow and firn only to a depth of about 80 m; only reflections can yield information about the lower part of the ice shelf. Seismic wave attenuation is much lower in ice than in most other materials encountered in seismic work, so high-frequency energy propagates easily over long distances with little loss. Signal frequencies greater than 100 Hz are common in reflection shooting on ice sheets, and ocean bottom reflections with frequencies of 200 Hz are routinely recorded from beneath ice shelves. These frequencies are substantially greater than those normally used in seismic

prospecting (typically 8-80 Hz).

Here we report on three types of seismic experiments: (1) short-refraction shooting was used to determine the compressional (P) and shear (S) wave velocities and, from the P wave velocities, the density as a function of depth in the upper part of the shelf; (2) surface wave studies provided an independent check on the refraction results and also gave an indication of anisotropy in the upper layers of the firn; (3) seismic reflections were used to measure the thickness of the water layer and in many places the ice thickness also. Radar sounding normally is the primary means of determining ice thickness, but during RIGGS III an equipment failure meant that the field party operating out of the base camp at C-16 lacked a radar system for much of the season. As a result, only seismic measurements were available at 21 stations in the grid northeastern quadrant of the ice shelf.

Recording was done with 24-channel SIE model RA-49R seismograph systems modified to record frequencies up to 500 Hz. An SIE R-6 oscillograph was used to record the shots; no tape recording system was available. The shot instant was recorded on a separate channel, either by a direct connection from the shot box or by radio transmission. Normal seismic shooting procedures were used; either hammer blows or explosives (blasting caps at short distances, 0.4-kg charges at longer distances) served as the source. Shot holes up to 15 m deep were drilled by hand in the ice using a SIPRE auger. Both horizontal and vertical geophones were used, usually with one geophone per channel.

Short-Refraction Shooting

The purpose of short-refraction shooting is to investigate the properties of the upper layers of the ice sheet. By measuring the travel time of a seismic wave as a function of shot-receiver distance, the velocity as a function of depth can be determined. A very useful empirical equation formulated by Kohnen [1972] gives the density of the ice from the P wave velocity. If S wave velocities are also determined, the elastic constants of the ice can be calculated.

Lines to record P waves, SV waves (shear waves polarized in the plane of propagation), and SH waves (shear waves transversely polarized) were shot at the base camps C-16, J9DC, and Q13; short P wave lines were shot at the 2-day stations H13, M14, and N19 during RIGGS III and at O11, O19, and R16 during RIGGS IV (see Figure 1). The detailed results of the RIGGS IV refraction experiments are compiled in Appendix A; those from RIGGS III are presented by Kirchner [1978] [Kirchner et al., 1979; Kirchner and Bentley, this volume]. (All appendix material is on microfiche, enclosed in a pocket inside the back cover of this minibook.) Robertson [1975] [Robertson and Bentley, this volume] and Crary et al. [1962a, b] have reported on previous refraction work on the ice shelf.

For the refraction experiments discussed here, the detecting spread consisted of 24 vertically oriented geophones set at 2-m intervals. The spread was left unchanged, while the shot point was moved from the end of the spread out to a distance of 400 m in 40-m increments. This shooting procedure results in a 6-m overlap for adjacent shots. At station R16 an additional shot was set off 710 m from the farthest geophone. At some locations, direct arrivals from reflection shots with a geophone spacing of 30 m were used to give additional travel times for longer distances. The time breaks for all shots were recorded on a separate channel through a wire directly connecting the shot box with the recording unit. Typical seismic refraction records are shown in Figures 2 and 3. (Ice bottom and water bottom reflections do not appear on these records because of small charge sizes at short distances and no low-cut filtering on any refraction records.)

A larger reproduction of one record is shown in Figure 4. This seismogram is from a 1 lb (0.4 kg) charge in a 1-m hole, 336 m from the nearest geophone. The first arrival at each geophone is the refracted P wave (P_1), followed by a series of refracted multiples (P_m) that have been reflected m-1 times from the ice-air interface. The velocity of these waves across the detecting spread at distance x is equal to the velocity of a P_1 arrival at x/m. The shear wave arrival (S) is next on the record, followed by higher-mode Rayleigh waves (R_H) and the fundamental mode Rayleigh wave (R_1). The Rayleigh waves are discussed in a later section.

The first arrival times at each geophone were read from the seismograms, using a 7X magnifier, to a precision of 0.1 ms and an accuracy of 0.2-0.3 ms. A computer program was then used to smooth the travel times, t(x), by fitting them to an equation of the form (see Kirchner and Bentley [this volume] for explanation and discussion)

$$t(x) = t_1(1 - e^{-a_1 x}) + t_2(1 - e^{-a_2 x}) + v_m^{-1} \qquad (1)$$

where a_1, a_2, t_1, t_2, and v_m^{-1} are parameters chosen for the best least squares fit. Table 1 shows the parameters determined for the RIGGS IV P wave refraction experiments. An example of a P wave travel time plot (from station R16) is shown in Figure 5. The best fit regression line fits the data points

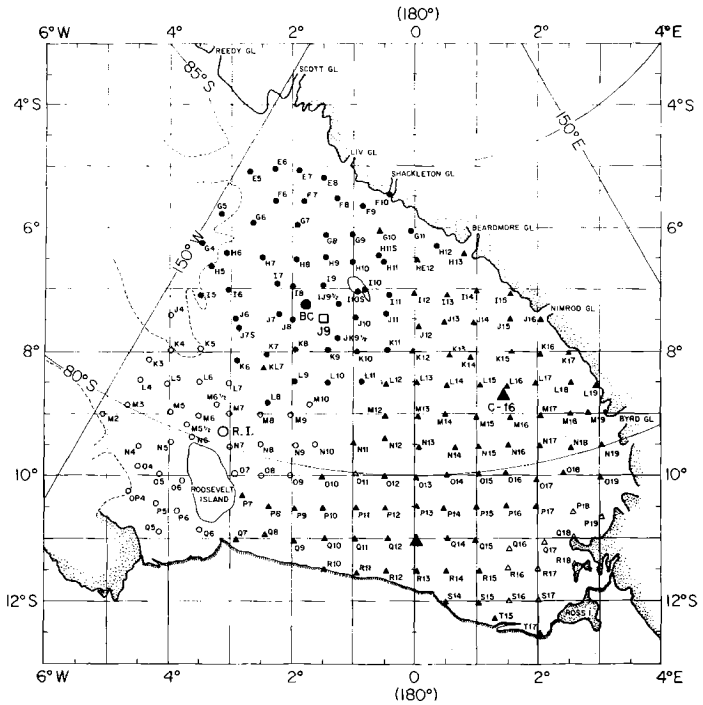

Fig. 1. Map of RIGGS stations [from Bentley, 1984]. Stations occupied during RIGGS III and IV are indicated by solid triangles and open triangles, respectively. In the rectangular grid coordinate system shown, meridians are parallel to the Greenwich meridian, with grid north toward Greenwich. The origin of the system is at the South Pole, and 1° of grid latitude or longitude equals 1° of geographic latitude.

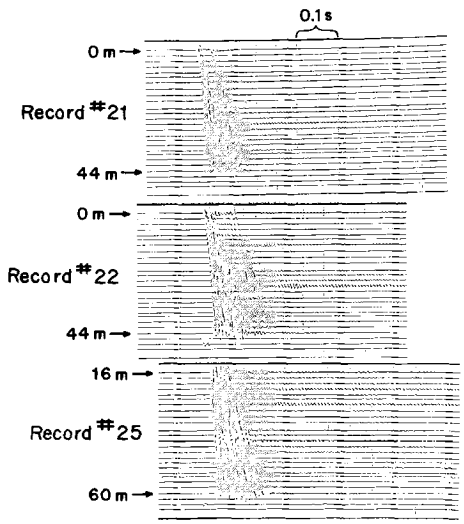

Fig. 2. Sample P wave short-refraction records at small separations, from station R16. Geophones were 2 m apart; distances for closest and most distant geophone for each record are marked. The energy source for each record was a hammer blow.

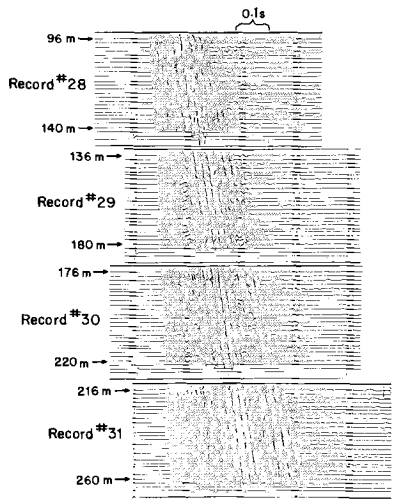

Fig. 3. Sample P wave short-refraction records at relatively large separations, from station R16. Geophones were 2 m apart; distances for closest and most distant geophone for each record are marked. The energy source for each record was a 0.4-kg charge in a 1-m hole.

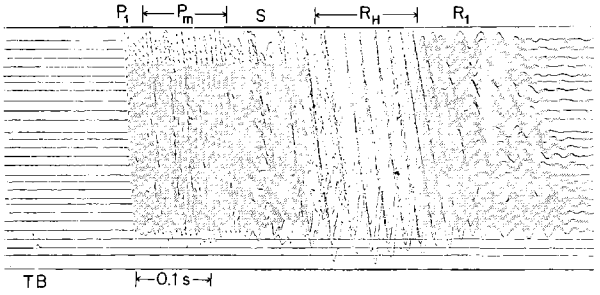

Fig. 4. Enlargement of a short-refraction record (record 39) from station R16. The geophone interval was 2 m, the minimum distance was 336 m, and the energy source was a 0.4-kg charge in a 1-m hole.

extremely closely (the line is not drawn in the figure because it would obscure the points), as is necessary if equation (1) is satisfactorily to represent the observed travel times. The standard deviation in the fit of equation (1) to the observed travel times is about half a millisecond at all three stations (Table 1).

The choice of equation (1) was based on the assumption that the wave speed increases continuously with depth. To test this assumption, a graph of the time interval measured between geophones versus distance for a record close to the shot point was plotted (Figure 6). For reference, the time interval calculated from equation (1) is also shown. If the firn comprised a series of discrete layers, each having a distinct velocity, the graph would appear to be steplike. The plotted points show no evidence of discrete velocity layers, although there are deviations from the smooth curve larger than the reading error that are due, we believe, to lateral inhomogeneities. (The seismogram from which this plot was made is record 21 in Figure 2.)

Once the parameters of equation (1) have been determined, the body wave velocity, v(x), can be found by differentiation. The Wiechert-Herglotz-Bateman (WHB) integral [see Grant and West, 1965] can then be used to find v(z), the velocity as a function of depth, using a numerical program developed by Robertson [1975] [Robertson and Bentley, this volume].

From the P wave velocities the density as a function of depth, $\rho(z)$, can be calculated from Kohnen's [1972] empirical equation:

$$\rho(z) = \frac{0.915}{1 + \{[(v_p)_{max} - v_p(z)]/2250\}^{1.22}} \quad (2)$$

where ρ is in megagrams per cubic meter, the maximum P wave velocity in the ice ($(v_p)_{max}$), is taken to be 3860 m s^{-1}, 0.915 Mg m^{-3} is the density assumed for the depth of the maximum velocity, and $v_p(z)$ is in meters per second. The other constants in equation (2) were derived from refraction velocities and densities measured at Byrd Station on the inland ice sheet of West Antarctica. (Robertson and Bentley [this volume] use $(v_p)_{max}$ = 3850 m s^{-1} instead of 3860 m s^{-1}; the corresponding difference in ρ amounts to no more than 0.003 Mg m^{-3}. See Robertson and Bentley [this volume] for a further discussion.) Kirchner et al. [1979] found good agreement between densities measured directly on cores from a borehole at station J9DS and those calculated from equation (2) for shooting carried out close to the borehole. However, differences as large as 5%, believed to reflect real differences in the ice, were found relative to densities calculated from a refraction experiment carried out only 2 km away from the borehole at station J9DC. The differences in the structure of the firn over such a short distance interval have been attributed by Kirchner et al. [1979] to a remanent effect of a high-stress zone 100 km upstream from station J9DC, through which the ice column passed about 300 years ago.

The travel time to the surface from a charge (0.4 kg) fired in a 8.8-m shot hole at station R16 was used to check the results of the refraction experiment there. The measured time was 5.0 ms, compared with 5.4 ms calculated from the velocities determined by the refraction experiment. The two values are in satisfactory agreement in view of the reading error (0.2 ms) and the fact that the

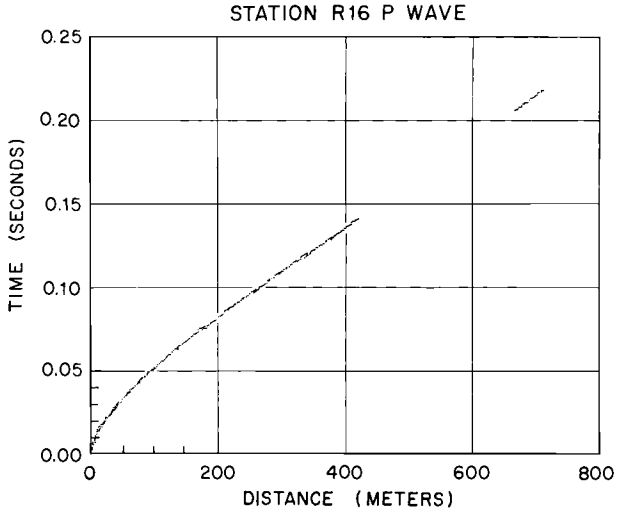

Fig. 5. P wave travel time plot from station R16.

TABLE 1. Least Squares Fit Parameters for the P Wave Travel Time Equation (Equation (1)) for RIGGS IV

Station	n	Maximum Distance, m	t_1, ms	a_1, km^{-1}	t_2, ms	a_2, km^{-1}	v_m, $ms\ km^{-1}$	v_m, $m\ s^{-1}$	Standard Error in t, ms
O11	251	420	22.5	19	8.7	229	267.0	3745	0.5
O19	297	1160	22.9	15	6.3	161	263.5	3795	0.6
R16	331	710	23.6	15	7.1	189	263.7	3792	0.5

Here n is the number of travel time points used in the determination.

hole was sprung (i.e., a charge had already been fired in it), so that the explosive shock wave much have traveled some tenths of meters at high speed.

The maximum velocity measured on each short-refraction profile is given by v_m (Table 1). Previous experience has shown that the true maximum velocity in the ice shelf is not reached until shot-detector distances exceed at least 600 m, and perhaps 1000 m [Robertson, 1975; Robertson and Bentley, this volume]. Only at stations O19 and R15 were those distances exceeded on the short-refraction profiles (except for a shot without a shot break at station O11). The corresponding maximum velocities are 3795 m s^{-1} and 3792 m s^{-1}, respectively. These are slightly less than the average (3811 ± 7 m s^{-1}) calculated for the grid western half of the Ross Ice Shelf by Robertson [1975] [Robertson and Bentley, this volume], but in close agreement with the mean from eight profiles at three RIGGS III stations (3792 ± 16 m s^{-1} [Kirchner and Bentley, this volume]) and with the mean for the whole ice shelf (3790 ± 30 m s^{-1}) calculated from Crary et al. [1962a, Table 7]. As usual, the velocity is much less than that found on the grounded ice sheet at a similar temperature (3850 ± 4 m s^{-1} at -24°C according to Kohnen [1974]). For further discussions, see Robertson and Bentley [this volume].

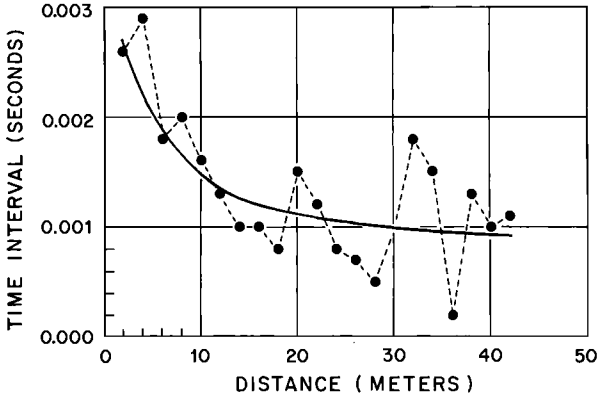

Fig. 6. Travel time interval between geophones versus distance for shot 21 at station R16 (see Figure 2). Solid circles are observed values; the smooth curve is calculated from equation (1).

Another method of measuring the maximum velocity is to calculate the cross-spread velocity on individual shots at sufficiently large distances. This method has the advantage of being unaffected by uncertainties in time breaks and total distances but the disadvantage of providing a determination over only a short distance interval (i.e., the length of the array). When the firn layers are uniform and horizontal, the velocity determinations can be excellent.

The results of this method, which was applied at stations O11, O19, Q13, and R16, are given in Table 2 (the selection criterion was a mean distance greater than 600 m). The means and errors for shots 8-11 at station Q13 and for the separate directions at station O19 were calculated on the assumption that the individual velocities were samples of the same population; the velocities were weighted by inverse variances. The error for station O19, on the other hand, was calculated on the assumption that the single-direction means represent physically different velocities (the first being down dip and the second up dip). Since the profile was not truly reversed, that error cannot be taken as the uncertainty in the determination of the true wave velocity in the ice.

Several conclusions can be drawn from the numbers in Table 2. First, velocities across a spread only 44 m long (shot 53 at station O11 and shot 41 at station R16) are not useful, a fact that is not surprising, since a speed difference of 100 m s^{-1} corresponds to a travel time difference of only 0.3 ms

TABLE 2. Cross Spread P Wave Velocities Determined From Least Squares Analyses of Individual Shots

Station	Shot Number	n	Minimum Distance, m	Spread Length, m	Velocity, m s^{-1}
O11	50	22	593	300	3705 ± 6
	53	23	680	44	3860 ± 50
O19	87N	22	470	690	3784 ± 8
	88N	22	470	690	3776 ± 8
	89N	18	470	690	3789 ± 7
Mean for grid north					3783 ± 5
	91S	21	440	690	3897 ± 9
	93S	20	440	690	3900 ± 12
Mean for grid south					3898 ± 7
Mean for O19					3840 ± 9
Q13	8	12	1110	330	3824 ± 19
	9	12	1110	330	3817 ± 10
	10	12	1170	330	3820 ± 16
	11	12	1170	330	3810 ± 14
Mean for 8-11					3817 ± 7
	69	15	8782	570	3880 ± 32
R16	41	23	666	44	3533 ± 45

N and S denote shots to the grid north and grid south of the spread, respectively; n is the number of travel time points used for each shot.

over a 44-m interval.

Second, it is clear from the shooting in opposite directions at station O19 (even though the profile was not truly reversed) that the constant velocity surfaces are not horizontal there. This was already suspected in the field, because of bending of the ice shelf associated with large bottom crevasses at O19 (S. Shabtaie, personal communication, 1977). A dip of less than 1° (depending on the details of the geometry [see Robertson and Bentley, this volume]) would suffice to produce the observed results. A similar bending caused by bottom crevasses at station O11 is a likely cause of the very low velocity, 3705 m s^{-1}, observed on the unreversed profile there.

Third, the long shot (shot 69) at station Q13 gives a velocity much higher than those measured at 1100 to 1500 m (shots 8-11) on a different spread. Here again we suspect irregularities in the structure, as indicated not only by the high velocity but also by the large scatter of the travel times, which lead to the relatively large standard error in the velocity estimate (±32 m s^{-1}). Observed travel times fall off the least squares regression line by as much as 2 ms, much more than is usually found. Another possible explanation for the high velocity is that the waves are penetrating to an anisotropic layer in which the wave velocity for horizontal propagation is enhanced. A strongly concentrated vertical orientation of crystal c axes could yield a velocity as high as 3880 m s^{-1} [Bentley, 1971]. Gow [1963, 1970] found strongly developed fabrics in the ice cores from Little America V (at the ice shelf front grid south of station Q6 (Figure 1)), but they were characterized by two or more poles offset from the vertical by about 25°, an orientation that would not result in a high horizontal wave velocity. Furthermore, no velocities close to 3880 m s^{-1} were found in

ultrasonic measurements on cores from Little America V [Bennett, 1972; Kohnen and Gow, 1979]. A single-bullseye pattern with most of the axes within 25° of the vertical would be required. Such a pattern is commonly observed on the grounded inland ice, both in Antarctica [Kohnen and Gow, 1979; Russell-Head and Budd, 1979; Korotkevich et al., 1978] and Greenland [Herron and Langway, 1982; Herron et al., 1985] but has not yet been reported in an ice shelf.

Reflections

One of the primary objectives of the RIGGS survey was to measure the ice and water thicknesses over the entire ice shelf on a 55-km (½°) grid. Radar sounding yields a strong reflection from the ice-water interface and is used to measure the ice thickness. However, since radio waves do not penetrate seawater, seismic (acoustic) reflections must be used to measure the depth to the ocean bottom. The two geophysical techniques complement each other, since seismic reflections from the ice-water interface (I_1) are often masked by arrivals propagating along or near the surface of the ice shelf. The difficulty in detecting I_1 is especially great at stations near the edge of the shelf where the ice is relatively thin and the reflection time is short. Most of the stations discussed in this paper were in this area.

The techniques used on the ice shelf differed from those normally used on land in two important respects. First, because the reflections contain such high frequencies, sharp low-cut filters with a -3 dB point at 90 Hz were used to eliminate surface waves (see the section on surface waves below) and to enhance the reflections; high-cut filters were set above 300 Hz or not used at all.

The second major difference was in the use of multiple reflections. Multiples are regarded as a type of noise in most seismic processing, and sophisticated computer techniques have been developed to eliminate them from the seismic records. On the ice shelf, because of the very few reflecting horizons and their high reflection coefficients, multiples not only appear commonly on the seismic records but are easily identified. The multiples thus can be used to confirm the seismic travel times through the ice and water layers found from the primary reflections; this information is especially important in view of the difficulty in detecting I_1. Figure 7 shows ray paths for commonly recorded primary and multiple reflections and gives the nomenclature Crary et al. [1962a] used to label them (see Robertson and Bentley [this volume] for a discussion on how to identify reflection types). A complete seismic record from station P19 and an enlargement of sections of a record from station R17, both showing I_1 and various multiples, are reproduced in Figures 8 and 9. Note the contrast in the appearance between these reflection records and unfiltered records used in refraction and surface wave studies (Figures 2, 3, 11, and 12).

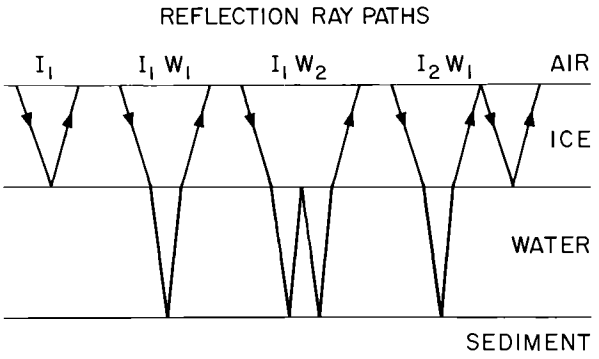

Fig. 7. Reflection ray paths and nomenclature. After Crary et al. [1962a].

Seismic soundings were made at 79 stations during the RIGGS III field season, and 11 more were made during RIGGS IV (Figure 1). To convert the reflection times to layer thicknesses, wave speeds had to be assigned to the ice and the seawater. The sound speed in the water layer was taken to be 1442 m s^{-1}, as calculated by Crary et al. [1962a] from oceanographic data near Little America V. Assigning an average wave speed to the ice was more difficult. Refraction measurements are unsuitable for this because of the temperature-related decrease in velocity below a depth of about 100 m, as pointed out earlier. The average velocity within a layer can be found from the change in reflection time across the detecting spread ("normal moveout") but only if good oblique I_1 reflections are recorded. Robertson [1975] and Robertson and Bentley [this volume] were able to record I_1 reflections clearly enough to use this technique during RIGGS I and RIGGS II at stations on the grid western half of the ice shelf where the ice was relatively thick. Their values for the average speed through the ice shelf, including the upper firn layers, range from 3600 m s^{-1} to 3870 m s^{-1}, with an average of 3688 ± 15 m s^{-1} (corresponding to an average ice thickness of 635 m) for 10 determinations. In the grid eastern half of the ice shelf the ice is thinner; so I_1 is rarely recorded, and even then only poorly.

Since the oblique reflection technique

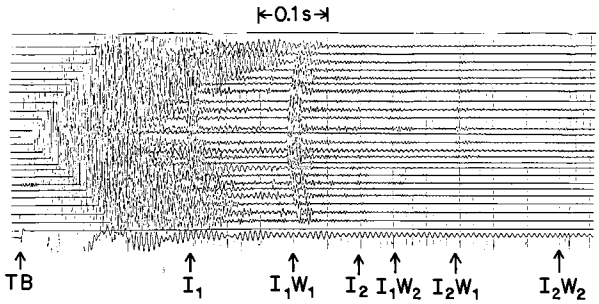

Fig. 8. Sample reflection seismogram (shot 116 from station P19). The energy source was a 150-g charge in a 5-m hole. Geophone spacing was 30 m; 90-Hz low-cut filtering was used. Arrivals are labeled according to Figure 7.

could not be used in our study, a mean vertical velocity was determined indirectly. A vertical travel time of 0.033 s to a depth of 100 m was calculated from the refraction measurements (Table 3). For greater depths a velocity of 3810 m s^{-1} at 100 m [Robertson and Bentley, this volume], a velocity-temperature coefficient of -2.3 m s^{-1} K^{-1} [Kohnen, 1974] and temperature measurements from Crary [1961] and Rand [1975] were used to calculate an average speed below 100 m of 3785 m s^{-1}. Combining these results yielded

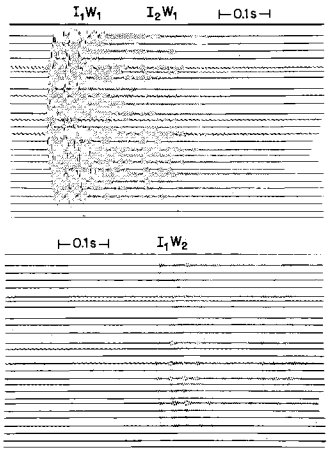

Fig. 9. Enlargement of a reflection seismogram (shot 15 from station R17) showing the bottom reflection (I_1W_1) and the two primary multiple reflections (I_2W_1 and I_1W_2). Note the subbottom reflection that appears 0.03 s after the initial I_1W_1 pulse. The energy source was 150 g in a 5-m hole. Geophone spacing was 30 m; 90-Hz low-cut filtering was used.

TABLE 3. Vertical Travel Time for P Waves to a Depth of 100 m, Calculated From Refraction Shooting

Profile	Travel Time, s	Station Mean
C-16-2	0.0330	0.0330
C-16-3	0.0329	
H13	0.0328	0.0328
J9-1	0.0330	
J9-2	0.0330	0.0329
J9-3	0.0327	
M14	0.0329	0.0329
O11	0.0332	0.0332
O19	0.0323	0.0323
Q13-1	0.0333	0.0332
Q13-2	0.0331	
R16	0.0326	0.0326
Overall mean		0.0328 ± 0.0003

the average velocities through various thicknesses of ice presented in Table 4, which were used to calculate seismic ice thicknesses, h_i(seismic). (These velocities are about 50 m s^{-1} less than those used by Robertson and Bentley [this volume] primarily because of lower velocities very near the surface.)

Radar reflections from the bottom of the ice were recorded at 71 surface stations. At one station where a measurement was not made on the surface, an echo time was taken from airborne sounding on an overflight (station M12), and at one other (station T17S) the ice thickness was extrapolated from a nearby station. Radio echo times in microseconds, t_r, were converted to ice thicknesses in meters, h_i(radar), by the equation $h_i(\text{radar}) = 84.3t_r + 7.6$ [Robertson and Bentley, this volume].

Ice thicknesses (h_i) determined from radar and seismic reflections, water layer thicknesses (h_w), and depths to the seafloor (d_w) at all stations are given in Table 5; a more complete tabulation, including travel times, is given in Appendix B. Both types of h_i values contributed to the map of ice thickness published by Bentley et al. [1979], although that map was based primarily on airborne radar sounding. The ice thickness map, updated along the West Antarctic grounding line (see Robertson and Bentley [this volume]) is reproduced in color in Plate 1. To be consistent, where h_i was measured both by radar and seismic reflections, the latter were used to calculate h_w and d_w. Surface elevations, e, which were needed to obtain d_w, were calculated according to the equation $e = 0.118h_i + 11.6$ m found by Shabtaie and Bentley [1982].

TABLE 4. Calculated Average P Wave Velocities Through the Ice Shelf, as a Function of Ice Shelf Thickness

Ice Thickness, m	One-Way Travel Time, s	Average Velocity, m s^{-1}
250	0.0726	3443
300	0.0858	3495
350	0.0990	3534
400	0.1122	3564
450	0.1254	3587
500	0.1387	3606
550	0.1519	3622
600	0.1651	3635
650	0.1783	3646
700	0.1915	3656
750	0.2047	3664
800	0.2179	3672

A map showing the thickness of the water layer beneath the entire ice shelf, updated from Greischar and Bentley [1980], is reproduced in color in Plate 2.

Direct comparison of actual ice and water column thicknesses with values determined by seismic shooting and by radar is possible at station J9DC because of the hole melted through the shelf during the 1977-1978 season [Clough and Hansen, 1979]. A series of seismic records made during RIGGS III, using a 150-m shot hole, yielded values of 414 ± 2 m and 244 ± 6 m for the ice and water layer thicknesses, respectively. The ice thickness determined by radar was 423 ± 5 m. Measurements in the access hole (T. D. Foster and J. W. Clough, personal communication, 1978) indicate that the ice and water columns are 417 ± 2 m and 240 ± 2 m thick, respectively.

At the 10 RIGGS III stations where h_i(radar) and h_i(seismic) were both found, the difference between them was numerically less than 10 m (Table 5). On the other hand, at the six RIGGS IV stations where both measurements were made (stations P19, Q16, R16, T17, S16, S17), all in the grid southeast corner of the ice shelf, h_i(radar) - h_i(seismic) ranged from 11 to 27 m, with an average of 17 m. Whether this difference is significant as a characteristic of the ice shelf or represents an otherwise unrecognized systematic error in RIGGS IV measurements is difficult to say with so few data. Electromagnetic waves, because of their dependence on the conductive properties of the ice and because their wavelengths are about an order of magnitude smaller than seismic wavelengths (5 m, 3.5 m, and 1.2 m at 35 MHz, 50 MHz, and 150 MHz, respectively, compared with 38 m and 19 m for 100-Hz and 200-Hz seismic waves), are more sensitive than seismic waves to the effect of a transition zone at the base of the ice, such as could be caused by saltwater penetration into the ice or by freezing of seawater on the bottom. However, radar reflection from a transition zone would yield ice thickness values that were too small rather than too large. It is difficult to conceive of a physically realistic model that would incorporate a deeper radar boundary than seismic boundary on floating ice. (Substantially deeper radar reflections were encountered on the grounded ice of Roosevelt Island by Jiracek and Bentley [1971].) As the difference was seen only in RIGGS IV data and not in those from RIGGS III, we must also consider the possibility of a systematic error, even though equipment, procedures, and personnel were the same on RIGGS III and RIGGS IV. If there is an error and it is in the radar measurements, then the same error presumably would apply to h_i(radar) at the other RIGGS IV stations (P18, Q17, Q18, and R18), in which case the water depth at those stations would be some 15 m too great. The uncertainty is not enough to affect materially the maps in Plates 2 and 3.

Using the values of d_w given in Table 5 along with values from other investigations on the Ross Ice Shelf [Crary et al., 1962a, b; Robertson, 1975; M. P. Hochstein and C. R. Bentley, personal communication, 1979], the depth to the ocean bottom beneath the entire shelf was mapped and contoured by Robertson et al. [1982]. Albert et al. [1978] connected that map to maps produced from investigations in the adjacent areas of the open Ross Sea [Hayes and Davey, 1975] and the Rockefeller Plateau [Rose, 1982]. The combined map of the "Ross Embayment" (Plate 3) shows that the region from the continental shelf in the grid western Ross Sea inland beneath the grid western half of the Ross Ice Shelf and for several hundred kilometers inland beyond the grounding line forms a continuous physiographic province with the same average submarine/subglacial elevation over the entire area. The grid eastern section beneath the Ross Ice Shelf and Ross Sea and the deeper lying bed in the grid northwesternmost extremity of the embayment are distinctly different. For further discussion, see Robertson et al. [1982] and Davey [1981].

Seismic reflections from sediments beneath the ocean bottom were recorded at five locations during RIGGS III and IV (a good example can be seen in Figure 9). Unfortunately, because of the short spreads used, it was not possible to determine wave speeds in the sediments by the oblique reflection technique. Another method of estimating wave speeds is

TABLE 5. Ice Thicknesses (h_i), Water Layer Thicknesses (h_w), Depths to the Seafloor, and $\Delta h_i = h_i(\text{radar}) - h_i(\text{seismic})$

Station	Season	h_i(radar), m	h_i(seismic), m	Δh_i, m	h_w, m	Depth to the Seafloor, m Below Sea Level
Q13	III	328	336	-8	445	730
C-16	III	356	356	0	425	727
H13	III	758	NR		502	1159
I12	III	NM	681		126	715
I13	III	NM	460		353	747
I14	III	395	NR		383	720
I15	III	298	NR		588	839
J9DC	III	423	414	9	244	598
J12	III	NM	389		187	518
J13	III	383	NR		298	624
J14	III	410	NR		375	725
J15	III	336	NR		535	820
J16	III	631	NR		175	720
K12	III	408	NR		129	477
K13	III	NM	395		257	594
K14	III	357	NR		373	676
K15	III	368	NR		539	852
K16	III	408	NR		470	818
K17	III	207	NR		500	671
KL7	III	475	NR		250	657
L12	III	NM	395		296	633
L13	III	NM	391		122	455
L14	III	NM	380		229	553
L15	III	328	NR		396	674
L16	III	362	NR		441	749
L17	III	307	NR		376	635
L18	III	391	NR		585	918
L19	III	313	NR		184	448
M12	III	345	NR		364	657
M13	III	NM	368		200	513
M14	III	345	NR		359	652
M15	III	307	NR		432	691
M16	III	NM	393		330	665
M17	III	NM	388		371	702
M18	III	NM	342		505	795
M19	III	NM	292		631	877
N11	III	425	NR		168	531
N12	III	370	371	-1	315	631
N13	III	NM	371		265	581
N14	III	NM	360		450	756
N15	III	NM	366		418	729
N16	III	NM	328		296	574
N17	III	NM	419		362	720
N18	III	NM	395		497	834
N19	III	556	NR		185	664
O11	IV	379	NR		210	533
O12	III	370	NR		293	608

TABLE 5. (continued)

Station	Season	h_i(radar), m	h_i(seismic), m	Δh_i, m	h_w, m	Depth to the Seafloor, m Below Sea Level
O13	III	382	NR		360	685
O14	III	345	NR		458	751
O15	III	379	NR		329	652
O16	III	NM	395		233	570
O17	III	NM	389		363	694
O18	III	NM	482		541	955
O19[a]	III	471	400		493	834
P7	III	345	NM			
P8	III	412	NM			
P9	III	404	403	1	225	569
P10	III	357	NM			
P11	III	383	NR		241	567
P12	III	340	NR		308	596
P13	III	372	NR		405	722
P14	III	319	NR		463	733
P15	III	341	NR		232	521
P16	III	235	NR		353	549
P17	III	416	NR		385	740
P18	IV	412	NR		797	1149
P19	IV	459	447	13	108	491
Q7	III	336	NR		181	466
Q8	III	379	NR		223	546
Q9	III	345	NR		281	574
Q10	III	336	NR		153	438
Q11	III	365	NR		270	580
Q12	III	341	NR		344	633
Q14	III	325	NR		411	686
Q15	III	332	NR		201	482
Q16	IV	395	384	11	582	909
Q17	IV	362	NR		651	959
Q18	IV	509	NM			
R10	III	303	304	-1	188	445
R11	III	293	285	8	322	562
R12	III	315	310	5	375	637
R13	III	302	NR		519	774
R14	III	327	NR		351	628
R15	III	331	NR		501	781
R16	IV	353	342	11	551	841
R17	IV	320	302	18	590	845
R18	IV	218	NR		365	546
S14	III	212	NR		537	712
S15	III	244	NR		604	808
S16	IV	328	306	22	559	817
S17	IV	252	225	27	688	875
T15	III	266	NR		513	736
T17	III	161	NM			
T17S	III	155[b]	NR		739	864

NR, no reflection could be picked; NM, no measurement was attempted.

[a]Station occupied twice; h_i(radar) and h_i(seismic) are not at same spot.

[b]Estimated from station T17, which was 1.6 km away, and the ice thickness gradient.

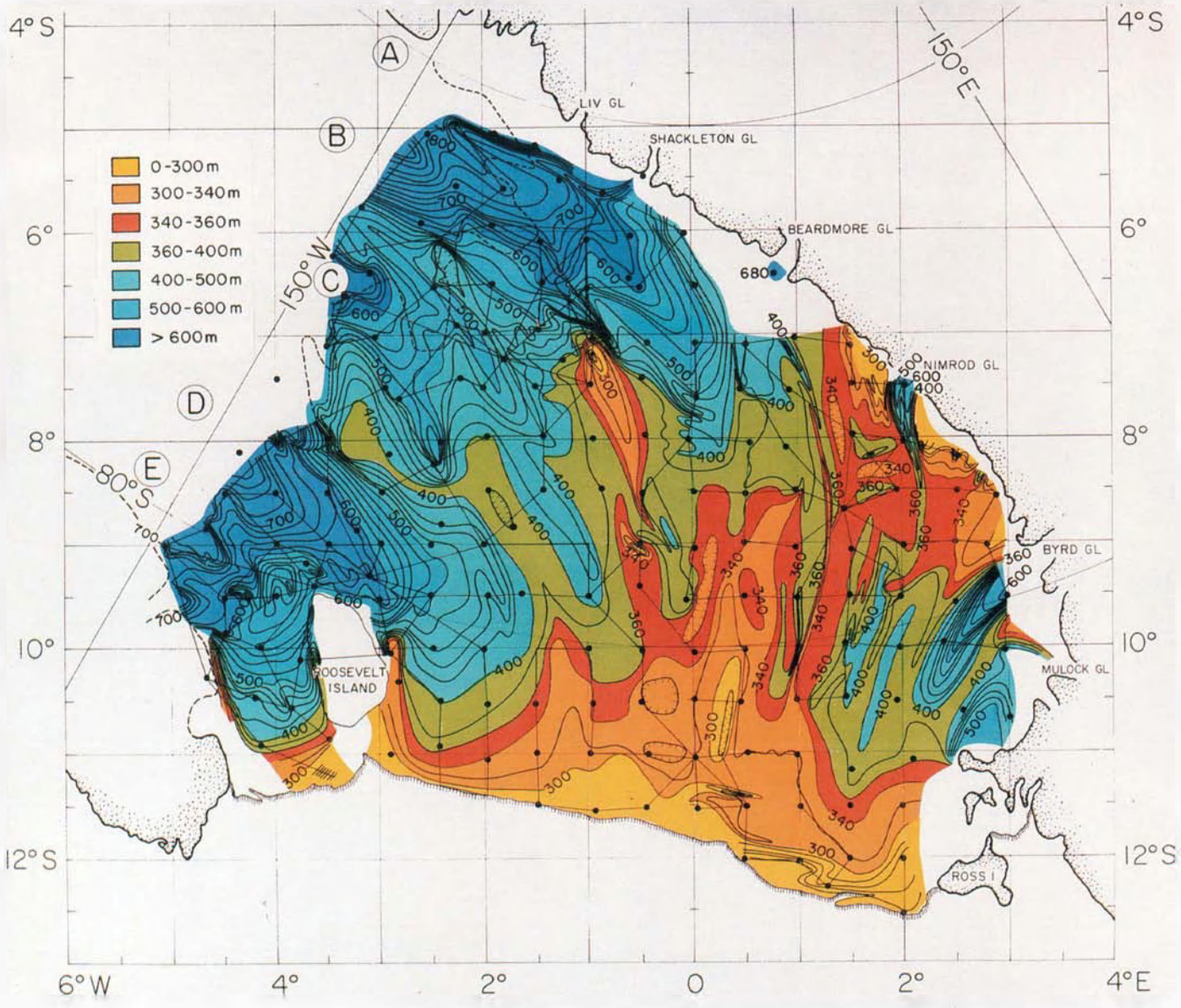
0-300m
300-340m
340-360m
360-400m
400-500m
500-600m
>600m
A
B
C
D
E
LIV GL
SHACKLETON GL
BEARDMORE GL
NIMROD GL
BYRD GL
MULOCK GL
ROOSEVELT ISLAND
ROSS I
680
150°W
150°E
80°S
4°S
6°
8°
10°
12°S
6°W
4°
2°
0
2°
4°E

[redacted]

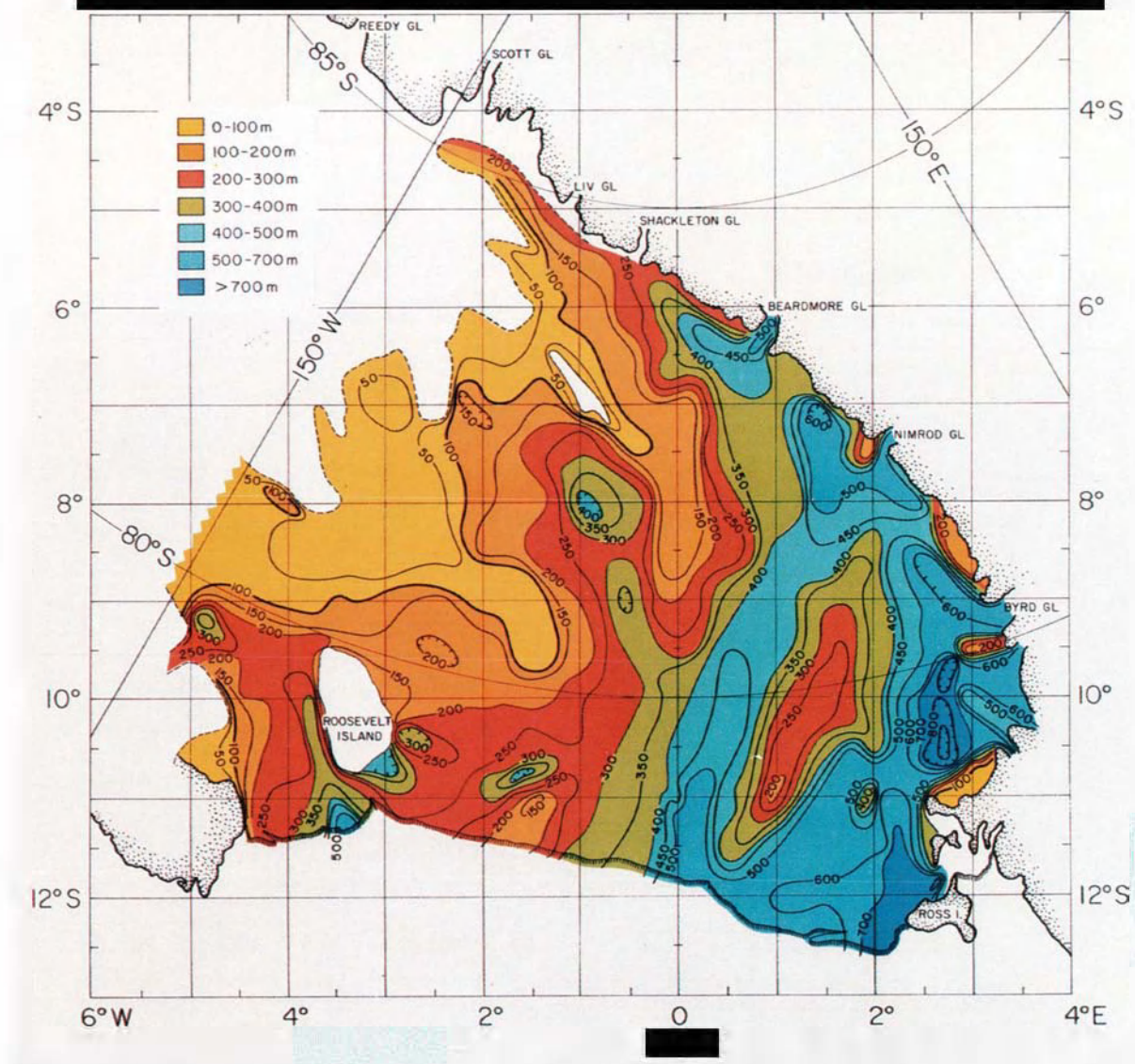

[redacted]

[redacted]

[redacted]

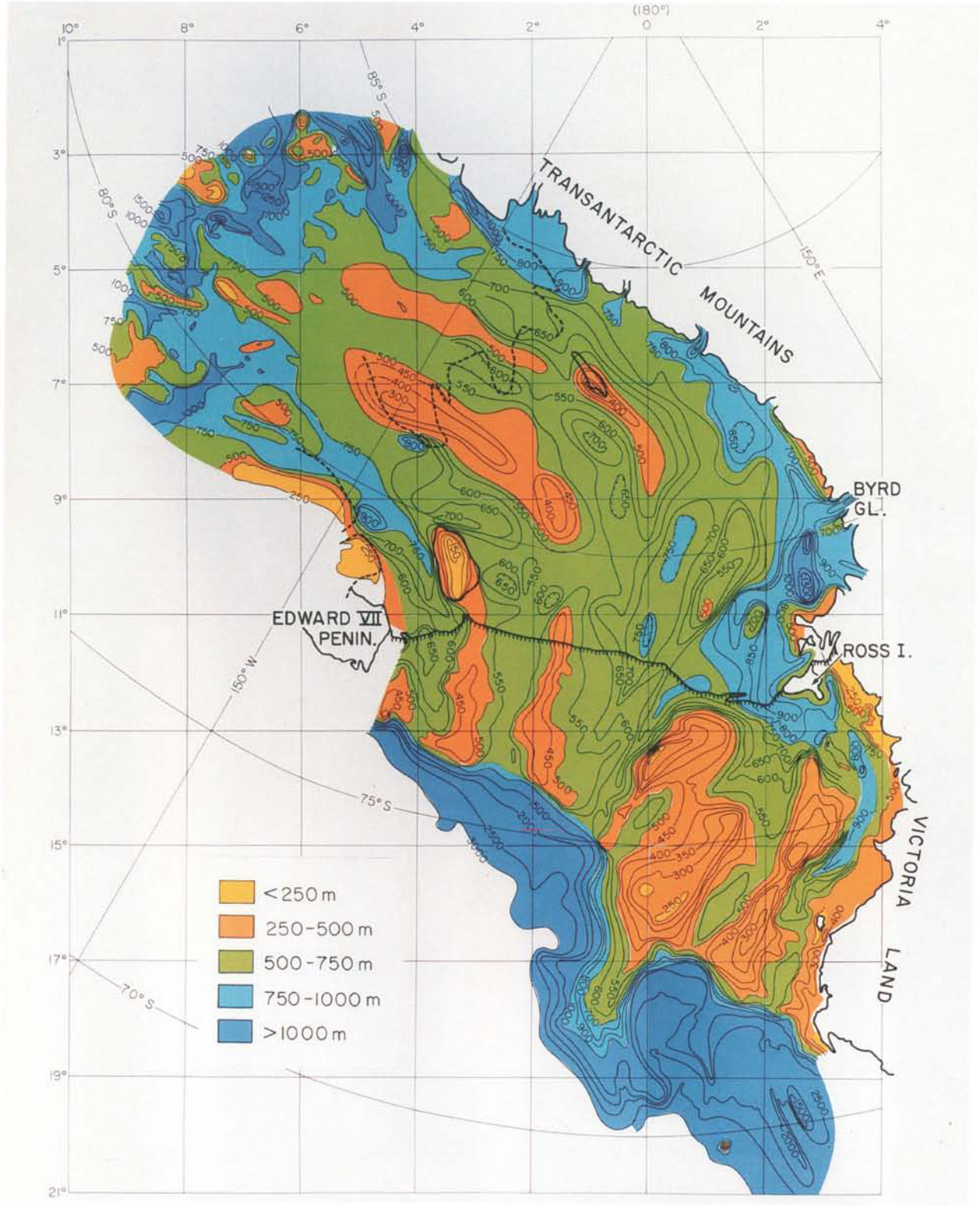

Plate 3. Map of the combined submarine and subglacial topography for the entire "Ross Embayment." First presented by Albert et al. [1978].

of a peak or trough across the spread of detectors), are related by the equation

$$U = c + k \frac{dc}{dk}$$

where k is the wave number.

Surface waves appeared clearly on the RIGGS III refraction records, especially where the shot was more than 1 km from the

spread. Because only vertical component geophones had been used, however, the types of waves could not be identified positively. On the basis of the information from the refraction records, an experiment was designed for RIGGS IV specifically to study surface waves. Horizontal-longitudinal (HL), horizontal-transverse (HX), and vertical (V) geophones all were used in the detecting spread. Charge sizes, shot depths, and shot distances were varied to produce as many different types of surface waves as possible. Table 6 lists the parameters of the shots at Q13 along with the types of waves detected.

First-mode (R_1) and second-mode (R_2) Rayleigh waves were identified on the seismograms (see Figures 11 and 12) by their elliptical motion. The particle motion observed for the first-mode Rayleigh waves was generally retrograde elliptical, but sometimes the ellipse degenerated nearly to a straight line. We suspect minor interference from other wave arrivals, but note that the maximum phase shift was only 90°. With a minimum frequency of 15 Hz and a minimum travel time of 1 s, a 90° phase shift would only cause at most a 2% error in the group velocity. This might be a minor cause of the scatter exhibited in the dispersion data but could not be a source of major error in group velocities. Particle motion at the surface in the second mode is prograde, as expected.

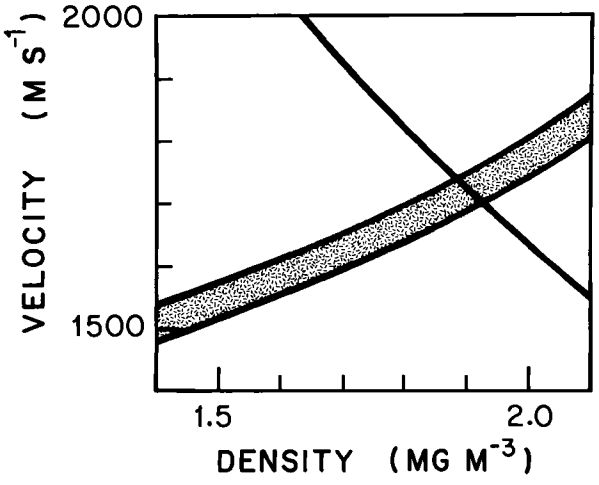

Fig. 10. Plots of velocity versus density in ocean floor sediment beneath station P19. The single curve is the relation found from the measured acoustic impedance; the shaded area denotes the range of values shown by Nafe and Drake [1963] and Hamilton [1971, 1982].

Surface waves with transverse motion, identified as Love waves, also appear on most of the seismic records. Group and phase velocity dispersion curves for all the observed Rayleigh and Love waves are plotted

TABLE 6. Seismic Records Used to Study Surface Waves at Station Q13

Shot Number	Charge, kg	Depth, m	Minimum Distance, m	Spread Length, m	Types of Waves Observed, by Component V	HL	HX
8	1	3	1110	330	R_2	R_2[a]	L
9	1	3	1110	330	R_2[a]	R_2,R_1	L
10	1	5	1170	330	R_2	R_2[a]	L
11	5	5	1170	330	R_2	R_2[a]	L[b]
12	23	5	1170	330	R_1	R_1	L
13	11	3	1140	330	R_2, R_1	R_2, R_1	L
66[c]	5	5	9752	330	PL, R_2	PL	PL
67	39	5	9752	330	PL, R_2	PL	PL
69	380	100	8782	570	PL, R_2	PL	PL

Surface wave types: R_1 and R_2, first and second Rayleigh modes; L, first Love mode; PL, leaky mode.

[a]Superimposed on other modes.

[b]Weak.

[c]All waves very weak.

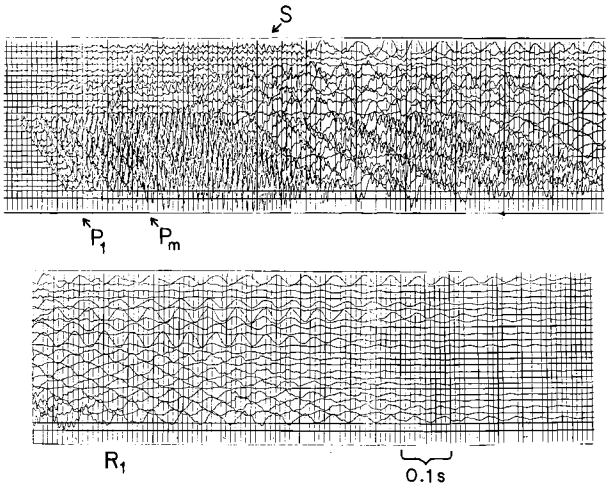

Fig. 11. Seismogram for shot 12 at station Q13; 23 kg in a 5-m hole, 1500 m from the most distant geophones (1 and 24). Geophone spacing: 30 m. Geophone orientations: traces 1, 5, 7, 9, and 11, HL; traces 2, 3, 4, 6, 8, and 10, HX; all others, V. There is a 0.04-s overlap between the upper and lower sections of the record.

in Figures 13 through 16.

Rayleigh and Love waves both propagate at speeds less than that of shear waves. Another wave train, detected from shots at distances of around 10 km, arrives much sooner than the shear wave and only slightly after the compressional wave. We identify these as leaky mode waves [see Laster et al., 1965] that develop from the constructive interference of the low-frequency components of P_m at large m (i.e., a large number of surface reflections) [Robinson, 1968]. Their observed dispersion properties are shown in Figures 17 and 18. Because of the impulsive nature of P_m arrivals for small m, the group and phase velocities of these waves could not be determined until about 450 ms after the first P wave.

The group velocity dispersion is fairly well defined for the leaky mode waves, but the phase velocity dispersion is not. We believe that this stems from the small time differences involved in the passage of these fast waves across the spread, combined with some phase distortion from remaining impulsive P_m arrivals. As no computer program was available to calculate the dispersion of leaky modes, these waves have not been considered further.

A computer program for calculating theoretical Rayleigh and Love wave dispersion curves from a layered model [Dorman, 1962] was used to calculate the dispersion expected from the values of v_p, v_s (two measured curves each for P, SV, and SH), and ρ (calculated from v_p) obtained by short-refraction shooting at station Q13 [Kirchner, 1978; Kirchner and Bentley, this volume] in this volume. The surface waves whose dispersion we measured all had frequencies greater than 13 Hz, corresponding to wavelengths of less than 125 m. As the ice thickness at station Q13 is about 330 m, the effect of the underlying water on the dispersion should be negligible. To check this, we calculated first- and second-mode Rayleigh waves for two models, one with ice and the other with water as the lower half-space, using a program from Herrmann [1978]. There was no difference to the nearest meter per second in phase or group velocities for frequencies greater than 20 Hz for the first mode and 30 Hz for the second mode. At lower frequencies the program failed for technical reasons related to the low wave velocity in the water layer. It is clear, however, that inclusion of a water layer would have no significant effect on the model fitting that we discuss below; so the water was ignored. For the curves presented, 39 layers were used; the layers were 1 m thick down to 30 m, then 5 m thick down to 70 m, with a half-space of ice beneath. Calculations for one particular case showed that using a larger number of layers does not change the calculated results but that 15 layers (all 5 m thick) are too few.

Dispersion curves for first- and second-

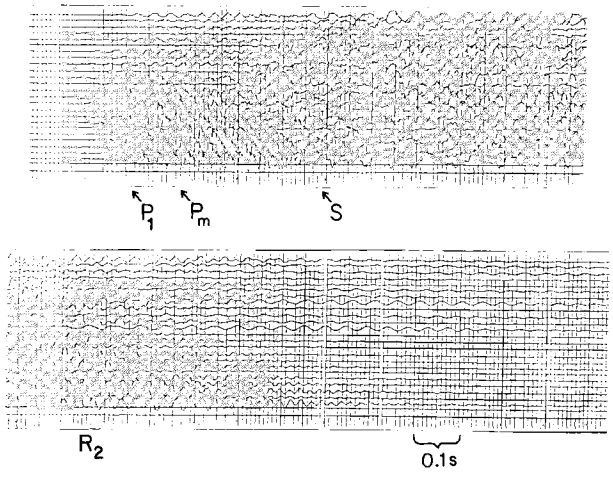

Fig. 12. Seismogram for shot 9 at station Q13. The energy source was a 0.9-kg charge in a 3-m hole, 1440 m from the most distant geophones (1 and 24). Geophone spacing and orientations as in Figure 10. There is a 0.10-s overlap between the upper and lower sections of the record.

mode Rayleigh waves and first-mode Love waves were calculated; they are shown, along with the observed data, in Figures 13 to 16. All models and velocities discussed in this section are tabulated in Appendix C.

The calculated dispersion curves are everywhere higher in velocity than the observed dispersion points. An examination of Poisson's ratio (σ) as a function of depth for the velocities used shows that the values in the upper few meters are certainly incorrect. The values for the first meter are negative, which is physically impossible, and other values at shallow depths are definitely too low. Furthermore, the four curves of σ versus depth (from SV and SH waves each on two different profiles) are widely different in the top 30 m. Three additional models with more reasonable values of σ were therefore investigated. Since the shear wave arrivals can be distorted by P waves and are more difficult than P arrivals to read accurately from the seismograms, we assumed for these models that the P wave velocities are correct; v_s was calculated from the assumed values of σ.

The three new models for v_s, designated A, B, and C, were calculated by assuming that in model A, σ decreases upward from 0.30 to 0.17 in the upper 10 m; in model B, σ is constant at a value of 0.32 in this region, and in model C, σ decreases upward from 0.30 to 0.23. Models A and B represent approximate lower and upper bounds, respectively, to the values of Poisson's ratio found in measurements on polar snow [Mellor, 1964, Figure III-5]. Model C represents reasonable values of σ and is based on the measurements of Thiel and Ostenso [1961] and Kohnen and Bentley [1973]. Only 15 layers (rather than 39) were used in the calculation; the effect of this is to overestimate velocities by an amount that is negligible for phase velocities at the observed frequencies and reaches a maximum of about 100 m s^{-1} for the highest-frequency group velocities.

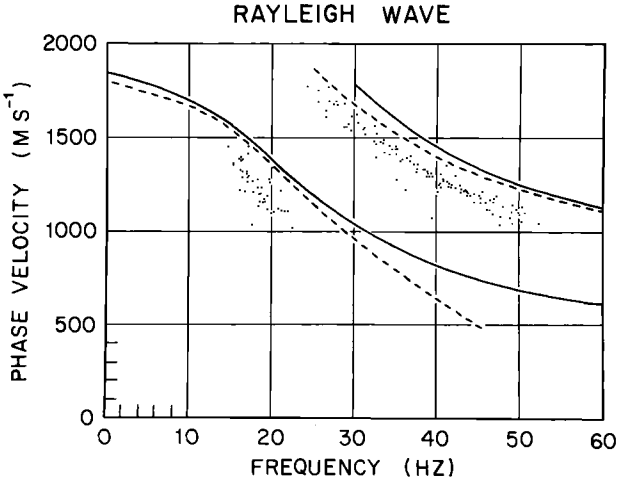

Fig. 14. Rayleigh wave phase velocity dispersion at station Q13, first and second modes. Dots are observed values; lines are calculated according to models SV1 (solid lines) and SV2 (dashed lines).

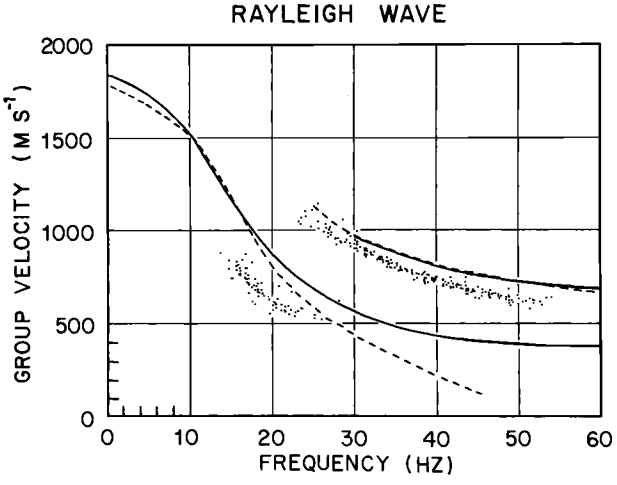

Fig. 13. Rayleigh wave group velocity dispersion at station Q13, first and second modes. Dots are observed values; lines are calculated according to models SV1 (solid lines) and SV2 (dashed lines).

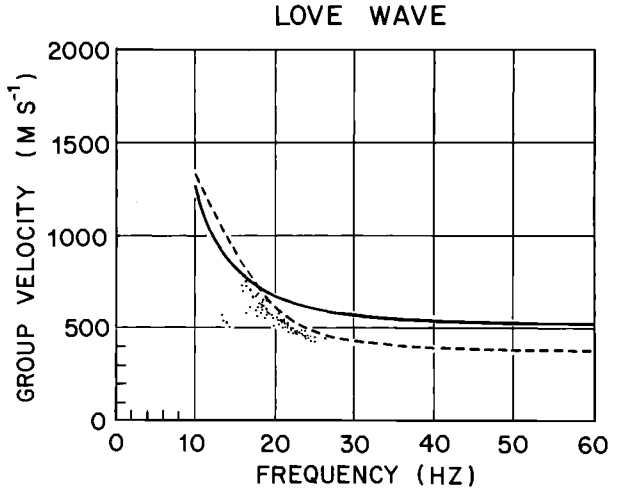

Fig. 15. Love wave group velocity dispersion at station Q13. Dots are observed values; lines are calculated according to models SH1 (solid line) and SH2 (dashed line).

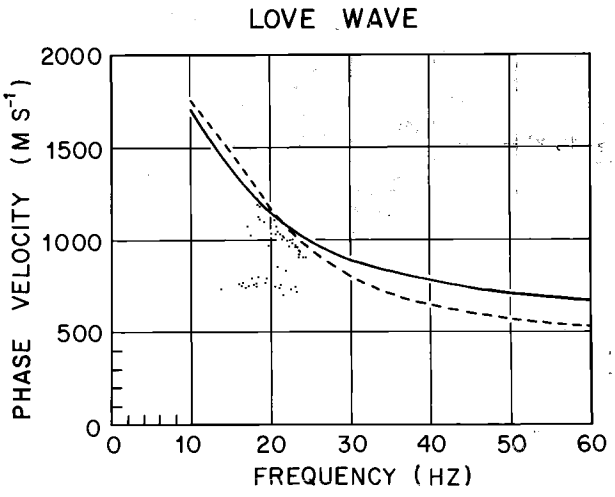

Fig. 16. Love wave phase velocity dispersion at station Q13. Dots are observed values, lines are calculated according to models SH1 (solid line) and SH2 (dashed line).

Plots of the Rayleigh wave dispersion curves calculated using these models (Figures 19 to 24) show a striking change in the second mode, which is much lower in velocity for the new models than for the model based on measured values of v_s. Models A and C both show good agreement with the observed second-mode dispersion. The changes in the first mode are less, since it is less dependent than the higher modes on wave velocities at shallow depths [Kovach, 1978].

These models show clearly how strongly the higher-mode dispersion curves depend on the shear wave velocity in the upper 10 m of the ice. When reasonable velocities are used, good agreement can be obtained between the observed and calculated second-mode Rayleigh wave. Unfortunately, the velocities in the first mode are changed very little in these models. It appears that we must look to a cause other than incorrect v_s in the uppermost firn layers to explain the difference in the first mode between theory and observation.

Robinson [1968] studied surface wave dispersion at four of the sites occupied by the Ross Ice Shelf Traverse (RIST), but only at RIST station C-16 were the shear wave velocities measured at the same site. Geographically, RIGGS station C-16 was about 8 km grid southeast of RIST C-16. Because of ice movement, however, RIST C-16 actually was about 10 km grid southwest of RIGGS C-16 at the time of occupation of the latter. As a check on the comparability of results, we have calculated dispersion curves for RIGGS C-16 using velocities determined by Kirchner [1978] [Kirchner and Bentley, this volume]. Robinson's [1968] and our calculated dispersion curves are in agreement.

Robinson [1968] found a large discrepancy between the observed and calculated dispersion at station C-16, just as we have at station Q13. He also found that assuming an anisotropy in shear wave velocities of 20%, with vertical velocities lower than horizontal velocities, brought the theoretical dispersion curves into good agreement with observations.

We have not calculated dispersion curves for anisotropic models, but we can draw some conclusions by comparing our results with Robinson's [1968]. The observed group velocities for the fundamental mode Rayleigh waves observed at our station Q13 (Figure 12) are essentially identical with those found by

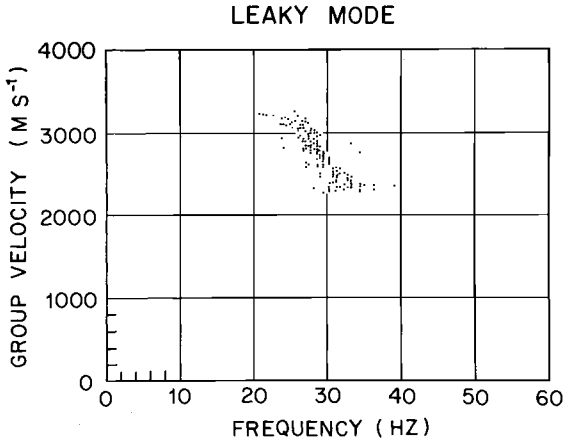

Fig. 17. Observed leaky mode group velocity dispersion at station Q13.

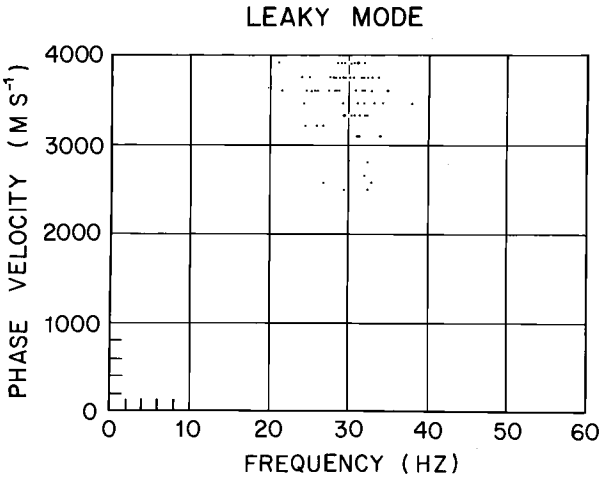

Fig. 18. Observed leaky mode phase velocity dispersion at station Q13.

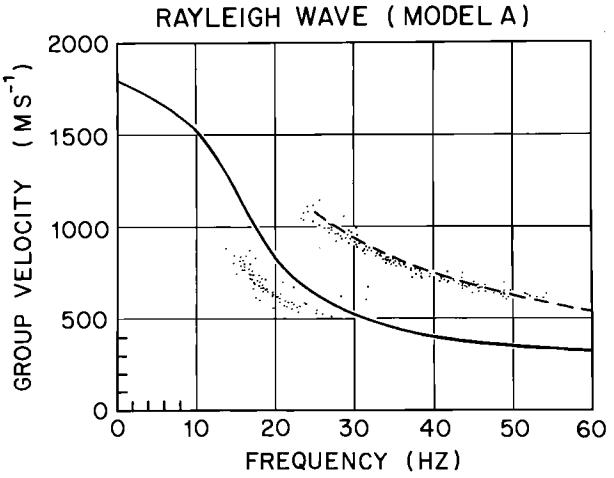

Fig. 19. Rayleigh wave group velocity dispersion at station Q13. Data as in Figure 14. Curves calculated according to model A.

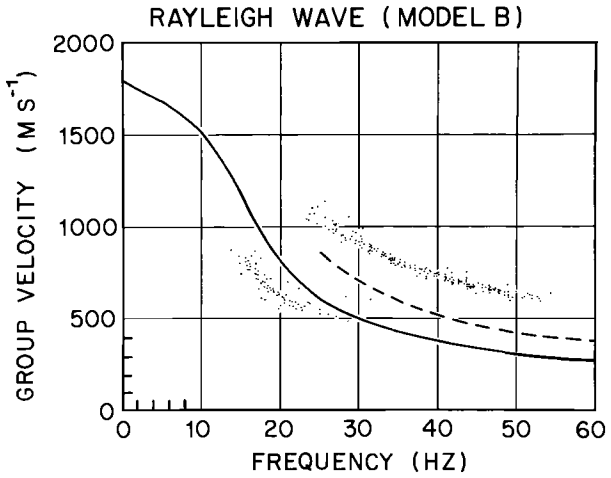

Fig. 21. Rayleigh wave group velocity dispersion at station Q13. Data as in Figure 14. Curves calculated according to model B.

Robinson [1968] for station C-16. The theoretical dispersion curves assuming isotropy (i.e., ours for station Q13 and his for station C-16) are also close to each other. It follows, then, that the 20% anisotropy which he proposed also should bring the theoretical and observed dispersion into agreement at station Q13. If a 20% anisotropy in shear wave velocity exists, it is too large to be the result solely of anisotropy in crystalline structure; it would presumably arise at least in part from the different characteristics of the different layers in the stratigraphic sequence. If we may use crystalline anisotropy as an analogy, however, then it is quite consistent to find low values of v_s associated with normal or even relatively high values of v_p for propagation in the vertical direction [Bennett, 1972], such as those suggested by the uphole time measurement at station R16 (discussed above).

A difficulty that arises with this model is that it could destroy the agreement between theory and observation for the second-mode Rayleigh waves found by correcting Poisson's ratio in the uppermost firn. This problem perhaps can be circumvented by attributing the anisotropy more to the deeper layers, where it could be attri-

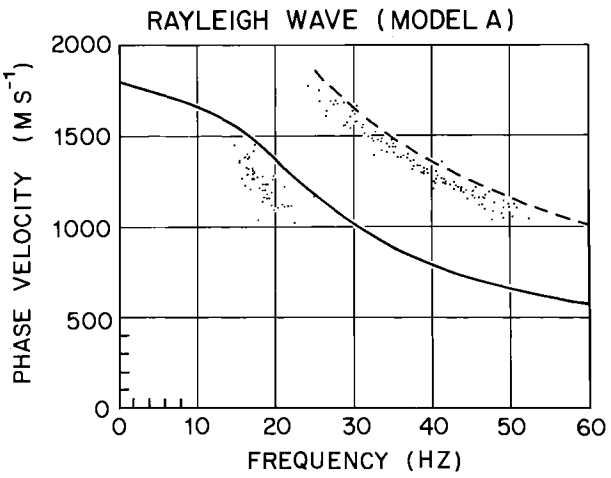

Fig. 20. Rayleigh wave phase velocity dispersion at station Q13. Data as in Figure 15. Curves calculated according to model A.

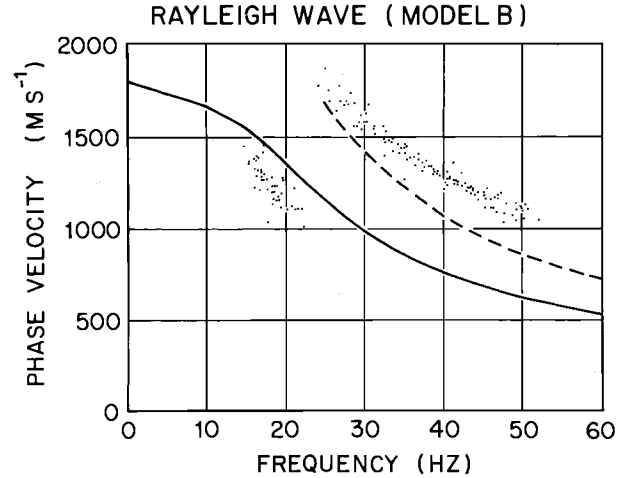

Fig. 22. Rayleigh wave phase velocity dispersion at station Q13. Data as in Figure 15. Curves calculated according to model B.

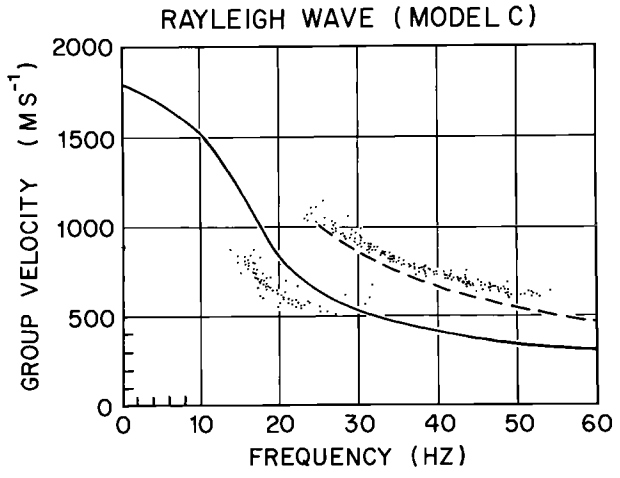

Fig. 23. Rayleigh wave group velocity dispersion at station Q13. Data as in Figure 14. Curves calculated according to model C.

butable partly to crystalline anisotropy [Gow, 1963].

Summary

Inversion of travel time curves from refraction shooting shows P wave velocities that increase monotonically with depth in the upper layers of the ice. The measured P wave velocities at three locations on the ice shelf increase from about 500 m s^{-1} at the surface to about 3800 m s^{-1} at a depth of 60 m. The density as a function of depth at these three locations has been calculated from the P wave velocities using the empirical equation of Kohnen [1972]. Maximum P wave velocities measured at four locations on the ice shelf show a large range of values (3530 to 3900 m s^{-1}) primarily indicative of lateral inhomogeneities (e.g. sloping constant-velocity surfaces) but perhaps also resulting from anisotropy.

The values of ice thickness and water thickness determined from seismic reflection shooting at station J9DC agree very closely with those measured in the access hole there. Water thickness values for 89 additional stations have been determined by reflection shooting, and a bathymetric map of the entire Ross Embayment has been drawn.

Reflection amplitudes were used, along with standard curves of velocity versus density in marine sediments, to calculate a density of 1.90 ± 0.12 Mg m^{-3} and a velocity of 1.72 ± 0.06 km s^{-1} in the uppermost sediment beneath one station (P19).

Rayleigh waves, Love waves, and leaky mode waves were recorded in surface wave experiments at station Q13. An analysis based on measured velocities shows that a layered model, with layers 1 m thick in the upper 30 m and 5 m thick below, suffices for calculating dispersion curves. Theoretical dispersion curves calculated from the measured P wave and S wave velocities give higher values than those observed. An examination of Poisson's ratio as a function of depth reveals errors in the velocities determined by refraction shooting in the upper 10 m of the ice. Correcting those errors by assuming that v_p was measured accurately and taking a reasonable variation in Poisson's ratio bring the calculated and observed second-mode dispersion curves into agreement but have little effect on the first mode. The introduction of S wave anisotropy characterized by a higher vertical than horizontal velocity could bring the observed and calculated first-mode dispersions into agreement.

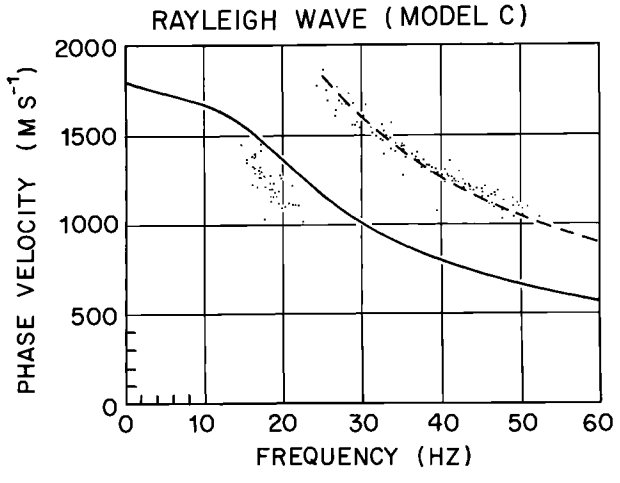

Fig. 24. Rayleigh wave phase velocity dispersion at station Q13. Data as in Figure 15. Curves calculated according to model C.

Acknowledgments. The authors wish to express their appreciation to the other members of the University of Wisconsin field parties, L. L. Greischar, K. C. Jezek, J. F. Kirchner, H. Pollak, and S. Shabtaie, for their aid in all aspects of our work. We are also grateful for the cooperation of members of the groups from the University of Maine, the U.S. Geological Survey, and the University of Copenhagen. Excellent air support in Twin Otter aircraft was supplied by the British Antarctic Survey and Bradley Air Services, Ltd. We thank P. Dombrowski and S. H. Werther for drafting illustrations, and A. N. Mares and J. V. Campbell for manuscript preparation. H. J. Dorman kindly made avail-

able to us the computer program we used to calculate surface wave dispersion. This work was supported by the National Science Foundation under grants DPP72-05802, DPP76-01415, DPP79-20736, and DPP-8119989. This is contribution 435 of the Geophysical and Polar Research Center, University of Wisconsin, Madison.

References

Acharya, H. K., Surface wave dispersion in Byrd Land, Antarctica, Bull. Seismol. Soc. Am., 62, 955-959, 1972.

Acharya, H. K., and C. R. Bentley, Investigation of surface wave dispersion in an inhomogeneous medium by the finite difference method, Bull. Seismol. Soc. Am., 68, 1381-1386, 1978.

Albert, D. G., C. R. Bentley, and L. L. Greischar, Submarine topography of the Ross Embayment from the continental shelf to the Byrd Subglacial Basin (abstract), Eos Trans. AGU, 59, 308-309, 1978.

Bennett, H. F., Measurements of ultrasonic wave velocities in ice cores from Greenland and Antarctica, CRREL Res. Rep. 237, U.S. Army Cold Regions Res. and Eng. Lab., Hanover, N. H., 1972.

Bentley, C. R., Seismic anisotropy in the West Antarctic ice sheet, in Antarctic Snow and Ice Studies II, Antarct. Res. Ser., vol. 16, edited by A. P. Crary, pp. 131-177, AGU, Washington, D. C., 1971.

Bentley, C. R., The Ross Ice Shelf geophysical and glaciological survey (RIGGS): Introduction and summary of measurements performed, in The Ross Ice Shelf: Glaciology and Geophysics, Antarct. Res. Ser., vol. 42, edited by C. R. Bentley and D. E. Hayes, pp. 1-20, AGU, Washington, D. C., 1984.

Bentley, C. R., J. W. Clough, K. C. Jezek, and S. Shabtaie, Ice thickness patterns and the dynamics of the Ross Ice Shelf, J. Glaciol., 24, 287-294, 1979.

Clough, J. W., and B. L. Hansen, The Ross Ice Shelf Project, Science, 203, 433-434, 1979.

Cooper, A. K., F. J. Davey, and J. C. Behrendt, Seismic stratigraphy and structure of the Victoria Land Basin, western Ross Sea, Antarctica, in The Antarctic Continental Margin: Geology and Geophysics of the Western Ross Sea, CPCEMR Earth Sci. Ser., vol. 5B, edited by A. K. Cooper and F. J. Davey, pp. 27-76, Circum-Pacific Council for Energy and Mineral Resources, Houston, Texas, 1987.

Crary, A. P., Glaciological studies at Little America Station, Antarctica, 1957 and 1958, IGY Glaciol. Rep. 5, Am. Geogr. Soc., New York, 1961.

Crary, A. P., E. S. Robinson, H. F. Bennett, and W. W. Boyd, Jr., Glaciological studies of the Ross Ice Shelf, Antarctica, 1957-1960, IGY Glaciol. Rep. 6, Am. Geogr. Soc., New York, 1962a.

Crary, A. P., E. S. Robinson, H. F. Bennett, and W. W. Boyd, Jr., Glaciological regime of the Ross Ice Shelf, J. Geophys. Res., 67, 2791-2807, 1962b.

Davey, F. J., Geophysical studies in the Ross Sea region, J. R. Soc. N. Z., 11, 465-479, 1981.

Davey, F. J., K. Hinz, and H. Schroeder, Sedimentary basins of the Ross Sea, in Antarctic Earth Science, edited by R. L. Oliver, P. R. James, and J. B. Jago, Australian Academy of Science, Canberra, 1983.

Dorman, J., Period equation for waves of Rayleigh type on a layered, liquid-solid half space, Bull. Seismol. Soc. Am., 52, 389-397, 1962.

Gow, A. J., The inner structure of the Ross Ice Shelf at Little America V, Antarctica, as revealed by deep core drilling, IASH Publ. 61, 272-284, 1963.

Gow, A. J., Deep core studies of the crystal structure and fabrics of Antarctic glacier ice, CRREL Res. Rep. 282, 21 pp., U. S. Army Cold Regions Res. and Eng. Lab., Hanover, N. H., 1970.

Grant, F. S., and G. F. West, Interpretation Theory in Applied Geophysics, 583 pp., McGraw-Hill, New York, 1965.

Greischar, L., and C. R. Bentley, Isostatic equilibrium grounding line between the West Antarctic ice sheet and the Ross Ice Shelf, Nature, 283, 651-654, 1980.

Hamilton, E. L., Prediction of in-situ acoustic and elastic properties of marine sediments, Geophysics, 36, 266-284, 1971.

Hamilton, E. L., Sound velocity and related properties of marine sediments, J. Acoust. Soc. Am., 72, 1891-1904, 1982.

Hayes, D. E., and F. J. Davey, A geophysical study of the Ross Sea, Antarctica, Initial Rep. Deep Sea Drill. Proj., 28, 807-907, 1975.

Herrmann, R. B. (Ed.), Computer Programs in Earthquake Seismology, vol. 2, Surface Wave Programs, Publ. 241, Department of Earth and Atmospheric Sciences, St. Louis University, St. Louis, Mo., 1978.

Herron, S. L., and C. C. Langway, Jr., A comparison of ice fabrics and textures at Camp Century, Greenland, and Byrd Station, Antarctica, Ann. of Glaciol., 3, 118-124, 1982.

Herron, S. L., C. C. Langway, Jr., and K. A. Brugger, Ultrasonic velocities and crystalline anisotropy in the ice core from Dye 3, Greenland, in Greenland Ice Core: Geophysics, Geochemistry, and the

Environment, Geophys. Monogr. Ser., vol. 33, edited by C. C. Langway, Jr., H. Oeschger, and W. Dansgaard, pp. 23-31, AGU, Washington, D. C. 1985.

Houtz, R., and F. J. Davey, Seismic profiler and sonobuoy measurements in Ross Sea, Antarctica, J. Geophys. Res., 78, 3448-3468, 1973.

Jiracek, G. R., and C. R. Bentley, Velocity of electromagnetic waves in Antarctic ice, in Antarctic Snow and Ice Studies II, Antarct. Res. Ser., vol. 16, edited by A. P. Crary, pp. 199-208, AGU, Washington, D. C., 1971.

Kirchner, J. F., Seismic refraction studies on the Ross Ice Shelf, Antarctica, M.S. thesis, Univ. of Wis., Madison, Wis., 1978.

Kirchner, J. F., and C. R. Bentley, RIGGS III: Seismic short-refraction studies using an analytical curve-fitting technique, in The Ross Ice Shelf: Glaciology and Geophysics, Antarctic Res. Ser., vol. 42, edited by C. R. Bentley and D. E. Hayes, AGU, Washington, D. C., this volume.

Kirchner, J. F., C. R. Bentley, and J. D. Robertson, Lateral density differences at a site on the Ross Ice Shelf, Antarctica, from seismic measurements, J. Glaciol., 24, 309-312, 1979.

Kohnen, H., Uber die Beziehung zwischen seismischen Geschwindigkeiten und der Dichte in Firn und Eis, Z. Geophys., 38, 925-935, 1972.

Kohnen, H., The temperature dependence of seismic waves in ice, J. Glaciol., 13, 144-147, 1974.

Kohnen, H., and C. R. Bentley, Seismic refraction and reflection measurements at Byrd Station, Antarctica, J. Glaciol., 12, 101-111, 1973.

Kohnen, H., and A. J. Gow, Ultrasonic velocity investigations of crystal anisotropy in deep ice cores from Antarctica, J. Geophys. Res., 84, 4865-4874, 1979.

Korotkevich, E. S., V. N. Petrov, N. I. Barkov, L. I. Suchonosora, D. N. Smitriyev, and V. G. Portnov, Results of the study of the vertical structure of Antarctic ice sheet in the vicinity of Vostok, Antarctica (in Russian), Sov. Antarct. Exped. Inf. Bull., 97, 135-147, 1978.

Kovach, R. L., Seismic surface waves and crustal and upper mantle structure, Rev. Geophys., 16, 1-13, 1978.

Laster, S. J., J. G. Foreman, and A. F. Linville, Theoretical investigation of modal seismograms for a layer over a half space, Geophysics, 30, 571-596, 1965.

Mellor, M., Properties of snow, CRREL Monogr. III-A1, U. S. Army Cold Regions Res. and Eng. Lab., Hanover, N. H., 1964.

Nafe, J. E., and C. L. Drake, Physical properties of marine sediments, in The Sea, vol. 3, edited by M. N. Hill, pp. 794-815, John Wiley, New York, 1963.

Rand, J. H., 100-meter ice cores from the South Pole and the Ross Ice Shelf, Antarct. J. U. S., 10, 150-151, 1975.

Robertson, J. D., Geophysical studies on the Ross Ice Shelf, Antarctica, Ph.D. thesis, Univ. of Wis., Madison, Wis., 1975.

Robertson, J. D., and C. R. Bentley, Seismic studies on the grid western half of the Ross Ice Shelf: RIGGS I and RIGGS II, in The Ross Ice Shelf: Glaciology and Geophysics, Antarct. Res. Ser., vol. 42, edited by C. R. Bentley and D. E. Hayes, AGU, Washington, D. C., this volume.

Robertson, J. D., C. R. Bentley, J. W. Clough, and L. L. Greischar, Sea bottom topography and crustal structure below the Ross Ice Shelf, in Antarctic Geoscience, edited by C. Craddock, pp. 1083-1090, University of Wisconsin Press, Madison, Wis., 1982.

Robinson, E. S., Seismic wave propagation on a heterogeneous polar ice sheet, J. Geophys. Res., 73, 739-753, 1968.

Rose, K. E., High density radio echo sounding of bedrock in Marie Byrd Land, Antarctica, in Antarctic Geoscience, edited by C. Craddock, pp. 985-992, University of Wisconsin Press, Madison, Wis., 1982.

Russell-Head, D. S., and W. F. Budd, Ice-sheet flow properties derived from bore-hole shear measurements combined with ice-core studies, J. Glaciol., 24, 117-130, 1979.

Shabtaie, S., and C. R. Bentley, Tabular icebergs: Implication from geophysical studies of ice shelves, J. Glaciol., 28, 413-430, 1982.

Thiel, E., and N. A. Ostenso, Seismic studies on Antarctic ice shelves, Geophysics, 26, 706-715, 1961.

(Received December 23, 1987;
revised August 18, 1989;
accepted November 22, 1989.)

The Ross Ice Shelf: Glaciology and Geophysics
Antarctic Research Series, Volume 42, Paper 5, Pages 109-126

RIGGS III: SEISMIC SHORT-REFRACTION STUDIES USING AN ANALYTICAL CURVE-FITTING TECHNIQUE

Joseph F. Kirchner

Atlantic Richfield Company, Houston, Texas 77056

Charles R. Bentley

Geophysical and Polar Research Center, University of Wisconsin
Madison, Wisconsin 53706

Abstract. Several short-refraction profiles completed on the Ross Ice Shelf, Antarctica, during the 1976-1977 summer (austral) season (RIGGS III) have been analyzed and interpreted. Instead of estimating slopes from the travel time curves graphically, we have fit the travel times with an analytical function of a hybrid exponential and linear form by means of a nonlinear regression computer program. Differentiation of the resulting expression for the best fitting curve produces the velocity-distance function. Velocity-depth curves were evaluated via the WHB integral, and from these, density-depth values were computed using Kohnen's (1972) empirical relation. Comparisons of P waves and S waves (both horizontally and vertically polarized) along different azimuthal directions at three sites indicate substantial anisotropy in at least the upper 30-40 m and show further that transverse isotropy cannot serve as a good model for this region. Velocity gradients calculated and fit segmentally by exponential functions after the manner of Kohnen and Bentley (1973) and Robertson and Bentley (1975) yielded estimates of depths to different densification horizons. The results are in agreement with those of other similar studies.

Contents

Introduction

Seismic refraction experiments were conducted at several sites on the Ross Ice Shelf, Antarctica, as part of the Ross Ice Shelf Geophysical and Glaciological Survey (RIGGS) during the summer season of 1976-1977 (RIGGS III). Compressional (P) waves and shear (S) waves of both horizontal (SH) and vertical (SV) polarization were all recorded. The object was to determine travel time curves and from them the velocity variations as a function of depth. With this information, density as a function of depth could be determined and an assessment could be made, at least qualitatively, about the anisotropy in the upper 70-80 m of the ice shelf.

The P wave velocity v_p and the S wave velocity v_s both increase with depth in the upper part of the ice shelf. The gradient is very large near the surface, then gradually decreases with depth down to the maximum velocity, which is reached at about 80 m. Below that the velocities decrease owing to downwardly increasing temperatures. The seismic waves are therefore refracted downward in the lower shelf; so only the velocity structure in the upper shelf can be determined from refraction shooting.

P wave short-refraction experiments were made at stations C-16, J9DC, Q13, M14, H13, and N19 (see Figure 1 for map of locations and Bentley [1984] and Thomas et al. [1984] for tabulated positions). Stations C-16, J9DC, and Q13 were base camp sites, and it was at these locations that the shear wave studies and more detailed work were carried out. Stations H13, M14, and N19 were remote field stations each occupied for only 1 day; so there was time only for limited P wave experiments.

Method of Operation

All measurements were recorded on two SIE (model RS-49R) 24-channel analog amplifier and filter systems and SIE (model R-6B)

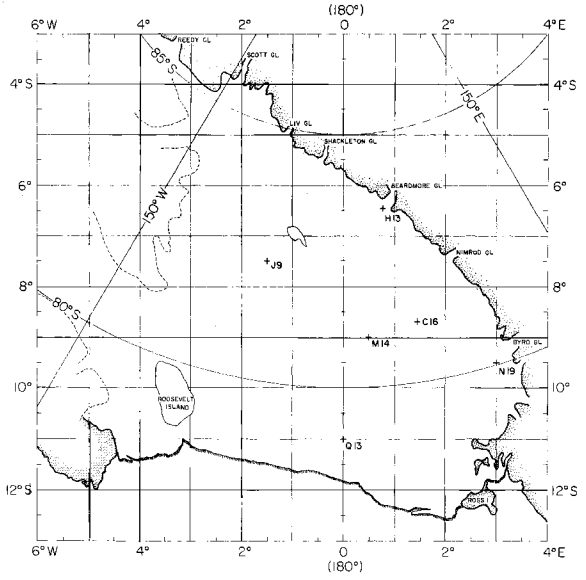

Fig. 1. Map of the Ross Ice Shelf showing the locations of the stations at which short-refraction experiments were carried out during RIGGS III. Stations J9DS and J9DC are at essentially the same location as station J9. In the rectangular grid coordinate system shown, meridians are parallel to the Greenwich meridian, with grid north toward Greenwich. The origin of the system is at the South Pole, and 1° of grid latitude or longitude equals 1° of geographic latitude.

recording oscillographs. The systems have a basic frequency range of 2-300 Hz (between the 3-dB points) and constant-gain amplifiers variable from 15 to 105 dB. Vertical and horizontal geophones with a resonant frequency of 7-30 Hz were used. Data were recorded on dry-writing photosensitive paper. Some sample seismograms are shown in Figure 2.

The usual field procedure was to lay out a 24-geophone in-line spread with 2-, 5-, and 10-m intervals between receivers and to record a series of hammer blows on a 4-by-4 wooden stake at the end of the spread and at distances out to about 350 m, usually with 50 m between shot points. Distances were measured by steel tape (good to 1 part in 10^4) and by Tellurometer (accurate to 20 or 30 mm). To record P waves, the geophones were oriented vertically and the 4 x 4 wooden stake was hit vertically. For distances greater than 300-400 m, small explosive charges were used as the source. Shear waves were recorded by placing geophones on their sides and hitting the stake horizontally. Transverse and longitudinal polarizations (SH and SV, respectively) were generated and detected with the appropriate orientations of the hammer blows and geophones [cf. Robertson and Bentley, this volume, Figure 17]. Since explosions do not induce good shear arrivals, the S wave profiles were limited in length by the signal strengths of the hammer blow method. Time breaks (shot instants) were provided by a geophone next to the stake, when it was used, or by radio from the blaster when explosive charges were set off. The specifications of all the short-refraction experiments are listed in Table 1.

At the base camp stations C-16, J9DC, and Q13, two or three profiles with a common center point were completed along different azimuths, thus permitting comparison of P waves and S waves along different directions.

Data Analysis

Travel times on the seismograms were picked to a precision of 0.1 ms with a Bausch and Lomb 7 power magnifier scaled to 0.1 mm/division. The picking accuracy is estimated to be 0.2-0.4 ms, depending upon the clarity of the arrival. The travel times were plotted and found in most cases to increase monotonically with distance, with the rate of increase decreasing with time, so that the travel time curve asymptotically approached a straight line. The inverse slope of the asymptote gives the maximum velocity in the ice.

The travel time curves were then converted to curves of apparent velocity versus distance. Methods previously used for obtaining the slope usually combined a graphical technique for data points at the smaller distances, where the curvature is more pronounced, with least squares fits to straight line segments, record by record, at the larger distances (>200-300 m) [e.g., Robertson and Bentley, this volume]. However, the graphical method has the disadvantage of being subject to observer bias, and the least squares fitting by segments does not take full advantage of the continuity of the entire travel time curve. We therefore sought a more analytical way to determine the slope.

After some investigation we settled on the form given by equation (1), which was found to provide a close fit to the travel time curves:

$$t = t_1(1 - \exp(a_1 x)) + t_2(1 - \exp(-a_2 x)) + v_m^{-1} x \qquad (1)$$

where t_1, a_1, t_2, a_2, and v_m^{-1} are the constants to be determined by the best fit, x is the distance between shot point and receiver, and t is the travel time. Correspondingly,

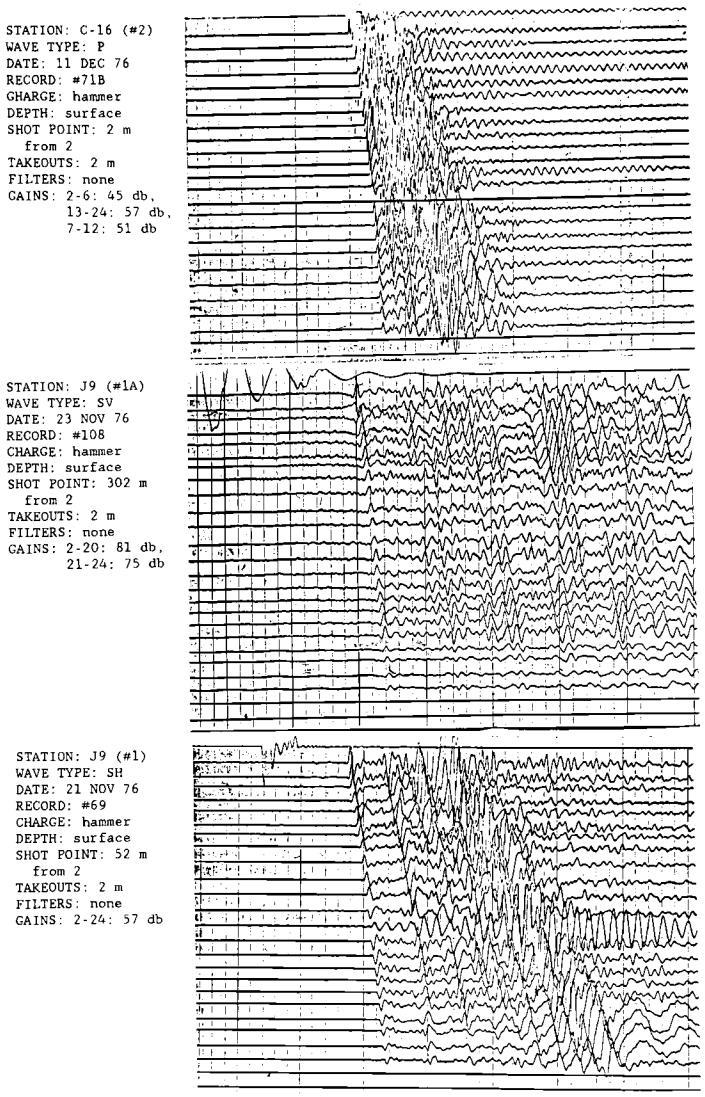

Fig. 2. Sample seismograms, RIGGS III short-refraction shooting.

the slope of the travel time curve is

$$\frac{dt}{dx} \equiv v^{-1} = v_1^{-1} \exp(-a_1 x) + v_2^{-1} \exp(-a_2 x) + v_m^{-1} \qquad (2)$$

where $v_1^{-1} = a_1 t_1$, $v_2^{-1} = a_2 t_2$, and v is the apparent velocity measured at distance x. Clearly, v_m is the asymptotic apparent velocity at large distance.

The exponential form of equation (1) satisfies the requirement of monotonic increase in velocity. That requirement comes both from the physical nature of the densification process, which causes a monotonic increase of density (hence velocity) with depth, and from the analytical requirement for unique conversion of the travel time curve into a velocity-depth curve. Two exponential terms are the minimum necessary to fit the initially rapid and then more gradual changes in slope, and the linear term forces the curve to approach a straight line at large distances, corresponding to the maximum velocity zone.

Fitting the travel time data to equation (1) can be done best by nonlinear regression techniques. In order for convergence to be rapid, good preliminary estimates of the constants are needed. Initial estimates for the constants to within an order of magnitude or better are easily obtained from the time-distance curves. As a test, however, values wrong by several orders of magnitude were fed into the model, and although the convergence was much slower, the final values matched

TABLE 1. Specifications for Short-Refraction Profiles, RIGGS III

Station	Profile Number	Magnetic Azimuth	Wave Type	Maximum Distance, m
C-16	1	000°	P	246
			SV	250
			SH	300
	2	120°	P	1256
	3	060°	P	1754
J9DC	1	000°	P	1242
			SV	346
			SH	346
	1A	090°	SV	396
			SH	446
	2	120°	P	1150
	3	060°	P	1012
Q13	1	000°	P	1012
			SV	297
			SH	500
	2	045°	P	1012
			SV	368
			SH	322
H13		000°	P	320
M14		000°	P	322
N19		000°	P	325

those obtained with good initial estimates. One can be reasonably certain, therefore, that the model selected will provide a unique fit to the data.

Many statistical tests appropriate for the linear case are not appropriate for the non-linear case [Draper and Smith, 1966]. One simple statistic that still applies is the standard deviation in travel time, or root-mean-square residual r, which in all cases was less than 1 ms. The P waves generally exhibited less scatter than the S waves, especially at short distances. This is to be expected, since the S wave travel times are more difficult to pick as a result of P wave interference and because structural irregularities in the upper few meters of snow affect the S wave arrivals more than the P wave arrivals. Also, more P wave than S wave data were available, resulting in better defined P wave travel time curves.

The velocities computed from equation (2) were converted to velocities as a function of depth z by numerical integration utilizing the program WHB written by J.D. Robertson [Robertson, 1975; Robertson and Bentley, this volume] to evaluate the Weichert-Herglotz-Bateman integral (see, e.g., Grant and West 1965). Figures 3 and 4 show the velocity-depth curves for all P wave and S wave data from RIGGS III; travel time plots are shown in Appendix A, and numerical results are presented in Appendix B. (All appendix material is on microfiche, enclosed in a pocket inside the back cover of this minibook.)

The coefficients that result from the least squares fitting to equation (1) are presented in Table 2, along with several other characteristic numbers related to equations (1) and (2). The constants from equation (2) are tabulated as velocities rather than slownesses. Also given are the apparent velocity at zero distance ($x = 0$), the distance x_1 at which the contributions of the first two terms to equation (2) are equal, and the total length of each profile (maximum x).

The first term in equation (2), which predominates at small distances, becomes less important than the second term for $x > x_1$. However, it does not diminish immediately to insignificance. At $x = 2x_1$, for example, the ratio of the second term to the first term is v_2/v_1, which on the average is about 4 (the range of v_2/v_1 for P waves in Table 2 is 2 to 6). Conversely, at $x = \frac{1}{2}x_1$, the first term is only $(v_2/v_1)^{\frac{1}{2}}$, or about twice the second. Furthermore, the linear term, v_m^{-1}, contributes importantly at all distances. Thus it is not possible to divide up the travel time curve, or the velocity-distance curve, into single-term segments.

In divising the piecewise exponential form of equation (1), we had secondarily in mind the piecewise exponential form of the velocity gradient as a function of depth in the firn, found widely on the Antarctic ice sheet, particularly by Robertson and Bentley [1975], and also discussed below and by Robertson and Bentley [this volume] and Albert and Bentley [this volume]. However, the "crossover" distance x_1 clearly does not correspond to any of the major changes in slope of the velocity gradient plots. The shallowest of the latter changes, at "B," occurs at an average depth of 14 m (Table 5), where the average velocity is about 2500 m s^{-1}; whereas the mean distance of x_1 for the same profiles is 10 m (about 3-m depth), corresponding to a velocity of only 1200 m s^{-1}. There is thus no simple correspondence between equation (1) and the variation of velocity gradient with depth, presumably

because of the opacity of the WHB integral. We, therefore, do not attach any specific physical significance to the form of equation (1) and consider it only as a means of obtaining a good, monotonic fit to travel time data. Nevertheless, we should note that the number of exponential terms in equation (1) will determine the maximum number of straight line segments that will appear on a plot of ln (dv_2/dz) versus z.

The constant v_m gives an asymptotic velocity that corresponds to the zone of maximum velocity in the ice shelf only if there are travel time points at large enough distances. A shot-to-spread distance of 600 m or more, which generally is achieved on the P wave profiles, is usually sufficient to assure that v_m differs insignificantly from the maximum velocity v_{max}; in our work the difference for v_p is no more than 26 m s^{-1} and mostly much less (compare Tables 2 and 3). In the case of the S waves, however, the maximum distance never exceeds 500 m and is often considerably less (Table 1), so the v_m values do not represent real maximum velocities. (In fact, for two profiles, C-16 line 1 SH and J9DC line 1A SV, the travel times were sufficiently well fit by the first two terms of equation (1), a fact that is shown in Table 2 by a very large value of v_m, meaning v_m^{-1} was assigned a value close to, or equal to, zero.) This suggests that it would be better to assign v_m an appropriate fixed value, that is, the S wave velocity in solid, isotropic ice. (The constants in equation (1) are interdependent; holding v_m^{-1} fixed compels changes in the other four constants.)

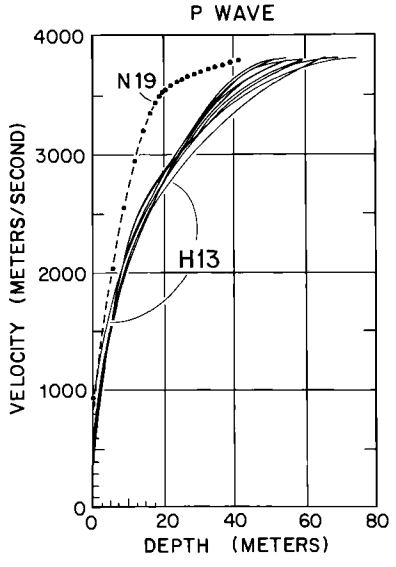

Fig. 3. Velocity-depth curves for P waves, all stations.

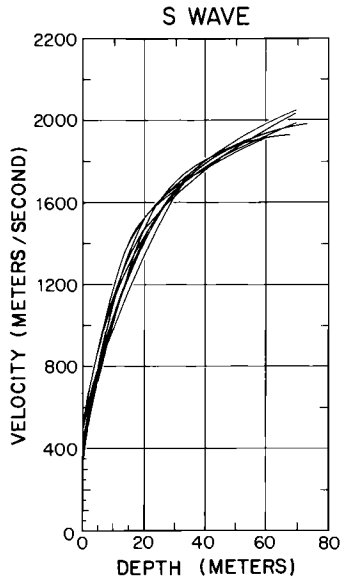

Fig. 4. Velocity-depth curves for S waves, all stations.

To test this, a comparison was made at two stations between the calculated velocity-depth values for v_m fixed at 1950 m s^{-1} and those for v_m floating. The wave velocities derived by the two methods from the shortest of the S wave profiles (C-16 SV; v_m = 2508 m s^{-1}) showed differences that varied in sign and numerically did not exceed 10 m s^{-1} at a given depth until z = 48 m. From z = 48 m to z = 51 m, the largest depth sampled according to the v_m-fixed model, the difference increased to 15 m s^{-1} in accordance with the higher value of v_m in the v_m-floating case.

The velocities from the longest S wave profile (Q13 SH line 1; v_m = 1993 m s^{-1}) showed a very similar variation: alternations in sign with magnitude less than 10 m s^{-1} down to 66 m, the maximum depth sampled by the v_m-fixed model. The velocity continued to increase to 1980 m s^{-1} at z = 74 m in the v_m-floating model, again reflecting the higher value of v_m. We conclude that the unrealistic values of v_m listed in Table 2 will have little effect on the calculated velocities except in the final 10 m or so in depth, a range in which depths to a given velocity should be treated with caution in any case because of the weak velocity gradient. The v_m-fixed model, therefore, was not applied to the S wave data from the other profiles, since the rewards would not have justified the added cost.

The temperatures in the ice shelf vary only a few degrees over the upper 100-m depth [Gow, 1963; Clough and Hansen, 1979]. Kohnen

TABLE 2. Characteristics of Travel Time Curves Derived From Least Squares Fits of Equations (1) and (2) to Short-Refraction Profiles, RIGGS III

Station	Line No.	t_1, ms	a_1, km^{-1}	v_1, $m\ s^{-1}$	t_2, ms	a_2, km^{-1}	v_2, $m\ s^{-1}$	v_m, $m\ s^{-1}$	Maximum x, m	Velocity at x = 0, $m\ s^{-1}$	x_1, m	r, ms
					P Waves							
C-16	1	11.6	114	754	28.1	8.1	4,410	4,196	246	560	17	0.3
	2	9.2	134	808	21.7	14.8	3,110	3,801	1,256	550	11	0.4
	3	10.6	131	717	20.9	11.8	4,050	3,808	1,754	520	14	0.6
J9DC	1	7.8	205	625	21.1	22.7	2,080	3,764	1,242	430	7	0.3
	2	8.1	185	668	21.4	23.3	2,000	3,802	1,150	440	7	0.6
	3	7.3	221	620	22.2	22.1	2,030	3,802	1,012	420	6	0.4
Q13	1	9.4	140	756	21.3	17.5	2,690	3,778	1,012	510	10	0.6
	2	9.0	178	623	21.4	18.9	2,480	3,791	1,012	440	9	0.4
H13		6.6	103	1458	26.8	12.1	3,080	3,909	320	790	8	0.3
M14		10.8	197	468	19.2	18.3	2,850	3,765	322	360	10	0.4
					S Waves							
C-16	1 SV	21.0	68	700	84.2	5.1	2,330	2,508	250	440	19	0.8
	SH	31.6	65	486	777.3	0.9	1,470		300	360	17	1.0
J9DC	1 SV	32.7	44	689	47.3	5.9	3,580	2,206	346	460	43	1.0
	SH	35.0	64	446	23.7	9.9	4,260	1,931	346	330	42	1.0
	1A SV	39.0	39	655	866.6	0.7	1,630	42,017	396	460	24	1.0
	SH	48.8	29.8	687	3.0	29.8	11,360	1,852	446	480	70	1.0
Q13	1 SV	22.1	76	600	62.4	5.8	2,790	2,302	297	410	22	0.6
	SH	29.8	48	695	31.7	9.0	3,500	1,993	500	450	41	0.4
	2 SV	13.3	98	769	39.8	16.0	1,570	1,933	368	410	9	0.7
	SH	27.3	96	381	128.1	3.2	2,420	2,909	322	300	20	0.7

TABLE 3. Maximum Values of v_p from Least Squares Analysis of Cross-Spread Velocities on Short-Refraction Stations, RIGGS III

Profile Number	Shot Number	Number of Points	Minimum Distance, m	Spread Length, m	Velocity m s^{-1}
			Station C-16		
1	27	8	617	110	3787 ± 30
	26	8	617	110	3762 ± 12
	31	21	654	170	3782 ± 8
Mean for Profile 1					3776 ± 8
2	102	14	602	130	3788 ± 30
	103	21	1036	220	3786 ± 19
Mean for Profile 2					3787 ± 16
3	95	16	600	150	3789 ± 27
	96	16	600	150	3803 ± 35
	97	17	1038	230	3830 ± 15
	100	8	1569	230	3774 ± 21
Mean for Profile 3					3807 ± 16
Mean for Station C-16					3783 ± 9
			Station J9DC		
1	18	18	602	180	3772 ± 13
	19	21	782	230	3789 ± 14
	20	24	1012	230	3793 ± 11
	21	18	1242	230	3786 ± 11
	22	24	1472	230	3709 ± 9
Mean for Profile 1					3790 ± 7
2	42A	10	600	90	3772 ± 45
	43	24	690	230	3801 ± 28
	44	24	920	230	3805 ± 18
Mean for Profile 2					3801 ± 16
3	57	19	602	180	3767 ± 26
	59	23	782	230	3777 ± 12
	60	23	1000	690	3810 ± 4
Mean for Profile 3					3806 ± 8
Mean for Station J9DC					3797 ± 7
			Station Q13		
1	241	18	602	180	3803 ± 17
	242	20	782	230	3801 ± 12
Mean for Profile 1					3802 ± 10
2	308	19	602	180	3802 ± 17
	309	24	782	230	3785 ± 16
Mean for Profile 2					3793 ± 13
Mean for Station Q13					3799 ± 9
Overall mean					3794 ± 6

[1974] estimated the temperature coefficients of velocity in the ice to be -2.3 ± 0.17 m s^{-1} K^{-1} for P waves and -1.2 ± 0.24 m s^{-1} K^{-1} for S waves. Corrections for the effect of temperature are therefore negligible and were not applied.

Calculating the error in the velocity-depth function as it propagates from the random scatter of the time-distance data through v(x) and the integration process is difficult. Instead, velocity-depth values were calculated separately for the subsets of the original travel time points falling respectively above and below the best fitting curve, and these curves were used as approximations to probable-error bounds. Error estimates made on the least and the most scattered data sets differed little. Standard errors calculated from the values of probable error thus obtained were, for v_p, ±60 m s^{-1} near the surface, dropping off to about ±30 m s^{-1} at 10-m depth, ±15 m s^{-1} at 50 m, and slightly less beyond this depth. For v_s the standard error estimates are about the same; in the lowest 10 m or so the estimated standard error of about ±15 m s^{-1} is superimposed upon the systematic error discussed earlier.

Previous determinations [Crary et al., 1962a, b] have placed a 100-m limit on the depth to the maximum velocity in the Ross Ice Shelf. To sample this depth, the shot-geophone separation should (from ray-tracing analyses) be about 6 times the depth, or about 600 m. Robertson [1975] and Robertson and Bentley [this volume] experimentally found this to be a satisfactory minimum distance. Therefore cross-spread velocity values were computed on P wave shots at distances beyond 600 m by linear least squares. From these, values for the maximum velocities were determined (Table 3) for comparison with those from the nonlinear regression analysis (Table 2).

Densities were computed as a function of depth using Kohnen's [1972] empirical relation between P wave velocity and density [Robertson, 1975; Kirchner et al., 1979; Robertson and Bentley, this volume]. (We chose 3860 m s^{-1} for the P wave velocity in solid ice, whereas Robertson and Bentley [this volume] use 3850 m s^{-1}; the corresponding difference in ρ amounts to no more than 0.003 Mg m^{-3}. See Robertson and Bentley [this volume] for a further discussion.) The densities calculated from the seismic velocities are listed in Appendix B (microfiche). Since the relationship between density and velocity based on Kohnen's relation is not linear, errors were approximated by evaluating the densities from the upper and lower velocity-depth curves described above. That process yields estimated standard errors of about ±0.024 Mg m^{-3} at the surface, decreasing to ±0.008 Mg m^{-3} at 40-m depth and to about ±0.002 Mg m^{-3} at the final depth.

Exponential functions of the form $dv_p/dz = (dv_p/dz)_o \exp(-\gamma z)$, where $(dv_p/dz)_o$ and γ are constants, were found by Kohnen and Bentley [1973], Robertson and Bentley [1975], and Robertson and Bentley [this volume] to fit segments of curves of P wave velocity versus depth at most of their stations in Antarctica. They also found that the depths at which the constants change correspond to depths at which there are changes in the predominant densification process. Accordingly, we have performed a similar analysis of dv_p/dz at the sites discussed in this paper. Plotted results are presented in Appendix C (microfiche), and the results are discussed in the discussion section.

Attempts to determine densification zones using S wave velocity gradients proved unsuccessful. In most cases the plots exhibited one break in slope, in the 15- to 30-m range (Figure 4); however, this break, which occurs in a range between breaks in the curves of dv_p/dz versus z, could not be correlated with any known physical property in the firn.

Stations

A detailed look at the results of each station is presented next. SV wave and SH wave velocities are designated v_{sv} and v_{sh}, respectively. The five constants and the rms residuals from the best fit to each data set are given in Table 2. Plots of travel times and the corresponding best fitting curves are in Appendix A. These graphs extend only to distances of 600 m to prevent smearing of earlier points due to scale compression.

Station C-16

At station C-16, three lines were laid out 60° apart in azimuth. P waves were recorded along all three lines; S waves (both SH and SV) were recorded along the magnetic N-S line (line 1) only. Curves of v_p versus depth derived from each of the three profiles are plotted together in Figure 5. Lines 1 and 3 agree well throughout the depth range, whereas line 2 exhibits a 4-5% lower velocity in the 10- to 30-m depth range. This difference, which is about 140 m s^{-1} maximum, is significantly larger than the experimental error (about ±30 m s^{-1}) and indicates some minor anisotropy or inhomogeneity. Results from a topographic survey of the local area around C-16 indicate a wavelike distribution of ridges with a wavelength of about 1 km and a height of about 0.5 m [Shabtaie and Bentley, 1982]. These ridges trend approximately parallel to the flow direction and

are believed to be remanent from longitudinally trending rolls observable on air photos of Beardmore Glacier, the source region for the ice at C-16 (S. Shabtaie, personal communication, 1984). Profile 2 was oriented nearly parallel to the ridges.

The maximum values of v_p for lines 2 and 3 were 3803 m s^{-1} at 69-m depth and 3809 m s^{-1} at 77-m depth, respectively. (Line 1 was not long enough to reach maximum velocity.) These values are close to the values for the cross-spread velocities at distances greater than 600 m (see Table 3).

A velocity-depth curve at C-16 also was obtained from a short-refraction profile on the 1957-1958 Ross Ice Shelf traverse [Crary et al., 1962a]. The 1957-1958 values at a given depth (the azimuth of the profile was not recorded) fall within the range of values for the three profiles of the present study, which indicates that the firn-ice column in this area has not changed measurably over the intervening 19 years.

Shear waves were recorded only along line 1; the resulting curves of v_{sh} and v_{sv} versus depth are given in Figure 6. Significant variations in the velocities exist between these wave types. Two intersections between the two velocity-depth curves, such as are seen here, occur also on the shear wave profiles at RIGGS III base camp RI [Robertson, 1975; Robertson and Bentley, this volume] and at stations Q13 and J9DC (this paper; see Table 4).

Station J9DC

Profiles were completed along four lines at J9DC, the site of the Ross Ice Shelf drilling project. P waves were recorded along lines 1, 2, and 3, which were separated by 60° in azimuth, and SH and SV waves were recorded along lines 1 and 1A, 90° apart (see Table 1 for specifications of the lines). Previous measurements of v_p at a site about 2 km away (J9DS) were conducted during the RIGGS II survey [Robertson, 1975; Robertson and Bentley, this volume].

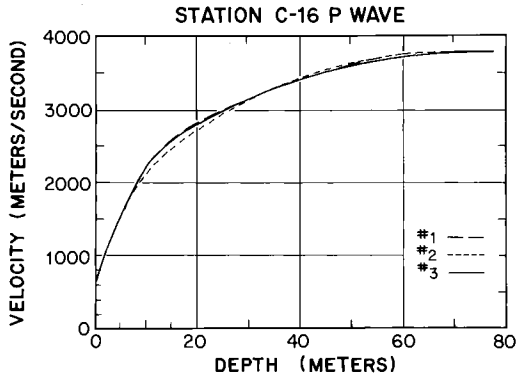

Fig. 5. Velocity-depth curves, station C-16, P waves.

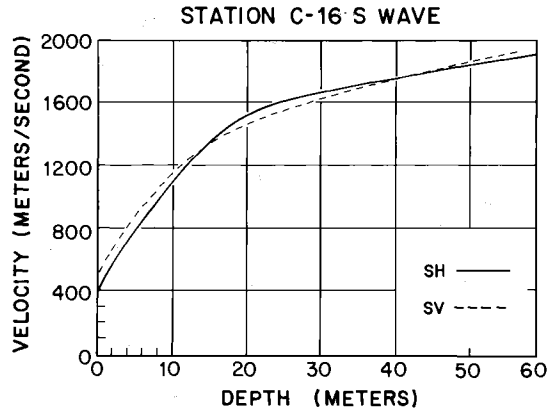

Fig. 6. Velocity-depth curves, station C-16, S waves.

The three v_p versus depth functions (Appendix B) do not differ significantly from each other until the maximum velocity is approached. Lines 2 and 3 reach velocities of 3802 m s^{-1} at 54 m (650-m distance) and 3801 m s^{-1} at 56 m (600-m distance), respectively, whereas line 1 reaches only 3764 m s^{-1} at 53-m depth (600-m distance), as reflected in the low value of v_m (Table 2). Although this difference does not show clearly in the velocity-depth plot (Figure 7), it does in the travel time plots (Appendix A), the travel time being about 5 ms greater at 600 m for profile 1 than for profiles 2 and 3. However, the cross-spread velocities determined from least squares at distances beyond 600 m (Table 4) suggest that all three profiles approach velocities slightly over 3800 m s^{-1} at distances over a kilometer or so. We interpret these results as meaning that there is a slight deviation from horizontal layering in the firn layers around 50 m deep but that the ice beneath is isotropic, at least transversely.

A comparison of the travel time data from station J9DC with those from RIGGS II station J9DS, about 2 km away, reveals a pronounced divergence (Figure 8). Arrivals for the profile at J9DS are as much as 6 ms later than those at J9DC for the same distances. Density-depth plots calculated from the two seismic profiles are shown in Figure 9, along with densities [Langway, 1975] measured on core recovered from a 100-m hole at J9DS. Clearly, the directly measured and seismically derived densities at J9DS are in much closer agreement with each other than with the seismically derived densities at J9DC.

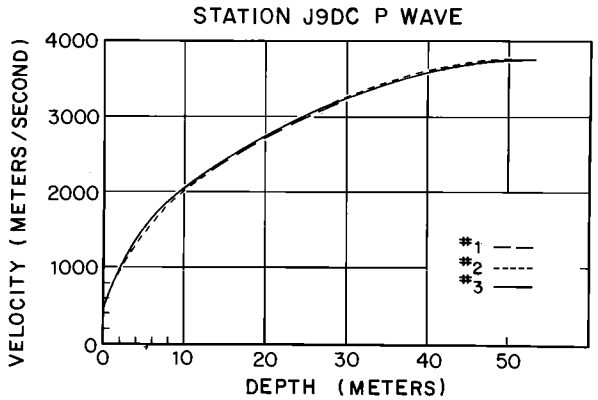

Fig. 7. Velocity-depth curves, station J9DC, P waves.

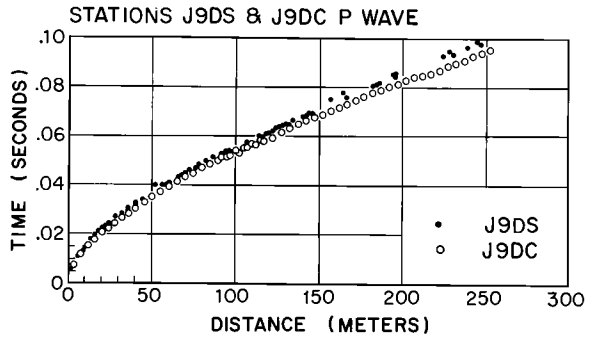

Fig. 8. Travel times for P wave profiles at adjacent stations J9DS and J9DC.

Apparently, there is a significant horizontal variation in density even over a distance of only about 2 km in a region far from any evident large stress gradients. For a further discussion, see Kirchner et al. [1979].

The velocity-depth curves for the shear waves along lines 1 and 1A are combined in two ways, to compare v_{sh} and v_{sv} on each line (Figures 10 and 11) and to compare the two curves for each wave type (Figures 12 and 13). Line 1 (Figure 10) shows the doubly intersecting pattern mentioned previously in the section on station C-16, but line 1A (Figure 11) does not. Figure 12 shows that the SV waves along the two lines give rather similar results, particularly when one recalls the uncertainty associated with the deeper parts of the velocity-depth curves. The two v_{sh} profiles (Figure 13), however, are markedly different, as can be seen also by comparing the travel time curves (Appendix A) directly. These results seem clearly to indicate some kind of anisotropy, rather than just inhomogeneity, in the firn layers. We have not been able to devise a model to explain the P, SV, and SH observations all at once.

Station Q13

At Q13, about 100 km from the ice front, two lines, 45° apart, were profiled. Both lines extended beyond 1000 m for the P wave, but line 1 was fitted only out to 782 m because the record for the distance range 782 m to 812 m did not have a good time break. However, that record was still useful in determining the maximum cross-spread velocity. The SH and SV profiles extend to various distances because of different signal-to-noise ratios.

The two curves of v_p versus depth are very similar (Figure 14) with only a slight divergence below 30-m depth. This difference (line 2 greater by about 1%) is not large enough surely to be real.

The shear wave data from station Q13 (Figures 15 to 18), of all the sites, exhibited the least scatter when applied to the fitted model, as shown by the rms residual (Table 2). The Q13 S wave data as a whole indicate that pronounced anisotropy occurs in the upper 30 m of the firn. Surprisingly enough, at depths between 10 m and about 30 m, v_{sh} on line 2 shows closest agreement with v_{sv} on line 1, and v_{sh} on line 1 agrees with v_{sv} on line 2. At about 30- to 35-m depth,

TABLE 4. Depth to Intersections of v_{sv} and v_{sh} Curves and v_p Gradient Changes

	C-16 Line 1, m	J9DC Line 1, m	Q13 Line 2, m	R.I.,[a] m
Depth to "B"	17	10[b]	12	13
$v_{sv} > v_{sh}$ to $v_{sv} < v_{sh}$	14	13	8	12
$v_{sv} < v_{sh}$ to $v_{sv} > v_{sh}$	41	43	35	43
Depth to "D"	54[c]	~35[b]	~40	54

[a]From Robertson and Bentley [this volume].
[b]From J9DC line 3.
[c]From C-16 line 2.

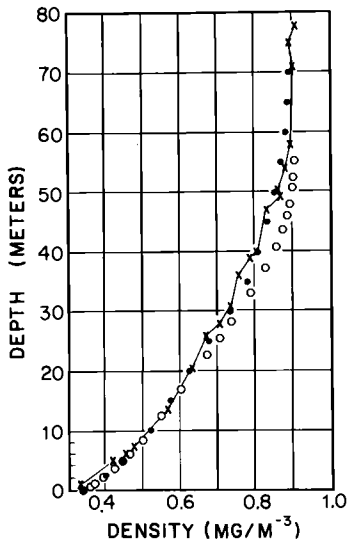

Fig. 9. Density versus depth as measured on core samples at station J9 (crosses), calculated from v_p at station J9DS (solid circles), and calculated from v_p at station J9DC (open circles).

all the curves converge to within 1% of each other; the apparent divergence in the deepest 10 m is of doubtful reality for the reason explained earlier.

Station H13

Station H13 is located near the mouth of Beardmore Glacier. Surface ridges that suggest a history of large horizontal compressive stresses were visible in this area. However, the seismic work was performed within a region of relatively flat surface topography. This station was occupied for 1 day only; so the seismic information is limited to P wave studies to a maximum distance of 322 m.

Comparison of the curve of v_p versus depth (Figure 19) from this station with those from our other stations (Figure 3) and with all of the other RIGGS short-refraction profiles [Robertson and Bentley, this volume; Albert and Bentley, this volume] shows that velocities are slightly higher than average in the near-surface region (to 10 m) and lower than average from 20- to 50-m depth. The maximum velocity (3809 m s^{-1} at 66 m), however, is similar to velocities from other stations. These characteristics are reflected in the density-depth curves shown in Figure 23.

The portion of the ice shelf adjacent to Beardmore Glacier is in a region of high

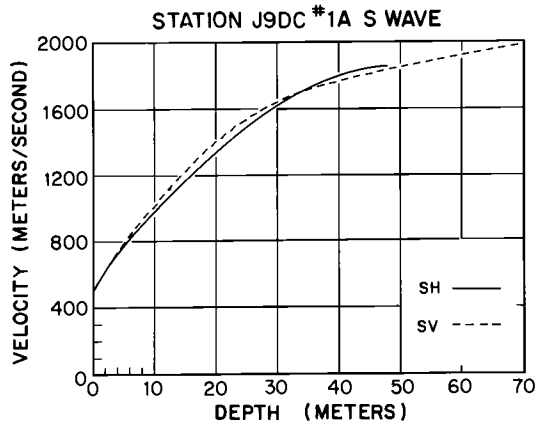

Fig. 11. Velocity-depth curves, station J9DC line 1A, S waves.

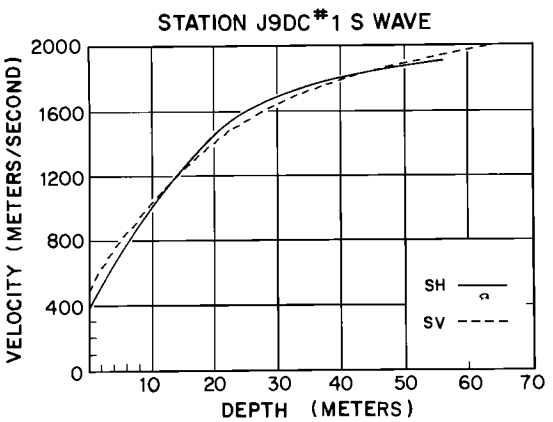

Fig. 10. Velocity-depth curves, station J9DC line 1, S waves.

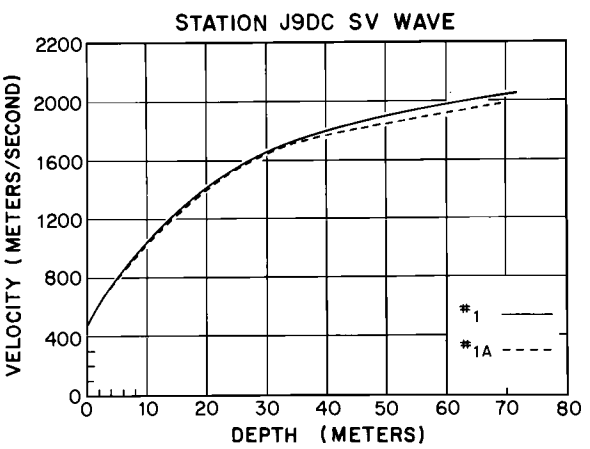

Fig. 12. Velocity-depth curves, station J9DC, both lines, SV waves.

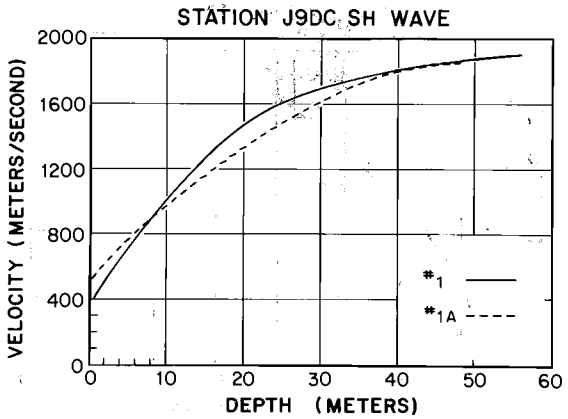

Fig. 13. Velocity-depth curves, station J9DC, both lines, SH waves.

accumulation rate [Clausen et al., 1979]. At a given temperature a greater accumulation rate leads to a more gradual increase of density with depth [Gow, 1968]. This is probably the reason for the lower than average densities found in the 20- to 50-m depth range. The cause of the higher than average near-surface velocity is not certain; it may be wind packing by strong drainage winds blowing down the glacier or a strong barrier wind blowing parallel to the mountain front.

Station M14

Station M14 is located near the center of the ice shelf. As at the other 1-day stations, only v_p was measured. The velocity-depth curve (Figure 20) shows no unusual trend. Maximum velocity was not reached by the 320-m-long profile.

Station N19

Station N19 was located about 15 km downstream from the mouth of Byrd Glacier. The profile was in a region of complicated stress history, as is shown by the numerous surface cracks, blue ice patches, and pressure ridges. The ridges were approximately 50-75 m apart and trended nearly perpendicular to the outflow direction. The surface was observed to be free of recent accumulation and wind packing was evident.

The P wave time-distance plot (Figure 21) exhibits large deviations from a smooth curve. The two nearly straight line segments between 0 and 50 m represent separate records, and the second half of each record exhibits nearly complete attenuation of the arriving energy, which suggests a buried crevasse beneath the spread. Direct arrivals on the reflection records at this site also exhibited this loss of energy. The lack of curvature evident in the near-surface region indicates discrete layers, and the offsets suggest a large dip of the layers (estimated to be about 10°-15°) beneath the recording spread. At large distances the time-distance curve exhibits large scatter as well as the en echelon pattern indicative of dipping horizons; both effects presumably stem from the extreme crevassing on Byrd Glacier [Swithinbank, 1963].

Because of this scatter, curve fitting to this profile was unsatisfactory. Smoothing was attempted in several ways but without success, since different initial estimates for the constants always generated different curve shapes. Two approximate curves were therefore drawn by eye, representing two bounding fits to the travel times in a smoothed sense (Figure 21), thus yielding a reasonable range for the velocities. (The fits were less awkward when low travel times at distances <200 m were combined with high travel times at distances >200 m and vice

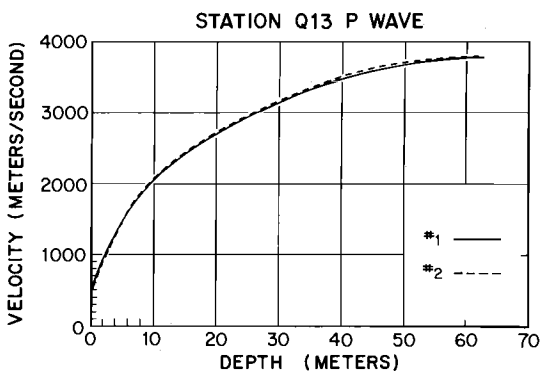

Fig. 14. Velocity-depth curves, station Q13, P waves.

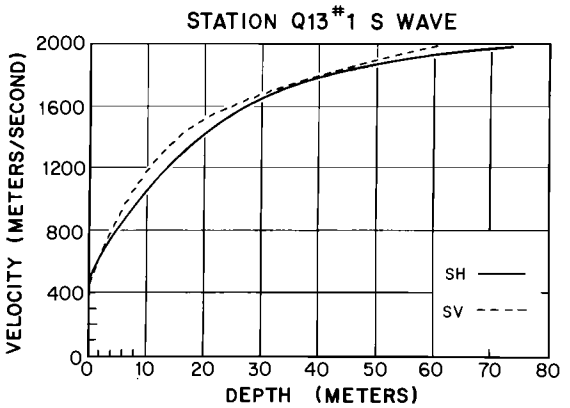

Fig. 15. Velocity-depth curves, station Q13, line 1, S waves.

versa, as was done in Figure 21, than when all high and all low values were fit separately.) An average of the two v_p versus depth curves was taken; all three curves are shown in Figure 22, and the average curve is included in Figure 3. The velocities (and hence the derived densities) at all depths are much larger than those at other sites. Relatively high densities are also shown by apparent resistivities which, at station N19, are much less than those at stations C-16, Q13, J9DC, and M14 [Shabtaie and Bentley, 1979]. The high densities presumably result from the combined effects of high deflation and stress on Byrd Glacier, as discussed by Crary and Wilson [1961] for another outlet glacier.

Future profiles in areas near high-stress fields should be located, if possible, on less deformed surfaces and should be reversed.

Discussion

At stations C-16, J9DC, and Q13, v_p exhibits only small differences as a function of azimuth (the largest is about 4% in the 10-to 25-m range at station C-16); so the calculated velocity-depth and density-depth curves, assuming Kohnen's equation is valid, are probably accurate. A plot of density versus depth for each station is shown in Figure 23, and the discrete values are found in Appendix B. The maximum variation of density at a given depth is about 10% for the RIGGS III stations, as it is for all stations on the Ross Ice Shelf, except those in areas of unusually high stress [Crary et al., 1962a; Robertson, 1975; Robertson and Bentley, this volume].

The variations presumably reflect different densification rates at different places on the ice shelf. The densification rate is known to be a function of accumulation rate (b_o) and temperature (T). Areas of high accumulation tend to show smaller densities at a given depth than areas of low accumulation, and higher temperatures tend to speed up the densification process [Gow, 1968].

As an approach to quantifying those relationships, Robertson and Bentley [1975] considered plots of $\ln (dv_p/dz)$ versus z. It had already been proposed by Kohnen and Bentley [1973] that segments of constant slope on such plots represent depth regions within which a particular densification process predominates and consequently that abrupt slope breaks correspond to the depths at which the densification mechanism changes. Robertson and Bentley [this volume] correlate horizon "B" with the depth below which no further packing of the grains by grain boundary sliding can occur [Alley, 1987]; that depth corresponds to a density of about 0.5-0.6 Mg m^{-3}. Another break ("D") corre-

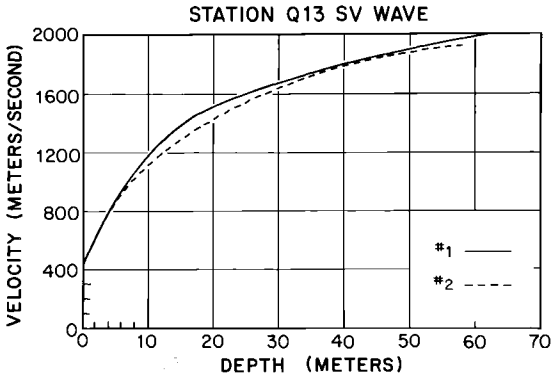

Fig. 17. Velocity-depth curves, station Q13, both lines, SV waves.

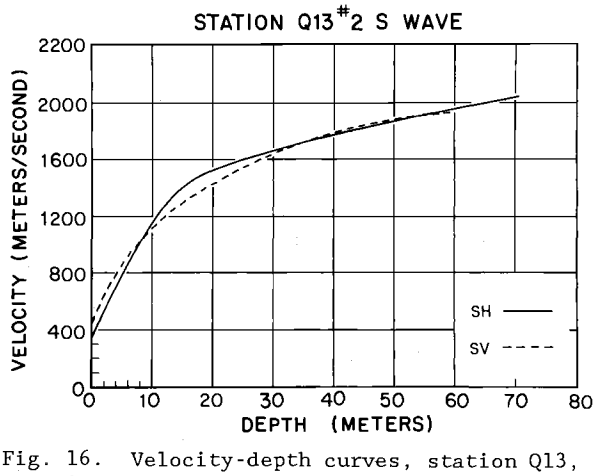

Fig. 16. Velocity-depth curves, station Q13, line 2, S waves.

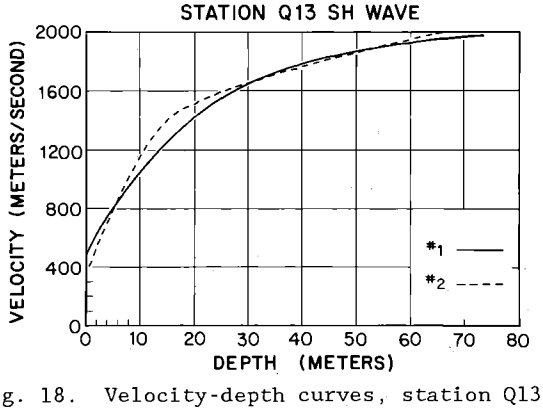

Fig. 18. Velocity-depth curves, station Q13, both lines, SH waves.

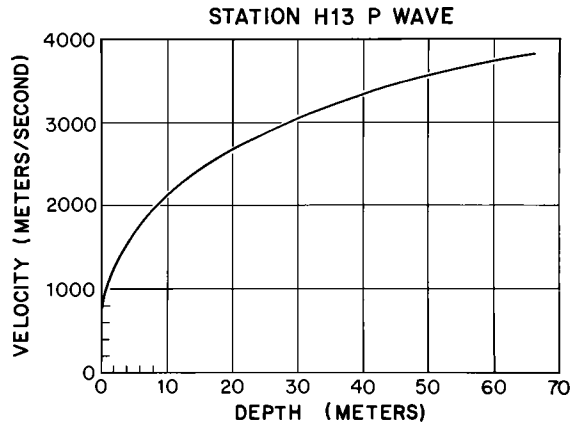

Fig. 19. Velocity-depth curve, station H13, P waves.

lates with the firn-ice boundary (the depth at which the firn becomes impermeable).

In the present study the mean value for the depth to "B," 14 ± 3 m, is greater than that, 9 ± 2 m, for the West Antarctic stations from Robertson and Bentley [1975], although the difference is not highly significant statistically. Our value is closer to the mean depth of 11 ± 2 m found by Robertson and Bentley [this volume] for RIGGS I and II stations on the grid western portion of the ice shelf. Robertson and Bentley [1975] found a good correlation between the depth to B and the mean temperature and mean accumulation rate. Unfortunately, the range of accumulation rates and temperatures in the present study is not great enough to provide any test of Robertson and Bentley's [1975] regression coefficients (Table 5).

Robertson and Bentley [1975] reported a "C" break in slope between "B" and "D," principally at stations where the accumulation rate was relatively high. The form of our equation (1) does not allow for a third exponential segment in the velocity gradients. Because of the relatively low accumulation rate on the Ross Ice Shelf [Clausen et al., 1979] and the excellent fit to the data provided by equation (1), we have not sought a "C" break at our stations. However, studies at Dome C on the East Antarctic plateau carried out since this work was done showed that at least there, a third exponential term does further improve the fit to the observed data [Gassett, 1982], as one might expect from the three velocity gradient zones in the firn found by Robertson and Bentley [1975]. We have not pursued this point in the present paper.

Maximum P wave velocities, $(v_p)_{max}$, obtained from refraction shooting on the ice shelf, are lower than those both from refraction shooting on grounded ice sheets and from laboratory measurements (see discussion by Robertson and Bentley [this volume]). The mean v_m computed using nonlinear regression is 3792 ± 16 m s^{-1}, and the mean value $(v_p)_{max}$ obtained by least squares fit of the cross-spread velocities on all shots at a distance of 600 m or greater is 3794 ± 6 m s^{-1} (Table 3). These values are essentially the same as those found in a similar way by Albert and Bentley [this volume], also in the grid eastern part of the ice shelf: 3792 m s^{-1} and 3795 m s^{-1} for two measurements of v_m and 3705 m s^{-1} to 3880 m s^{-1} for the several cross-spread velocities (spread length ≥300 m) at large distances. They also agree reasonably well with the mean from the grid western part of the ice shelf: 3811 ± 7 [Robertson, 1975; Robertson and Bentley, this volume]. The cause of the difference between velocities measured on ice shelves and those measured on

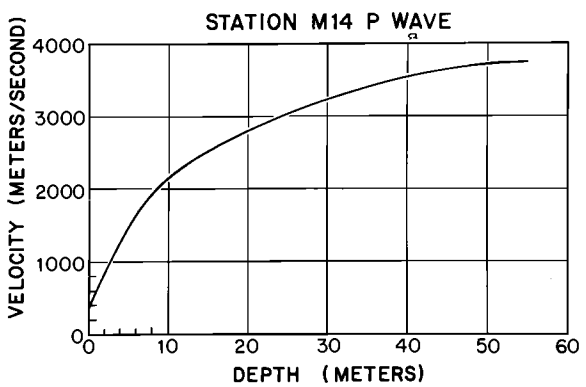

Fig. 20. Velocity-depth curve, station M14, P waves.

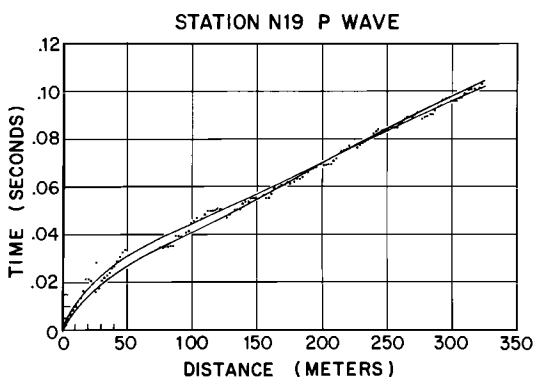

Fig. 21. Travel times (dots) for P waves at station N19, together with two bounding fitted curves.

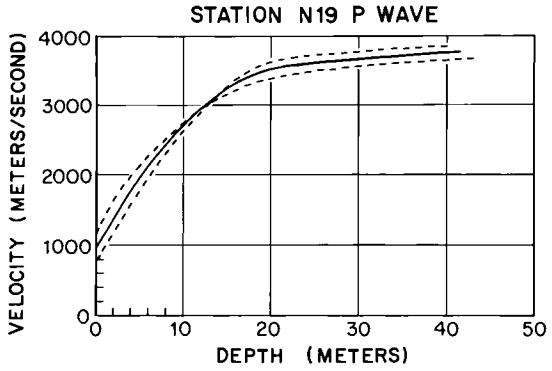

Fig. 22. Velocity-depth curves, station N19, for the fitted travel time curves of Figure 2 (dashed lines), together with an average velocity-depth curve (solid line).

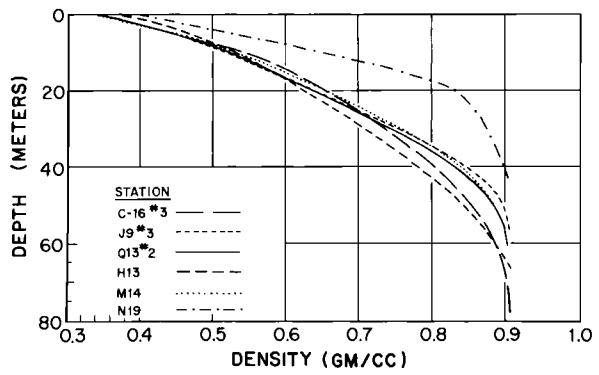

Fig. 23. Density-depth curves calculated from v_p at each of the stations.

grounded ice (~3850 m s^{-1} at the same temperature) is not understood (see discussion by Robertson and Bentley [this volume]).

S waves are more sensitive indicators of anisotropy than P waves because, in a single crystal, the two polarizations exhibit different velocities for all nonzero angles of propagation relative to the c axis. Also, v_{sv} in particular shows a greater deviation from the isotropic mean than v_p (the deviation is about 10% for v_{sv}, 6% for v_{sh}, and 5% for v_p). The velocity differences at stations C-16, J9DC, and Q13 indicate that the firn in the upper 30 or 40 m of the ice shelf (at least at these stations) is not transversely isotropic about a vertical axis of symmetry.

The v_{sh} curves (Figures 6, 10-13, and 15-18) show large differences along different azimuths: as much as 30-40% in the upper 5-10 m and 9-12% down to 30- to 40-m depth. The differences are not so large for v_{sv}: a maximum of 8% in the 5- to 35-m depth range at station Q13. Plots of v_{sv} and v_{sh} along the same line show either a doubly intersecting pattern (Figures 6, 10, and 16), as was previously reported at RIGGS III base camp RI by J. D. Robertson [Robertson, 1975; Robertson and Bentley, this volume], or a curve in which v_{sv} is higher over most of the depth range sampled (Figures 11 and 15). For the profiles exhibiting the doubly intersecting pattern (C-16, Figure 6; J9DC line 1, Figure 10; and Q13 line 2, Figure 16), v_{sv} and v_{sh} along the same line show differences as large as 25% in the upper 10-15 m and 5-8% between 15- and 40-m depth. The other two pairs of curves of v_{sh} and v_{sv} along a single line (J9 line 1A, Figure 11; Q13 line 1, Figure 15) show v_{sv} a maximum of 6-12% larger over the 5- to 35-m depth range; profile J9 line 1A also shows v_{sh} larger beyond 35 m by

TABLE 5. Depths to Slope Breaks in Semilog Plots of dv_p/dz Versus Depth, With Associated Surface Accumulation Rates (Water Equivalent) and Ten-Meter Temperatures

Station	Accumulation Rate, m	Temperature	Profile Number	Depth to Break B, m	Depth to Break D, m
C-16	0.11[a]	-26.4	1	17	≥53
			2	14	54
J9DC	0.09[b]	-27.6[b]	3	10	~35
Q13	0.16	-27.1	2	12	~40
H13	0.19	-21.1		17	≥60
M14	0.09[a]	-26.9[c]		13	46
Mean				13.8 ± 2.8	

[a]Interpolated from Clausen et al. [1979].
[b]Taken from station J9.
[c]Interpolated from Thomas et al. [1984].

about 2%, but the reality of this is questionable because it appears near the ends of the velocity-depth curves.

At the four stations where the "double-intersection" pattern is seen, the intersections occur at similar depths (see Table 4). Furthermore, in all cases except Q13 line 2, the profiles trend approximately parallel to the flow vectors, which might indicate some sort of regional effect. Profile Q13 line 2, which is the closest to the ice front and also is the most different in terms of depths to the intersections, trends about perpendicular to the flow.

The depths to the intersections, accurate to about ±1 m, agree roughly with the "B" and "D" levels from the analyses of dv_p/dz (Table 4), so it seems likely that the different $v_{sv} > v_{sh}$ and $v_{sv} < v_{sh}$ zones are also related to the zones of different densification processes. It is reasonable to suppose that in the upper zone of grain rearrangement on the Ross Ice Shelf, as well as on the neighboring Siple Coast of the West Antarctic inland ice [Alley, 1987], the connectivity between grains is greater vertically than horizontally. This should apply to all profiles, if it is a general phenomenon, and indeed v_{sv} is greater than v_{sh} in the upper 15 m or so on all profiles.

The results at greater depth are complex and do not yield a ready explanation. Bentley [1971] used a single-crystal model as a reasonably good approximation to a random distribution of c axial directions within a cone (if the apex angle of the cone is not larger than 25°). We have attempted to fit the J9DC and Q13 maximum velocities (v_p, v_{sv}, and v_{sh}) to a single-crystal model utilizing the velocities calculated as a function of c axis inclination I and azimuth and angle of incidence of the seismic ray [see Bentley, 1971, Tables 1 and 2]. The angle of incidence in our case is 90°. Inspection of the J9DC data, which consist of lines along four different azimuths (see Table 1), showed that no fit was possible for $I \leq 30°$ and that the best fits occurred for I between 75° and 90°. The Q13 data consist of only two lines and are therefore less constrained, with several fits possible. No fit was found for $I < 20°$, but several possible fits were found for I between 20° and 90°, with the best fit occurring for $I \geq 75°$. If the single-crystal model were valid, therefore, it would imply that a near-horizontal preferred orientation of the c axes would be likely.

A study of cores recovered at Little America V, near the front of the Ross Ice Shelf, shows instead a preferred vertical c axis orientation that appears first at about 60 m and becomes well developed by 100 m [Gow, 1963]. However, a single-maximum pattern is not observed at all; instead, several maxima, lying more or less conically about the vertical, occur. For example, the petrofabric diagram at 116-m depth shows 75% of the c axes oriented within 35° of the vertical, but very few within 10°.

Several factors thus make model fitting a difficult task:

1. A single-maximum model almost surely is not relevant; the Little America V petrofabrics reveal multiple maxima, and the seismic evidence at other stations that requires a large inclination of the pole of a single-maximum pattern, if it were to exist, also makes such a model unlikely.

2. The rapid changes in the number of maxima with depth, if they occur elsewhere as at Little America V, further complicate the matter. These changes may occur over a small depth range, in which case the seismic waves, with wavelengths of several meters, may be averaging several orientations.

3. Crystal anisotropy may be only a partial cause of the observed velocity distribution; structural effects (such as ice lenses, subsurface fold structures, etc.) may contribute also. These surely occur in the upper 30-40 m of the ice shelf (as they do at Little America V [Gow, 1963]), where large velocity differences occur; there may be lingering effects at greater depths also.

The results at stations J9DC and Q13 indicate anisotropy in the horizontal as well as the vertical plane. Although the fact that stations J9DC and Q13 are widely separated on the ice shelf suggests that the phenomenon could be widespread, we have no supporting or contradictory evidence, since shear wave profiles along different azimuths do not exist elsewhere. Anisotropy in the horizontal plane could arise from anisotropy in the crystalline fabric, if there were multiple poles, such as found by Gow [1963] at Little America (but there they occur only at depths greater than 65 m). Another possibility is textural anisotropy; for example, Gow [1963] found air bubble elongation preferentially along a particular horizontal direction at depths between 90 and 130 m at Little America. However, with so little information, we will not speculate further on the cause of the seismic anisotropy. We will comment only that the seismic refraction results seem to support ice thickness measurements [Bentley et al., 1979] and paleo-flow-line studies [Jezek, 1984] in indicating an ice shelf not only acted on by a complicated field of stress, but also still showing the effects of earlier deformational events.

Acknowledgments. The authors wish to express their appreciation to the other mem-

bers of the University of Wisconsin field party, D. G. Albert, L. L. Greischar, K. C. Jezek, H. Pollak, and S. Shabtaie, for their aid in all aspects of our work. We are also grateful for the cooperation of members of the groups from the University of Maine, the U.S. Geological Survey, and the University of Copenhagen. Excellent air support in Twin Otter aircraft was supplied by the British Antarctic Survey and Bradley Air Services, Ltd. We thank P. Dombrowski and S. H. Werther for drafting illustrations and A. N. Mares and J. V. Campbell for manuscript preparation. This work was supported by the National Science Foundation under grants DPP72-05802, DPP76-01415, DPP79-20736, and DPP-8119989. This is contribution 491 of the Geophysical and Polar Research Center, University of Wisconsin, Madison.

References

Albert, D. G., and C. R. Bentley, Seismic studies on the grid eastern half of the Ross Ice Shelf: RIGGS III and RIGGS IV, in The Ross Ice Shelf: Glaciology and Geophysics, Antarct. Res. Ser., vol. 42, edited by C. R. Bentley and D. E. Hayes, AGU, Washington, D. C., this volume.

Alley, R. B., Texture of polar firn for remote sensing, Ann. Glaciol., 9, 1-4, 1987.

Bentley, C. R., Seismic anisotropy in the West Antarctic ice sheet, in Antarctic Snow and Ice Studies II, Antarct. Res. Ser., vol. 16, edited by A. P. Crary, pp. 131-177, AGU, Washington, D. C., 1971.

Bentley, C. R., The Ross Ice Shelf Geophysical and Glaciological Survey (RIGGS): Introduction and summary of measurements performed, in The Ross Ice Shelf: Glaciology and Geophysics, Antarct. Res. Ser., vol. 42, edited by C. R. Bentley and D. E. Hayes, pp. 1-20, AGU, Washington, D. C., 1984.

Bentley, C. R., J. W. Clough, K. C. Jezek, and S. Shabtaie, Ice thickness patterns and the dynamics of the Ross Ice Shelf, J. Glaciol., 24, 287-294, 1979.

Clausen, H. B., W. Dansgaard, J. Nielson, and J. W. Clough, The surface accumulation on the Ross Ice Shelf, Antarct. J. U. S., 14, 68-72, 1979.

Clough, J. W., and B. L. Hansen, The Ross Ice Shelf Project, Science, 203, 433-434, 1979.

Crary, A. P., and C. R. Wilson, Formation of "blue" glacier ice by horizontal compressive forces, J. Glaciol., 3, 1045-1050, 1961.

Crary, A. P., E. S. Robinson, H. F. Bennett, and W. W. Boyd, Jr., Glaciological studies of the Ross Ice Shelf, Antarctica, 1957-60, IGY Glaciol. Rep. 6, Int. Geophys. Year World Data Center A, Glaciol., Am. Geogr. Soc., New York, 1962a.

Crary, A. P., E. S. Robinson, H. F. Bennett, and W. W. Boyd, Jr., Glaciological regime of the Ross Ice Shelf, J. Geophys. Res., 67, 2791-2807, 1962b.

Draper, N. R., and H. Smith, Applied Regression Analysis, 683 pp., chap. 3 and 10, John Wiley, New York, 1966.

Gassett, R. M., Seismic refraction study at Dome C, Antarctica, M.S. thesis, Univ. of Wis., Madison, Wis., 1982.

Gow, A. J., The inner structure of the Ross Ice Shelf at Little America V, Antarctica, as revealed by deep core drilling, IASH Publ. 61, 272-284, 1963.

Gow, A. J., Deep core studies of the accumulation and densification of snow at Byrd Station and Little America V, Antarctica, Res. Rep. 197, U.S. Army Cold Regions Res. and Eng. Lab., Hanover, N. H., 1968.

Grant, F. S., and G. F. West, Interpretation Theory in Applied Geophysics, 583 pp., McGraw-Hill, New York, 1965.

Jezek, K. C., Recent changes in the dynamic condition of the Ross Ice Shelf, Antarctica, J. Geophys. Res., 89, 409-416, 1984.

Kirchner, J. F., C. R. Bentley, and J. D. Robertson, Lateral density differences at a site on the Ross Ice Shelf, Antarctica, from seismic measurements, J. Glaciol., 24, 309-312, 1979.

Kohnen, H., Uber die beziehung zwischen seismischen geschwindigkeiten und der dichte in firn und eis, Z. Geophys., 38, 925-935, 1972.

Kohnen, H., The temperature dependence of seismic waves in ice, J. Glaciol., 13, 144-147, 1974.

Kohnen, H., and C. R. Bentley, Seismic refraction and reflection measurements at Byrd Station, Antarctica, J. Glaciol., 12, 101-111, 1973.

Langway, C. C., Jr., Antarctic ice core studies, Antarct. J. U. S., 10, 152-153, 1975.

Robertson, J. D., Geophysical studies on the Ross Ice Shelf, Antarctica, Ph.D. dissertation, 214 pp., Univ. of Wis., Madison, Wis., 1975.

Robertson, J. D., and C. R. Bentley, Investigations of polar snow using seismic velocity gradients, J. Glaciol., 14, 39-48, 1975.

Robertson, J. D., and C. R. Bentley, Seismic studies on the grid western half of the Ross Ice Shelf: RIGGS I and RIGGS II, in The Ross Ice Shelf: Glaciology and Geophysics, Antarct. Res. Ser., vol. 42, edited by C. R. Bentley and D. E. Hayes, AGU, Washington, D. C., this volume.

Shabtaie, S., and C. R. Bentley,

Investigation of bottom mass balance rates by electrical resistivity soundings on the Ross Ice Shelf, Antarctica, J. Glaciol., 24, 331-343, 1979.

Shabtaie, S., and C. R. Bentley, Tabular icebergs: Implication from geophysical studies of ice shelves, J. Glaciol., 28, 413-430, 1982.

Swithinbank, C. W. M., Ice movement of valley glaciers flowing into the Ross Ice Shelf, Antarctica, Science, 141, 523-524, 1963.

Thomas, R. H., D. R. MacAyeal, D. H. Eilers, and D. R. Gaylord, Glaciological studies on the Ross Ice Shelf, Antarctica, 1973-1978, in The Ross Ice Shelf: Glaciology and Geophysics, Antarct. Res. Ser., vol. 42, edited by C. R. Bentley and D. E. Hayes, pp. 21-53, AGU, Washington, D. C., 1984.

(Received December 23, 1987;
revised August 18, 1989;
accepted November 22, 1989.)

THE ANTARCTIC RESEARCH SERIES: STATEMENT OF OBJECTIVES

The Antarctic Research Series, an outgrowth of research done in the Antarctic during the International Geophysical Year, was begun early in 1963 with a grant from the National Science Foundation to AGU. It is a book series designed to serve scientists and graduate students actively engaged in Antarctic or closely related research and others versed in the biological or physical sciences. It provides a continuing, authoritative medium for the presentation of extensive and detailed scientific research results from Antarctica, particularly the results of the United States Antarctic Research Program.

Most Antarctic research results are, and will continue to be, published in the standard disciplinary journals. However, the difficulty and expense of conducting experiments in Antarctica make it prudent to publish as fully as possible the methods, data, and results of Antarctic research projects so that the scientific community has maximum opportunity to evaluate these projects and so that full information is permanently and readily available. Thus the coverage of the subjects is expected to be more extensive than is possible in the journal literature.

The series is designed to complement Antarctic field work, much of which is in cooperative, interdisciplinary projects. The Antarctic Research Series encourages the collection of papers on specific geographic areas (such as the East Antarctic Plateau or the Weddell Sea). On the other hand, many volumes focus on particular disciplines, including marine biology, oceanology, meteorology, upper atmosphere physics, terrestrial biology, snow and ice, human adaptability, and geology.

Priorities for publication are set by the Board of Associate Editors. Preference is given to research projects funded by U.S. agencies, long manuscripts, and manuscripts that are not readily publishable elsewhere in journals that reach a suitable reading audience. The series serves to emphasize the U.S. Antarctic Research Program, thus performing much the same function as the more formal expedition reports of most of the other countries with national Antarctic research programs.

The standards of scientific excellence expected for the series are maintained by the review criteria established for the AGU publications program. The Board of Associate Editors works with the individual editors of each volume to assure that the objectives of the series are met, that the best possible papers are presented, and that publication is achieved in a timely manner. Each paper is critically reviewed by two or more expert referees.

The format of the series, which breaks with the traditional hard-cover book design, provides for rapid publication as the results become available while still maintaining identification with specific topical volumes. Approved manuscripts are assigned to a volume according to the subject matter covered; the individual manuscript (or group of short manuscripts) is produced as a soft cover 'minibook' as soon as it is ready. Each minibook is numbered as part of a specific volume. When the last paper in a volume is released, the appropriate title pages, table of contents, and other prefatory matter are printed and sent to those who have standing orders to the series. The minibook series is more useful to researchers, and more satisfying to authors, than a volume that could be delayed for years waiting for all the papers to be assembled. The Board of Associate Editors can publish an entire volume at one time in hard cover when availability of all manuscripts within a short time can be guaranteed.

BOARD OF ASSOCIATE EDITORS
ANTARCTIC RESEARCH SERIES